A SEARCH FOR LAYERING IN THE OCEANIC CRUST

by

John Anthony Collins

B.Sc., National University of Ireland (1979)

M.Sc., University College of North Wales (1981)

SUBMITTED IN PARTIAL FULFILLMENT
OF THE REQUIREMENTS FOR THE DEGREE
OF DOCTOR OF PHILOSOPHY

at the

MASSACHUSETTS INSTITUTE OF TECHNOLOGY

and the

WOODS HOLE OCEANOGRAPHIC INSTITUTION

October 6, 1988

Signature of Author _____
Joint Program in Oceanography, Massachusetts Institute of Technology
and Woods Hole Oceanographic Institution

Certified by _____
Dr. G. Michael Purdy, Thesis Supervisor
Dept. of Geology and Geophysics, Woods Hole Oceanographic Institution

Accepted by _____
Dr. Marcia K. McNutt
Chair, Joint Committee for Geology and Geophysics, Massachusetts
Institute of Technology/Woods Hole Oceanographic Institution

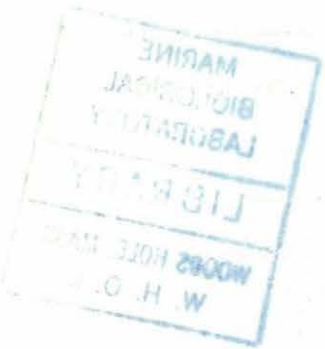
MARINE
BIOLOGICAL
LABORATORY
LIBRARY
WOODS HOLE, MASS.

A SEARCH FOR LAYERING IN THE OCEANIC CRUST

by

JOHN ANTHONY COLLINS

Submitted to the Department of Earth, Atmospheric and Planetary Sciences,
Massachusetts Institute of Technology
and
the Department of Geology and Geophysics,
Woods Hole Oceanographic Institution
on October 6, 1988
in partial fulfillment of the requirements
for the degree of Doctor of Philosophy

ABSTRACT

The results of numerous seismic refraction and reflection experiments have shown that the seismic structure of the oceanic crust can be usefully parameterized by a small number of locally horizontal layers within which the rates of change of velocity and impedance as a function of depth are approximately constant. Layer boundaries are defined by changes in velocity and/or impedance gradient. This dissertation discusses the structure of seismic layer boundaries within the oceanic crust, and investigates the relationships between the seismic characteristics of these boundaries and the geological structure of the crust.

The seismic signature of the crust/mantle boundary (Moho) is a prominent event on multichannel seismic (MCS) reflection data. In the Western North Atlantic, the character of the Moho reflection event varies from a single well-defined phase to a more complex event consisting of two or more overlapping phases of up to 1.0 s total duration. In Chapter 1 of this dissertation, the geological structures generating Moho reflections are investigated by calculating synthetic reflection profiles for three laterally varying velocity models totaling 64 km in length. These velocity models were derived from the observed distribution of lithologies that comprise the inferred fossil crust/mantle transition found in the Bay of Islands Ophiolite. Along the synthetic profiles, the Moho reflection is characterized by both single-phase and multi-phase events, the geometry and durations of the latter being similar to those observed on MCS data from the Western North Atlantic. In addition, the lateral variation in Moho travel time, up to 0.25 s over distances of less than 10 km, is similar to that observed on MCS data. The similarities between the observed and synthetic data suggest that the complicated interlayered sequences of mafic and ultramafic rocks that comprise the inferred crust/mantle transition in ophiolites might also be characteristic of the oceanic crust.

Although ophiolites provide a useful model of the lithological structure of the oceanic crust, the unambiguous correlation of geologic and seismic structures can only be achieved by conducting seismic experiments in the vicinity of deep crustal drillholes. Chapters 2 and 3 of this dissertation present analyses of the velocity and reflectivity structure of the crust in the immediate vicinity of Deep Sea Drilling Project Hole 504B in the Panama Basin, currently the deepest drillhole (1.288 km) into oceanic igneous crust.

Reflectivity synthetic seismogram modeling of amplitude features common to four sonobuoy profiles collected in the immediate vicinity of Site 504B shows that crustal thickness at the drillsite is only 5 km. A critical constraint on this interpretation is the observation, on four MCS profiles passing through the drillsite, of a near-normal-incidence reflection event with a crustal travel time of 1.4-1.5 s. This event is assumed to correlate with a wide-angle reflection/refraction event observed at ranges of 16-28 km on the sonobuoy profiles. Seismic modeling demonstrates that both of these events are generated at the Moho. The crustal velocity-depth profile at Site 504B is unusual in comparison to typical oceanic profiles in having high velocity gradients (up to 0.6 km s^{-1} km^{-1}) in the middle crust and a 1.8 km thick low-velocity zone (V_p=7.1-6.7 km s^{-1}) immediately above Moho. A simple explanation for this unusual profile is that the velocity of the middle crust has been increased by the addition of a high-velocity mineral component such as olivine. The olivine concentration of the middle crust need be no greater than 34-37%.

Hole 504B is the only site where the volcanics/sheeted-dike boundary, predicted by the ophiolite model to be a fundamental feature of oceanic crust, has been drilled. The downward change in rock type coincides with changes in a variety of logged physical properties. The normal-incidence travel time to this boundary is similar to the travel times of shallow reflection events observed in other areas. Accordingly, Site 504B is an ideal location to test the hypothesis that shallow reflection events correlate with the extrusives/dike boundary.

Despite extensive processing, MCS data collected in the immediate vicinity of Hole 504B show no conclusive evidence for a laterally coherent reflection event generated within the upper crust. The lack of a detectable reflection event from the upper crust is consistent with the results of synthetic seismogram modeling of velocity-depth profiles constructed from the logged downhole variation in physical properties. On these normal-incidence synthetic seismograms, low-amplitude reflections from the volcanic/dike contact are obscured by the high-amplitude basement reflection and by sediment-column multiples. In contrast to the synthetic reflection data, the seismic signature of the volcanics/dike boundary is readily recognizable on a synthetic wide-angle reflection/refraction profile. The change in velocity across this boundary causes focusing of refracted arrivals in the range window 6-7 km. High-amplitude arrivals are observed at similar ranges on the sonobuoy profiles collected near the drillsite, suggesting that at Site 504B, variations in depth to this layer boundary are more easily mapped with the wide-angle reflection/refraction method.

TABLE OF CONTENTS

PAGE

ACKNOWLEDGEMENTS

Mike Purdy provided much-needed encouragement, sound advice and example throughout the duration of my studies at WHOI. I thank Tom Brocher for guidance and support over the course of the work described here. Jeff Karson was quick to provide a geologist's perspective to my musings on oceanic seismic structure, and was always encouraging and supportive. I thank the other members of my committee, Peter Shaw and Jason Phipps Morgan, and the chairman of my defense, Dick Von Herzen, for their criticism and advice.

Many people made my stay at WHOI as productive and as pleasant as possible. Hans Schouten never allowed me to take my troubles too seriously. Kristin Rohr and Steve Swift were generous with both encouragement and criticism when needed. Lee Gove, David Dubois and Dickie Allison provided programming and data processing assistance. Doug Toomey and I endured much together during our years as a student. Maggie Goud gave greatly-appreciated encouragement, particularly over the last two years. Abbie Jackson and Jake Pierson were alwaps helpful. Julie Jones and Mark Hickey generously provided shelter and cheer during my many summers at WHOI. Brian O' Donovan provided a readily-accessible escape from the sometimes cloistered life in Woods Hole. I thank my parents for their encouragement and support throughout the many years of my formal education.

The work described in this dissertation was funded by the following National Science Foundation grants: OCE-81-17210, EAR-80-26445, EAR-83-9535, OCE-80-25206, OCE-84-10658, and OCE-87-00806.

INTRODUCTION

Study of the seismic structure of oceanic crust is motivated by the desire to understand the thermal, chemical and mechanical processes that control crustal accretion along spreading centers and crustal evolution as a function of age. To achieve this goal, marine geologists and geophysicists envision correlating seismic and geological structure, and subsequently using seismically determined variations in geological structure to constrain quantitative models of crustal accretion and evolution. In practice, attempts to understand these tectonic processes are unavoidably circular in logical approach; more detailed knowledge of seismic and geological structure prompts the development of more sophisticated models and vice versa. Obstacles to understanding these processes include (i) incomplete knowledge of seismic structure at appropriate length scales, (ii) difficulties in relating seismic and geological structure, and (iii) limited predictive powers of existing thermal, chemical and mechanical models. This dissertation is an effort towards overcoming the first two of these barriers.

Seismology is an imperfect tool for mapping the geological structure of oceanic crust; seismic velocities cannot be uniquely associated with rock type (e.g. Spudich and Orcutt, 1980a, 1980b; Karson and Fox, 1986), and seismic impedance contrasts, if derivable from the observed amplitudes of near-normal-incidence reflection events, cannot be uniquely related to changes in geological structure. Despite these obstacles, the goal of using seismic methods to map geological structure is probably achievable. This optimistic view is based on the remarkable similarity in crustal seismic structure from ocean to ocean, irrespective of such parameters as

crustal age and spreading rate (Table 1). Oceanic seismic structure can be characterized by a small number of locally horizontal layers within which the rates of change of velocity and impedance as a function of depth are approximately constant. Layer boundaries are defined by changes in velocity and/or impedance gradient. This layered seismic structure suggests that the geological structure of oceanic crust is also horizontally layered at seismic length scales. Determination of the geological transitions that correlate with these seismic layer boundaries is a necessary first step toward mapping crustal geological structure.

Table 1. Seismic Structure of Oceanic Crust

LAYER	V_0[1]	K[2]	ΔZ[3]	COMMENTS
2	2-5.0	1-3	1-3	Can show azimuthal anisotropy (20-25%); Velocity increases with age
3	6.5-6.7	~0.1	~4	Can have low-velocity zone
Moho	6.7-7.2	~2	0.5-1.0	Commonly reflective
Mantle	~8.0	~0.1		Can show azimuthal anisotropy (5%)

[1] Velocity at top of layer (km s^{-1})
[2] Velocity gradient (s^{-1})
[3] Layer thickness (km)
References: Raitt (1963); Raitt et al. (1969); Spudich and Orcutt (1980b); White (1984); Mutter et al. (1985); Stephen (1985); Purdy and Ewing (1986); Purdy (1987).

Oceanic Velocity and Reflectivity Structure

A variety of experimental geometries and interpretation techniques have been used to measure the velocity structure of the oceanic crust (e.g. Purdy and Ewing, 1986). Recent reviews of oceanic velocity

structure have proposed that much of the diversity in the reported velocity-depth profiles is due to these widely differing acquisition and interpretation methods rather than to inherent differences in seismic structure (Kennett, 1977; Spudich and Orcutt, 1980a, 1980b; White, 1984; Purdy and Ewing, 1986). The current view is that, away from fracture zones and spreading centers, crustal velocity structure can be represented by a small number of locally horizontal layers of linear velocity gradient (Figure 1, Table 1).

This simplicity in the measured velocity structure is due to a combination of factors: the lateral and vertical resolution attainable with seismic methods, the techniques commonly employed to interpret wide-angle reflection/refraction data, and probably the inherent simplicity of oceanic velocity structure. The resolving power of the wide-angle reflection/refraction technique is typically kilometers to tens of kilometers in the horizontal direction and hundreds of meters to kilometers in the vertical direction. Consequently, structural heterogeneities of smaller dimensions are not resolvable, and the measured velocity structure is a smoothed representation of crustal structure. Wide-angle reflection/refraction data are typically interpreted in terms of a horizontally layered earth (e.g. Kennett, 1977) and hence it is difficult to quantify the degree of lateral heterogeneity. However, data acquired with ocean-bottom arrays imply that in comparison to travel time errors introduced by variable basement topography, horizontal velocity gradients are often negligible (e.g. Purdy, 1983; Bratt and Purdy, 1984).

This approximation of local lateral homogeneity is not always appropriate. Certainly, it would not be useful to attempt to measure the velocity structure of the upper 0.5 km of the crust across a fault-bounded block. Along fracture zones and spreading centers, horizontal velocity gradients cannot be neglected, and the measured velocity structure is more complex (e.g. Purdy and Ewing, 1986; Purdy and Detrick, 1986). Even in these locations, however, a layered velocity structure can be recognized. Although only an approximation, the representation of oceanic seismic structure as a series of layers provides a convenient framework for the comparison of velocity-depth profiles. Lateral changes in velocity structure can often be expressed in terms of changes in layer thickness and velocity gradient. Bratt and Purdy (1984) have mapped variations in the thickness of Layer 2 along a 200 km segment of the East Pacific Rise. However, the geological implications of this varying structure are unknown.

The picture of a layered velocity structure is supported by near-normal-incidence, multichannel seismic (MCS) reflection data (Figure 2). The resolution obtainable with the MCS technique - tens to hundreds of meters in the vertical direction, and hundreds of meters to kilometers in the horizontal direction - is significantly greater than that attainable with wide-angle reflection/refraction methods. It is as yet uncertain how the structures generating the near-normal-incidence reflection events relate to the layer boundaries determined from wide-angle reflection/refraction data. This question can only be answered by combined MCS reflection and wide-aperture experiments.

Correlation of Seismic and Geological Structures

The only unambiguous method to correlate seismic layer boundaries with geological structure is to drill many deep crustal holes and directly relate seismically determined changes in velocity gradient and impedance with the drilled lithological sequence and associated physical properties. Technological and financial limitations have precluded this approach and, at the time of writing, only Deep Sea Drilling Project (DSDP) Hole 504B in the Panama Basin has been drilled to a basement depth greater than 0.6 km into oceanic crust. In the absence of extensive deep crustal drilling, marine seismologists typically relate measured velocity and reflectivity structure to the sequence of rock types and geological structures found in ophiolites.

Ophiolites, horizontally stratified slabs of mafic and ultramafic rocks found in continental mountain belts, are thought to have been formed at spreading centers in either a back-arc basin or mid-ocean ridge setting (e.g. Coleman, 1977; Casey et al., 1985; Moores, 1985). The layered sequence of ophiolite rock types, ranging downward from volcanic extrusives through sheeted diabase dikes and gabbros to residual ultramafic rocks is conjectured to be representative of upper lithospheric structure in either tectonic setting. Vertical velocity profiles constructed from laboratory-measured velocities of ophiolite samples closely resemble velocity-depth profiles from oceanic crust (e.g. Christensen and Smewing, 1981; Christensen and Salisbury, 1982). Consequently, seismologists tentatively correlate seismic Layer 2 with extrusive volcanic and sheeted-dike sequences, seismic Layer 3 with a gabbroic sequence, and upper mantle velocities (V_p~8.0 km s^{-1}, by

definition) with unaltered ultramafic rock. Similarly, MCS reflection events are associated with these geological boundaries.

To date, results of oceanic crustal drilling have supported the ophiolite model of oceanic crust. At DSDP Site 504B, the drilled lithological sequence consisted of extrusive volcanics overlying diabase dikes, as predicted from ophiolite studies. At Ocean Drilling Project (ODP) Site 735 on the Southwestern Indian Ridge, the cored sequence consisted of ~500 m of gabbro (Leg 118 Shipboard Scientific Party, 1988). The velocity of this gabbroic sequence, as determined by a high-quality vertical seismic profiling experiment, was measured to be 6.5 ± 0.3 km s^{-1} (S. A. Swift, pers. comm.), in agreement with the correlation of typical Layer 3 velocities with gabbroic rock.

Lewis (1983) has objected to the uncritical relation of velocity structure to rock type. He presents an alternative model in which the primary control on velocity is not rock type but rather vertical variations in the extent of porosity, alteration, serpentinization, and pore pressure. This view is not necessarily incompatible with the ophiolite model, as these effects might dominate the velocity variations brought about by downward gradation in rock type. However, the magnitude of these effects cannot be readily estimated from ophiolite studies because of the difficulty in determining whether the observed cracking, alteration and serpentinization occurred during ophiolite obduction. Recent seismic and drilling experiments have confirmed that porosity variations and changes in porosity type can dramatically affect the velocity structure of the upper 1–2 km of oceanic crust. Purdy (1987) has shown that the differences (up to 3.7 km s^{-1}) between the

laboratory-measured and seismically-determined P-wave velocities of the upper 0.2 km of zero-age Atlantic crust is indicative of porosities as high as 30-50%. Logging results at DSDP Site 504B demonstrate that downhole variations in velocity strongly correlate with the observed downhole decrease in bulk porosity (Salisbury et al., 1985). However, both of these parameters also correlate with rock type. The varying extents to which variations in crustal lithology and physical properties control seismic velocity-depth profiles can only be resolved by extensive crustal drilling.

Dissertation Overview

This dissertation investigates the capabilities of controlled-source marine seismic techniques to detect and map seismic layering within the oceanic crust, and discusses the relationship between this layering and geological structure. These topics were studied by the calculation of synthetic seismogram models of appropriate velocity-depth profiles, and by the interpretation of both near-normal-incidence multichannel seismic data and wide-angle reflection/refraction profiles collected in the immediate vicinity of DSDP Site 504B in the Panama Basin.

In Chapter 1, the origins of Moho reflections are explored by comparing MCS data to synthetic, near-normal-incidence reflection profiles calculated for the two-dimensional velocity structure of the inferred fossil crust/mantle boundary exposed in ophiolites. Chapter 2 presents an analysis of the velocity structure of the middle and lower crust at DSDP Site 504B. At the time of writing, Hole 504B is the deepest drillhole into oceanic crust, having a total basement penetration of

1.288 km. The near-normal-incidence reflectivity structure of the upper 1-2 km of oceanic crust is discussed in Chapter 3. Synthetic seismograms calculated for velocity-depth profiles constructed from the logged downhole variations in physical properties at Hole 504B are compared with MCS data collected at the drillsite.

REFERENCES

Bratt, S. R., and G. M. Purdy, Structure and variability of oceanic crust on the flanks of the east Pacific Rise between 11° and 13°N, J. Geophys. Res., 89, 6111-6125, 1984.

Casey, J. F., D. L. Elthon, F. X. Siroky, J. A. Karson, and J. Sullivan, Geochemical and geological evidence bearing on the origin of the Bay of Islands and Coastal Complex Ophiolites of Western Newfoundland, Tectonophysics, 116, 1-40, 1985.

Christensen, N. I., and J. D. Smewing, Geology and seismic structure of the northern section of the Oman ophiolite, J. Geophys. Res., 86, 2545-2555, 1981.

Christensen, N. I., and M. H. Salisbury, Lateral heterogeneity in the seismic structure of the oceanic crust inferred from velocity studies in the Bay of Islands Ophiolite, Newfoundland, Geophys. J. R. Astron. Soc., 68, 675-688, 1982.

Coleman, R. G., Ophiolites, ancient oceanic crust?, Springer-Verlag, Berlin, 229 pp., 1977.

Karson, J. A., and P. J. Fox, Geological and geophysical investigations of the Mid-Cayman Spreading Centre: seismic velocity measurements and implications for the constitution of layer 3, Geophys. J. Roy. Astr. Soc., 85, 389-411, 1986.

Kennett, B. L. N., Towards a more detailed seismic picture of the oceanic crust and mantle, Marine Geophysical Research, 3, 7-42, 1977.

Leg 118 Shipboard Scientific Party, Ocean Drilling Program: plutonic rocks in fracture zones, Nature, 333, 115-116, 1988.

Lewis, B. T. R., The processes of formation of ocean crust, Science, 220, 151-157, 1983.

McCarthy, J, J. C. Mutter, J. L. Morton, N. H. Sleep, and G. T. Thompson, Relic magma chamber structures preserved within the Mesozoic North Atlantic crust?, Geol. Soc. Am. Bull., 100, 1423-1436, 1988.

Moores, E. M., Origin and emplacement of ophiolites, Rev. Geophys., 20, 735-760, 1985.

Mutter, J. C., and North Atlantic Transect (NAT) Group, Multichannel seismic images of the oceanic crust's internal structure: Evidence for a magma chamber beneath the Mesozoic Mid-Atlantic Ridge, Geology, 13, 629-632, 1985.

NAT Study Group, North Atlantic Transect: A wide-aperture, two-ship multichannel seismic investigation of the oceanic crust, J. Geophys. Res., 90, 10,321-10341, 1985.

ODP Science Operator Report, Leg 118: Fracture zone drilling on the Southwest Indian Ridge, JOIDES Journal, 14, 10-13, 1988

Purdy, G. M., The seismic structure of 140 Myr old crust in the western central Atlantic Ocean, Geophys. J. R. Astron. Soc., 72, 115-137, 1983.

Purdy, G. M., New observations of the shallow seismic structure of youmg oceanic crust, J. Geophys. Res., 92, 9351-9362, 1987.

Purdy, G. M., and J. I. Ewing, Seismic structure of oceanic crust, in The Geology of North America: The Western Atlantic Region, edited by B. E. Tulcholke, and P. R. Vogt, DNAG Ser., vol. 1, Geological Society of America, Boulder, Colo., 313-331, 1986.

Purdy, G. M., and R. S. Detrick, Crustal structure of the Mid-Atlantic Ridge at 23°N from seismic refraction studies, J. Geophy. Res., 91, 3739-3762, 1986.

Raitt, R., The crustal rocks, in The Sea, Vol. 3, edited by M. N. Hill, Wiley-Interscience, New York, 85-102, 1963.

Raitt, R. W., G.G. Shor, T. J. G. Francis, G. B. Morris, Anisotropy of the Pacific upper mantle, J. Geophys. Res., 74, 3095-3109, 1969.

Salisbury, M. H., N. I. Christensen, K. Becker, and D. Moos, The velocity structure of layer 2 at Deep Sea Drilling Project site 504 from logging and laboratory experiments, Initial Rep. Deep Sea Drill. Proj., 83, 529-539, 1985.

Spudich, P., and J. A. Orcutt, Petrology and porosity of an oceanic crustal site: results from waveform modeling of seismic refraction data., J. Geophys. Res., 88, 1409-1433, 1980a.

Spudich, P., and J. A. Orcutt, A new look at the seismic velocity structure of the oceanic crust, Rev. Geophys., 18, 627-645, 1980b.

Stephen, R. A., Seismic anisotropy in the upper oceanic crust, J. Geophys. Res., 90, 11383-11396, 1985.

White, R. S., Atlantic ocean crust: Seismic structure of a slow-spreading ridge, in Ophiolites and Oceanic Lithosphere, edited by I. G. Gass, S. J. Lippard, and A. W. Shelton, pp 101-111, Blackwell Scientific Publications, London, 1984.

FIGURE CAPTIONS

Figure 1. A typical velocity-depth profile for oceanic crust located away from fracture zones and spreading centers (from Purdy, 1983). Although only an approximation, this parameterization of oceanic seismic structure in terms of horizontal layers with uniform velocity gradients provides a useful framework in which to compare the velocity structure of different regions.

Figure 2. A portion of a multichannel seismic reflection profile (NAT Line 15), acquired on Mesozoic age crust in the Western North Atlantic (NAT Study Group, 1985). This migrated profile (from McCarthy et al., 1988) demonstrates the layered nature of the oceanic crust at length scales of less than 10 km. Possible interpretations of two of the observed reflection events are indicated.

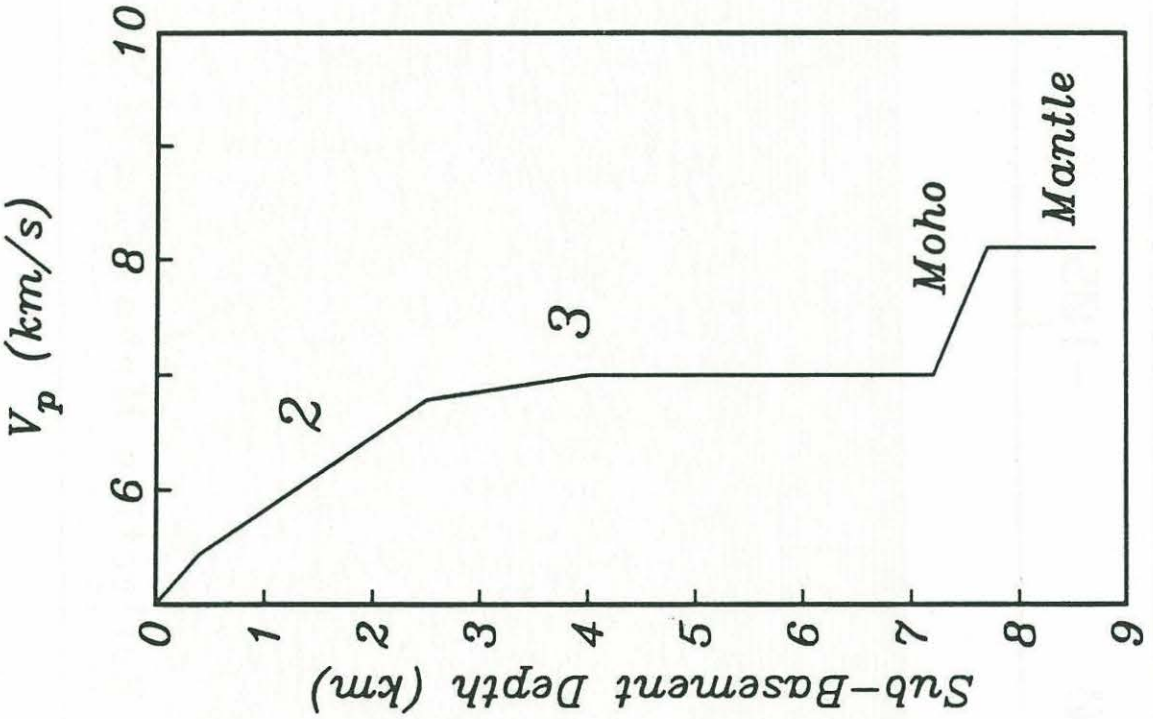

Figure 1

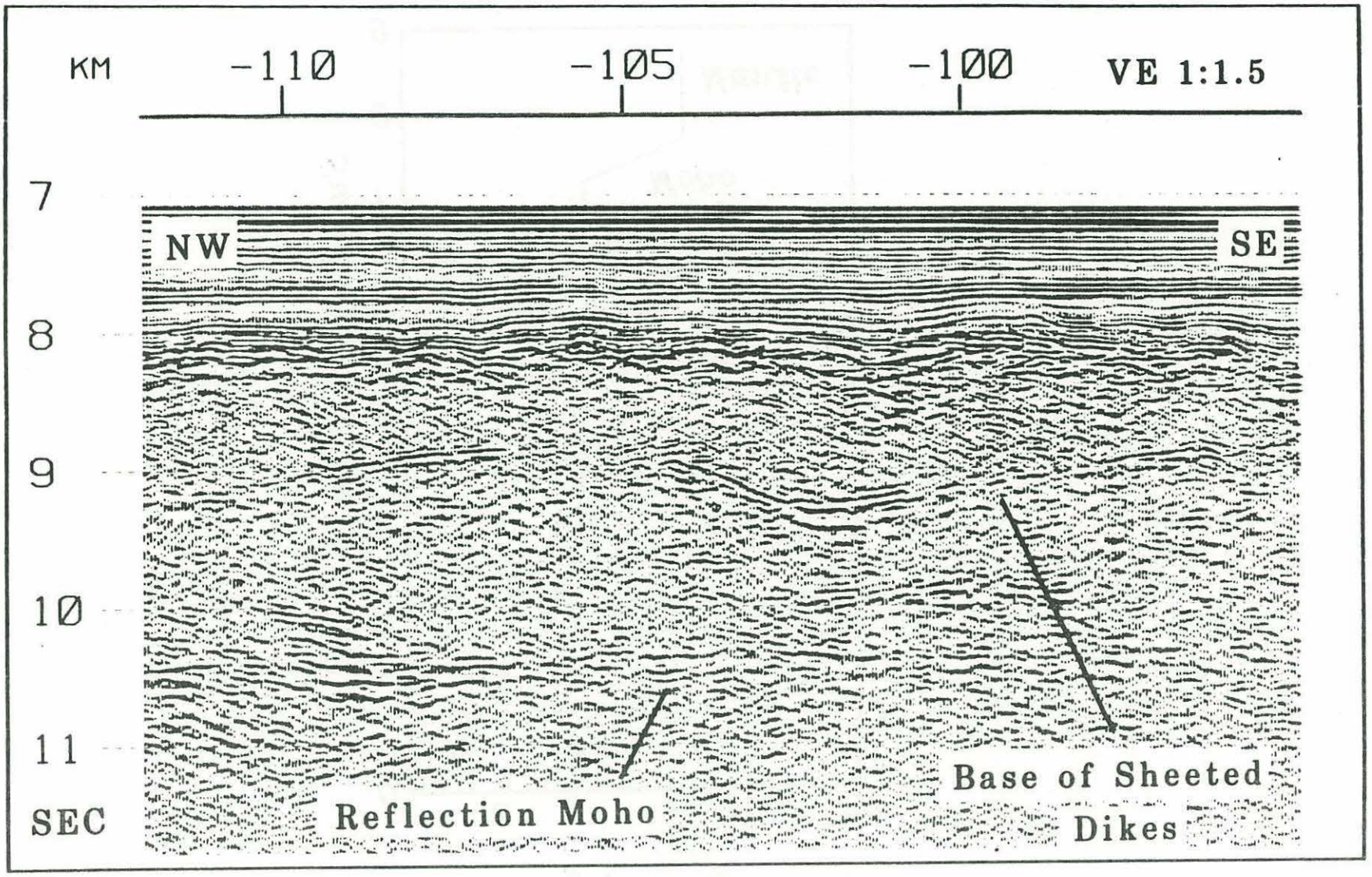
KM
-110
-105
-100
VE 1:1.5
7
8
9
10
11
SEC
NW
SE
Reflection Moho
Base of Sheeted
Dikes

Figure 2

CHAPTER 1

TWO-DIMENSIONAL SEISMIC REFLECTION MODELING OF THE INFERRED FOSSIL OCEANIC CRUST/MANTLE TRANSITION IN THE BAY OF ISLANDS OPHIOLITE

JOURNAL OF GEOPHYSICAL RESEARCH, VOL. 91, NO. B12, PAGES 12,520-12,538, NOVEMBER 10, 1986

TWO-DIMENSIONAL SEISMIC REFLECTION MODELING OF THE INFERRED FOSSIL OCEANIC CRUST/MANTLE TRANSITION IN THE BAY OF ISLANDS OPHIOLITE

John A. Collins

MIT/WHOI Joint Program in Oceanography, Department of Geology and Geophysics, Woods Hole Oceanographic Institution, Woods Hole, Massachusetts

Thomas M. Brocher[1] and Jeffrey A. Karson[2]

Department of Geology and Geophysics, Woods Hole Oceanographic Institution, Woods Hole, Massachusetts

Abstract. We investigate the origin and character of oceanic Moho reflections by computing two-dimensional synthetic seismogram profiles of the inferred fossil oceanic crust/mantle transition observed in the Bay of Islands Ophiolite. To simulate a seismic reflection experiment, we calculated near-vertical-incidence seismograms at a horizontal spacing of 500 m for three separate sections of the ophiolite totaling 64 km in length. In the synthetic profiles the Moho reflection event varies from a single phase to two or more phases of up to 1-s (two-way travel time) total duration. Individual phases show lateral variation in amplitude, and their two-way travel times vary by as much as 0.25 s over horizontal distances as short as 10 km. Lateral discontinuity of phases results in abrupt variations in the travel times of first-arriving, high-amplitude Moho phases. The geological structures generating the highest-amplitude Moho reflections vary from high- and low-velocity lenses of mafic and ultramafic material in the lower crust and upper mantle to interlayered mafic and ultramafic lithologies in the Moho Transition Zone. Reflection amplitudes from the residual upper mantle are insignificant, and our modeling suggests that using the first-arriving, high-amplitude Moho phase to estimate thickness of magmatic material might result in errors of up to 1-s two-way travel time (~3-4 km). Multichannel seismic data from both the western Pacific and western North Atlantic show Moho travel time variations similar to those observed in the synthetic profiles. The western North Atlantic data also show multiphase Moho reflection events that are laterally discontinuous on a scale similar to that observed in the synthetic data, suggesting that the structures observed in the inferred fossil crust/mantle transition of the ophiolite are characteristic of oceanic lithosphere.

Introduction

On the basis of seismic refraction data, marine seismologists define the oceanic crust/mantle transition, or oceanic Moho, to be the region, a few hundred meters to 2 km in thickness, across which compressional velocities increase with depth from ~7.2 km s^{-1} to ~8.0 km s^{-1} or greater [e.g., Spudich and Orcutt, 1980a, b; Purdy and Ewing, 1986]. The seismic expression of the Moho is a prominent event in both wide-angle reflection/refraction and near-vertical-incidence reflection data and is rivaled in amplitude and geological significance only by the seismic signature of oceanic basement. Synthetic seismogram modeling demonstrates that a crust/mantle transition characterized by a high linear velocity gradient (>0.4 s^{-1}), compared to the lower linear gradients of the overlying crust (~0.1 s^{-1}) and underlying mantle (<0.1 s^{-1}), accounts for the distinctive triplication in arrival times typically seen in marine refraction data at horizontal ranges of 25-30 km and greater [e.g., Spudich and Orcutt, 1980b].

Multichannel seismic (MCS) reflection data frequently show a prominent near-vertical-incidence reflection event at a depth of ~2-s two-way travel time below the top of oceanic crust [e.g., Grow and Markl, 1977; Stoffa et al., 1980; Watts et al., 1985; NAT Study Group, 1985]. Velocity analyses of wide-angle reflection/refraction data show that the travel times of these near-vertical-incidence reflection events approximate travel time to Moho [Stoffa et al., 1980; Purdy, 1983; Watts et al., 1985; Mithal, 1986; Chiang and Detrick, 1986]. Synthetic seismogram modeling of oceanic Moho demonstrates that a vertical sequence of thin (10-100 m) high- and low-velocity layers with a net positive velocity gradient generates both near-vertical-incidence reflection and wide-angle reflection/refraction events similar to those observed in field data [MacKenzie, 1984; K. MacKenzie and J. Orcutt, unpublished manuscript, 1986]. The finely layered Moho structure is in accord with ophiolite studies which document that fossil Moho is often characterized by mafic and ultramafic cumulate material, interlayered on scales ranging from less than 1 cm to several tens of meters [Karson et al., 1984]. Although Moho is defined solely in terms of velocity structure (and thus can only be identified from wide-angle reflection/refraction data), in this paper we loosely use the terms "Moho reflection" and "Moho reflection event" to refer to near-vertical-incidence reflection phases with travel times approximating travel time to Moho as identified on wide-angle reflection/refraction data. In the absence of wide-angle reflection/refraction data, we also apply these terms to near-vertical-incidence reflection phases at ~2-s two-way travel time

[1]Now at U.S. Geological Survey, Menlo Park, California

[2]Now at Department of Geology, Duke University, Durham, North Carolina

Paper number 5B5902.
0148-0227/86/005B-5902$05.00

below the top of oceanic crust and their laterally traceable equivalents.

The ubiquitous presence of Moho events in both oceanic wide-angle reflection/refraction and near-vertical-incidence reflection data suggests relating depth to Moho and Moho structure (e.g., thickness, velocity distribution, and reflectivity) to the geological structure of the crust and upper mantle. Because the high velocities immediately below Moho are uniquely characteristic of unaltered, olivine-rich ultramafic rocks, depth to Moho approximates the thickness of magmatic or melt-derived material. However, recovery of ultramafic cumulate rocks from ocean-floor escarpments [e.g., Bonatti and Hamlyn, 1981] and observations of ultramafic cumulate sequences up to 3 km thick in ophiolites [Karson et al., 1984] caution against equating Moho with the melt/residue boundary recognized by petrologists. Our lack of knowledge of the extent of serpentinization in oceanic lithosphere further complicates relating depth to Moho to thickness of magmatic rocks. It is possible, especially near fracture zones, that "crustal velocities" (i.e., compressional velocities $< \sim 8.0$ km s^{-1}) represent serpentinized ultramafic rocks [e.g., Lewis, 1983; Calvert and Potts, 1985].

The thickness, velocity structure, and reflectivity of the Moho, as interpreted from seismic field data, are less readily related to geological structure. Ophiolite studies suggest that Moho reflectivity is controlled, at least in part, by the extent of cumulate interlayering at the crust/mantle transition and by the presence or absence of lenses of mafic and ultramafic material in the lower crust and upper mantle [MacKenzie, 1984; Brocher et al., 1985]. Alternatively, as discussed below, observed amplitude variability of individual Moho phases may be primarily controlled by basement topography and by lateral variability in the seismic structure of shallow oceanic crust rather than by lateral variations in Moho reflection coefficient. To demonstrate that a laterally heterogeneous crust/mantle transition can result in significant variability in Moho reflection amplitudes, Brocher et al. [1985] calculated one-dimensional, vertical-incidence synthetic seismograms for 19 velocity-depth profiles appropriate for the inferred fossil crust/mantle transition of the Bay of Islands and Samail ophiolites. They document significant lateral variability in Moho reflection waveforms, much of which would probably not be obscured by variability in shallow structure.

The synthetic seismogram calculations of Brocher et al. [1985] assume that velocity varies only as a function of depth and that all energy propagates vertically. The one-dimensional synthetic seismograms are derived from the acoustic wave equation and include all interlayer multiple reflections and the effects of intrinsic attenuation [Berryman et al., 1958]. However, such one-dimensional modeling of ophiolite structure cannot account for wave propagation effects caused by documented [e.g., Karson et al., 1984] lateral structural heterogeneity along the inferred fossil crust/mantle transition.

In this paper we extend the synthetic seismogram modeling of the crust/mantle transition observed in the Bay of Islands Ophiolite to include effects of two-dimensional elastic wave propagation. Our goal is to investigate the origin and character of oceanic Moho reflections. We present results of a simulated seismic reflection experiment in which we calculated near-vertical-incidence seismograms, at a horizontal spacing of 500 m, for three separate sections of the ophiolite totaling 64 km in length. We also present a synthetic 24-fold common midpoint (CMP) gather, and examine the effects of stacking Moho reflection phases given realistic static errors. Finally, we compare the results of our simulated reflection experiment with MCS data from oceanic lithosphere and discuss the implications of our modeling for the interpretation of MCS data.

Geological Models

The Bay of Islands Ophiolite Complex (BOIC) lies within an area about 100 km by 20 km (Figure 1) and crops out in four massifs (Lewis Hills, Blow Me Down Mountain, North Arm Mountain, and Table Mountain) which are separated from one another by strike-slip faults of unknown displacement. A linear belt of deformed and metamorphosed ophiolitic lithologies, called the Coastal Complex, is located immediately to the west of the Bay of Islands Complex (Figure 1). Casey et al. [1985] review the geological and geochemical evidence suggesting that the Bay of Islands Complex and Coastal Complex were accreted along a seafloor spreading center and ridge-ridge transform fault, respectively. On the basis of regional tectonic relationships in the western Newfoundland Appalachians, they argue that these two complexes were formed in a deep ocean basin rather than in a back arc basin. We present a brief summary of their observations and arguments pertaining to the origin of the BOIC [see Casey et al., 1985, and references therein].

Both the North Arm Mountain and Blow Me Down Mountain massifs exhibit the complete sequence of lithological units that defines an ophiolite suite [Penrose Conference Participants, 1972]. Pillow basalts, sheeted diabase dikes, isotropic and layered gabbros, layered ultramafic rocks, and residual ultramafic tectonites are all exposed in continuous vertical succession. In the two massifs, sheeted dikes crop out for a total of 35-40 km (perpendicular to the strike of the dikes), implying formation in an extensional environment such as a spreading center. A similar sequence of residual ultramafic, ultramafic cumulate, and mafic cumulate rocks is found in the Table Mountain massif, but no extensive exposures of sheeted dikes and pillow basalts are observed. Presumably, the dikes and lavas were removed by erosion during or after obduction. Sheeted dikes and pillow basalts do not crop out extensively in the Lewis Hills massif. Diabase dikes and lavas from the Blow Me Down and North Arm Mountain massifs are geochemically indistinguishable from mid-ocean ridge basalt and back arc basin basalt. Diabase dikes with a similar geochemistry are also found in the Lewis Hills massif, but the geochemistry of some rocks there cannot be unambiguously related to any known tectonic setting.

Attempts have been made to decipher the

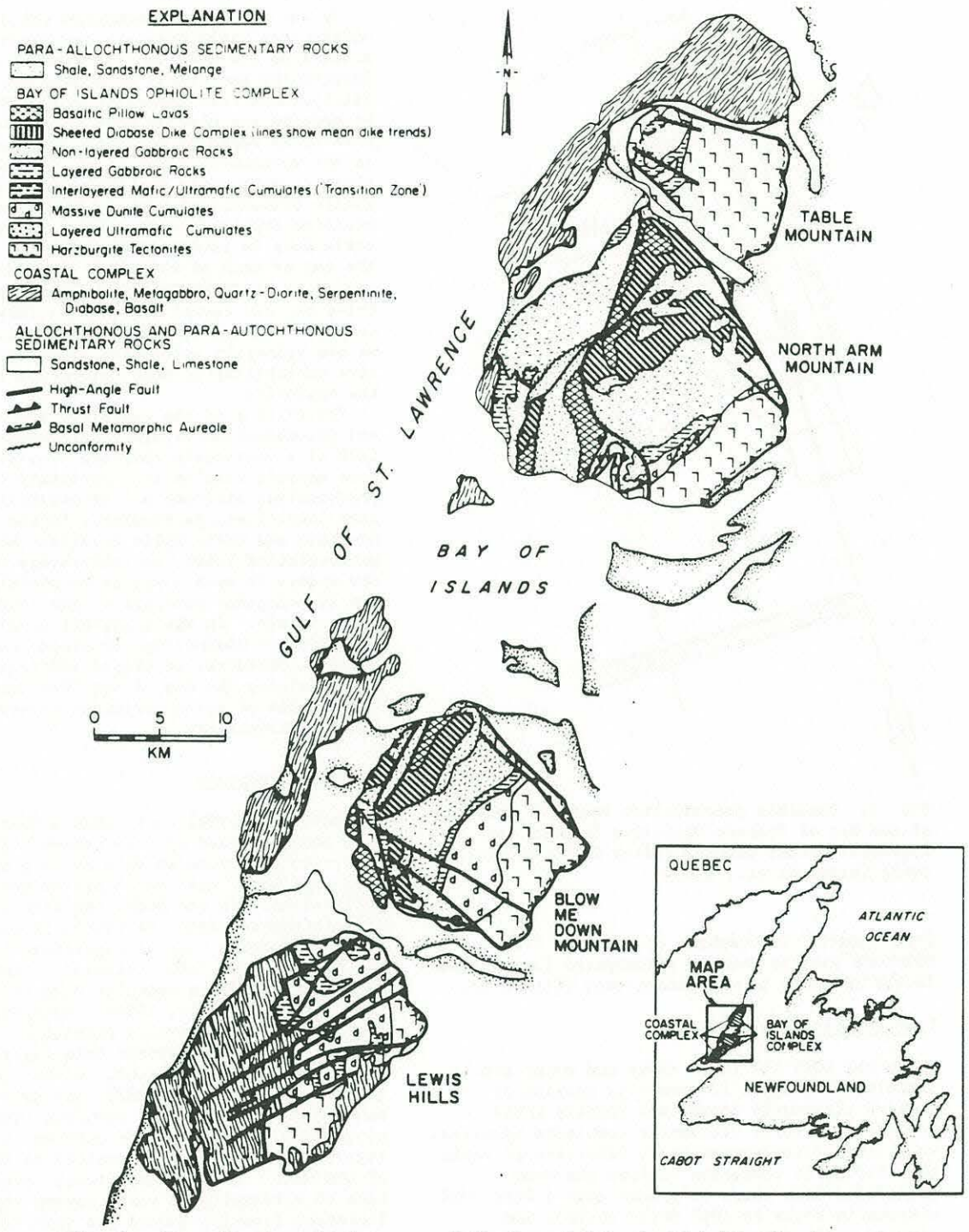

Fig. 1. Generalized geological map of the Bay of Islands Ophiolite Complex and Coastal Complex [after Karson et al., 1984].

preobduction geometry of the BOIC and Coastal Complex. As such a reconstruction involves some ambiguities, the ophiolite sections presented below may simply be considered as unrelated samples of lower oceanic crust and upper mantle that were accreted along a spreading center in either a back arc basin or deep ocean basin. Alternatively, as summarized by Casey et al. [1983], the ophiolite sections may be collectively interpreted as sampling the oceanic crust/mantle transition along a transect, at an oblique angle to a seafloor spreading flow line,

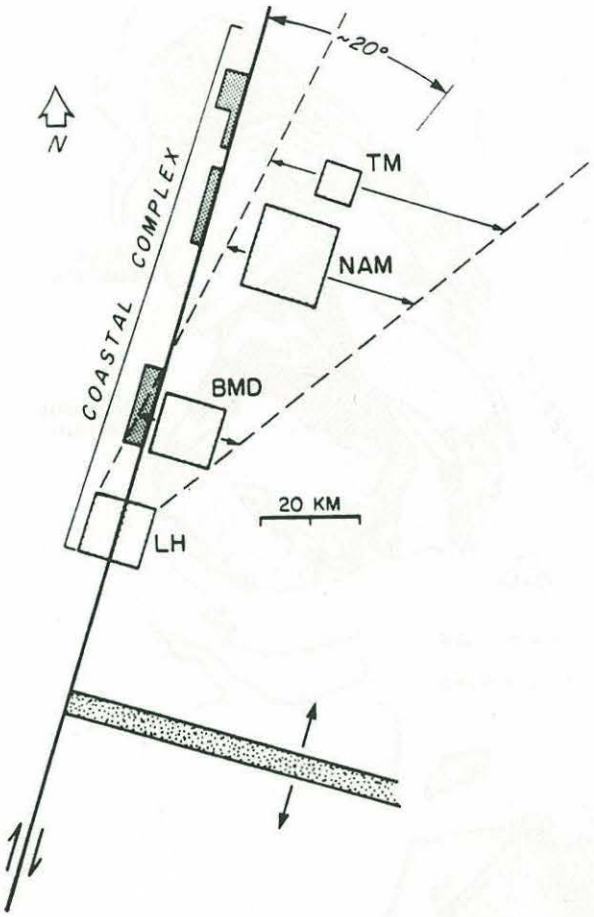

Fig. 2. Possible preobduction tectonic setting of the Bay of Islands Ophiolite Complex and adjacent Coastal Complex [after Casey et al., 1983; Karson et al., 1984].

from "normal" lithosphere formed away from a fracture zone to younger lithosphere formed immediately adjacent to a fracture zone (Figure 2).

Crust/Mantle Transition

In the BOIC the lower crust and upper mantle lithologies (Figure 3) generally consist of layered ultramafic tectonites (mostly harzburgites), layered ultramafic cumulates (dunites, wehrlites, clinopyroxenites), interlayered mafic and ultramafic cumulates (called the Moho Transition Zone where it grades upward from 100% ultramafic rocks to 100% mafic rocks), and layered mafic cumulates (gabbro, olivine-gabbro, troctolite). In the Moho Transition Zone (MTZ), layer thicknesses range from less than 1 cm to several tens of meters, and length-to-thickness ratios of these cumulate layers typically vary from 10:1 to 100:1 [Karson et al., 1984]. Sharp contacts typically bound the cumulate layers in the MTZ and layered gabbro sections, whereas gradational contacts characterize the metamorphic layering within the harzburgite unit [Karson et al., 1984].

In our synthetic seismogram calculations we modeled the Table Mountain and North Arm mountain massifs as a single section because the intervening geological structure can be readily interpolated [see Karson et al., 1984, Figure 6]. We modeled the Blow Me Down and Lewis Hills massifs as separate sections. Because the BOIC is not vertically complete at all locations, we chose to model only the lower crust and upper mantle component of each ophiolite section. To minimize amplitude variability caused by lateral variations in geometrical spreading, we extended the top of each of the three geological models upward by approximately the same amount (~2-s two-way travel time). The lack of complete crustal sections is not critical because we are primarily interested in documenting relative variability in Moho reflection response along the ophiolite.

The tilting of the ophiolite due to obduction and postobduction deformation combined with the lack of a vertically complete crustal section in some massifs results in uncertainty in the preobduction attitude of lithological contacts at some localities, particularly in the Table Mountain and Lewis Hills massifs. Where uncertainties exist, we arbitrarily constructed our models in such a way as to minimize dip on the lithological contacts of the lower crust and upper mantle. In the trade-off involved in collectively minimizing the slopes on these nonparallel contacts, we placed particular emphasis on minimizing the dip of the Moho Transition Zone. This choice of datum minimizes structural-induced seismic variability.

Velocity Structure

MacKenzie [1984] shows that a Moho Transition Zone characterized by interbedded high- and low-velocity layers as thin as 10 m can generate high-amplitude, near-vertical-incidence reflections. In the BOIC, individual layers of this thickness cannot be traced laterally beyond 1 km, a distance that is significantly less than the Fresnel zone (the footprint of the incident seismic wave) for a specular Moho reflection event [Karson et al., 1984]. However, it is probable that a laterally extensive stack of these randomly distributed thin layers would act as a significant reflector. Within the Moho Transition Zone of the BOIC, the detailed lateral and vertical geometry of cumulate layers less than about 40 m in thickness is unknown, but these thin layers typically extend parallel to the boundaries of the MTZ. At this structural level the proportion of ultramafic to mafic layers typically increases downward toward the underlying continuous ultramafic unit. Accordingly, in the absence of cumulate layering greater than 40 m thick we approximated the velocity structure of the Moho Transition Zone by a linear velocity gradient between velocities appropriate for 100% mafic material and velocities appropriate for 100% ultramafic material. Similarly, we used two linear gradients to approximate the velocity structure of high- and low-velocity lenses of mafic and ultramafic material in the lower crust and upper mantle. Figure 4 shows a test of our

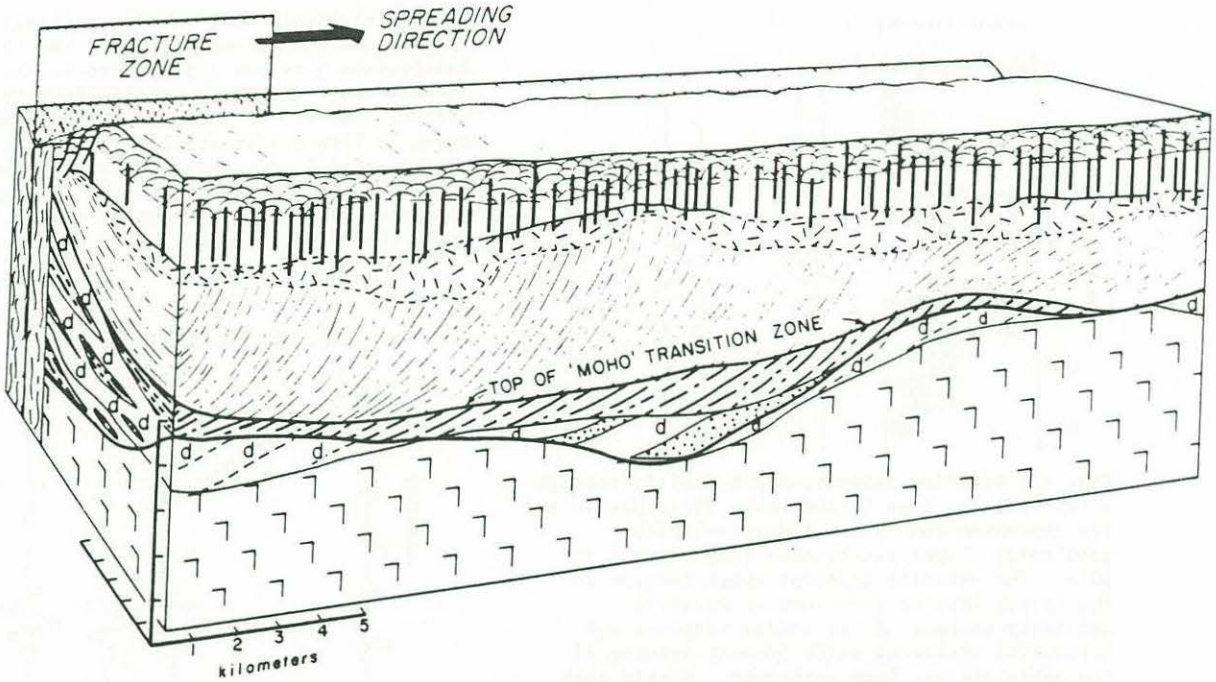

Fig. 3. Schematic block diagram illustrating the internal structure of the inferred fossil oceanic lithosphere represented in the Bay of Islands Ophiolite Complex. Ornament is described in Figure 1 [after Karson et al., 1984].

assumption that the velocity structure of a thick sequence of layers can be approximated, at frequencies less than 25 Hz, by an appropriate choice of linear velocity gradients. For the case of vertically propagating energy, synthetic seismograms calculated for the layered model and its gradient approximation are surprisingly similar, especially at frequencies of 5-15 Hz.

The rock velocity data that we used in constructing our velocity profiles are discussed in detail by Karson et al. [1984]. All velocities are based on measurements made at confining pressures appropriate to the lower crust and upper mantle. We used unserpentinized velocities for the ultramafic rocks because extensive serpentinization in the BOIC probably occurred during or after obduction [Karson et al., 1984]. The ultramafic velocities were generated using known modal compositions of these rocks and measured velocities of the constituent minerals [Christensen and Lundquist, 1982]. For each of the lithologies considered, we used the average minimum compressional wave velocity V_p of Karson et al. [1984] (layered gabbro, 6.7 km s^{-1}; wehrlite, 7.9 km s^{-1}; dunite, 8.2 km s^{-1}; harzburgite, 8.1 km s^{-1}) because these velocities are similar to velocities measured in refraction experiments [e.g., Spudich and Orcutt, 1980b; Purdy and Ewing, 1986]. In addition, because we consider near-vertical-incidence propagation only, the choice of minimum V_p for anisotropic ultramafic rocks is appropriate since the preferred crystallographic orientation of olivine in the BOIC is such that the slowest velocity is oriented vertically [Salisbury and Christensen, 1978; Karson, 1982]. Finally, we assumed a linear relationship [Birch, 1961] between density ρ and velocity ($\rho = 0.613 + 0.328V_p$).

Synthetic Seismogram Calculation

We used a ray theory method described by Cerveny et al. [1977] to calculate the two-dimensional synthetic seismogram profiles presented in this paper. The SYNS83 and SEIS83 computer codes (written by V. Cerveny and I. Psencik, Univerzita Karlova, Prague) calculate seismograms for normal-incidence rays (defined to be rays which leave an interface at normal incidence) and wide-angle rays, respectively. Both codes calculate elastic reflection and transmission coefficients, compute geometrical spreading, and allow the addition of user-specified, multiple-reflection events. Neither code includes effects of diffracted energy. In computing reflection and transmission coefficents for the ophiolite models we assumed a compressional wave velocity to shear wave velocity ratio of 1.732 (Poisson's ratio = 0.25), in agreement with observed values for the lower oceanic crust and upper mantle [Spudich and Orcutt, 1980a]. We chose not to compute reflection and transmission coefficents for the surface of the model. The two-dimensional synthetic seismograms presented below include only compressional wave arrivals.

The SYNS83 and SEIS83 codes do not accurately calculate the frequency-dependent reflection coefficients of velocity gradients. Accordingly, we approximated a linear velocity gradient by a stack of thin, constant velocity layers. The validity of this approximation, well established in the literature [e.g., White and Stephen, 1980;

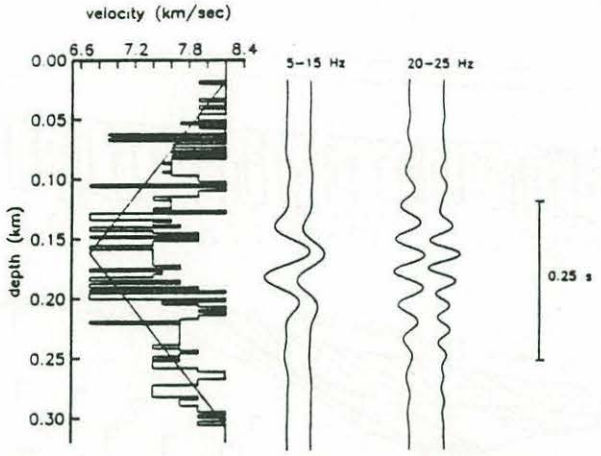

Fig. 4. Detailed velocity-depth profile through a low-velocity lens in the Lewis Hills Massif and its approximation by two linear velocity gradients. Layer thicknesses range from 1 to 20 m. The velocity gradient approximation to the finely layered structure is generally necessary because of the coarse vertical and horizontal scales at which present mapping of the ophiolite has been performed. Within each seismogram pair the seismogram on the left was generated from the layered model using a one-dimensional code that assumes a layered velocity-depth function; the seismogram on the right was generated from the gradient approximation using a one-dimensional code that assumes a velocity-depth function consisting of a series of linear velocity gradients. Both synthetic seismogram codes implicitly include the effects of multiply-reflected energy. All seismograms include only vertically propagating, compressional wave arrivals. Within each seismogram pair, displacement amplitudes are comparable. Positive amplitudes are plotted to the left. A zero-phase wavelet was used to compute all seismograms.

Chapman and Orcutt, 1985], is demonstrated in Figure 5 for the case of vertically propagating energy. In both examples presented, the response of the gradient model computed with the previously described one-dimensional synthetic seismogram code is approximately identical to the response of the layered model computed with the SYNS83 code. In computing the two-dimensional synthetic seismogram profiles we used a layer thickness of 33 m in approximating linear velocity gradients. This choice of layer thickness (approximately one ninth of a wavelength for a maximum frequency of 24 Hz and a minimum velocity of 6.7 km s^{-1}) is conservative [Chapman and Orcutt, 1985].

The two-dimensional synthetic seismograms presented below do not include effects of multiply-reflected energy because the excellent match (Figure 5) between the one-dimensional synthetic seismograms (which implicitly include all multiple reflections) and the seismograms computed with the SYNS83 code (which do not include any multiple reflections) suggests that multiply-reflected energy can be neglected at frequencies of interest. We also assumed that our geological models were perfectly elastic, because attenuation can be neglected for the lithology-independent Q values appropriate to the lower oceanic crust and upper mantle [Spudich and Orcutt, 1980a]. On the basis of the comparisons shown in Figure 5 we concluded that the approximations used in our two-dimensional modeling were warranted and that the synthetic seismograms presented here are satisfactory analogs of MCS data. The source wavelets used in this study

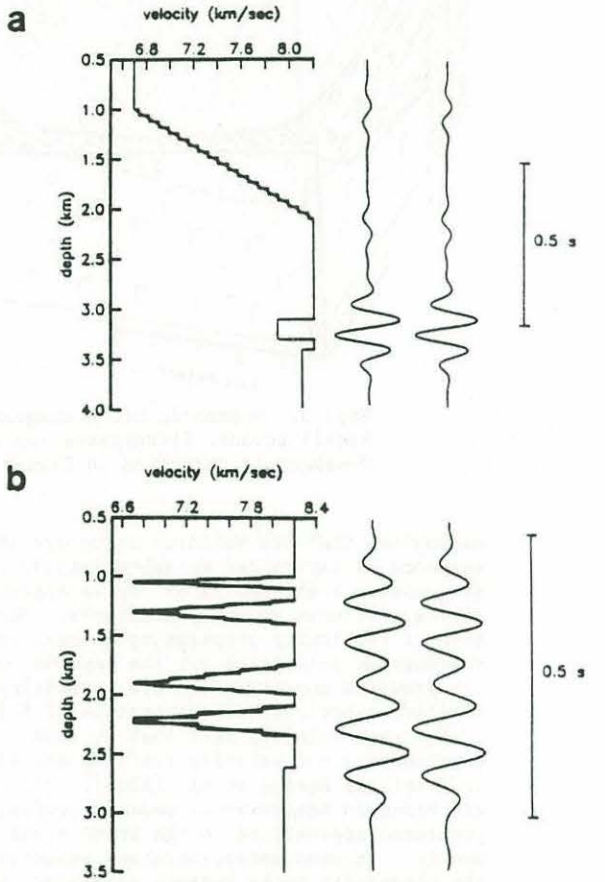

Fig. 5. (a) Linear velocity gradient from the Table Mountain/North Arm Mountain model and its layered approximation necessary for accurate application of the SYNS83 and SEIS83 synthetic seismogram codes. Layer thickness is 60 m, approximately one ninth of a wavelength for a frequency of 12 Hz and a velocity of 6.7 km s^{-1}. The seismogram on the left was calculated from the layered approximation to the linear gradient with the SYNS83 code. The seismogram on the right was calculated from the linear velocity gradient using a one-dimensional code that assumes a velocity-depth function consisting of a series of linear velocity gradients. The latter code implicitly includes the effects of multiply-reflected energy.. Both seismograms include only vertically propagating, compressional wave arrivals and were computed with identical zero-phase 12-Hz source wavelets. Positive displacement amplitudes are plotted to the left. (b) As in Figure 5a, but the velocity-depth profile comes from the Lewis Hills model.

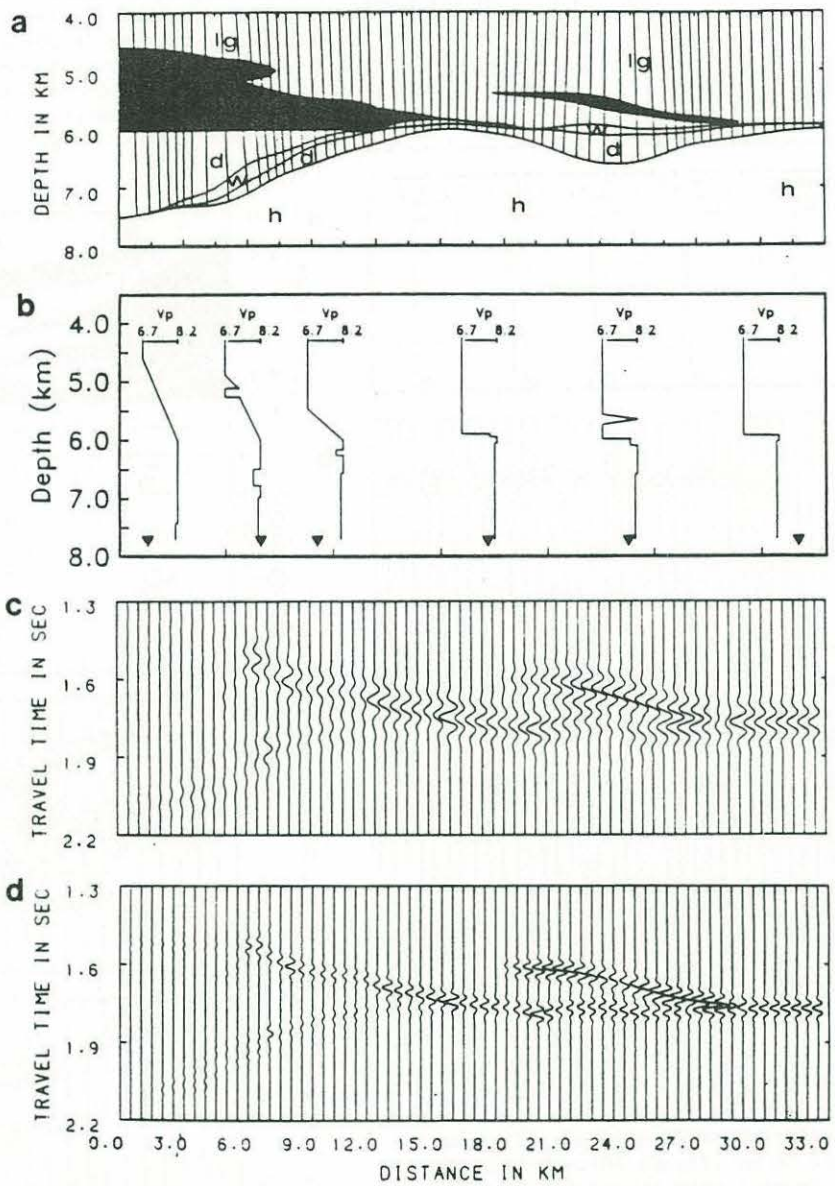

Fig. 6. (a) Geological model of the lower crust and upper mantle in the Table Mountain/North Arm Mountain Massifs. Labels are h, harzburgite; d, dunite; w, wehrlite; lg, layered gabbro. The solid unit on the left represents the Moho Transition Zone, while that on the right represents a lens of lithologies grading from 100% layered gabbro at the top and bottom to 100% dunite at the center. All interfaces in this and other models are represented by cubic splines. The near-vertical lines represent ray paths from the top of the harzburgite layer. (b) Representative velocity (in kilometers per second)/depth profiles for the geological model shown in Figure 6a. The solid triangles at the base of the figure show profile locations. (c) Synthetic, compressional wave, normal-incidence seismograms generated from Figure 6a using the SYNS83 code and a 12-Hz source wavelet. Seismogram spacing is 500 m. The vertical-component displacement amplitudes are scaled relative to the largest amplitude in the figure which is plotted at half the seismogram spacing. Positive amplitudes are plotted to the left. (d) As for Figure 6c, but with a 24-Hz source wavelet.

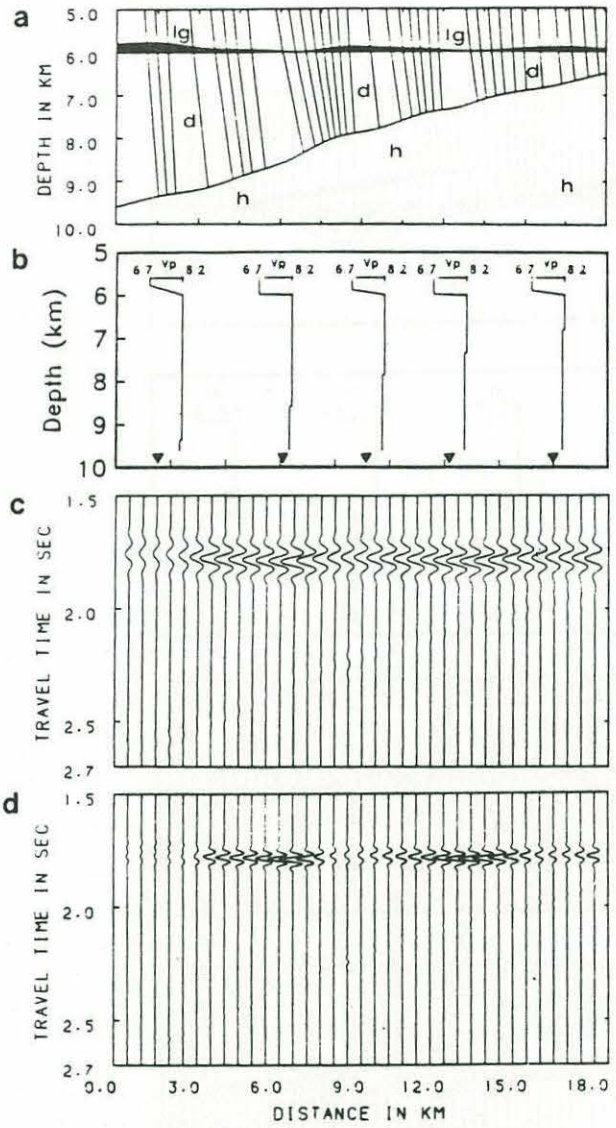

Fig. 7. Geological model of the Blow Me Down Mountain Massif (Figure 7a), representative velocity-depth profiles (Figure 7b), and synthetic seismograms at frequencies of 12 Hz (Figure 7c) and 24 Hz (Figure 7d). Labels are described in Figure 6 with the exception that here the solid unit represents the Moho Transition Zone. The near-vertical lines in Figure 7a represent ray paths from the top of the harzburgite layer. Amplitudes are scaled and plotted as described in Figure 6.

were narrow-band, zero-phase, noncausal wavelets with predominant frequencies of 12 and 24 Hz [Cerveny et al., 1977].

Synthetic Seismogram Results

Overview

For each of the three ophiolite sections modeled (Table Mountain/North Arm Mountain, Blow Me Down Mountain, and Lewis Hills), we present synthetic normal-incidence profiles at predominant frequencies of 12 and 24 Hz (Figures 6, 7, and 8). These profiles were computed with the SYNS83 code. Seismogram spacing is 500 m for all profiles. In an attempt to provide a quantitative comparison between the synthetic profiles, we show plots of total reflected energy as a function of range along each profile (Figure 9).

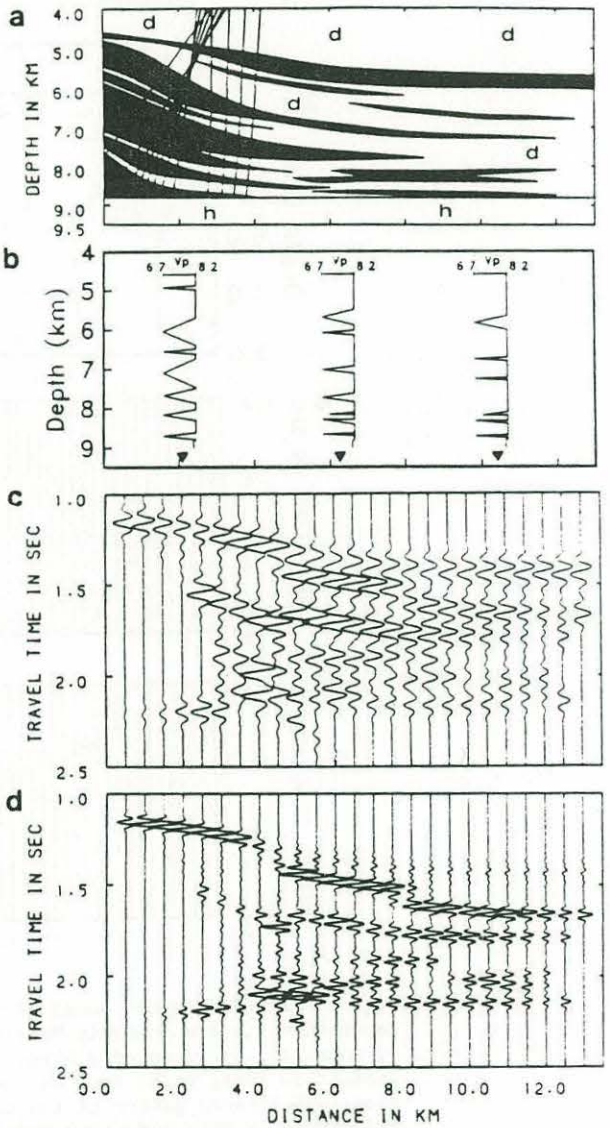

Fig. 8. Geological model of the Lewis Hills Massif (Figure 8a), representative velocity-depth profiles (Figure 8b), and synthetic seismograms at frequencies of 12 Hz (Figure 8c) and 24 Hz (Figure 8d). Labels are described in Figure 6 with the exception that here the solid units represent layers and lenses that grade from 100% dunite at the top and bottom to 100% layered gabbro at the center. The steeply dipping lines in Figure 8a represent ray paths from the top of a low-velocity lens. Amplitudes are scaled and plotted as described in Figure 6.

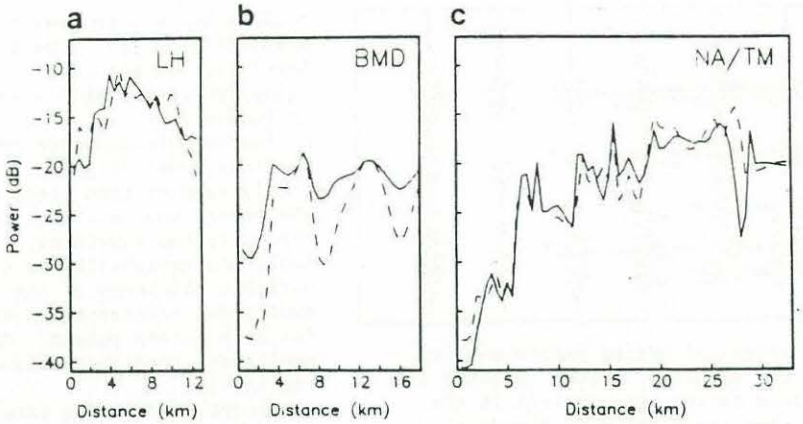

Fig. 9. Total reflected energy (sum of squared amplitudes) of the Moho events as a function of range for the Lewis Hills (Figure 9a), Blow Me Down Mountain (Figure 9b), and Table Mountain/North Arm Mountain (Figure 9c) synthetic profiles, at frequencies of 12 Hz (solid line) and 24 Hz (dashed line). The window length is 1.5 s. Amplitude and range scales are identical for all plots.

The normal-incidence synthetic seismograms are not strictly analogous to the seismograms of MCS data that are generated by stacking seismograms having a common midpoint. Accordingly, we show a CMP gather calculated for the Lewis Hills model and compare the resulting stacked trace to a normal-incidence seismogram calculated at the same location. We used the SEIS83 code to compute the seismograms of the CMP gather. For all the synthetic seismogram profiles presented here, we plot the vertical component of particle displacement.

Model 1: Table Mountain/North Arm Mountain Massifs

The geological model for these massifs (Figure 6a) is characterized by a laterally discontinous MTZ which pinches out at a horizontal range of ~15km. The lens of material at a horizontal range of 17-29 km and a depth of 5-6 km is characterized by gradation from 100% gabbro at the top and bottom to 100% dunite at the center. Beneath the MTZ, a layer of cumulate dunite thins from a maximum thickness of ~1.5 km at short ranges to zero thickness at a horizontal range of about 11 km. At greater depths the model is characterized by undulating layers of wehrlite and dunite overlying the harzburgite unit that represents the residual upper mantle. Representative velocity-depth profiles for this model are shown in Figure 6b.

The normal-incidence synthetic seismograms calculated for this model are shown in Figures 6c and 6d at predominant frequencies of 12 and 24 Hz, respectively. The duration of the Moho reflection event is up to 0.5 s two-way travel time in places. The highest-amplitude phases are generated by the high-velocity lens described above. In the high-frequency plot (Figure 6d) the amplitudes of these reflections decrease toward the center of the lens, at a horizontal range of 23 km, where the lens is thickest. In contrast, reflection amplitudes increase toward the center of the lens in the low-frequency plot (Figure 6c). These contrasting responses are readily explained in terms of the resolving power of the two source wavelets. The thickness of the lens at 23 km is

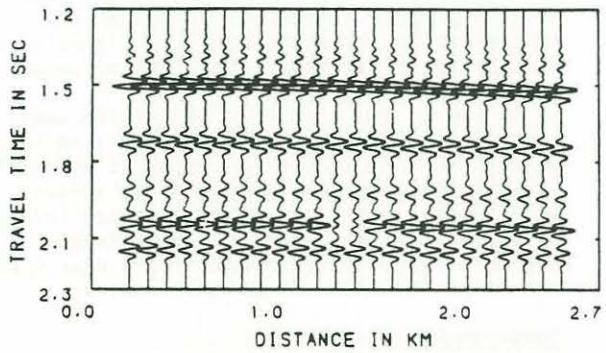

Fig. 10. Twenty-four-fold CMP gather computed at a midpoint range of 6.5 km in the Lewis Hills massif using the SEIS83 code and a 24-Hz source wavelet. Amplitudes are scaled and plotted as described in Figure 6.

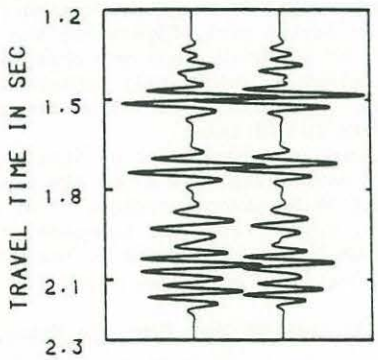

Fig. 11. Comparison of the stacked 24-fold CMP gather (left) with the normal-incidence seismogram (right) calculated at the same midpoint for a frequency of 24 Hz.

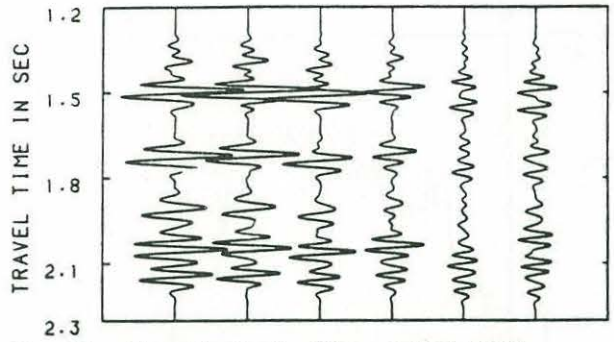

Fig. 12. The effect of adding random static errors to the CMP gather of Figure 10 prior to stack. The trace on the extreme left is the error-free stacked trace shown in Figure 11. From left to right, the other five stacked seismograms show effects of applying random, two-way travel time shifts, uniformly distributed within the ranges ±0.01, ±0.02, ±0.03, ±0.04, and ±0.05 s, to the CMP gather of Figure 10.

sufficiently small that the reversed velocity gradients cannot be resolved at frequencies less than or equal to 12 Hz; at these frequencies the two gradients may be approximated by a velocity discontinuity. Toward the edges of the lens, the rapid velocity reversal results in cancellation of the long-duration, phase-reversed, 12-Hz waveforms reflected from the top and bottom of this layer. In contrast, the velocity gradients at the center and edges of the lens can be resolved with the shorter-duration 24-Hz source wavelet.

Reflection amplitudes from the top of the MTZ increase as this unit thins laterally toward greater ranges. At greater travel times a low-amplitude reflection from the dunite/wehrlite contact is seen. Note that reflection amplitudes from the harzburgite layer are negligible. The difference in resolving power of the two source wavelets is again evident in the reflection response of the layered gabbro/wehrlite contact between 17 and 29 km. Directly below the high-velocity lens, this contact can be clearly resolved with the 24-Hz source wavelet, whereas in the low-frequency plot the reflection from this contact merges with the reflection from the lens. In this latter plot (Figure 6c) the travel time offset of the high-amplitude phase at a range of 19 km might be incorrectly interpreted as the seismic expression of a fault through the Moho if observed in MCS data.

Figure 9c shows a plot of total reflected energy versus distance along the profile for the 12- and 24-Hz source wavelets. For the 24-Hz source, higher reflected energies at ranges of 18-29 km can be attributed to the increased resolving power discussed above.

Model 2: Blow Me Down Mountain Massif

The geological model for this massif is characterized by a thin, approximately horizontal MTZ and a dunite layer which thins from a thickness of ~3.5 km to ~0.5 km over the length of the model (Figure 7a). The top of the harzburgite layer dips at about 10°. Representative velocity-depth profiles for this model are shown in Figure 7b.

The normal-incidence seismograms calculated for this model (Figures 7c and 7d) are considerably simpler than those calculated for model 1. The source wavelets are readily recognizable in the reflected waveforms of Figures 7c and 7d. Amplitude variability is controlled by the variable thickness of the MTZ. Maximum reflection amplitudes correspond to minimum MTZ thicknesses for both source pulses. As in model 1, reflection amplitudes from the residual upper mantle are negligible.

Figure 9b compares total reflected energy as a function of distance along the profile for the two source wavelets. The higher reflected energies and less variable response of the 12-Hz source can be attributed to the fact that at low frequencies the linear gradient of the MTZ better approximates a simple velocity discontinuity.

Model 3: Lewis Hills Massif

The geological model (Figure 8a) for this massif is the most complex considered here. The model consists of layers and lenses of transitional lithologies, each of which is characterized by a gradation from 100% gabbro at the center to 100% dunite at the top and bottom. The top of the harzburgite layer is assumed to be horizontal. Representative velocity-depth profiles for this model are shown in Figure 8b.

The normal-incidence seismograms for this model (Figures 8c and 8d) show reflected waveforms of up to 1-s two-way travel time duration. As expected, individual layers and lenses are better resolved in the high-frequency plot. At ranges greater than 4 km the higher amplitudes of the first-arriving phase in the 12-Hz plot, compared to the 24-Hz plot, are attributed to the frequency-dependent reflection coefficient of the reversed velocity gradients that characterize the velocity structure of the shallowest low-velocity layer. As for the other two geological models, reflection amplitudes from the harzburgite layer are negligible. Note that the two-way travel times of reflections from the top of the MTZ decrease by ~0.25 s toward shorter ranges in the low-frequency plot. A decrease of ~0.5 s is evident in the high-frequency plot, ignoring the low-amplitude, first-arriving phase at ranges greater than 5 km.

At ranges less than 4 km, reflection amplitudes are reduced (Figures 8c, 8d and 9a) by an increase in the thickness and dip of lenses of transitional lithologies. Rays incident on these steeply dipping interfaces are reflected toward larger ranges (Figure 8a), resulting in decreased reflection amplitudes at ranges less than 4 km and increased amplitudes at greater ranges.

Common Midpoint Synthetics

To assess the capability of the common midpoint stacking technique to reproduce the reflected waveforms of a CMP gather and also to compare a stacked seismogram to an equivalent

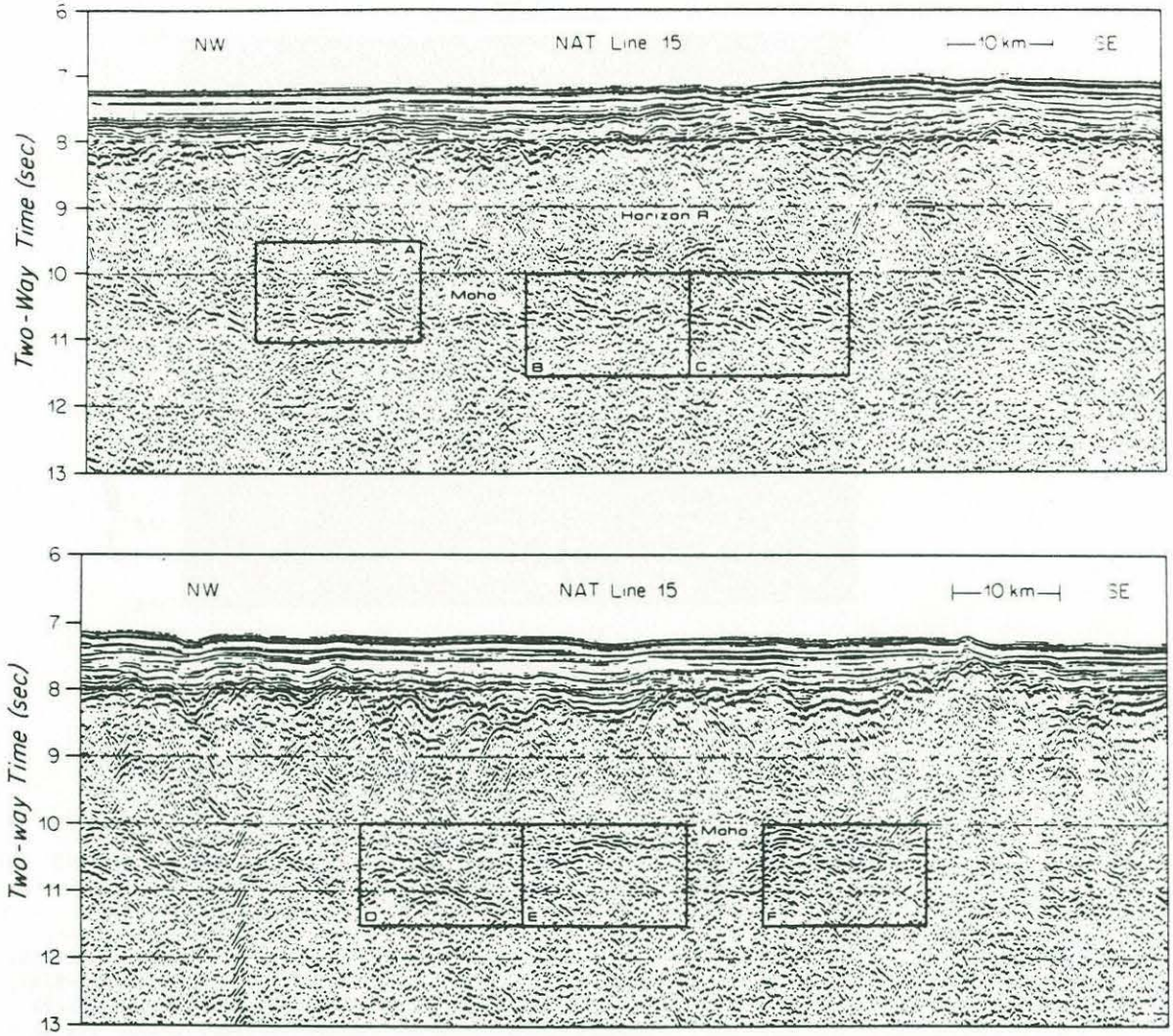

Fig. 13. Two adjoining sections of MCS data from NAT line 15. The data extend northwest from the "East Fracture Zone" of Mutter et al. [1985] which is located to the right of the lower plot. The data are band pass filtered from 6 to 30 Hz, corrected for spherical divergence, and plotted with automatic gain control.

normal-incidence seismogram, we calculated a 24-fold gather at a midpoint of 6.5 km in the Lewis Hills model. The group separation and initial source-receiver offset for this calculation were assumed to be 100 m and 200 m, respectively. The computed CMP gather, at a frequency of 24 Hz, is shown in Figure 10. We show the gather at a frequency of 24 Hz only because any spurious amplitude effects introduced by stacking should be most pronounced at high frequencies. These seismograms, which have not been corrected for normal moveout, show insignificant variability in waveform or travel time as a function of angle of incidence. Figure 11 shows the stacked seismogram plotted alongside a normal-incidence seismogram calculated for a receiver at the midpoint. The waveforms of the stacked trace, CMP gather, and normal-incidence seismogram are similar. These results suggest that stacking Moho reflection phases does not introduce spurious waveform variability in a stacked seismogram or obscure any waveform variability observed in a CMP gather. Note that the CMP data shown in Figure 10 were calculated for a Moho depth of ~2-s two-way travel time and thus simulate a CMP gather collected with a 2.4-km-long multichannel array located at the ocean floor. The data collected with such an experimental geometry are equivalent to data collected with a 4-km-long array located at the surface of a 4-km-deep ocean.

The calculations described above ignore complications such as static time shifts associated with variable topography. In regions characterized by rough basement topography, static time shifts might degrade the effectivness of a CMP stack. To assess how static errors affect a CMP stack, we applied random two-way travel time shifts, uniformly distributed within the ranges ±0.01, ±0.02, ±0.03, ±0.04, and ±0.05 s, to the CMP gather of Figure 10. In oceanic crustal studies, static errors of this magnitude would result from variations in basement topography of

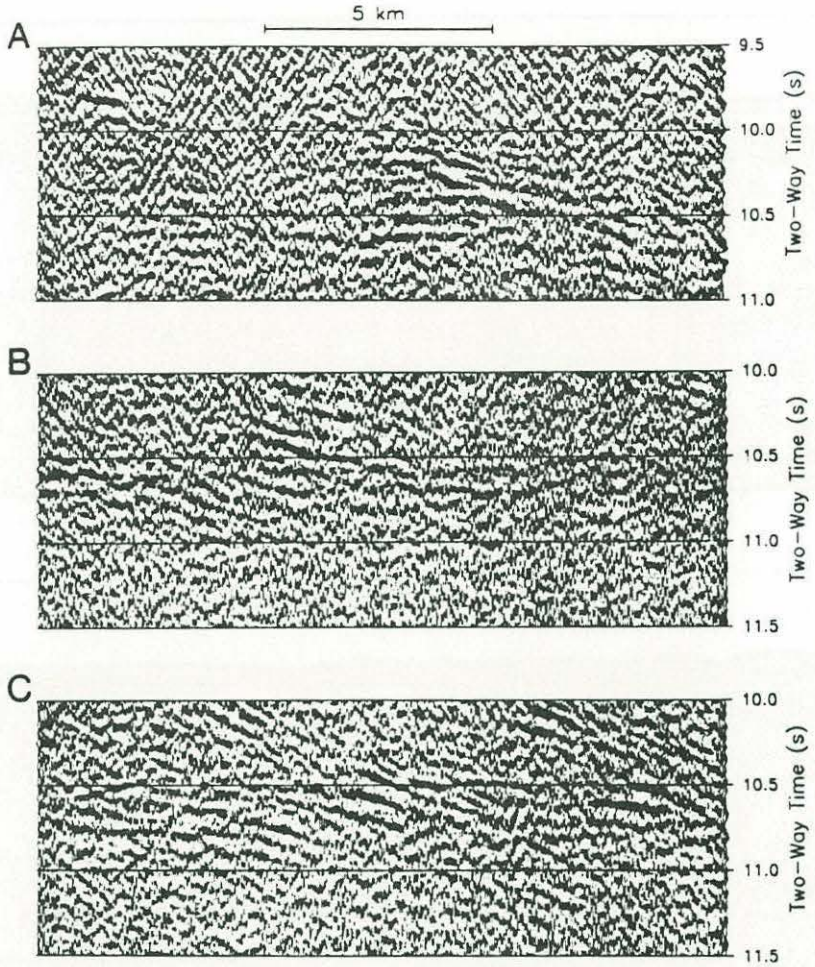

Fig. 14. True relative-amplitude plots of the six segments outlined in Figure 13. Amplitudes are identically scaled in all six plots. The CMP numbers are 9300-9599 (Figure 14a), 9800-10,099 (Figure 14b), 10,100-10,399 (Figure 14c), 11,500-11,799 (Figure 14d), 11,800-12,099 (Figure 14e), and 12,240-12,539 (Figure 14f). The data are band pass filtered from 2 to 15 Hz.

up to 24, 48, 72, 96, and 120 m, respectively, along the aperture of the receiver array, assuming a sediment-free ocean floor with a basement velocity of 4 km s^{-1}. Figure 12 compares the error-free stack to five stacked seismograms calculated with the above time shifts. Differences in waveform and travel time between the stacked seismograms calculated with static errors and the error-free stack are negligible for time shifts less than ±0.02 s but are significant for time shifts of ±0.04 s, and ±0.05 s. However, topographic variations of 96-120 m over a horizontal range of 1-2 km are primarily confined to oceanic crust accreted at slow-spreading ridges [Phillips and Fleming, 1978; Macdonald et al., 1984]. Moreover, when oceanic basement is buried beneath a flat, sediment-covered seafloor, time shifts associated with basement topographic variations decrease. Thick (>200 m) sediments are typically characterized by compressional velocities greater than 2.0 km s^{-1} [e.g., Tulchoke, et al., 1982]; in this case, basement topographic variations of 96-120 m would correspond to two-way travel time shifts of less than ±0.02 and ±0.03 s, respectively. We conclude that random static errors due to topographic variations significantly affect a CMP stack only for data collected on thinly sedimented crust accreted along slow-spreading ridges.

Comparison of Synthetic Seismograms With Observed Data

In the synthetic profiles the Moho reflection event varies from a single phase to two or more phases of up to 1-s (two-way travel time) total duration. Individual phases show lateral variation in amplitude, and their two-way travel times vary by as much as 0.25 s over horizontal distances as short as 10 km. Lateral discontinuity of phases results in abrupt variations in the travel times of first-arriving, high-amplitude Moho phases. To test whether these synthetic events closely resemble observed Moho reflections, we looked at MCS data from the western North Atlantic [NAT Study Group, 1985],

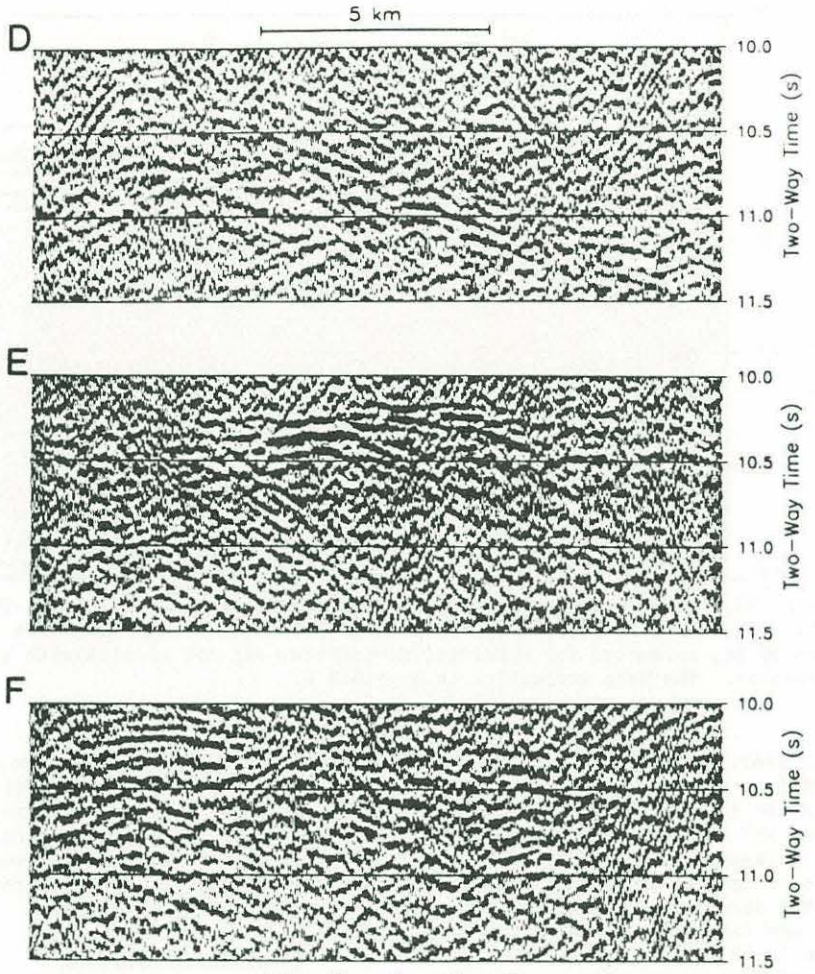

Fig. 14. (continued)

and western Pacific (provided by P. Buhl, Lamont-Doherty Geological Observatory). The North Atlantic Transect (NAT) line 15 data that are presented here were acquired on lithosphere between 118 and 135 m.y. old that was accreted at a half spreading rate of ~8 mm yr^{-1} [Klitgord and Schouten, 1986]. The western Pacific line 21 data come from lithosphere of similar age but characterized by a higher half spreading rate of ~40 mm yr^{-1} [Hilde et al., 1976]. All of the NAT data presented below are CMP stacks of 0-6 km gathers acquired with a two-ship, synthetic aperture receiver array and a 30-element air gun source array [NAT Study Group, 1985]. The conventional, near-vertical-incidence data from the western Pacific were acquired with an untuned air gun source array [Stoffa et al., 1980].

Although comparison of synthetic and observed data is hindered by the fact that our synthetic calculations do not include effects of diffracted and multiply-reflected energy, we interpret the observed data described below as showing Moho reflection events that are laterally variable on a scale similar to that observed in the synthetic profiles. We note that the travel time variations observed in both MCS data sets, variations that are similar to those observed in the synthetic profiles, cannot be explained by travel time variations in the overlying sedimentary section. Also, the multiphase Moho reflection events observed in the NAT data, which are also similar to those observed in the synthetic profiles, cannot be explained by "pegleg" multiples reverberating within the sediment column. These similarities between synthetic and observed data suggest that the structures observed in the inferred fossil crust/mantle transition of the ophiolite are characteristic of oceanic lithosphere. However, not all variability in Moho reflection response can be readily related to variability in Moho structure. We show that amplitude variability of an individual Moho phase in a section of western Pacific data can be most simply explained by variations in reflectivity of the seafloor and sediment/basement interface rather than by variations in Moho reflection coefficient. In the ensuing argument, we assume that all reflected phases were generated in the plane of the seismic profile.

North Atlantic Transect Data

The portion of NAT line 15 shown in Figure 1? extends northwestward from the "East Fracture Zone" described in Mutter et al. (1985). The data have been interpreted [Mutter et al., 1985; NAT

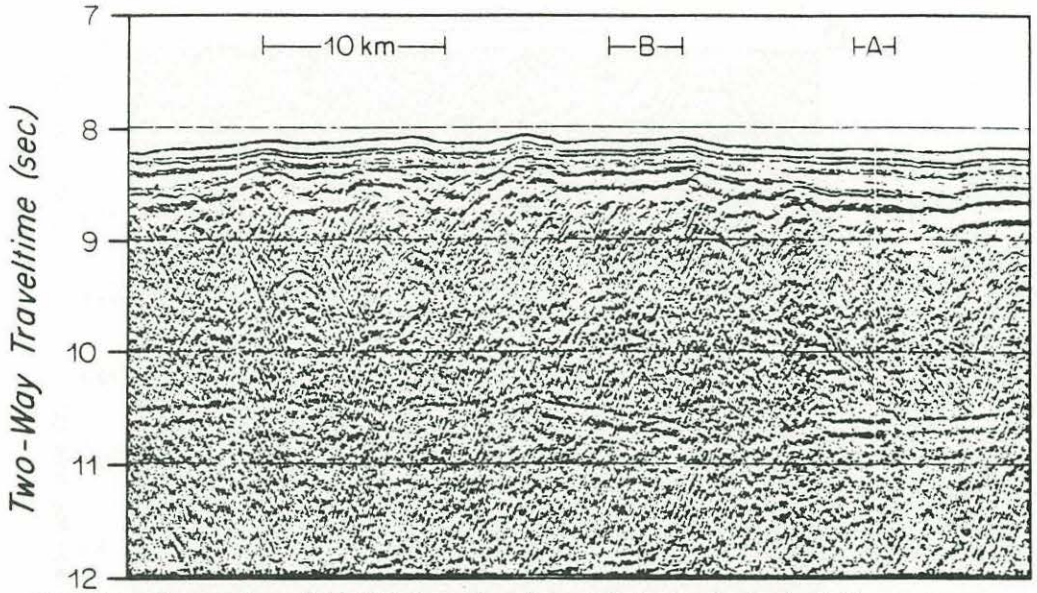

Fig. 15. Twenty-four-fold MCS data from Lamont-Doherty Geological Observatory line 21, western Pacific. The data have been deconvolved, band pass filtered from 8 to 30 Hz, corrected for spherical divergence, and are plotted with automatic gain control. The Moho reflection is at ~10.5 s.

Study Group, 1985; Mithal, 1986; Chiang and Detrick, 1986] as showing an intracrustal reflection event (horizon R) and a Moho reflection event. Along NAT line 15, the Moho event varies from a single phase that appears laterally continuous over tens of kilometers [Mutter et al., 1985; NAT Study Group, 1985] to two or more phases that are laterally discontinuous on a scale of less than 10-20 km. Here, we consider the latter type of Moho event only.

Six segments of the data shown in Figure 13, totaling 90 km in length, are shown in Figure 14. In all six segments the Moho reflection is a multiphase, laterally discontinuous event. Figure 14a shows overlapping reflection phases between 10.1 and 10.7 s two-way travel time. Note the abrupt travel time offset of the first-arriving Moho phase from ~10.1 s to ~10.6 s. The lateral and vertical dimensions of this overlapping feature are quite similar to part of the synthetic seismogram profile shown in Figure 6. A similar overlapping feature can be seen in Figure 14b, and Figure 14c shows a Moho reflection event that consists of a number of overlapping, laterally discontinuous phases at ~10.5 s. Figure 14d shows two Moho phases diverging toward the right of the plot from a common travel time of ~10.7 s. One phase shallows to a travel time of ~10.2 s, while the other deepens to a travel time of ~11.3 s. In Figure 14e, two overlapping Moho phases are seen at travel times of ~10-10.5 s. Figure 14f shows a portion of NAT data from the immediate vicinity of the East Fracture Zone. We tentatively suggest that the ~1-s sequence of laterally discontinuous reflected phases is similar to the sequence of reflected phases calculated for the Lewis Hills geological model (Figure 8), which is also interpreted as coming from the immediate vicinity of a fracture zone [e.g., Karson, 1984].

Individually, the six segments of Figure 14 show amplitude and travel time variability on a scale of 5-10 km. Collectively, the segments show variability on a scale of 10-20 km. Our synthetic profiles (Figures 6-8) suggest a similar variability, accepting the preobduction model of the BOIC (Figure 2).

Western Pacific Data

In contrast to the NAT data the Moho reflection event of Figure 15 consists of a single phase. Note, however, the ~0.25-s change in two-way travel time of the Moho event over a lateral distance of less than 10 km. A similar single-phase Moho reflection event can also be seen along part of the International Phase of Ocean Drilling/U.S. Geological Survey (IPOD/USGS) multichannel seismic reflection line from the western North Atlantic [e.g., Purdy, 1983, Figure 8]. Two segments of the data presented in Figure 15 are shown in Figures 16 and 17.

It is tempting to associate the lateral variations in Moho reflectivity evident in Figures 16a and 17a to lateral variations in Moho structure. However, the amplitude of an individual Moho phase may be primarily controlled by basement topography and by lateral variations in seismic structure of the shallow crust rather than by lateral variations in Moho reflection coefficient. Indeed, a cursory examination of Figure 16a suggests that high-amplitude Moho reflections are associated with low basement reflectivity.

We attempt to quantify the relationship between Moho reflectivity and the reflectivity of shallow structure (seafloor and sediment/basement interface) in Figures 16b and 17b. Here, we show total reflected energy as a function of range in two time windows, one from 8 to 9 s and the other

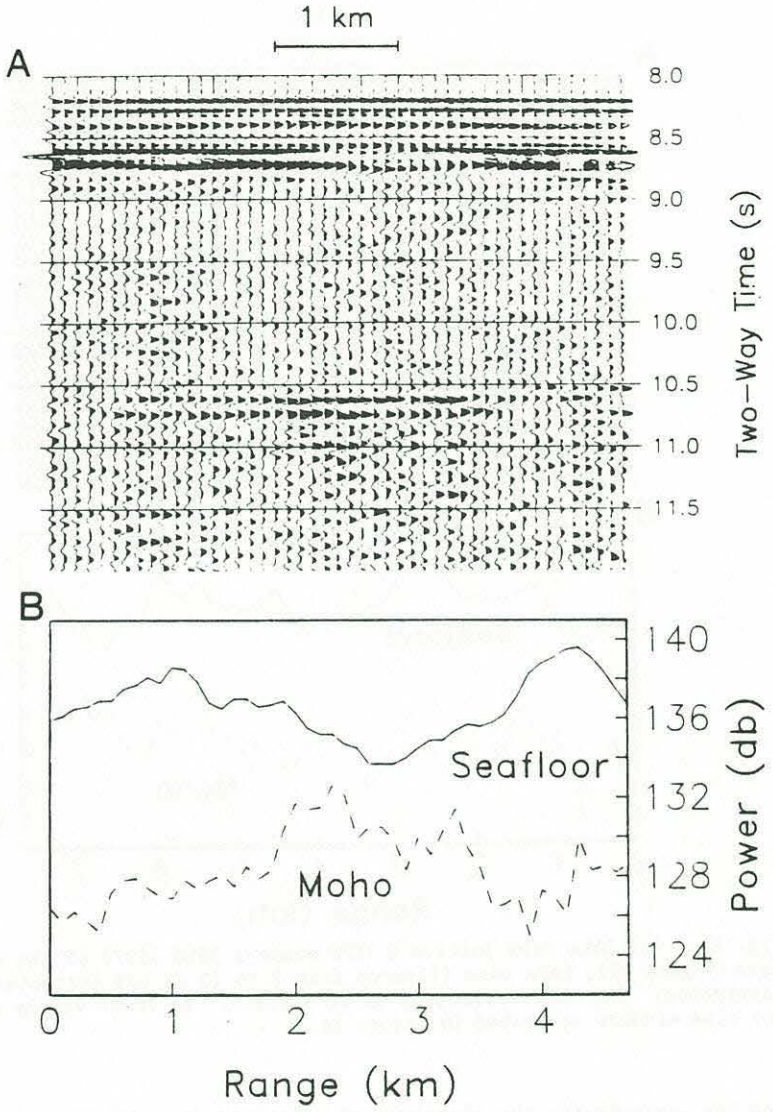

Fig. 16. (a) A detailed view of the portion of western Pacific data designated A (CMP numbers 3280-3356) in Figure 15. The data are band pass filtered from 2 to 15 Hz and are corrected for spherical divergence. The Moho reflection is at 10.6 to 10.7 s. (b) Power (sum of squared amplitudes) versus range in two time windows, one from 8 to 9 s and the other from 10.5 to 11.5 s. The shallow window includes the seafloor and sediment/basement reflection events; the deeper window encompasses the Moho reflection event.

from 10.5 to 11.5 s. The shallow window includes the seafloor and sediment/basement reflection events; the deeper window encompasses the Moho reflection event. In Figure 16b an inverse correlation between reflection power in the two windows further suggests that low reflectivity of the shallow structure has allowed greater transmission of seismic energy to the Moho and hence increased Moho reflection amplitudes. However, a similar analysis of adjacent data (Figure 17a) is inconclusive. Variability in Moho reflectivity shows no unambiguous correlation with the reflectivity of shallow structure (Figure 17b) and may result from lateral variations in Moho reflection coefficient.

Toward More Realistic Synthetic Seismograms

The synthetic seismogram data of Figures 6-8 are noise-free and are calculated with an impulsive, nonreverberative source. The advantage of such a simplification is that the seismic responses of the geological models are readily recognizable. In Figures 18 and 19 we show how the addition of a realistic source waveform and uniformly distributed random noise obscures the fine-scale variability observed in the synthetic seismograms calculated for the Table Mountain/North Arm Mountain and Lewis Hills geological models respectively. The source signature used to calculate the noise-free seismograms of

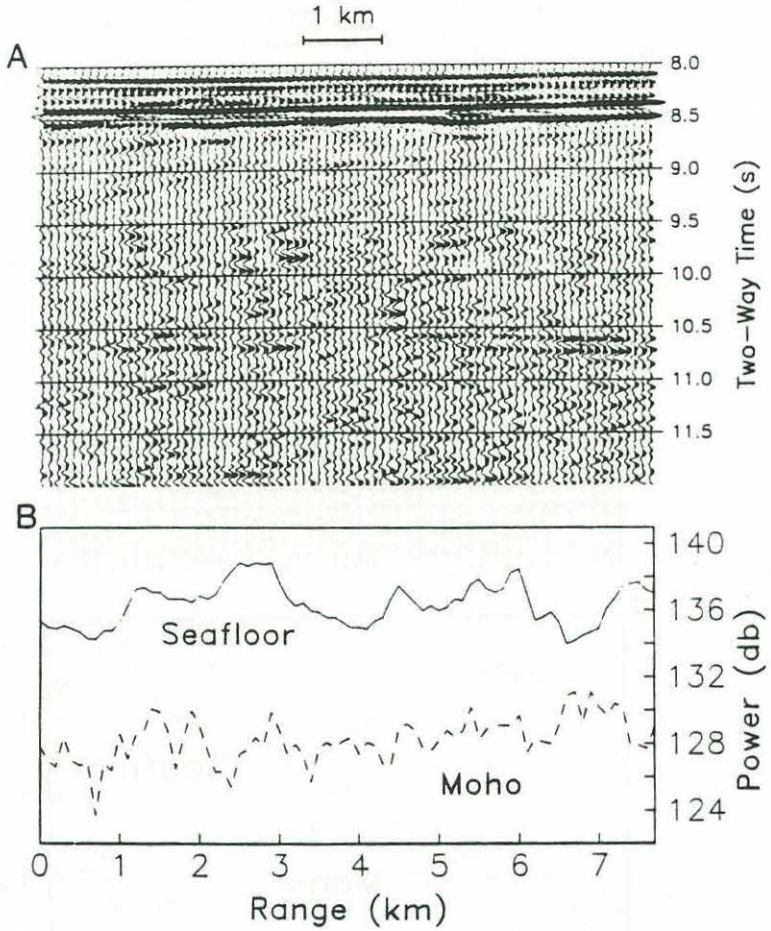

Fig. 17. (a) Data from portion B (CMP numbers 3550-3597) of the western Pacific data (Figure 15), band pass filtered from 2 to 15 Hz and corrected for spherical divergence. The Moho reflection is at ~10.5 s. (b) Power versus range for the two time windows described in Figure 16.

Figures 18a and 19a approximates the signature of a source array used by Lamont-Doherty Geological Observatory that consists of four air guns, each with a capacity of 466 cubic inches. This air gun source array was used to collect the western Pacific data shown in Figure 15 [Stoffa et al., 1980]. Note that much of the amplitude and travel time variability observed in the ideal synthetic data (Figures 6 and 8) can still be identified in the synthetic seismograms of Figures 18b and 19b, which were calculated with the reverberative source and have a signal-to-noise ratio of approximately 2:1. The inclusion of source-generated noise such as side-scattered and diffracted energy would further obscure Moho reflection waveforms.

Implications for Along-Spreading-Axis Variability in Crustal Structure

Mutter et al. [1985] interpreted NAT line 15 as showing systematic increases in crustal travel time to Moho away from fracture zones. They comment that such systematic variation in Moho travel time is consistent with recent models of oceanic crustal accretion that predict that the magma budget at any point along a spreading center is controlled by the distance of the point from centers of magmatic upwelling located approximately midway between adjacent fracture zones [Francheteau and Ballard, 1983; Whitehead et al., 1984; Schouten et al., 1985].

As discussed by Karson [1984], the rocks of the Lewis Hills Massif are considered to have been accreted immediately adjacent to a fracture zone. The two-way travel times of the first-arriving high-amplitude Moho phase in the Lewis Hills profile (Figure 8) decrease by ~0.25-0.5 s toward shorter ranges, in the direction of the inferred fossil fracture zone. However, it is clear from the Lewis Hills profiles that observed shallowing of the Moho phase is not associated with thinning of magmatic material. The structures that generate high-amplitude reflections in the Lewis Hills model are low-velocity lenses of mafic and ultramafic cumulate material. Negligible reflection amplitudes from the residual upper mantle (represented by the harzburgite unit) in

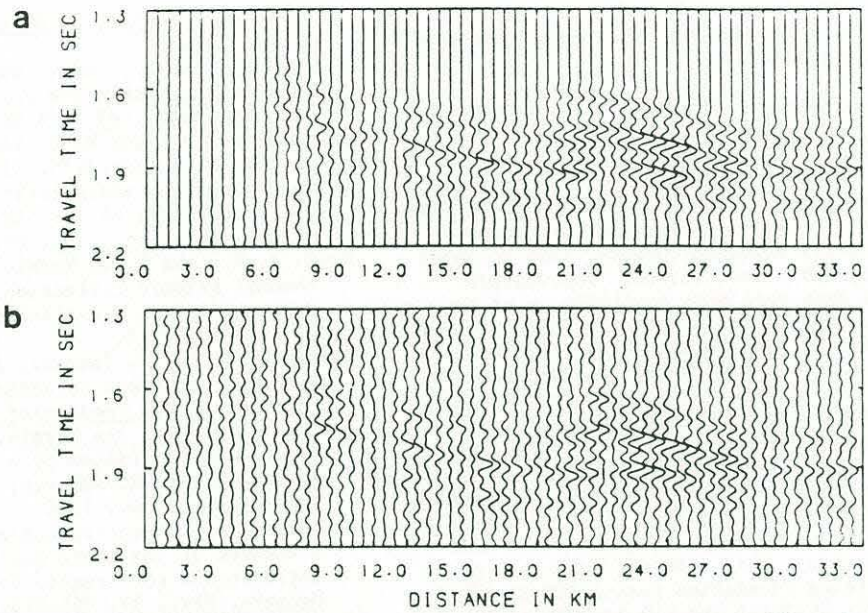

Fig. 18. (a) Two-dimensional normal-incidence synthetic seismogram profile of the Table Mountain/North Arm Mountain geological model (Figure 6), computed with a source waveform that approximates the output of a source array consisting of four air guns, each with a capacity of 466 cubic inches. The data are band pass filtered from 10 to 15 Hz. (b) As for Figure 18a but uniformly distributed random noise has been added to the section. Signal-to-noise ratio is approximately 2:1.

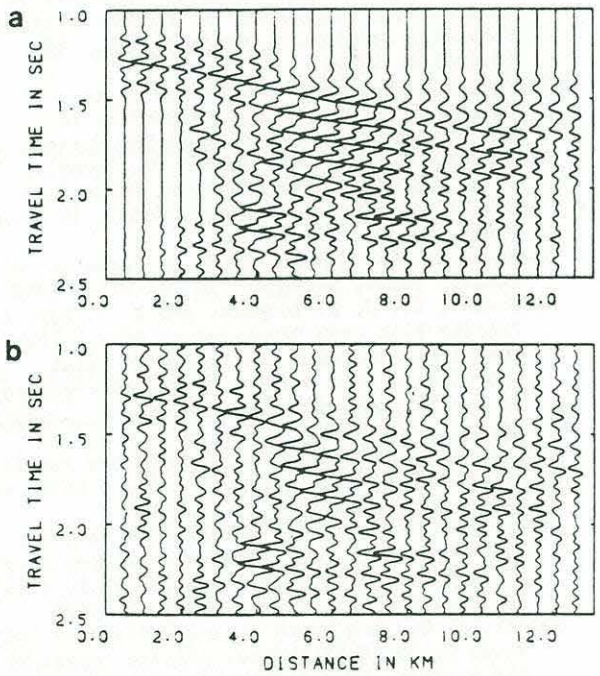

Fig. 19. (a) Two-dimensional normal-incidence synthetic seismogram profile of the Lewis Hills geological model (Figure 8), computed with the source described in Figure 18. The data are band pass filtered from 10 to 15 Hz. (b) As for Figure 19a, but uniformly distributed random noise has been added to the section. Signal-to-noise ratio is approximately 2:1.

all three synthetic profiles demonstrate that two-way travel time to Moho only approximates thickness of magmatic material.

Conclusions

1. In the synthetic profiles the Moho reflection event varies from a single phase to two or more phases of up to 1-s (two-way travel time) total duration. Individual phases show lateral variation in amplitude, and their two-way travel times vary by as much as 0.25 s over horizontal distances as short as 10 km. Lateral discontinuity of phases results in abrupt variations in the travel times of first-arriving, high-amplitude Moho phases.

2. The geological structures generating the highest-amplitude Moho reflections vary from high- and low-velocity lenses of mafic and ultramafic material in the lower crust and upper mantle to interlayered mafic and ultramafic lithologies in the Moho Transition Zone. Reflection amplitudes from the residual upper mantle are insignificant, and our modeling suggests that using the first-arriving, high-amplitude Moho phase to estimate thickness of magmatic material might result in errors of up to 1-s two-way travel time (~3-4 km).

3. Multichannel seismic data from both the western Pacific and western North Atlantic show Moho travel time variations similar to those observed in the synthetic profiles. The western North Atlantic data also show multiphase Moho reflection events that are laterally discontinuous on a scale similar to that observed in the synthetic data, suggesting that the structures

observed in the inferred fossil crust/mantle transition of the ophiolite are characteristic of oceanic lithosphere.

Acknowledgements. We thank V. Cerveny and I. Psencik for making their SYNS83 and SEIS83 synthetic seismogram codes available to the scientific community. Bob Nowack supplied both programs, and Dennis Lindwall modified SEIS83 for a CMP geometry. Kelly Luetkemeyer and Robert Chase generously provided computer time at Woods Hole Oceanographic Institution. The western Pacific MCS data were made available to us by Peter Buhl, and the North Atlantic Transect data were provided by John Mutter and Bob Detrick. The record sections from which we generated Figures 13 and 15 were supplied by John Mutter and Peter Buhl, respectively. We thank John Diebold for providing the air gun source array signature. John Ewing criticized an early draft of the manuscript. Mike Purdy's suggestions and comments greatly improved this work. We thank John Mutter, John Orcutt, and Steve Swift for critical reviews. This work was supported by National Science Foundation grants OCE 81-17210 (T.M.B.), EAR 80-26445 and EAR 83-9535 (J.A.K.), and by OCE 80025206 (J.A.C., awarded to G. M. Purdy). Woods Hole Oceanographic Institution contribution 6193.

References

Berryman, L. H., P. L. Goupillaud, and K. H. Waters, Reflections from multiple transition layers, part 1, Theoretical results, Geophysics, 23, 223-243, 1958.

Birch, F., The velocity of compressional waves in rocks to 10 kilobars, II, J. Geophys. Res., 66, 2199-2224, 1961.

Bonatti, E., and P. Hamlyn, Oceanic ultramafic rocks, in The Sea, vol. 7, edited by C. Emiliani, pp. 119-218, John Wiley, New York, 1981.

Brocher, T. M., J. A. Karson, and J. A. Collins, Seismic stratigraphy of the oceanic Moho based on ophiolite models, Geology, 11, 62-65, 1985.

Calvert, A. J., and C. G. Potts, Seismic evidence for hydrothermally altered mantle beneath old crust in the Tydeman fracture zone, Earth Planet. Sci. Lett., 75, 439-449, 1985.

Casey, J. F., J. A. Karson, D. Elthon, E. Rosencrantz, and M. Titus, Reconstruction of the geometry of accretion during formation of the Bay of Islands Ophiolite Complex, Tectonics, 2, 509-528, 1983.

Casey, J. F., D. L. Elthon, F. X. Siroky, J. A. Karson, and J. Sullivan, Geochemical and geological evidence bearing on the origin of the Bay of Islands and Coastal Complex ophiolites of western Newfoundland, Tectonophysics, 116, 1-40, 1985.

Cerveny, V., I. A. Molotkov, and I. Psencik, Ray Method in Seismology, 214 pp., Univerzita Karlova, Prague, Czechoslovakia, 1977.

Chapman, C. H., and J. A. Orcutt, The computation of body wave synthetic seismograms in laterally homogeneous media, Rev. Geophys., 23, 105-163, 1985.

Chiang, C. S., and R. S. Detrick, The seismic structure of the lower oceanic crust and Moho from P and S wave synthetic seismogram modeling, Geophys. J. R. Astron. Soc., in press, 1986.

Christensen, N. I., and S. Lundquist, Pyroxene orientation within the upper mantle, Geol. Soc. Am. Bull., 93, 279-288, 1982.

Francheteau, J., and R. D. Ballard, The East Pacific Rise near 21°N, 13°N and 20°S: Inferences for alongstrike variability of axial processes of the Mid-Ocean Ridge, Earth Planet. Sci. Lett., 64, 93-116, 1983.

Grow, J. A., and R. G. Markl, IPOD-USGS multichannel seismic reflection profile from Cape Hatteras to the Mid-Atlantic Ridge, Geology, 5, 625-630, 1977.

Hilde, T. W. C., N. Isezaki, and J. M. Wageman, Mesozoic sea-floor spreading in the North Pacific, in The Geophysics of the Pacific Ocean Basin and Its Margin, Geophys. Monogr. Ser., vol. 19, edited by G. H. Sutton, M. H. Manghnani, and R. Moberly, pp. 205-226, AGU, Washington, D. C., 1976.

Karson, J. A., Reconstructed seismic velocity structure of the Lewis Hills Massif and implications for oceanic fracture zones, J. Geophys. Res., 87, 961-978, 1982.

Karson, J. A., Variations in structure and petrology in the Coastal Complex, Newfoundland: Anatomy of an oceanic fracture zone, in Ophiolites and Oceanic Lithosphere, edited by I. G. Gass, S. J. Lippard, and A. W. Shelton, pp. 131-144, Blackwell, London, 1984.

Karson, J. A., J. A. Collins, and J. F. Casey, Geologic and seismic velocity structure of the crust/mantle transition in the Bay of Islands Ophiolite Complex, J. Geophys. Res., 89, 6126-6138, 1984.

Klitgord, K. D., and H. Schouten, Plate kinematics of the Central Atlantic, in The Geology of North America: The Western Atlantic Region, edited by B. E. Tucholke and P. R. Vogt, DNAG Ser., vol. 1, Geological Society of America, Boulder, Colo., in press, 1986.

Lewis, B. T. R., The processes of formation of oceanic crust, Science, 220, 151-157, 1983.

Macdonald, K., J. C. Sempere, and P. J. Fox, East Pacific Rise from Siqueiros to Orozco Fracture Zones: Along-strike continuity of axial neovolcanic zone and structure and evolution of overlapping spreading centers, J. Geophys. Res, 87, 6049-6069, 1984.

MacKenzie, K., Crustal stratigraphy and realistic seismic data, Ph.D. thesis, 121 p., Univ. of Calif., San Diego, La Jolla, 1984.

Mithal, R., Evidence for a basal low velocity zone in oceanic crust, and new methods of phase analysis and extremal inversion, Ph.D. thesis, 195 pp., Columbia Univ., New York, 1986.

Mutter, J. C., and North Atlantic Transect (NAT) Study Group, Multichannel seismic images of the oceanic crust's internal structure: Evidence for a magma chamber beneath the Mesozoic Mid-Atlantic Ridge, Geology, 13, 629-632, 1985.

NAT Study Group, North Atlantic Transect: A wide aperture, two-ship multichannel seismic investigation of the oceanic crust, J. Geophys. Res., 90, 10,321-10,341, 1985.

Penrose Conference Participants, Ophiolites, Geotimes, 17, 24-25, 1972.

Phillips, J. D., and H. S. Fleming, Multi-beam sonar study of the Mid-Atlantic Ridge rift valley, 36°-37° N, Geol. Soc. Am. Map Ser., MC-19, 1978.

Purdy, G. M., The seismic structure of 140 Myr old crust in the western central Atlantic Ocean, Geophys. J. R. Astron. Soc., 72, 115-137, 1983.

Purdy, G. M., and J. I. Ewing, Seismic structure of the oceanic crust, in The Geology of North America: The Western Atlantic Region, edited by B. E. Tucholke and P. R. Vogt, DNAG Ser., vol. 1, Geological Society of America, Boulder, Colo., in press, 1986.

Salisbury, M. H., and N. I. Christensen, The seismic velocity structure of a traverse through the Bay of Islands Ophiolite Complex, Newfoundland: An exposure of oceanic crust and upper mantle, J. Geophys. Res., 83, 805-817, 1978.

Schouten, H., K. D. Klitgord, and J. A. Whitehead, Segmentation of mid-ocean ridges, Nature, 317, 225-229, 1985.

Spudich, P., and J. Orcutt, Petrology and porosity of an oceanic crustal site: Results from wave form modeling of seismic refraction data, J. Geophys. Res., 85, 1409-1433, 1980a.

Spudich, P., and J. Orcutt, A new look at the seismic velocity structure of the oceanic crust, Rev. Geophys., 18, 627-645, 1980b.

Stoffa, P. L., P. Buhl, T. J. Herron, T. K. Kan, and W. J. Ludwig, Mantle reflections beneath the crestal zones of the East Pacific Rise from multichannel reflection data, Mar. Geol., 35, 83-97, 1980.

Tulchoke, B. E., R. E. Houtz, and W. J. Ludwig, Sediment thickness and depth to basement in the western North Atlantic Ocean Basin, Am. Assoc. Pet. Geol. Bull., 66, 1384-1395, 1982.

Watts, A. B., U. S. ten Brink, P. Buhl, and T. M. Brocher, A multichannel seismic study of lithosphere flexure across the Hawaiian-Emperor Seamount chain, Nature, 315, 105-111, 1985.

White, R. S., and R. A. Stephen, Compressional to shear wave conversion in oceanic crust, Geophys. J. R. Astron. Soc., 63, 547-565, 1980.

Whitehead, J. A., J. B. Dick, and H. Schouten, A mechanism for magmatic accretion under spreading centers, Nature, 312, 146-148, 1984.

T. M. Brocher, U.S. Geological Survey, 345 Middlefield Road, MS/977, Menlo Park, CA 94025.

J. A. Collins, MIT/WHOI Joint Program in Oceanography, Woods Hole Oceanographic Institution, Woods Hole, MA 02543.

J. A. Karson, Department of Geology, Duke University, Durham, NC 27706.

(Received December 11, 1985;
revised July 15, 1986;
accepted July 16, 1986.)

CHAPTER 2

SEISMIC VELOCITY STRUCTURE AT DSDP SITE 504B, PANAMA BASIN: EVIDENCE FOR THIN OCEANIC CRUST

Abstract

We present an analysis of wide-angle reflection/refraction data collected in the immediate vicinity of Deep Sea Drilling Project Hole 504B in the Panama Basin, currently the deepest drillhole (1.288 km) into oceanic crust. The data were acquired with a 1785 $inch^3$ airgun array and fixed-gain sonobuoy receivers, and consist of four intersecting profiles shot along three different azimuths. Near-normal-incidence, multichannel seismic (MCS) reflection data were acquired simultaneously. Observed P- and S-wave arrivals out to maximum ranges of 30 km constrain the crustal velocity structure at basement depths of ~0.5-5 km. Comparison of the travel times and amplitudes of the P- and S-wave arrivals on all four profiles reveals important similarities. These common features were modeled using the reflectivity synthetic seismogram method, the emphasis of the analysis being on the determination of the velocity structure of the middle and lower crust. Forward modeling shows that in contrast to standard oceanic velocity models, a velocity-depth profile that better explains the observed data is characterized by high velocity gradients (up to 0.6 km s^{-1} km^{-1}) in the middle crust, a 1.8 km thick low-velocity zone (V_p=7.1-6.7 km s^{-1}) immediately above Moho, and a total crustal thickness of only 5 km. Interpretation of the high velocity gradients in the middle crust is constrained by the observation of P3-branch amplitude focusing at ranges of 16-19 km. Although not as well developed in comparison to the P-wave arrivals, S3-branch arrivals show similar focusing. Total crustal thickness is constrained by the combined interpretation of a P-wave, wide-angle reflection event observed at a range of 16-28 km, and an MCS reflection

event with a crustal travel time of 1.4-1.5 s. Although these events cannot be directly correlated, their travel times are consistent with the assumption that both have a common origin. Amplitude modeling of the wide-angle event demonstrates that these events are generated at the Moho.

Introduction

Repeated observations have shown that, away from spreading centers and fracture zones, the seismic velocity structure of oceanic crust can typically be characterized by a small number of locally horizontal layers of positive velocity gradient; layer thicknesses, initial velocities, and gradient magnitudes show only limited regional variation (Raitt, 1963; Spudich and Orcutt, 1980a, 1980b; Purdy, 1983; White, 1984). This simplicity is dependent on the resolving power of the wide-angle reflection/refraction technique, typically hundreds of meters and kilometers in the vertical and horizontal directions, respectively (e.g. Purdy, 1983; Bratt and Purdy, 1984). Near-normal-incidence, multichannel seismic (MCS) reflection data suggest that the oceanic crust is characterized by a locally horizontal, layered reflectivity structure at even smaller length scales (e.g. Mutter et al., 1985). The capability of wide-angle reflection/refraction and MCS reflection techniques to map variations in seismic layer thickness (e.g. Bratt and Purdy, 1984) and reflector depth (e.g. Mutter et al., 1985) is an incentive to correlate seismic and geologic structures, and to investigate changes in crustal structure as a function of parameters such as crustal age and proximity to fracture zones. This task is made difficult by the large number of parameters that control rock velocity (e.g. Purdy and Ewing, 1986), and by the wide range of seismic impedance variations - not necessarily resolvable with wide-angle reflection/refraction techniques - that can generate detectable near-normal-incidence reflections (e.g. MacKenzie, 1984; Brocher et al., 1985; Collins et al., 1986).

Marine seismologists typically relate the layered velocity-depth

structure that they derive from refraction experiments to geological structure in terms of the vertical distribution of lithologies that are found in ophiolite sequences. In this approach, seismic Layer 2 is correlated with extrusive volcanic and sheeted-dike sequences, seismic Layer 3 is correlated with a gabbroic sequence, and mantle velocities of 8.0 km s^{-1} or greater are associated with residual ultramafic rocks. However, the validity of the ophiolite model of oceanic crustal stratigraphy is uncertain. An alternative viewpoint is that the observed velocity layering can be correlated with approximately constant maximum depths of chemical alteration and cracking in either a compositionally homogeneous or layered crust (e.g. Lewis, 1983).

An unambiguous, albeit non-unique, correlation of seismic and geologic structures awaits extensive deep crustal drilling. In this paper, we present results of a wide-angle reflection/refraction experiment conducted in the vicinity of Deep Sea Drilling Project (DSDP) Hole 504B, currently the deepest drillhole into the igneous oceanic crust. Hole 504B has been drilled to a basement depth of 1.288 km, approximately a fifth of typically reported values of oceanic crustal thickness; currently it is the only hole in oceanic crust that has been drilled to a basement depth greater than 600 m. The seismic data discussed here consist of four intersecting wide-angle reflection/ refraction profiles that were shot along three different azimuths to maximum source-receiver offsets of ~30 km. The data provide constraints on the crustal velocity structure at basement depths of ~0.5-5.0 km. Interpretation of the wide-angle reflection/refraction profiles is constrained by simultaneously acquired near-normal-incidence MCS

reflection data. Iterative forward modeling of the wide-aperture P- and S-wave travel times and amplitudes shows that the data cannot be explained by standard oceanic velocity-depth models. In contrast, the data are consistent with the existence of a high-velocity layer in the middle crust, a low-velocity zone immediately above Moho, and a total crustal thickness of only 5.0 km.

Study Area

DSDP Site 504B is located on the Nazca plate, about 225 km south of the Costa Rica Rift, the easternmost segment of the Cocos-Nazca plate boundary (Figure 1a). Water depth and sediment thickness at the drillsite are 3460 m and 275 m respectively, and the crustal age is estimated to be 5.9 Myr (Hobart et al., 1985). The Costa Rica Rift is characterized by asymmetric spreading; at crustal ages less than 8 Myr, observed magnetic anomalies can be satisfactorily modeled by assuming spreading rates of 30 mm/yr to the north and 36-38 mm/yr to the south (Hey et al., 1977; Klitgord et al., 1975). Within a radius of 50 km about the drillsite, basement topography has amplitudes typically less than 100 m (Langseth et al., 1983); basement topographic highs strike east-west, parallel to the Costa Rica Rift (Searle, 1983).

Langseth et al. (1983) interpreted wide-angle reflection/refraction data acquired with sonobuoy receivers in the vicinity of the drillsite as showing basement P-wave velocities of 4.0-5.0 km s^{-1}, in agreement with the results of borehole seismic experiments described by Stephen (1983), Stephen (1985), and Little and Stephen (1985). Particle motion and travel time analyses of the borehole data also showed evidence for

azimuthal anisotropy that is confined to the upper 500m of oceanic crust. P-wave velocities vary from 4.0 to 5.0 km s^{-1} in directions approximately perpendicular to and parallel to, respectively, the local magnetic anomalies (Little and Stephen, 1985; Stephen, 1985). The observed variation in the S-wave velocities over the same azimuthal range is from 2.3 to 2.8 km s^{-1}. Crustal thickness was estimated to be 4.5-6.5 km (Langseth et al., 1983).

Hole 504B was initially drilled during DSDP Legs 69 and 70 (CCRUST, 1982). Repeated drilling during DSDP Leg 83 (Anderson et al., 1982) and Ocean Drilling Project (ODP) Leg 111 (Shipboard Scientific Party, 1988) has resulted in a total basement penetration of 1.288 km, making Hole 504B the deepest drillhole into oceanic crust at the time of writing. An extensive and varied set of downhole geophysical data were collected on these legs and also on DSDP Leg 92 (Moos et al., 1986).

The sedimentary sequence at Site 504B consists predominantly of nannofossil oozes and chalks that are characterized by low P-wave velocities of 1.51-1.53 km s^{-1} (Wilkens and Langseth, 1983). Immediately above basement, up to 30 m of interbedded limestones and cherts (V_p=4.25 km s^{-1}) were drilled (CCRUST, 1982; Wilkens and Langseth, 1983). From the top of oceanic crust downward, the drilled igneous sequence consists of 0.575 km of extrusive basalt flows and pillows, 0.209 km of extrusive/intrusive transitional lithologies, and finally 0.504 km of dikes (Anderson et al., 1982; Shipboard Scientific Party, 1988). The dikes are distinguished from extrusive rocks on the basis of texture and the absence of volcanic glass (Anderson et al., 1982). The vertical sequence of extrusives and dikes drilled at 504B is

consistent with the ophiolite model of oceanic crust (e.g. Coleman, 1977). Consequently, the dike succession at DSDP Site 504B is referred to as a sheeted-dike sequence.

Seismic Data at Site 504B

In May 1985, R.V. ROBERT D. CONRAD was used to collect approximately 1700 km of near-normal-incidence MCS data in the vicinity of DSDP Site 504B (Figure 1a). Simultaneously, wide-angle reflection/refraction data were acquired by deploying over 40 fixed-gain, free-drifting sonobuoys. Two different sound sources were used during the experiment, an untuned array consisting of 4 airguns with an individual capacity of 466 cubic inches, and a tuned array of 4 airguns with chamber sizes of 235, 350, 500, and 700 cubic inches. Both sources were fired at pressures of 2000 pounds per square inch. The source signatures of these arrays have durations of ~300 ms and ~150 ms respectively, and are characterized by predominant frequencies of ~9 Hz and ~30 Hz, respectively. Shot separation was ~50 m. The 2.4 km long receiver array consisted of 48 channels with a group separation of 50m. The MCS data were collected into 24 fold common-mid-point (CMP) gathers, resulting in a CMP spacing of ~25 m.

MCS Data

Common mid-point stacks of the MCS data collected in the immediate vicinity of DSDP Site 504B (Figure 2) show a reflection event at a travel time of 6.4-6.5 s, about 1.4-1.5 s below the top of oceanic crust. The high stacking velocity of this event (~3.0 km s^{-1}), together with its

identification on four profiles collected along four different azimuths, strongly suggests that this event is a lower crustal or upper mantle reflection rather than a scattered reflection from the seafloor or oceanic basement. The crustal travel time of this event is 0.5 s less than typically reported values for Moho reflections, and based on the near-normal-incidence data alone, it is uncertain whether this event is an intracrustal or Moho reflection. However, regardless of the origin of the 1.4-1.5 s reflection event, its observation is a significant constraint on the velocity-depth structure at the drillsite. A large impedance contrast is required at a travel time of 1.4-1.5 s below the top of oceanic crust.

Wide-Angle Reflection/Refraction Data

The primary goal of this study was to determine the velocity structure at the drillsite so that it may be correlated with the results of anticipated future drilling. We analysed four wide-angle reflection/refraction profiles that were collected along three different azimuths in the immediate vicinity of the drillsite. All of these profiles were acquired with the tuned airgun array. Profile 504B03 was shot from east to west, profile 504B12 was shot from south-west to north-east, and profiles 504B19 and 504B21 were shot from north-west to south-east (Figure 1b). Profile 504B19 is shown in Figure 3 as an example of the data quality.

Shot-receiver ranges for the wide-angle reflection/refraction profiles were measured by multiplying the arrival times of the source/receiver direct wave by the water-surface velocity estimated from

bathythermograph data. We assumed negligible sonobuoy drift away from the ship's track. The errors in shot-receiver range are estimated to be less than 3% at horizontal ranges less than ~18 km. At ranges greater than 18 km, the water-wave was not recorded, and shot-receiver ranges were estimated by extrapolating a best-fit straight line to the observed travel times. Assuming that variations in ship speed were less than 6%, the errors in range are less than 7%.

The wide-angle reflection/refraction profiles show P- and S-wave arrivals out to maximum ranges of ~30 km. No P- or S-wave arrivals with phase velocities typical of the upper mantle (V_p~8.1 km s^{-1}, V_s~4.7 km s^{-1}) are observed (e.g. Figure 3). The lack of such Pn or Sn arrivals means that crustal thickness can only be inferred indirectly from wide-angle reflections and refractions from the Moho transition zone.

Travel-Time Analysis

Travel-Time Data

We determined the travel times of over 1000 P-wave arrivals and about 400 S-wave arrivals at ranges of ~5-22 km. Picking precision is estimated to be ~0.01s and ~0.015s for P- and S-wave arrivals, respectively. Merged P- and S-wave travel times are shown in Figure 4. A water-delay correction (e.g. Purdy, 1982) was added to the travel times for profile 504B12 because the hydrophone on the sonobuoy used to acquire this profile was inadvertently deployed 73 m deeper (91 m versus 18 m) than the hydrophones used to acquire the other three profiles.

We attempted to quantify the extent of scatter in the data by fitting

quadratic splines to both sets of arrivals; the splines were constrained to have negative second derivatives (ensuring decreasing slopes at greater ranges) and to minimize the root-mean-square deviation of the observed data. This parameterization is appropriate for a velocity-depth function consisting of a continuous sequence of positive, linear velocity gradients. The splines shown in Figures 4 fit the merged P- and S-wave data with root mean square deviations of 0.049 s and 0.054 s respectively, values greater than the estimated picking precision. However, for the merged profiles the standard deviation about mean water depth is 35m or 0.046s travel time. Consequently, the scatter in the merged P- and S-wave travel times is most simply explained by variations in seafloor and basement depth. The data were not corrected for these topographic effects because of the difficulty in accurately estimating ray-entry points given the likelihood of receiver drift. Accordingly, we conclude that within the resolution afforded by these travel time data alone, the seismic structure of the upper to middle crust at Site 504B is laterally homogeneous.

Travel-Time Modeling

The travel time curves predicted by the simple velocity-depth model shown in Figure 5a satisfactorily match the P- and S-wave arrival times observed on profile 504B19 (Figure 5b). We used profile 504B19 because clear arrivals are observed to ranges of 28 km. This initial solution, which is typical of 'normal' oceanic crust (e.g. Purdy and Ewing, 1986), is a starting point for the iterative forward modeling of the observed amplitude distribution. The velocity at the top of oceanic basement is

unconstrained because arrivals that have turned in the upper 0.5 km of the oceanic crust are obscured by the seafloor and basement reflections (Figure 3). Consequently, we assumed a P-wave velocity structure for the upper 0.5 km that is similar to the preferred model of Little and Stephen (1985). As suggested by the observation of a deep reflection event in the MCS data (Figure 2), the velocity model has a discontinuity at a crustal travel time of 1.40 s. This velocity discontinuity, which represents the top of the Moho transition zone in the model shown in Figure 5a, predicts wide-angle reflection/refraction arrivals that match the travel times of the observed P-wave arrivals at ranges of ~16-28 km (Figure 5b). The S-wave velocity-depth profile was derived from the P-wave profile by assuming Vp/Vs ratios ranging from 2.1 in the upper crust to 1.7 in the upper mantle. These values of V_p/V_s are typical of oceanic crust (Hyndman, 1979; Spudich and Orcutt, 1980a).

Given that the predicted travel times satisfactorily match the observed data, we tentatively recognize four phases in the observed P- and S-wave arrivals (Figure 5b). These phases are: (i) P3-branch arrivals observed at ranges of 5-18 km, and characterized by a phase velocity of 6.5 km s^{-1}, (ii) PmP arrivals observed at ranges of 16-28 km, and characterized by phase velocities of 7.0-7.5 km s^{-1}, (iii) S3-branch arrivals observed at ranges of 7-20 km, and characterized by a phase velocity of 3.8 km s^{-1}, and (iv) SmS-branch arrivals observed at ranges of 17-27 km, and characterized by phase velocities of ~4.0-4.4 km s^{-1}. This nomenclature is in accordance with that proposed by Spudich and Orcutt (1980a). Although identification of these phases, particularly the PmP and SmS phases, cannot be justified solely on the

basis of travel times, introduction of this nomenclature simplifies the description of the sonobuoy profiles. As discussed below, synthetic seismogram modeling indicates that these phases are appropriately named, and that consequently the near-normal-incidence reflection event is a reflection from the Moho.

Observed Amplitude Variations

Allowing for travel time variations brought about by the seafloor and basement topography, comparison of the travel times of the P and S diving-wave arrivals in the range window 6-18 km suggests that the four profiles are indistinguishable. However, seismic amplitudes are a more sensitive indicator of velocity structure than travel time data alone (Kennett, 1977). Consequently, we used the amplitudes of P- and S-wave arrivals observed on the four profiles to provide a more meaningful comparison of the data sets.

Comparison of the P-wave amplitude patterns observed on each of the four profiles reveals important similarities (Figures 6a, 6b). High relative amplitudes are observed at horizontal ranges of ~6 and 16-19 km. Amplitudes of P3-branch arrivals at ranges greater than ~20 km are diminished. The 6 km peak has frequently been reported (e.g. Bratt and Purdy, 1984, Fischer and Purdy, 1986), and is indicative of a downward increase in velocity gradient in the upper oceanic crust. However, the focusing of P-wave energy at 16-19 km has not been widely described. This amplitude high consists of two separate peaks on profiles 504B03, 504B19, and 504B21, but is apparently made up of a single peak on profile 504B12 (Figure 6b). All four profiles show PmP arrivals. This wide-

angle reflection phase is observed at distances as short as 15-16 km on profiles 504B03, 504B12, and 504B19, and may possibly be traceable to similar ranges on profile 504B21 (Figure 6b). The travel time offset between the P3 branch and the PmP branch is ~0.2-0.3 s at a range of 20 km. The amplitude distribution along the PmP branch varies as a function of range on profiles 504B12, 504B19, and 504B21. The horizontal ranges of the amplitude highs along the PmP branches of profiles 504B12, 504B19, and 504B21 vary by less than 1 km.

The amplitude distribution of the S-wave arrivals also show similarities from profile to profile (Figure 6c). Multiply turned diving-wave arrivals are observed on profiles 504B03, 504B12, and 504B19. Focusing of S3-branch arrivals is observed at horizontal ranges of 15-19 km on all four profiles. At ranges greater than 20 km, the amplitude of the S3-branch arrivals are diminished. All four profiles are characterized by SmS arrivals which can be traced to horizontal ranges as short as 15 km.

In order to provide a more quantitative comparison of the observed amplitude patterns, we computed the power of P3- and S3-branch arrivals in a window of length 0.250 s (Figure 7). The profile-to-profile correlation of the P-wave power peaks that is presented in Figure 7a is guided by the similarities in the amplitude distributions evident in Figures 6a and 6b. We did not attempt to correlate the power peaks of the S-wave arrivals, but we note the gross similarity in the power distribution at horizontal ranges of 15-19 km (Figure 7b). The variability in the power distribution of the S3-branch arrivals may arise, in part at least, from lateral variations in the efficency of P-

to S-wave mode conversion.

The observation of high-amplitude P-wave arrivals at horizontal ranges of 16-19 km on all four profiles suggests that this focusing is not brought about by variable topography, but is due to variations in the velocity-depth structure of the middle crust. Furthermore, the velocity structure of the middle crust must be similar over the area bounded by the wide-aperture profiles. The similarities in the travel time and amplitude patterns of the PmP arrivals likewise suggest that these patterns represent information about the velocity structure of the lower crust. The S-wave profiles support the inference of lateral homogeneity of the middle and lower crust.

Of course, some of the observed variation in P- and S-wave amplitudes, both along each profile and from profile to profile, are probably due to variations in seafloor and basement topography. Stephen (1988) showed that the observed topographic variations at Site 504B can result in P-wave amplitude variations of up to 12 dB over lateral distances as short as 0.5 km. In addition, finite difference synthetic seismogram modeling of borehole seismic data acquired at Hole 504B indicates that the velocity structure of the upper 0.6 km of oceanic crust is laterally heterogeneous (Stephen, 1988). The inferred dimensions of areas of anomalous velocity gradient are 1-3 km, and horizontal velocity gradients are interpreted to be as high as 2 s^{-1}. However, the gross similarity in amplitude distribution described above suggests that the velocity structure of the middle and lower crust is similar from profile to profile. The focusing effects of variable seafloor and basement topography, together with shallow-level

heterogeneity, probably accounts for P3- and S3-branch amplitude highs that are not observed on two or more profiles (Figure 7).

Amplitude Modeling

We constrained the velocity structure at DSDP Site 504B by comparing the observed data to synthetic seismogram profiles calculated from over 20 velocity-depth models (Figure 8a). We used the reflectivity method (Fuchs and Muller, 1971; Kennett 1975a; Kennett, 1975b) to compute synthetic seismograms for phase velocities of 1.6-55.0 km s^{-1}, and frequencies of 5-35 Hz. The synthetic seismograms include all multiply-reflected and mode-converted phases. Densities were computed from the relationship $\rho = 0.252 + 0.379V_p$ (Spudich and Orcutt, 1980a). Linear velocity gradients were simulated by a stack of thin homogeneous layers; for each gradient layer, the homogeneous layer thickness was chosen to be less than the wavelength appropriate for a frequency of 45 Hz and a velocity equal to the minimum S-wave velocity. The source wavelet, described by a simple analytical expression, has a duration of ~0.15 s and a predominant frequency of ~17 Hz. These parameters are appropriate for the observed refracted arrivals.

Strategy

Our goal was to generate synthetic seismograms that simulated the gross amplitude patterns that are common to all four profiles. In particular, we sought to reproduce: (i) the high P-wave amplitudes that are observed at ~6 and 16-19 km, (ii) the high S-wave amplitudes at

15-19 km, and (iii) the observed amplitude distributions of the PmP and SmS branches. No attempt was made to match synthetic and observed waveforms because of the probability of waveform variation brought about by variable topography and upper crustal heterogeneity, and also because of the limited dynamic range of the sonobuoy receivers. Because of the similarities between the four profiles, modeling efforts were confined to reproducing the amplitude features of just one of the data sets. We chose 504B19 because this data set extends to comparatively large ranges, is characterized by high signal-to-noise ratios, and displays the amplitude features that we consider to be characteristic of the wide-angle reflection/refraction data collected at Site 504B.

Two well-known limitations of estimating velocity structure by iterative forward modeling via the reflectivity method are the related difficulties of objectively determining the 'best-fit' model and estimating the error bounds about the preferred solution. Although our choice of preferred velocity model (Figure 8b) is subjective, we demonstrate that in comparison to plausible alternative models, our preferred solution 'better' explains the observed amplitude distribution. The velocity models shown in Figures 8b and 8c and listed in Table 1 were chosen to test whether the key elements of our preferred solution - high-velocity gradients in the middle crust, a low-velocity zone in the lower crust, and a crustal thickness of only 5 km - are necessary to match the observed amplitude distribution. All of the models shown in Figures 8b and 8c are characterized by a velocity discontinuity at a crustal travel time of 1.4 s, in agreement with the interpretation of the MCS data. With the exception of Model 5, this velocity

discontinuity represents the Moho rather than an intracrustal reflector.

The travel-time curves for these velocity models are shown in Figure 9. At ranges less than ~6 km, the differences in the predicted travel-time curves are probably unresolvable in observed data because the first-arriving, seafloor-reflection phase typically obscures second-arriving, refracted phases (e.g Ewing and Purdy, 1982). Only Model 3, which does not have a low-velocity zone, predicts P3-branch and S3-branch arrivals beyond ~18 km. The satisfactory fit to the observed data of the travel-time curve predicted for Model 3 (Figure 5b), together with the similarity of the travel-time curves shown in Figure 9, demonstrates that with the exception of Model 4 all of the velocity models predict travel-time curves that match the observed data. In the following sections we show that these alternative models of the velocity structure at Site 504B can be distinguished on the basis of the predicted amplitude distribution. While we did not consider every possible velocity-depth model, we argue that the range of velocity structures that we have modeled demonstrates that the crust at DSDP Site 504B is unusual in comparison to the velocity structure typically reported for oceanic crust. We concentrated on matching the P-wave amplitudes because of the probability that the S-wave amplitudes are affected by variations in the the efficency of mode conversion.

Shallow Crust

The velocity structure of the upper 0.5 km of oceanic crust at DSDP Site 504B cannot be directly determined from our data because refracted arrivals from these depths are obscured by the seafloor and basement

TABLE 1. Velocity-Depth Models for Site 504B

Layer Thickness km	V_p (top/bottom) km s^{-1}	V_s (top/bottom) km s^{-1}	Layer Thickness km	V_p (top/bottom) km s^{-1}	V_s (top/bottom) km s^{-1}
	Model 1			Model 2	
3.550	1.50/1.50	0.00/0.00	3.550	1.50/1.50	0.00/0.00
0.260	1.52/1.52	0.50/0.50	0.260	1.52/1.52	0.50/0.50
1.000	4.50/6.50	2.10/3.71	0.815	4.00/6.50	1.80/3.71
0.800	6.50/6.70	3.71/3.83	0.750	6.50/6.65	3.71/3.80
0.400	6.70/6.85	3.83/3.91	0.350	6.65/6.80	3.80/3.89
0.400	6.85/7.10	3.91/4.06	0.300	6.80/6.95	3.89/3.97
0.500	7.10/6.70	4.06/3.75	0.250	6.95/7.10	3.97/4.06
1.200	6.70/6.70	3.75/3.75	0.500	7.10/6.70	4.06/3.85
0.700	7.40/8.10	4.30/4.74	1.500	6.70/6.70	3.85/3.85
1.000	8.10/8.10	4.74/4.74	0.600	7.40/8.10	4.30/4.74
			1.000	8.10/8.10	4.74/4.74
	Model 3			Model P	
3.550	1.50/1.50	0.00/0.00	3.550	1.50/1.50	0.00/0.00
0.260	1.52/1.52	0.50/0.50	0.260	1.52/1.52	0.50/0.50
1.165	5.00/6.50	2.40/3.71	1.165	5.00/6.50	2.40/3.71
0.600	6.50/6.65	3.71/3.78	0.600	6.50/6.65	3.71/3.78
2.650	6.65/6.90	3.78/3.92	0.350	6.65/6.80	3.78/3.85
0.500	7.50/8.10	4.36/4.74	0.300	6.80/6.95	3.85/3.93
1.000	8.10/8.10	4.74/4.74	0.250	6.95/7.10	3.93/4.02
			0.500	7.10/6.70	4.02/3.83
			1.300	6.70/6.70	3.83/3.83
			0.500	7.50/8.10	4.36/4.74
			1.000	8.10/8.10	4.74/4.74
	Model 4			Model 5	
3.550	1.50/1.50	0.00/0.00	3.550	1.50/1.50	0.00/0.00
0.260	1.52/1.52	0.50/0.50	0.260	1.52/1.52	0.50/0.50
1.165	5.00/6.50	2.40/3.71	1.165	5.00/6.50	2.40/3.71
0.600	6.50/6.65	3.71/3.78	0.600	6.50/6.65	3.71/3.78
0.350	6.65/6.80	3.78/3.85	0.350	6.65/6.80	3.78/3.85
0.300	6.80/6.95	3.85/3.93	0.300	6.80/6.95	3.85/3.93
0.250	6.95/7.10	3.93/4.02	0.250	6.95/7.10	3.93/4.02
1.850	7.10/7.10	4.02/4.02	0.500	7.10/6.70	4.02/3.83
0.500	7.50/8.10	4.36/4.74	1.300	6.70/6.70	3.83/3.83
1.000	8.10/8.10	4.74/4.74	1.000	7.50/7.50	4.36/4.36

reflections (Figure 3). However, interpretation of the P-wave velocity structure at the top of oceanic crust is indirectly constrained by the phase velocities and amplitudes of the observed S-wave arrivals; the efficency of mode conversion to S-waves of a given phase velocity is dependent on the P-wave velocity at the top of the igneous crust (Spudich and Orcutt, 1980a; White and Stephen, 1980). In particular, the amplitudes of S-wave arrivals with phase velocity equal to the P-wave velocity at the top of basement are predicted to be negligible (Spudich and Orcutt, 1980a).

In order to proceed with our modeling of observed arrivals, we assumed that the velocity structure of the upper crust was characterized by a linear velocity gradient. This simple assumption is in accord with the results of Little and Stephen (1985) who used a surface source and borehole receiver to measure the velocity structure of the uppermost 1.25 km of crust at DSDP Site 504B. The geometry of their experiment resulted in a direct determination of the shallow velocity structure. The initial velocity and thickness of the assumed velocity gradient must predict both the observed S-wave amplitudes and the high-amplitude P-wave arrivals of phase velocity ~6.5 km s^{-1} that are observed to emerge from the seafloor reflection at horizontal ranges of 5-6 km.

The shallow structure of our preferred velocity model is characterized by an initial P-wave velocity of 5.0 km s^{-1}, and a linear gradient of thickness and magnitude 1.2 km and 1.3 km s^{-1} km^{-1}, respectively. Synthetic seismograms calculated for this model (Figure 10a) reproduce both the high-amplitude P-wave arrivals at 6-7 km range and the high-amplitude SmS-branch arrivals observed at 18-20 km range.

The initial P-wave velocity of our preferred model is 0.7 km s^{-1} greater than the preferred model of Little and Stephen (1985). However, synthetic seismogram profiles (Figures 10b, 10c) calculated for models with lower initial velocities match the observed P-wave arrivals at ~6 km range, but do not predict the focusing of SmS-branch arrivals at 18-20 km range. This mismatch arises because the phase velocity of the SmS-branch arrivals at 18 km is ~4.5 km s^{-1}, i.e. close to the P-wave velocity at the top of basement for these less satisfactory models. The discrepancy between our preferred velocity model and the velocity model of Little and Stephen (1985) cannot be explained in terms of upper-crustal azimuthal anisotropy at Site 504B (Stephen, 1985) because profile 504B19 was not acquired along the east-west azimuth of maximum P-wave velocity.

High-resolution, wide-angle reflection/refraction data collected with on-bottom receivers demonstrate that the velocity structure of the upper oceanic crust is more complicated than our results suggest (e.g. Bratt and Purdy, 1984; Purdy, 1987). Results of downhole logging at Site 504B clearly demonstrate that our preferred solution is at best an average of the complicated sonic-velocity structure (Anderson et al., 1982; Salisbury et al., 1985). However, our experimental geometry prevents us from resolving such fine-scale structure in the upper crust at Site 504B. For similar reasons, it is infeasible to interpret our data in terms of known azimuthal anisotropy at Site 504B (Stephen, 1985).

We assumed no intrinsic attenuation (i.e. infinite seismic Q) for velocity-depth Models 1 and 2. However, we assumed Q factors of 450 (P-waves) and 225 (S-waves) for Models P, 3, 4, and 5; these values are

similar to those used by Spudich and Orcutt (1980a). Without the introduction of finite Q, synthetic seismograms calculated for models with a basement velocity of 5.0 km s^{-1} are characterized by S3-branch arrivals that are too high in amplitude, although the focusing at 16-19 km is still observed.

Middle to Lower Crust

In contrast to the shallow crust, interpretation of the velocity structure of the middle crust at DSDP Site 504B is well constrained by the phase velocities (~6.5 km s^{-1}) and amplitudes of the P3-branch arrivals at ranges of 5-19 km. The amplitude focusing at 16-19 km (Figure 6b) is not typically observed in marine wide-angle reflection/refraction profiles, but is a key constraint in interpreting our data. At greater ranges, the low-amplitude arrivals along the extrapolated P3-branch (Figure 6a) constrain the interpretation of the velocity structure of the lower crust.

The preferred velocity model for the middle and lower crust is characterized by (i) high positive velocity gradients of up to 0.6 s^{-1} at basement depths of ~2.6 km, and (ii) a 1.8 km thick low-velocity zone (V_p=7.1-6.7 km s^{-1}) in the lowermost crust. The high velocity gradients in the middle crust result in the required focusing of P-wave arrivals at a range of 16-19 km, and the low-velocity zone results in diminished amplitudes at ranges greater than 20 km (Figure 10a). In contrast, Model 3, which is typical of oceanic velocity-depth profiles in that it is characterized by decreasing velocity gradients with depth, fails to reproduce the observed P-wave focusing at 16-19 km (Figure 10d).

However, synthetic seismograms calculated for Model 4 (Figure 10e), which has high velocity gradients in the middle crust but no low-velocity zone in the lower crust, also reproduce the observed focusing and defocusing of P3-branch arrivals. In the next section, we show that the interpretation of a low-velocity zone in the lower crust can be justified by the need to match the slope and amplitudes of the PmP-branch arrivals.

In order to produce the observed P-wave focusing at 16-19 km, we prefered a velocity model characterized by a velocity gradient in the middle crust rather than a velocity discontinuity because (i) P-wave amplitude focusing is observed over a limited range window, (ii) no mid-crustal reflection events are observed on the MCS data, and (iii) the phase velocities of the extrapolated P3-branch arrivals are approximately equal to the phase velocities of the P3-branch arrivals at ranges of 6-19 km. The magnitude and thickness of the velocity transition are constrained by the amplitude of the P-wave arrivals, the length of the range window over which focusing is observed, and the lack of a near-normal-incidence reflection event at the appropriate travel time.

Lower Crust and Moho

The attenuated P3-branch arrivals observed at 19-30 km (Figure 3) do not require a low-velocity zone. However, the combined interpretation of the PmP arrivals and the near-normal-incidence Moho reflection justifies this interpretation. Synthetic seismograms must reproduce the following observed characteristics: (i) the time offset of the PmP branch relative to the P3 branch, (ii) the slope of the PmP branch, and (iii) the high-amplitude, PmP-branch arrivals observed at 20-21 km range.

We computed synthetic seismograms for Models 4 and 5 to investigate whether or not a low-velocity zone is required by the above constraints, and to test if the velocity transition at a crustal travel time of 1.4-1.5 s is the Moho or lies within the lower crust. Synthetic seismograms calculated for Model 4 (Figure 10e), which does not have a low-velocity zone, mismatch the slope (Figure 9) and amplitude distribution of the PmP arrivals. The predicted slope is too steep, implying that the mean velocity of the lower crust is too high. Synthetic seismograms calculated for Model 5 (Figure 10f), which has a low-velocity zone and an intracrustal velocity discontinuity from 6.7-7.5 km s^{-1}, matches the observed slope of the PmP branch but does not reproduce the focused P-wave arrivals that are observed at 20-21 km range. However, these high-amplitude arrivals are readily reproduced by assuming a velocity transition from 7.5 km s^{-1} to upper mantle velocities of 8.1 km s^{-1}, as in our preferred model.

Discussion of Modeling Results

Comparison of the synthetic seismogram profiles (Figure 10, Models P, 3, 4, and 5) shows that only the combination of high velocity gradients in the middle crust, low-velocity zone in the lower crust, and total crustal thickness of 5 km explains the primary features of the observed data. These features consist of the amplitude focusing at 16-19 km, the slope of the PmP arrivals, the high-amplitude PmP arrivals at ~20 km, and the near-normal-incidence reflection at a crustal travel time of 1.4-1.5 s. Comparison of the synthetic seismograms calculated for Model 3 (Figure 10d), which is representative of normal oceanic crust, to the

observed data shows that the requirement of matching the amplitude focusing at ranges of 16-19 km is critical to our preference for Model P. The synthetic seismogram profile for Model 3 reproduces all of the amplitude features that we consider to provide important constraints on the velocity structure at Site 504B except the amplitude focusing at 16-19 km range.

The lack of an identifiable near-normal-incidence reflection event at a travel times appropriate to the lid of the low-velocity layer constrains the magnitude of the change in velocity gradient at this depth. Computation of a full-waveform, normal-incidence synthetic seismogram for the preferred model shows that the amplitude of the reflection event generated at this depths is negligible, in agreement with observations.

The crustal travel time (1.4-1.5 s) of the near-normal-incidence Moho reflection event provides a key constraint on crustal thickness. For the velocity models shown in Figure 8, the crustal travel time and basement depth to the top of Moho is ~1.4s and 4.5 km, respectively. The assumption of a crustal travel time of 1.5 s implies a velocity-depth function which differs from the preferred model only in the thickness of the low-velocity layer; basement depth to Moho in this case would be ~4.8 km. Basement depth to the top of the Moho is unlikely to exceed 5 km because this implies a mean crustal V_p of 6.7 km s^{-1} or greater. These values are slightly greater than the mean velocities to Moho of 6.5 and 6.6 km s^{-1} reported for Pacific and Atlantic crust, respectively (Spudich and Orcutt, 1980a; Purdy, 1983). This argument can be strengthened by assuming that our preferred velocity model is an exact

representation of the velocity structure to a basement depth (2.67 km) corresponding to the top of the low-velocity layer. This portion of Model P is well constrained by first-arriving, diving-wave phases observed at horizontal ranges of less than 20 km. The 0.55-0.65 s difference between the crustal travel time to Moho (1.4-1.5 s) and the crustal travel-time to the top of the low-velocity layer (0.85 s) determines the mean velocity of the lower crust at Site 504B. A Moho depth of 5 km or greater requires a mean lower-crustal velocity of 7.25 km s^{-1} or greater. This value is clearly too high because both the move-out and amplitudes of the PmP arrivals predicted by Model 4, which has a mean lower crustal velocity of 7.1 km s^{-1}, mismatch the observed data (Figures 9 and 10e).

The preferred model does not reproduce the twin amplitude peaks at 16-19 km that are observed on profiles 504B03, 504B19, and 504B21 (Figures 6b, 7a). Attempts to reproduce these narrow peaks were unsuccessful, and consequently the inferred smooth increase in velocity gradient at basement depths of 2.1-3.1 km (Figure 8b) is only an approximation to the real structure.

With regard to the velocity structure of the upper oceanic crust, Model P is favoured on the basis that, in contrast to Models 1 and 2, it alone predicts the focused SmS arrivals at 18-20 km. Note that, in comparison to the synthetic seismogram profile calculated for Model P (Figure 10a), the profiles calculated for Models 1 and 2 (Figures 10b, 10c) better match the focused/defocused PmP arrivals that are observed on profiles 504B12, 504B19, and 504B21 (Figure 6a). Lateral variations in the amplitude of the PmP arrivals are brought about by interference

between these arrivals and the diving-wave arrivals that turn within the Moho transition zone. The less satisfactory match predicted by Model P could probably be improved by varying the gradient of the Moho transition zone.

The preferred S-wave velocity-depth profile produces a satisfactory fit to the observed arrivals. The P-wave to S-wave ratios vary downward from ~2.1 to ~1.7, values similar to those typically reported for oceanic crust (e.g., Hyndman, 1979). The attenuation factors of our preferred model (Q_p=450, Q_s=225), particularly those for S-waves, are probably too high in the shallow crust. Although multiply-turned S-wave arrivals are observed (Figures 3, 6c) the amplitude of the predicted S-wave multiples are too high in comparison to the observed data.

Implications for Crustal Structure

Our preferred velocity-depth model for Hole 504B indicates that the Layer 2/Layer 3 transition lies at a basement depth of ~1.2 km, within the drilled sheeted-dike sequence. The location of the Layer 2/Layer 3 boundary within the sheeted dike sequence rather than exclusively at the downward transition from dikes to gabbro has been suggested by geologists on the basis of ophiolite data (e.g. Christensen and Salisbury, 1982). As discussed above, the experimental geometry used to acquire the seismic data presented here ensures that the interpreted velocity structure of the upper 1 km of basement is only an approximation to the true structure. However, the interpretation that the Layer 2/Layer 3 boundary lies in the immediate vicinity of the bottom of the drillhole is supported by the high-resoultion borehole seismic data of Little and Stephen (1985).

Their preferred velocity-depth profile, although extending only to a basement depth of 1.2 km, is characterized by velocity gradients which decrease from ~2 km s^{-1} km^{-1} to ~0.8 km s^{-1} km^{-1} toward the bottom of the drillhole. The lower velocity gradients of Layer 3 may be due to the low bulk porosities (<2%) of the dikes at this depth (Becker, 1985), resulting in a decrease in the rate of increase of velocity with increasing lithostatic pressure.

In comparison to velocity-depth profiles typically reported for oceanic crust (e.g. Spudich and Orcutt, 1980b; White, 1984; Purdy and Ewing, 1986), our preferred velocity profile for DSDP Site 504B is unusual in having high velocity gradients in the middle crust, a low-velocity zone in the lower crust, and a total crustal thickness of only 5 km. However, the range of P- and S-wave velocities for the middle and lower crust (V_p=6.7-7.1 km s^{-1}, V_s=3.8-4.1 km s^{-1}) fall within the range of typically reported values for oceanic crust. These velocities are also typical of laboratory-measured velocities of dikes and gabbroic rocks found in ophiolite complexes (e.g. Christensen and Smewing, 1981; Christensen and Salisbury, 1982), and of gabbroic rocks dredged from the ocean floor (e.g. Karson and Fox, 1986). Consequently, our preferred model may be simply viewed as a perturbation of a typical oceanic velocity-depth profile. Notwithstanding the well-known ambiguities in relating seismic velocity to rock type (e.g. Spudich and Orcutt, 1980b), it is interesting to speculate on possible differences between the geological structure at Site 504B and that of areas characterized by typical velocity-depth profiles.

TABLE 2. Relative Enrichments of Olivine and Serpentine Required for P-Wave, High- and Low-Velocity Layers

		Background Phase (gabbro)	Added Phase (olivine)	Aggregate
High-Velocity Layer	V_p	6.7[1]	8.4*	7.1
	V_s	3.8[1]	4.9*	4.0
	ρ	2.8[2]	3.3*	
	Vol %	73-76	24-27	
		Background Phase (gabbro)	**Added Phase (serpentine)**	**Aggregate**
Low-Velocity Layer	V_p	7.1[1]	5.1*	6.7
	V_s	4.0[1]	2.4*	3.8
	ρ	2.9[2]	2.5*	
	Vol %	83-86	14-17	

Velocities (V_p, V_s) are in kilometers per second.
Densities (ρ) are in grams per cubic centimeter.
[1]Preferred velocity-depth model (Model P, Figure 8b)
[2]$\rho = 0.252 + 0.379V_p$ (Spudich and Orcutt, 1980a)
*Laboratory-measured values at 3 kilobars pressure (Christensen, 1982)

A simple way to transform a normal velocity-depth profile to our preferred model is to substitute a high-velocity layer at basement depths of 2.1-3.1 km for an approximately uniform-velocity (~6.7 km s^{-1}) middle and lower crust. In this scenario, the low-velocity layer in the lower crust is just an artifact of the increased velocities of the middle crust. A plausible geological interpretation associates the high-velocity layer with a layer of gabbroic rocks that are enriched in a high-velocity mineral component relative to overlying and underlying rocks. The addition of olivine is the most efficent way to increase the velocity because olivine has the fastest velocity of the minerals typically found in oceanic crustal rocks (e.g. Christensen, 1982). The relative enrichment in olivine that is required to increase the P-wave velocity

from 6.7 km s^{-1} to 7.1 km s^{-1} is 24-27% by volume (Table 2). These predicted enrichment values were estimated using the method proposed by Hashin and Shtrikman (1963) for the calculation of the elastic constants of multiphase media; the equations that we used are given in Watt et al. (1976). The relative enrichment in olivine that is required to increase the S-wave velocities from 3.8 km s^{-1} to 4.0 km s^{-1} is 20-23% by volume, slightly less than that for P-waves.

At Hole 504B, the concentration of olivine in rocks cored from basement depths of 0.562-1.076 km varies from <1% to 15% by volume, depending on rock type (Kempton et al., 1985). The maximum mean concentration of olivine over this interval, calculated from the known volume distribution of rock type and the maximum estimated olivine concentration for each type, is 10% by volume. Consequently, the increase in velocity from 6.7-7.1 km over a basement depth of 2.1-2.6 km requires an increase in olivine concentration from 10-37% by volume. These values are not unreasonable for olivine gabbros and troctolites. Gabbroic rocks with olivine concentration of up to 40% by volume have been sampled on the Mid-Atlantic ridge (Hodges and Papike, 1976). The calculation of the relative enrichment values of 24-27% does not assume preferential substitution of any of the original mineral phases by olivine. However, if olivine were preferentially substituted for relatively slow plagioclase rather than relatively fast pyroxene, the required enrichment values would be smaller than those quoted above.

Another interpretation for the high-velocity layer is suggested by the documented occurence of intrusive ultramafic layers throughout the gabbroic sequence of the Oman ophiolite (Juteau et al., 1988). These

intrusive wehrlitic bodies (V_p=7.9-8.4 km s^{-1}) have maximum vertical and horizontal dimensions of 100's of meters and kilometers, respectively. These dimensions are sigificantly less than those of the high-velocity layer at Site 504B, which is approximately a kilometer thick and at least 10's of kilometers in areal extent. An additional reason to rule out this explanation is the lack of a near-normal-incidence reflection event at a travel time corresponding to the top and/or bottom of the high-velocity layer. Such an event would be expected because the contrast in the P-wave velocities of gabbro and wehrlite is about 1 km s^{-1} (Karson et al., 1984).

An alternative interpretation as to why the velocity-depth models at Site 504B differs from typically reported profiles focuses on the velocity structure of the lower crust. In this view, the velocity of the lower crust has been decreased from a value greater than or equal to that of the middle crust (7.1 km s^{-1}) to 6.7 km s^{-1}. Low-velocity zones in the lower oceanic crust have been proposed by many workers (e.g. Lewis, 1978; Lewis and Snydsman (1979); Mithal, 1986; Duennebier et al., 1987), and are often interpreted in terms of the alteration of olivine-rich mafic and ultramafic rocks to serpentine (e.g. Lewis, 1978). The relative enrichment in serpentine required to lower the P-wave velocity from 7.1 km s^{-1} to 6.7 km s^{-1} is 14-18% by volume (Table 2). The extent of serpentinization required to lower the S-wave velocity from 3.8 km s^{-1} to 4.0 km s^{-1} is 7-11% by volume, slightly less than that for P-waves.

A difficulty with the serpentinization interpretation is that it does not explain the high velocity gradients of the middle crust.

Serpentinization confined to the lower crust implies that originally the lower crust was enriched in olivine relative to the middle crust. Accordingly, the high velocity gradients of the middle crust cannot be due to olivine enrichment. We prefer the 'high-velocity layer' interpretation because the assumption of an olivine-enriched middle crust explains the unusual velocity-depth profile of the middle and lower crust.

Although crustal temperatures at Site 504B are high - the measured heat flow of this young crust equals the value predicted by plate cooling theory (Langseth et al., 1983) - laboratory data on the effect of increasing temperature on rock velocity indicates that the low-velocity zone is unlikely to be a temperature-controlled phenomenon. For a gabbro sample from the Mid-Atlantic Ridge, Christensen (1979) shows that at a confining pressure of 2 kbars (basement depth of ~6 km), the rate of decrease in P-wave velocity with increasing temperature is only 0.57×10^{-3} km s^{-1} $°C^{-1}$ over a temperature range from 25-300°C. The mean temperature gradient of 60°C km^{-1} measured at Site 504B over the basement depth interval of 0.562-1.076 km (Becker at al., 1985; Shipboard Scientific Party, 1988) is an upper bound on the temperature gradient of the middle and lower crust. Accordingly, at Site 504B the decrease in velocity with increasing depth due to temperature effects alone would be less than 0.034 km s^{-1} km^{-1}. In contrast, the rate of increase of P-wave velocity over a confining pressure range from 0.6-2 kbars (basement depth of ~1-6 km) is ~ 0.2 km $s^{-1}kbar^{-1}$ (~0.056 km s^{-1} km^{-1}) for dike samples cored at Site 504B (Christensen et al., 1985). These estimates show that temperature effects are dominated by the effects of increased confining pressure.

The estimated total crustal thickness at Site 504B is only 5 km, about 1-2 km thinner than typically reported values for oceanic crust (e.g. White, 1984). Recently, Klein and Langmuir (1987) proposed a global correlation between oceanic crustal thickness and the major-element chemistry of basalts, particularly the wt % Na_2O at 8.5 wt % MgO. We have calculated the value of this geochemical parameter, which they term $Na_{8.0}$, from chemical analyses of glasses recovered from Site 504B (Natland et al., 1983). The value of $Na_{8.0}$ appropriate for Hole 504B is 2.1±0.2, which in the model of Klein and Langmuir (1987) is indicative of a crustal thickness of 6-8 km. This prediction assumes that the mantle concentration of Na_2O is 0.26 wt %. The discrepancy between our estimated value of crustal thickness and the predicted value may be reconciled by invoking an anomalously low concentration of Na_2O in the mantle beneath the Costa Rica Rift at the time of formation of the crust that is now found at Site 504B. This explanation is in accord with the geochemistry of basalts sampled in Hole 504B. Given the extent of fractionation, the majority of the basalts recovered from Hole 504B have slightly low concentrations of incompatible elements in comparison to most mid-ocean ridge basalts (Autio and Rhodes, 1983; Kempton et al., 1985). The geochemical data suggest that the basalts crystallized from a melt extracted from a depleted mantle which may have experienced a previous melting event (Autio and Rhodes, 1983; Kempton et al., 1985). The decreased volume of melt predicted by this interpretation (Kempton et al., 1985) is consistent with the relatively thin crust predicted by the seismic data. The association of the high-velocity layer in the middle crust with an olivine-enriched layer is also consistent with this

petrologic model because such a source could be expected to form magenesian-enriched melts.

Summary

Iterative forward modeling of travel time and amplitude features common to four wide-angle reflection/refraction profiles shows that, in comparison to typical oceanic velocity-depth profiles, the velocity structure at Site 504B is unusual in having high velocity gradients in the middle crust, a low-velocity zone in the lower crust, and a crustal thickness of only 5 km. Identification of the high velocity gradients in the middle crust is prompted by the observation of P-wave amplitude focusing at ranges of 16-19 km on all four profiles. Crustal thickness is constrained by the travel times and amplitudes of well-defined PmP arrivals, and by the 1.4-1.5 s crustal travel time to a Moho reflection event observed on near-normal-incidence MCS data. The lid of the low-velocity zone is apparently gradational in character because a near-normal-incidence reflections event is not observed at the appropriate travel time.

Our preferred model may be considered to be a perturbed version of a typical oceanic velocity-depth model, the velocity of the middle crust being increased relative to the surrounding rocks (Figure 11). A simple interpretation correlates the 'high-velocity layer' with a layer of gabbro with a mean olivine concentration 24-27% greater than that of surrounding rocks. The absolute mean olivine concentration of this layer need be no greater than 37% by volume.

Hole 504B is an ideal location to drill through the oceanic crust

into the upper mantle because the crustal thickness at the site is 1-2 km thinner than typically reported values. At the time of writing, the total basement penetration of 1.288 km is ~25% of the expected crustal thickness. Although the drilling rates attained in the diabase dike sequence have been low, less than 8m/day (Shipboard Scientific Party, 1988), it is likely that rates could increase significantly when the expected gabbroic sequence is reached. At ODP Site 735 on the Southwestern Indian Ridge, ~500 m of gabbro were drilled at an average rate of 30m/day (Leg 118 Shipboard Scientific Party, 1988; ODP Science Operator Report, 1988). In addition, the average core recovery rate was 84%. Assuming that the crust below the bottom of Hole 504B consists of gabbro, and that this high drilling rate could be achieved, the upper mantle could be reached in ~4 months of continuous drilling.

REFERENCES

Anderson, R. N., J. Honnorez, K. Becker, A. C. Adamson, J. C. Alt, R. Emmermann P. D. Kempton, H. Kinoshita, C. Laverne, M. Mottl, and R. L. Newmark, DSDP Site 504B, the first reference section over 1 km through layer 2 of the oceanic crust, Nature, 300, 589-594, 1982.

Autio, L. K., and J. M. Rhodes, Costa Rica Rift Zone basalts: Geochemical and experimental data from a possible example of multistage melting, Initial Rep. Deep Sea Drill. Proj., 69, 729-745, 1983.

Becker, K., Large-scale electrical resistivity and bulk porosity of the oceanic crust, Deep Sea Drilling Project Hole 504B, Costa Rica Rift, Initial Rep. Deep Sea Drill. Proj., 83, 419-427, 1985.

Becker, K., M. G. Langseth, R. P. Von Herzen, R. N. Anderson, and M. A. Hobart, Deep crustal geothermal measurements, Hole 504B, Deep Sea Drilling Project Legs, 69, 70, 83, and 92, Initial Rep. Deep Sea Drill. Proj., 83, 405-418, 1985.

Bratt, S. R., and G. M. Purdy, Structure and variability of oceanic crust on the flanks of the east Pacific Rise between 11° and 13°N, J. Geophys. Res., 89, 6111-6125, 1984.

Brocher, T. M., J. A. Karson, and J. A. Collins, Seismic stratigraphy of the oceanic Moho based on ophiolite models, Geology, 11, 62-65, 1985.

Christensen, N. I., Compressional wave velocities in rocks at high temperatures and pressures, critical thermal gradients, and crustal low-velocity zones, J. Geophys. Res., 84, 6849-6857, 1979.

Christensen, N. I., Seismic velocities, in Handbook of Physical Properties of Rocks, vol. II, edited by R. S. Carmichael, pp. 1-228, CRC Press, Boca Raton, Florida, 1982.

Christensen, N. I., and M. H. Salisbury, Lateral heterogeneity in the seismic structure of the oceanic crust inferred from velocity studies in the Bay of Islands ophiolite, Newfoundland, Geophys. J. R. Astron. Soc., 68, 675-688, 1982.

Christensen, N. I., and M. H. Salisbury, Seismic velocities, densities, and porosities of Layer 2B and Layer 2C basalts from Hole 504B, Initial Rep. Deep Sea Drill. Proj., 83, 367-370, 1985.

Christensen, N. I., and J. D. Smewing, Geology and seismic structure of the northern section of the Oman ophiolite, J. Geophys. Res., 86, 2545-2555, 1981.

Coleman, R. G., Ophiolites, ancient oceanic crust?, Springer-Verlag, Berlin, 229 pp., 1977.

Collins, J. A., T. M. Brocher, and J. A. Karson, Two-dimensional seismic reflection modeling of the inferred fossil oceanic crust/mantle transition in the Bay of Islands Ophiolite, J. Geophys. Res., 91, 12520-12538, 1986.

CRRUST, Geothermal regimes of the Costa Rica Rift, east Pacific, investigated by drilling, DSDP-IPOD Legs 68,69, and 70, Geol. Soc. Am. Bull., 93, 862-875, 1982.

Duennebier, F. K., B. Lienert, R. Cessaro, P. Anderson, and S. Mallick, Controlled-source seismic experiment at Hole 581C, Initial Rep. Deep Sea Drill. Proj., 88, 105-125, 1987.

Ewing, J. I., and G. M. Purdy, Upper crustal velocity structure in the ROSE area of the East Pacific Rise, J. Geophys. Res., 87, 8397-8402, 1982.

Fischer, K. M., and G. M. Purdy, Seismic amplitude modeling and the shallow crustal structure of the East Pacific Rise at 21°N, J. Geophys. Res., 91, 14006-14014, 1986.

Fuchs, K. M., and G. Muller, Computation of synthetic seismograms with the reflectivity method and comparison with observations, Geophys. J. R. Astron. Soc., 23, 417-433, 1971.

Hashin, Z., and S. Shtrikman, A variational approach to the elastic behaviour of multiphase materials, J. Mech. Phys. Solids, 11, 127-140, 1963.

Hey, R. N., G. L. Johnson, and A. Lowrie, Recent plate motions in the Galapagos area, Geol. Soc. Am. Bull. 88, 1385-1403, 1977.

Hobart, M. A., M. G. Langseth, and R. N. Anderson, A geothermal and geophysical survey on the south flank of the Costa Rica Rift: Sites 504 and 505, Initial Rep. Deep Sea Drill. Proj., 83, 517-528, 1985.

Hodges, F. N., and J. J. Papike, DSDP Site 334: Magmatic cumulates from oceanic Layer 3, J. Geophys. Res., 81, 4135-4151, 1976.

Hyndman, R. D., Poisson's ratio in the oceanic crust - a review, Tectonophysics, 59, 321-333, 1979.

Juteau, T., M. Ernewein, I. Reuber, H. Whitechurch, and R. Dahl, Duality of magmatism in the plutonic sequence of the Semail Nappe, Oman, Tectonophysics, in press, 1988.

Karson, J. A., J. A. Collins, and J. F. Casey, Geologic and seismic velocity structure of the crust/mantle transition in the Bay of Islands Ophiolite Complex, J. Geophys. Res, 89, 6126-6138, 1984.

Karson, J. A., and P. J. Fox, Geological and geophysical investigations of the Mid-Cayman Spreading Centre: seismic velocity measurements and implications for the constitution of layer 3, Geophys. J. Roy. Astr. Soc., 85, 389-411, 1986.

Kempton, P. D., L. K. Autio, J. M. Rhodes, M. J. Holdaway, M. A. Dungan, and P. Johnson, Petrology of basalts from Hole 504B, Deep Sea Drilling Project, Leg 83, Initial Rep. Deep Sea Drill. Proj., 83, 129-164, 1985.

Kennett, B. L. N., The effect of attenuation on seismograms, Bull. Seis. Soc. Am., 65, 1643-1651, 1975a.

Kennett, B. L. N., Theoretical seismogram calculation for laterally varying crustal structures, Geophys. J. Roy. Astr. Soc., 42, 579-589, 1975b.

Kennett, B. L. N., Towards a more detailed seismic picture of the oceanic crust and mantle, Marine Geophysical Research, 3, 7-42, 1977.

Klein, E. M., and C. H. Langmuir, Global correlations of ocean ridge basalt chemistry with axial depth and crustal thickness, J. Geophys. Res., 92, 8089-8115, 1987.

Klitgord, K. D., S. P. Huestis, J. D. Mudie, and R. L. Parker, An analysis of near-bottom magnetic anomalies: seafloor spreading and the magnetized layer, Geophys. J. Roy. Astr. Soc., 43, 387-424, 1975.

Langseth, M. G., J. R. Cann, J. H. Natland, and M. Hobart, Geothermal phenomena at the Costa Rica Rift: Background and objectives for drilling at Deep Sea Drilling Project Sites 501, 504 and 505, Initial Rep. Deep Sea Drill. Proj., 69, 5-29, 1983.

Leg 118 Shipboard Scientific Party, Ocean Drilling Program: plutonic rocks in fracture zones, Nature, 333, 115-116, 1988.

Lewis, B. T. R., Evolution of ocean crust seismic velocities, Ann. Rev. Earth Planet. Sci., 6, 377-404, 1978.

Lewis, B. T. R., The processes of formation of ocean crust, Science, 220, 151-157, 1983.

Lewis, B. T. R., and W. E. Snydsman, Fine structure of the lower oceanic crust on the Cocos plate, Tectonophysics, 55, 87-105, 1979

Little, S. A., and R. A. Stephen, Costa Rica Rift borehole seismic experiment, Deep Sea Drilling Project Hole 504B, Leg 92, Initial Rep. Deep Sea Drill. Proj., 83, 517-528, 1985.

MacKenzie, K., Crustal stratigraphy and realistic seismic data, Ph.D. thesis, 121 p., Univ. of Calif., San Diego, La Jolla, 1984.

Mithal, R., Evidence for a basal low velocity zone in oceanic crust, and new methods of phase analysis and extremal inversion, Ph.D. thesis, 199 pp., Columbia Univ., New York, 1986.

Moos, D., D. Goldberg, M. A. Hobart, and R. N. Anderson, Elastic wave velocities in Layer 2a from full waveform sonic logs at Hole 504B, Initial Rep. Deep Sea Drill. Proj., 92, 563-570, 1986.

Mutter, J. C., and North Atlantic Transect (NAT) Group, Multichannel seismic images of the oceanic crust's internal structure: Evidence for a magma chamber beneath the Mesozoic Mid-Atlantic Ridge, Geology, 13, 629-632, 1985.

Natland, J. H., A. C. Adamson, C. Laverne, W. G. Melson, and T. O'Hearn, A compositionally nearly steady state magma chamber at the Costa Rica Rift: evidence from basalt glass and mineral data Deep Sea Drillling Project Sites 501, 5044 and 505, Initial Rep. Deep Sea Drill. Proj., 69, 811-858, 1983.

ODP Science Operator Report, Leg 118: Fracture zone drilling on the Southwest Indian Ridge, JOIDES Journal, 14, 10-13, 1988

Purdy, G. M., The correction for the travel time effects of seafloor topography in the interpretation of marine seismic data, J. Geophys. Res., 87, 8389-8396, 1982.

Purdy, G. M., The seismic structure of 140 Myr old crust in the western central Atlantic Ocean, Geophys. J. R. Astron. Soc., 72, 115-137, 1983.

Purdy, G. M., New observations of the shallow seismic structure of youmg oceanic crust, J. Geophys. Res., 92, 9351-9362, 1987.

Purdy, G. M., and J. I. Ewing, Seismic structure of oceanic crust, in The Geology of North America: The Western Atlantic Region, edited by B. E. Tulcholke, and P. R. Vogt, DNAG Ser., vol. 1, Geological Society of America, Boulder, Colo., 313-331, 1986.

Raitt, R., The crustal rocks, in The Sea, Vol. 3, edited by M. N. Hill, Wiley-Interscience, New York, 85-102, 1963.

Salisbury, M. H., N. I. Christensen, K. Becker, and D. Moos, The velocity structure of layer 2 at Deep Sea Drilling Project site 504 from logging and laboratory experiments, Initial Rep. Deep Sea Drill. Proj., 83, 529-539, 1985.

Searle, R. C., Gloria survey over Costa Rica Rift: Sites 501, 504 and 505, Initial Rep. Deep Sea Drill. Proj., 69, 217-222, 1983.

Shipboard Scientific Party, Site 504: Costa Rica Rift, Proc. Ocean Drill. Proj., Init. Repts. (Pt. A), 111, 35-251, 1988.

Spudich, P., and J. A. Orcutt, Petrology and porosity of an oceanic crustal site: results from waveform modeling of seismic refraction data., J. Geophys. Res., 88, 1409-1433, 1980a.

Spudich, P., and J. A. Orcutt, A new look at the seismic velocity structure of the oceanic crust, Rev. Geophys., 18, 627-645, 1980b.

Stephen, R. A., The oblique seismic experiment on Deep Sea Drilling Project Leg 70, Initial Rep. Deep Sea Drill. Proj., 69, 301-308, 1983.

Stephen, R. A., Seismic anisotropy in the upper oceanic crust, J. Geophys. Res., 90, 11383-11396, 1985.

Stephen, R. A., Lateral heterogeneity in the upper oceanic crust at Deep Sea Drilling Project Site 504, J. Geophys. Res., 93, 6571-6584, 1988.

Watt, J. P, G. F. Davies, and R. J. O'Connell, The elastic properties of composite materials, Rev. Geophys., 14, 541-563, 1976.

White, R. S., Atlantic ocean crust: Seismic structure of a slow-spreading ridge, in Ophiolites and Oceanic Lithosphere, edited by I. G. Gass, S. J. Lippard, and A. W. Shelton, Blackwell Scientific Publications, London, pp 101-111, 1984.

White, R. S., and R. A. Stephen, Compressional to shear wave conversion in oceanic crust, Geophys. J. R. Astron. Soc, 63, 547-565, 1980.

Wilkens, R. H., and M. G. Langseth, Physical properties of sediments of the Costa Rica Rift, Deep Sea Drilling Project Sites 504 and 505, Initial Rep. Deep Sea Drill. Proj., 69, 659-674, 1983.

FIGURE CAPTIONS

Figure 1. (a) Location of DSDP Site 504B relative to the Costa Rica rift, a segment of the Cocos-Nazca plate boundary. Track lines and line numbers for cruise RC-2606 of the R. V. Robert D. Conrad are shown. (b) Location of the four wide-angle reflection/refraction profiles - 504B03, 504B12, 504B19, and 504B21 - that were used to constrain the velocity-depth structure at Site 504B. The large infilled point indicates the drillsite, and the stars indicate the deployment locations of the sonobuoys discussed in the text. Bathymetric contour interval is 100m (from Langseth et al., 1983).

Figure 2. (a) Migrated MCS profiles collected in the vicinity of DSDP Site 504B. Profile locations are shown in Figure 1a. Note the reflection event at approximately 6.4-6.5 s (1.4-1.5 s crustal travel time) travel time on all four profiles. (b) A segment of MCS Line 487 showing the 1.4-1.5 s event in greater detail. This segment is located ~5 km south-west of Site 504B.

Figure 3. (a) Wide-angle reflection/refraction profile 504B19, bandpass filtered 5-30 Hz, and plotted with a reduction velocity of 6.5 km s^{-1}. For clarity, only every second seismogram is shown. The amplitudes have been multiplied by a linear function of range; all of the observed wide-angle reflection/refraction data shown in this paper are identically scaled. (b) As for Figure 3a but the data are filtered 5-15 Hz.

Figure 4. P- and S-wave travel times for profiles 504B03, 504B12, 504B19, and 504B21, plotted with a reduction velocity of 6.5 km s^{-1}. The quadratic splines, constrained to have negative second derivitives as a function of range, misfit the P- and S-wave travel times with root-mean-square deviations of 0.049 s and 0.054 s respectively.

Figure 5. (a) Simple velocity-depth function that satisfactorily explains the travel time variations as a function of range observed on profile 504B19, and is consequently appropriate for profiles 504B03, 504B12, and 504B21. The velocity discontinuity at a basement depth of ~4.4 km generates a normal-incidence reflection at a crustal travel time of 1.4 s. (b) Travel time curves for the velocity-depth model shown in Figure 5a superimposed on profile 504B19 which has been filtered 5-30 Hz. The reduction velocity is 6.5 km s^{-1}. For clarity, only every second seismogram is shown.

Figure 6. P-wave (Figures 6a and 6b) and S-wave (Figure 6c) arrivals for profiles 504B03, 504B12, 504B19 and 504B21, plotted with reduction velocities of 6.5 km s^{-1} (a and b) and 3.8 km s^{-1} (c). All profiles are filtered 5-30 Hz. For clarity, only every second seismogram is shown in Figures 6a and 6c. All recorded seismograms in the range window 14-21 km are shown in Figure 6b. Arrivals on profile 504B12 are repeated because the hydrophone on the sonobuoy used to acquire this profile was deployed at a depth of 91 m, rather than at a depth of 18 m as for the other profiles.

Figure 7. Total power of P3-branch (Figure 7a) and S3-branch arrivals (Figure 7b) for profiles 504B03, 504B12, 504B19, and 504B21. For each seismogram, power was measured by summing the squares of the amplitudes in a 0.25 s window and then multiplying the resulting value by the square of the seismogram range. Power values are normalized relative to the maximum value for each individual profile. The beginning of the time window for each seismogram was chosen to be the arrival time predicted by the best-fit quadratic spline to the measured travel time data for each individual profile. No travel times were measured at horizontal ranges greater than ~18-20 km, but the predicted arrivals times were estimated by extrapolating the best-fit spline. The small letters indicate possible profile-to-profile correlations.

Figure 8. (a) Velocity-depth profiles for which reflectivity synthetic seismograms were calculated. (b) Velocity depth profiles for which reflectivity synthetic seismograms are shown. Note that Model 3 is identical to the velocity model shown in Figure 5a. For Models 1 and 2, the P-wave velocity at the top of the igneous crust is listed. (c) As for Figure 8b but profiles are superimposed for ready comparison.

Figure 9. Travel time curves for the velocity-depth models shown in Figures 8b, 8c. The reduction velocity is 6.5 km s^{-1}. The relative validity of the shallow velocity structure of these models cannot be readily determined because the predicted travel-time differences are confined to ranges at which arrivals are obscured by the seafloor reflection. With the exception of the curve for Model 4, the travel times of the PmP branch are indistinguishable.

Figure 10. Reflectivity synthetic seismogram profiles for the velocity-depth models shown in Figure 8b and 8c. Phase velocities of 1.6-55 km s^{-1}, and frequencies of 10-25 Hz were assumed. The source has a predominant frequency of 17 Hz. Each profile is plotted with a reduction velocity of 6.5 km s^{-1}, and amplitudes are multiplied by a linear function of range. At a given range, amplitudes are comparable from profile to profile.

Figure 11. Preferred velocity-depth model for Site 504B plotted with a velocity-depth profile (Model 3) more typical of oceanic crust. With the important exception of the amplitude focusing at ranges of 16-19 km, the synthetic seismogram profile calculated for Model 3 (Figure 10d) reproduces all of the amplitude and travel time features that we consider to be important constraints on the velocity structure at Site 504B. Comparison of the two velocity-depth profiles suggests that the preferred model is unusual in having a 'high-velocity layer' at basement depths of 2.1-3.1 km.

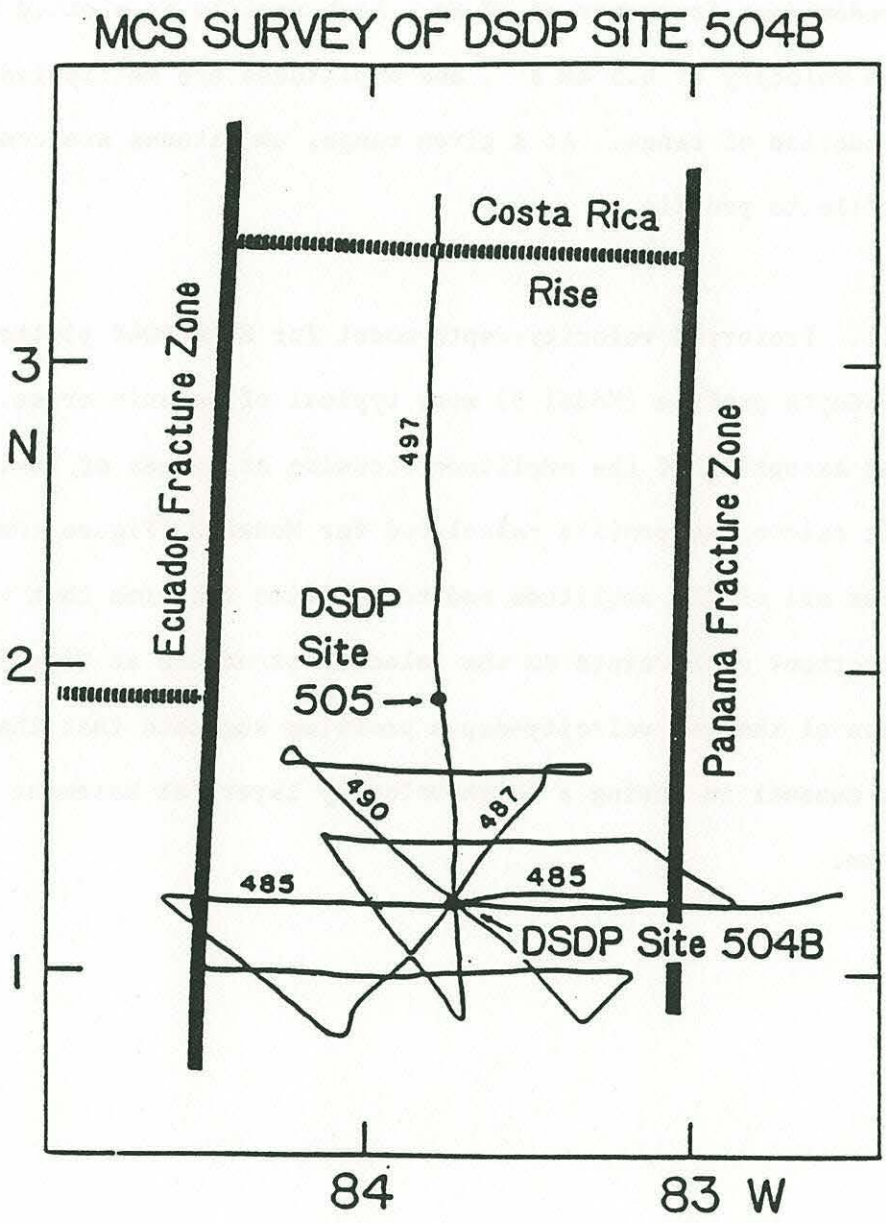
MCS SURVEY OF DSDP SITE 504B
Costa Rica
Rise
Ecuador Fracture Zone
Panama Fracture Zone
497
DSDP
Site
505
490
487
485
485
DSDP Site 504B
3
2
1
N
84
83 W

Figure 1a

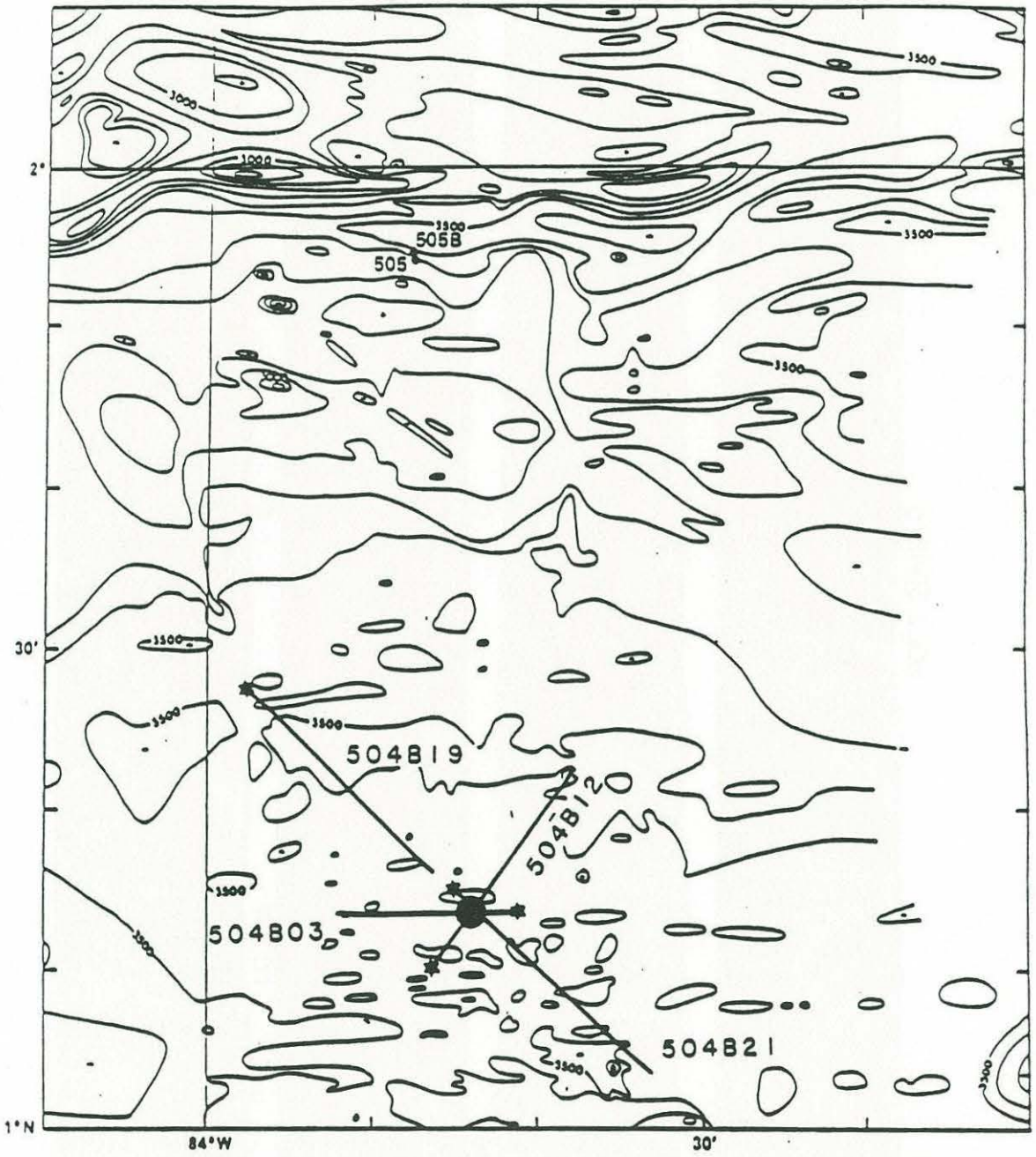

Figure 1b

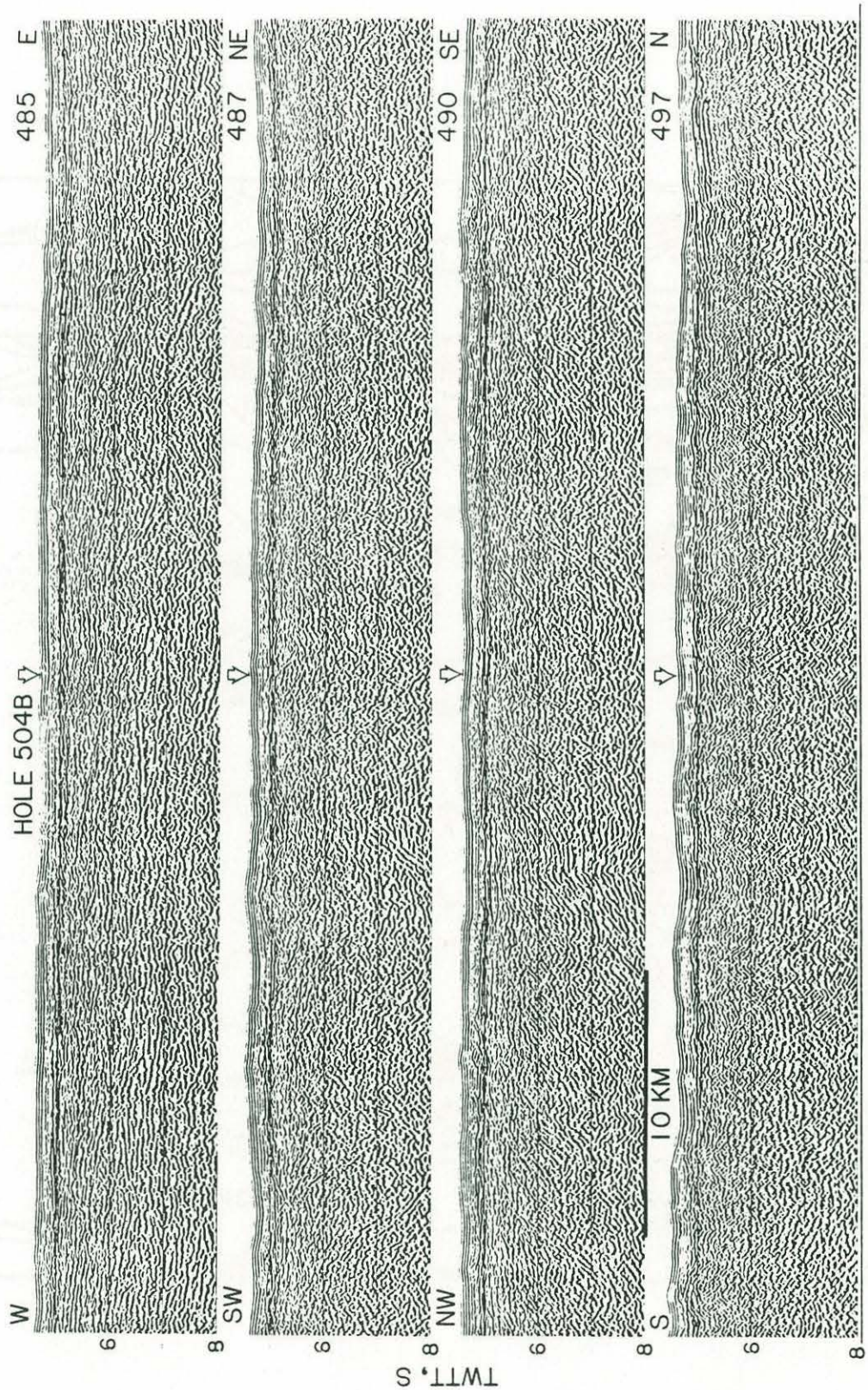

Figure 2a

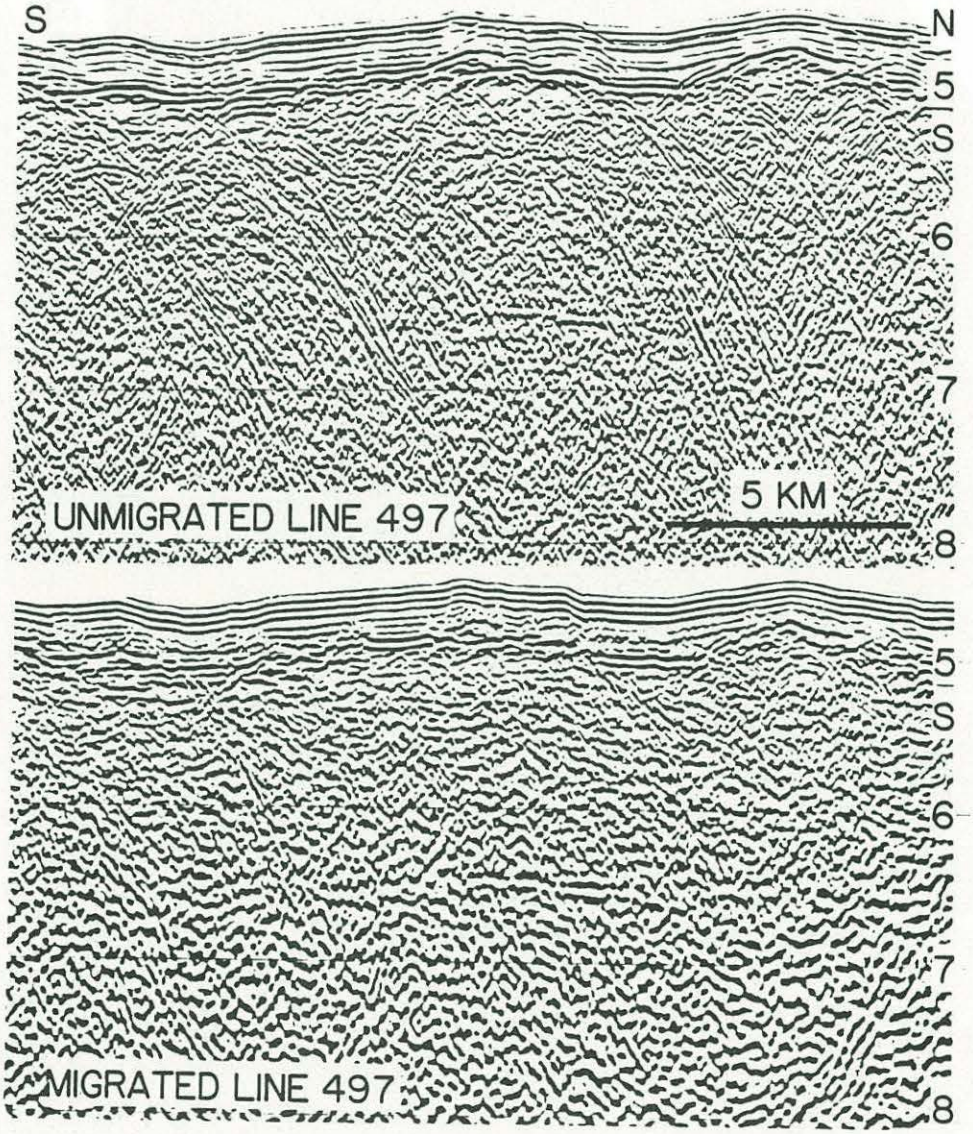

Figure 2b

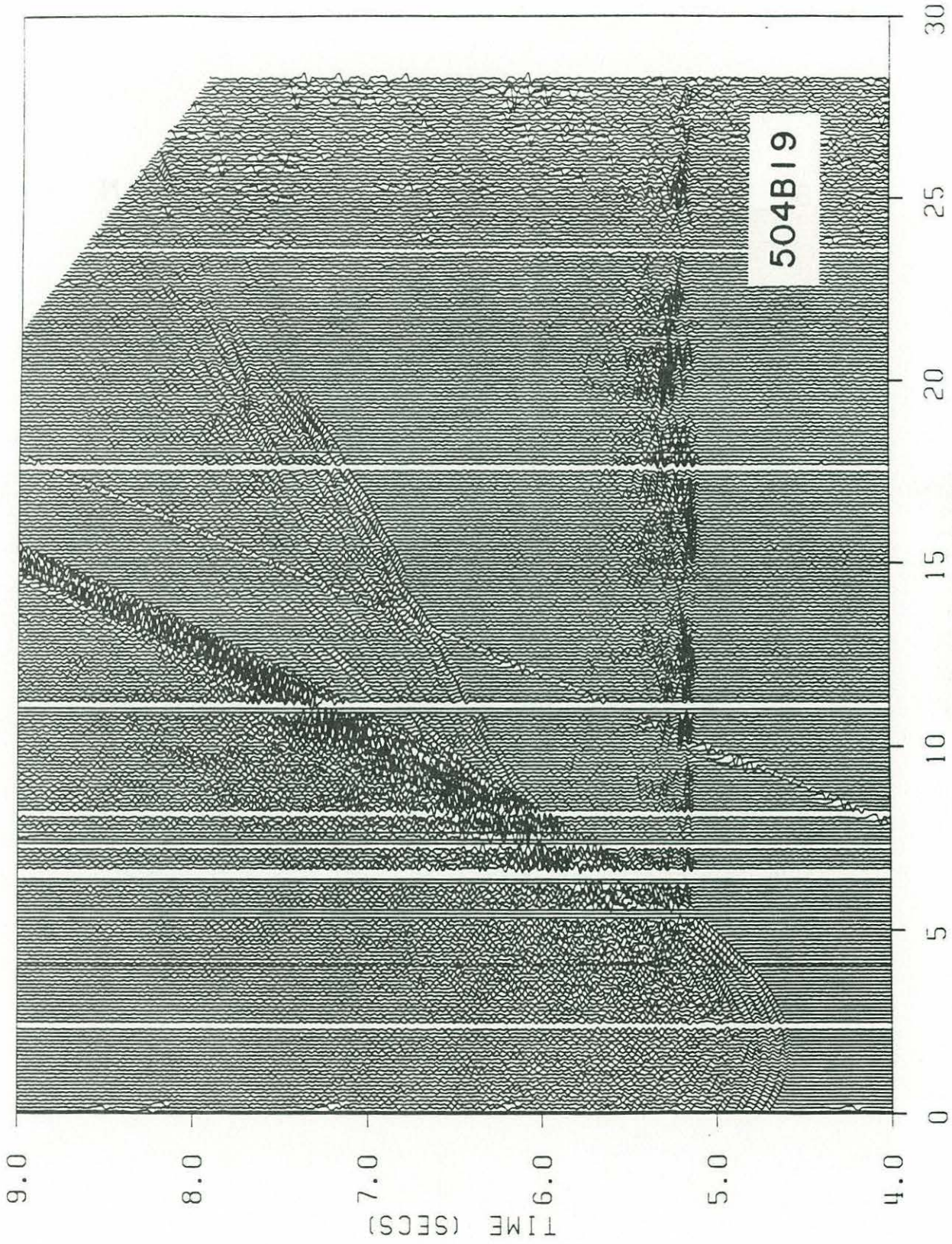

Figure 3a

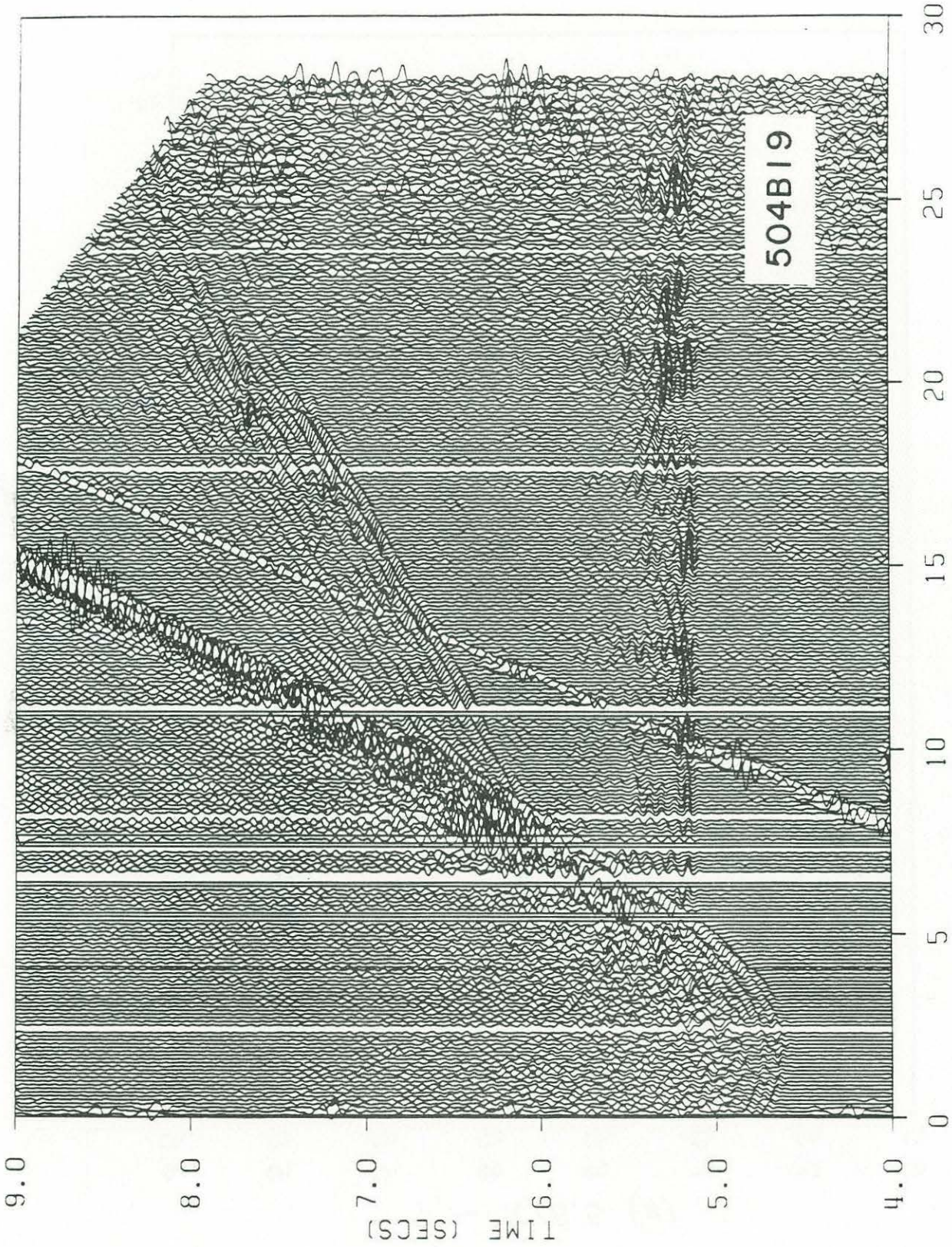

Figure 3b

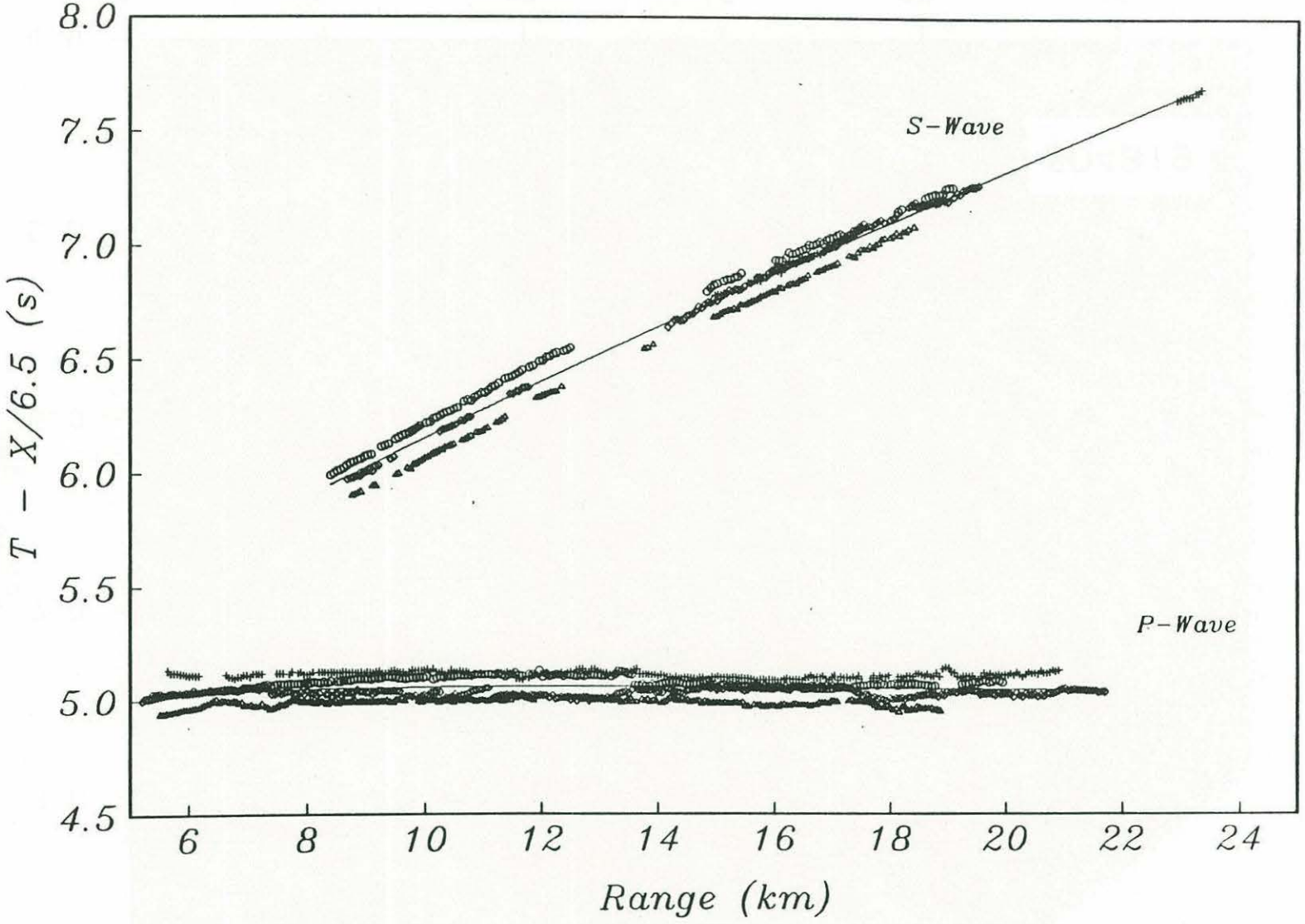
8.0
7.5
7.0
6.5
6.0
5.5
5.0
4.5
T - X/6.5 (s)
S-Wave
P-Wave
6
8
10
12
14
16
18
20
22
24
Range (km)

Figure 4

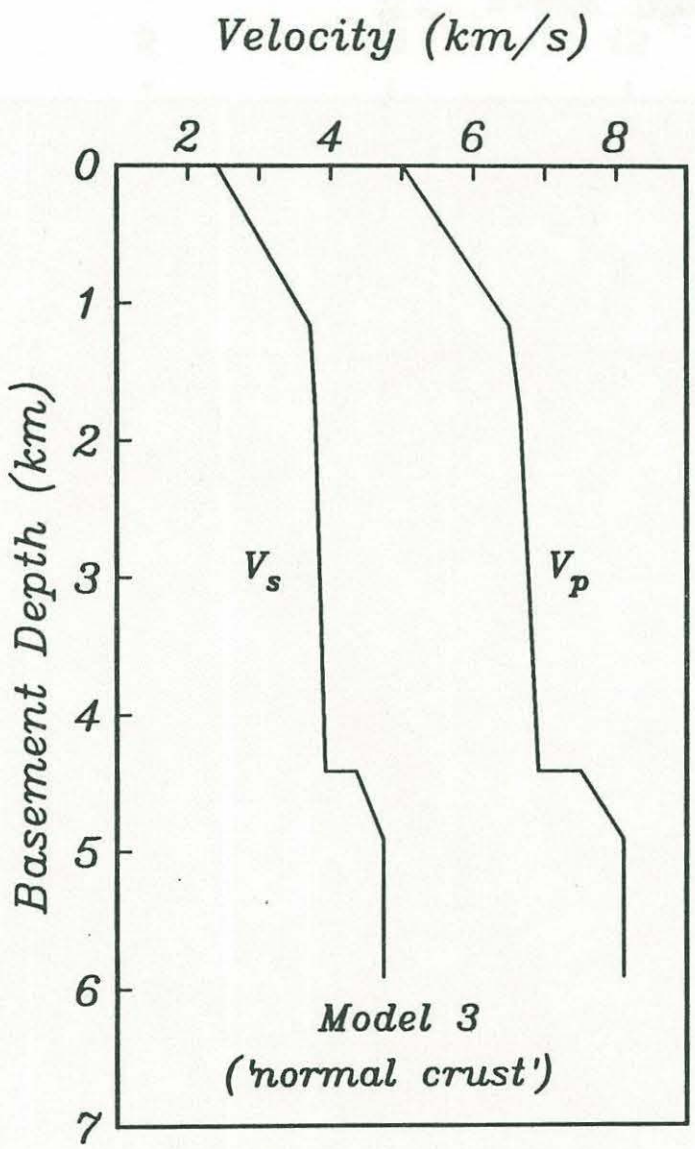
Velocity (km/s)
2
4
6
8
0
1
2
3
4
5
6
7
Basement Depth (km)
V_s
V_p
Model 3
('normal crust')

Figure 5a

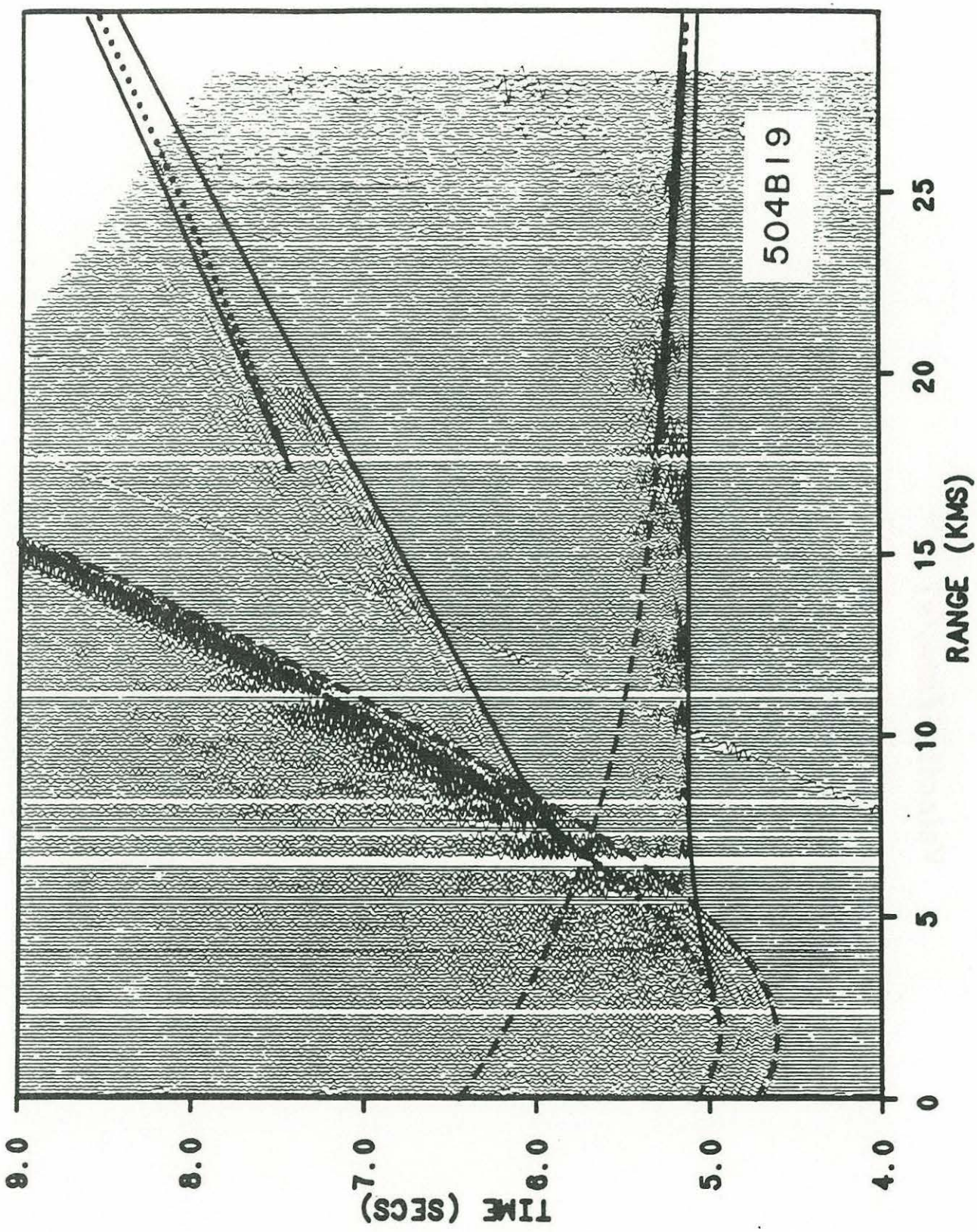

Figure 5b

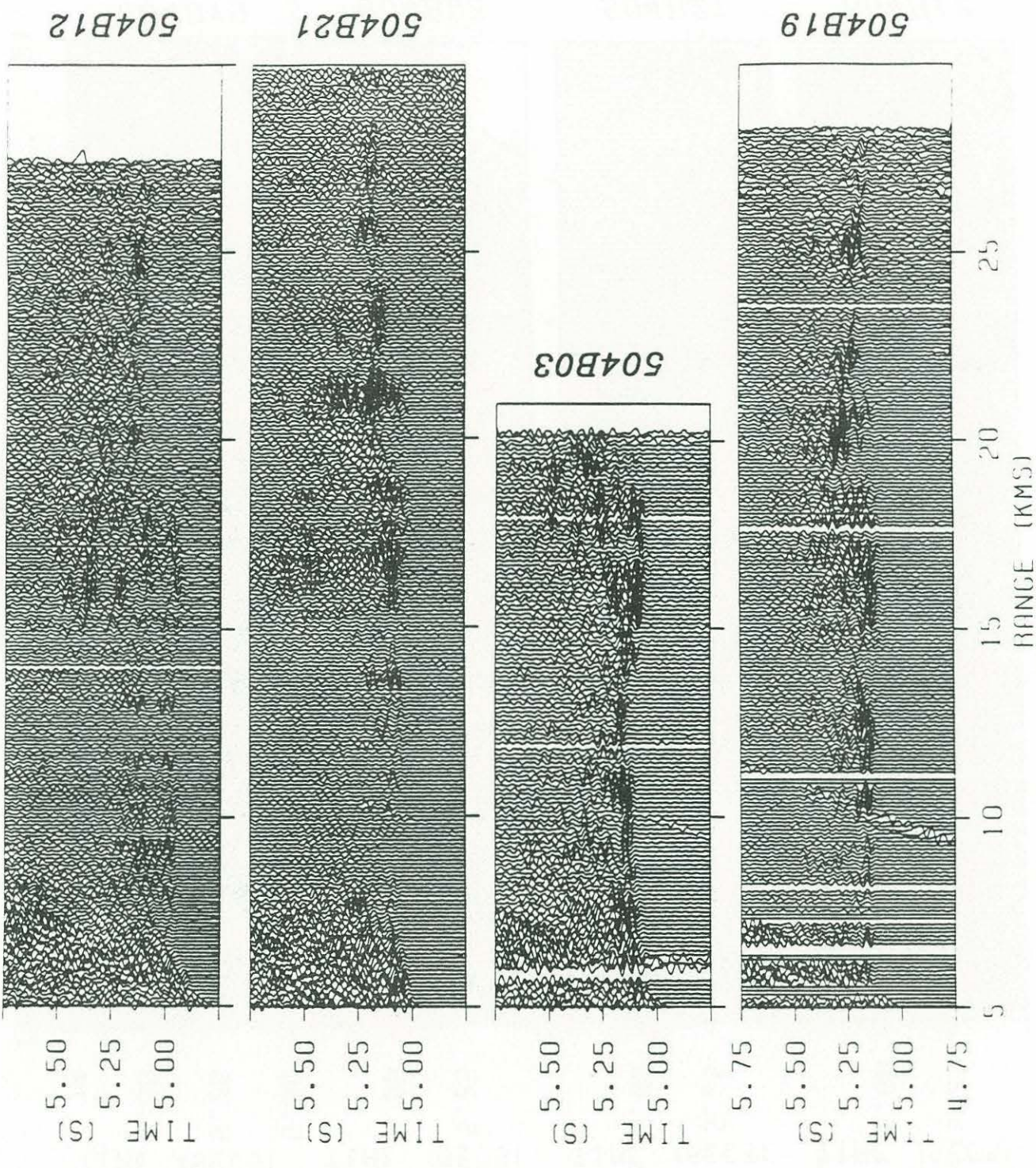
504B12
504B21
504B03
504B19
TIME (S)
5.50
5.25
5.00
5.75
4.75
5
10
15
20
25
RANGE (KMS)

Figure 6a

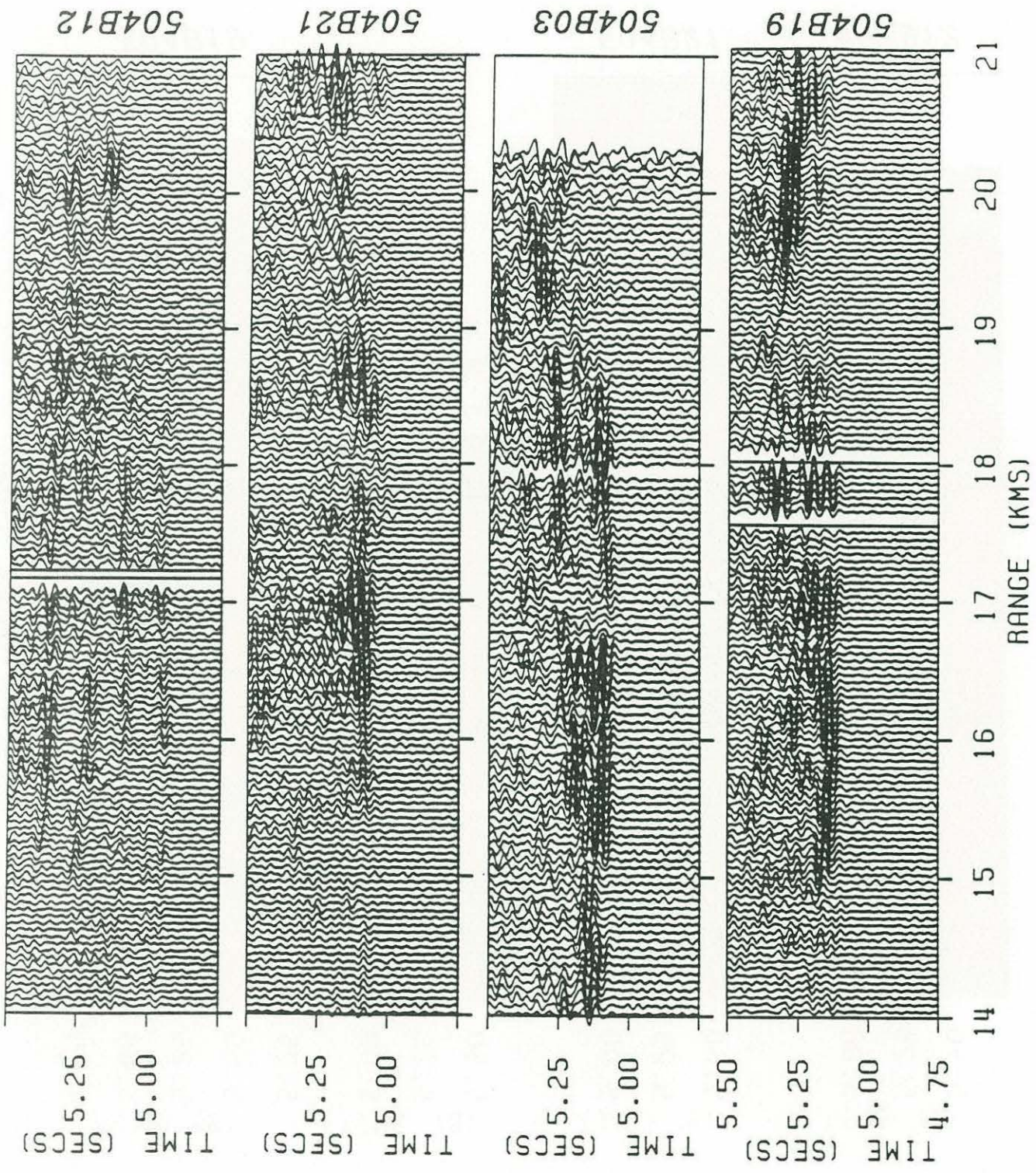
504B19
504B03
504B21
504B12
TIME (SECS)
5.50
5.25
5.00
4.75
14
15
16
17
18
19
20
21
RANGE (KMS)

Figure 6b

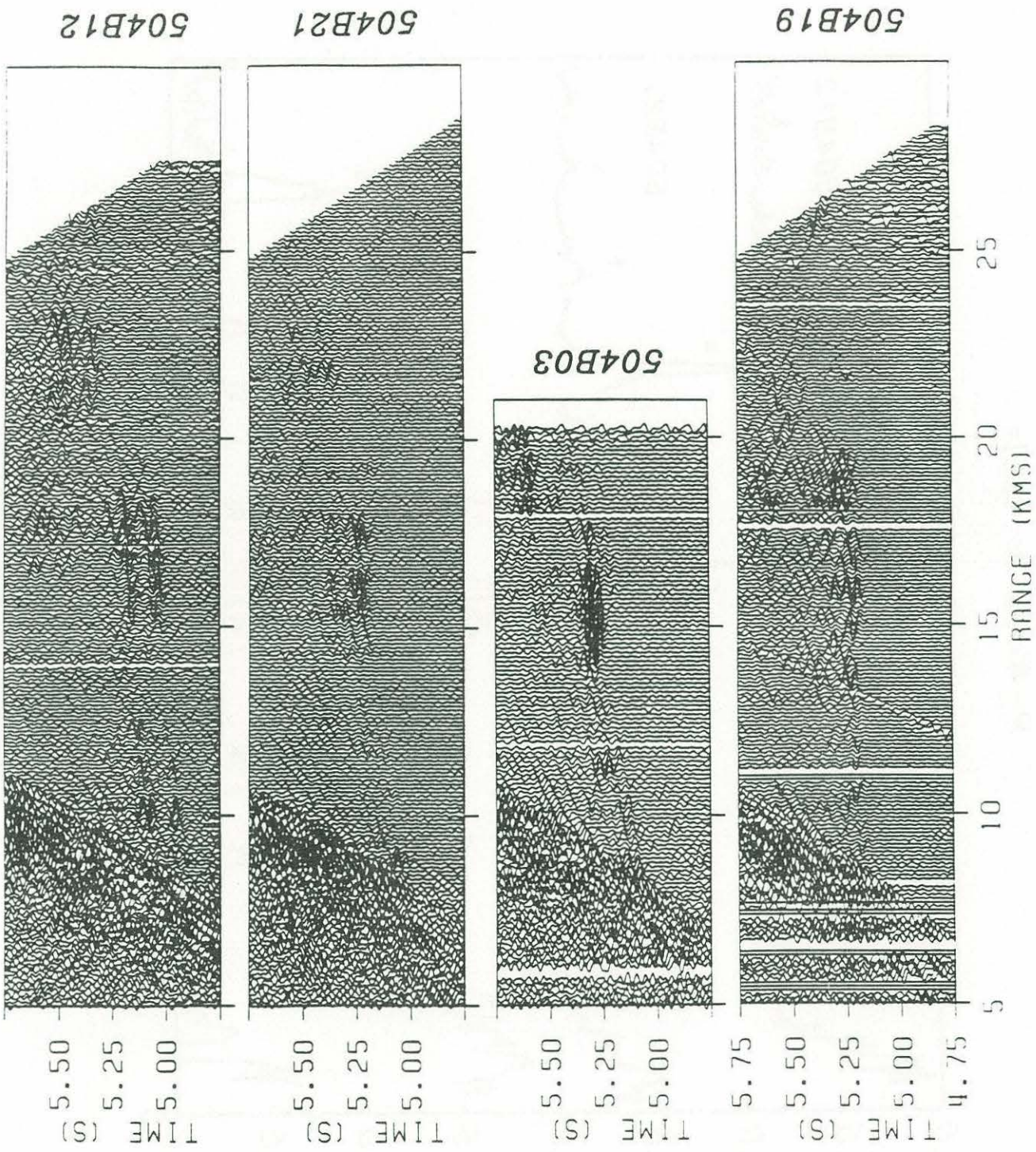
504B12
504B21
504B03
504B19
TIME (S)
5.50
5.25
5.00
5.75
4.75
5
10
15
20
25
RANGE (KMS)

Figure 6c

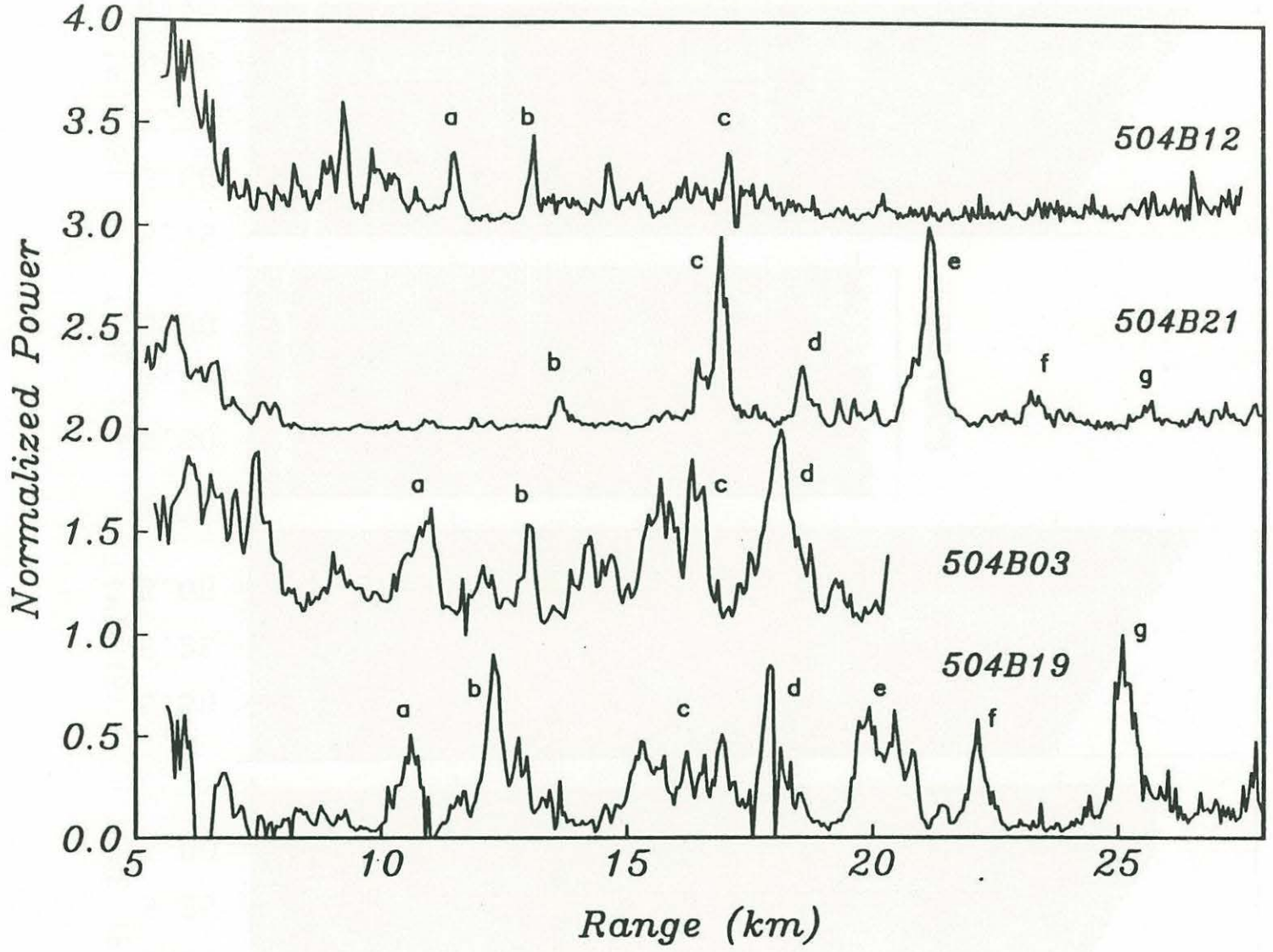
P–Wave Arrivals
Normalized Power
4.0
3.5
3.0
2.5
2.0
1.5
1.0
0.5
0.0
5
10
15
20
25
Range (km)
504B12
504B21
504B03
504B19
a
b
c
d
e
f
g

Figure 7a

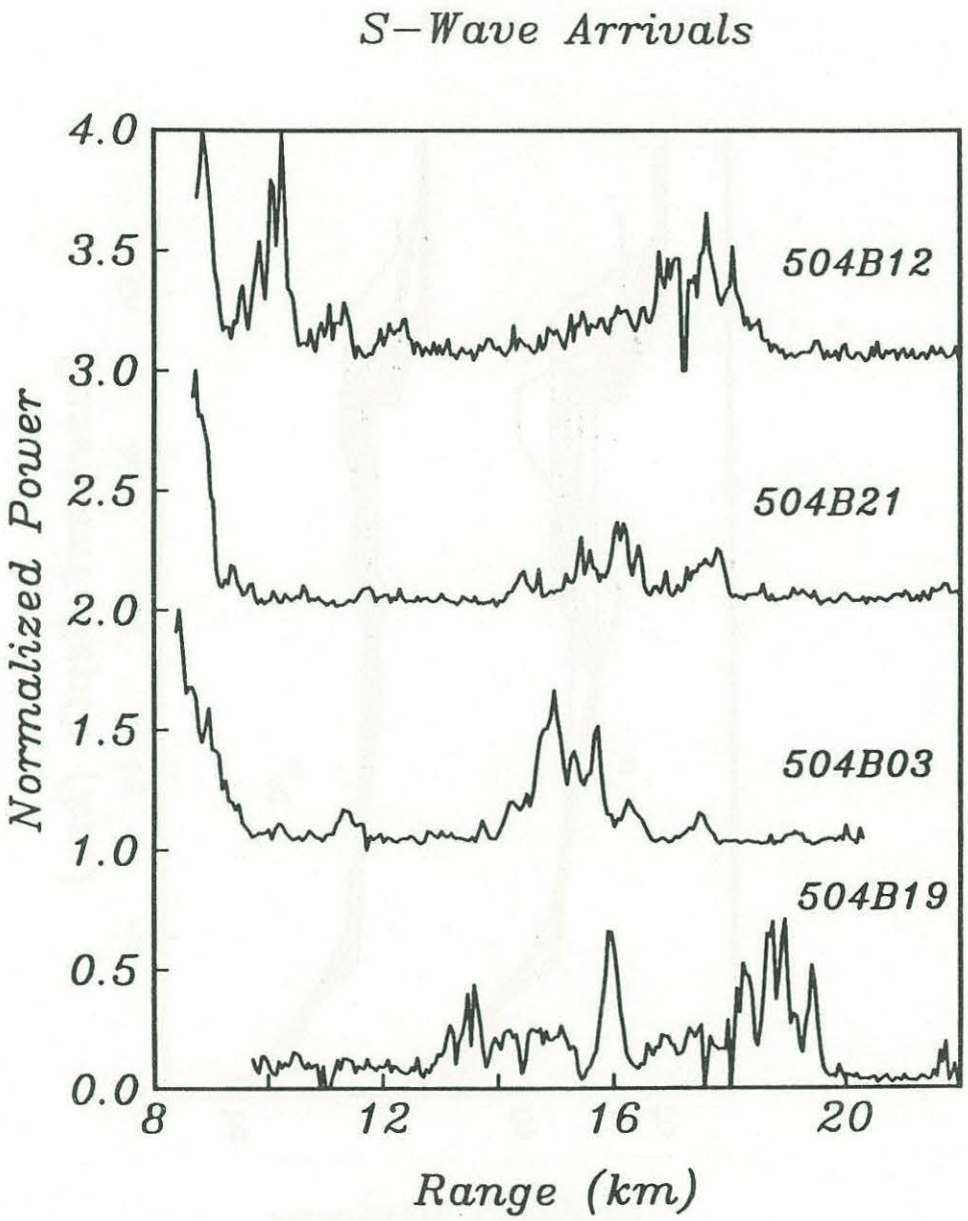
S−Wave Arrivals
4.0
3.5
3.0
2.5
2.0
1.5
1.0
0.5
0.0
Normalized Power
504B12
504B21
504B03
504B19
8
12
16
20
Range (km)

Figure 7b

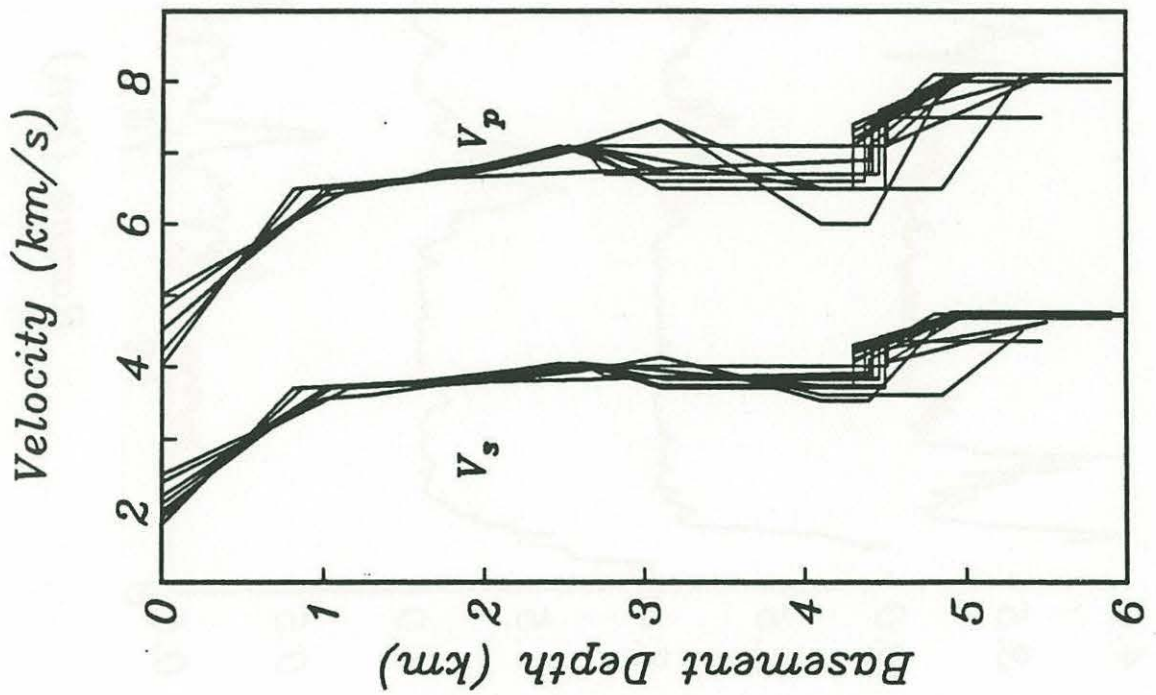

Figure 8a

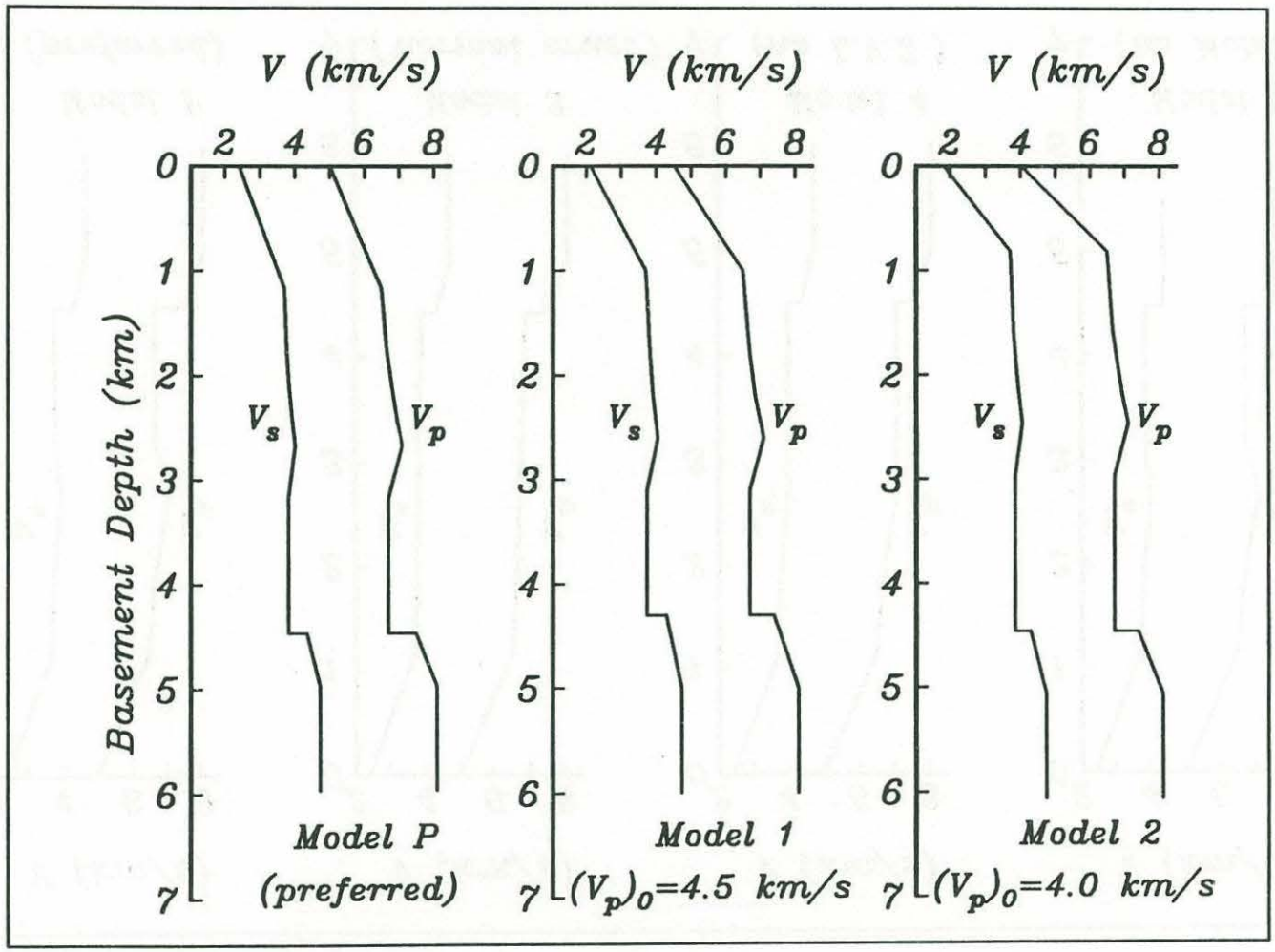
V (km/s)
2 4 6 8
0
1
2
3
4
5
6
7
Basement Depth (km)
V_s
V_p
Model P
(preferred)
V (km/s)
2 4 6 8
V_s
V_p
Model 1
$(V_p)_0$=4.5 km/s
V (km/s)
2 4 6 8
V_s
V_p
Model 2
$(V_p)_0$=4.0 km/s

Figure 8b

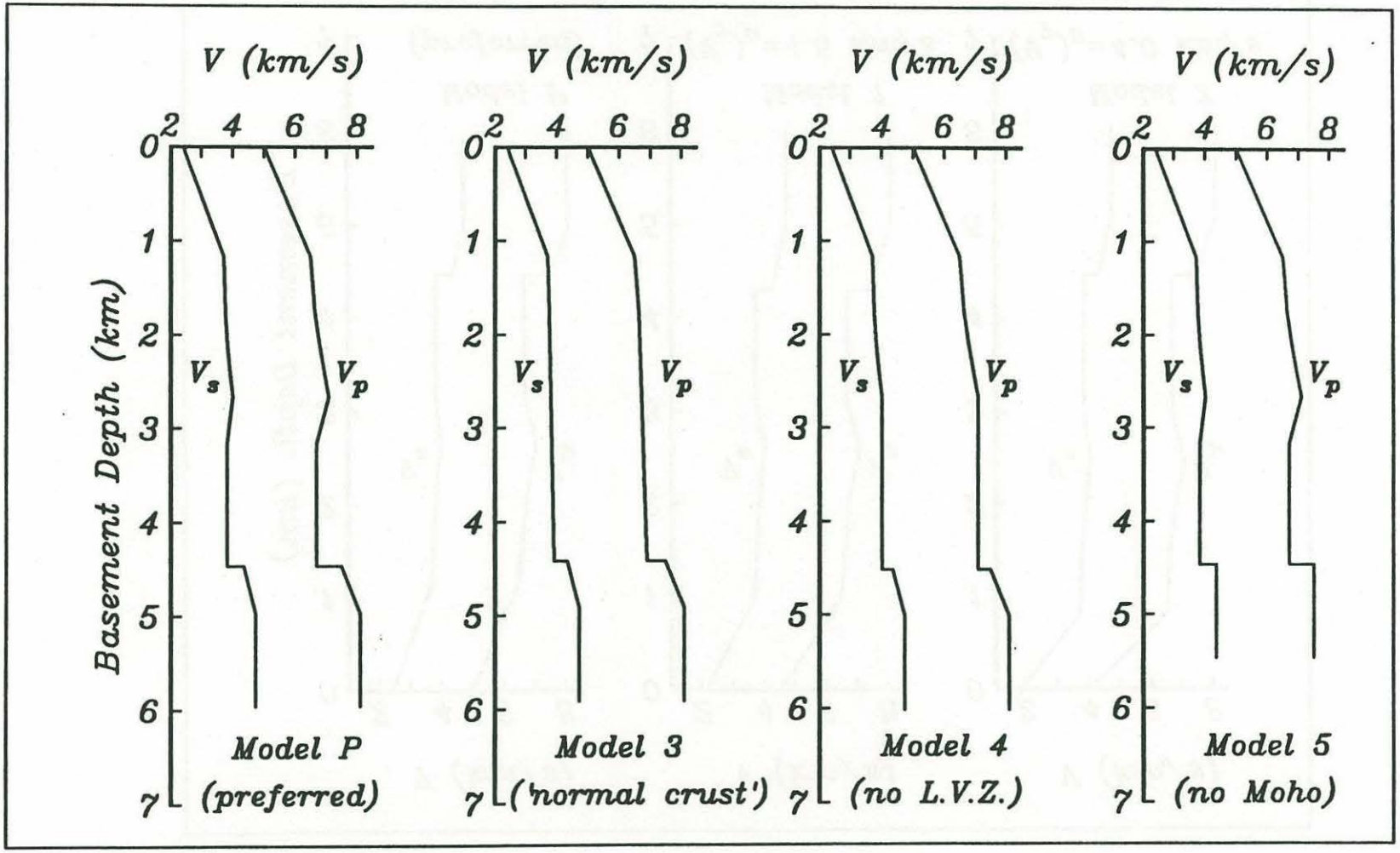

Figure 8b ctd.

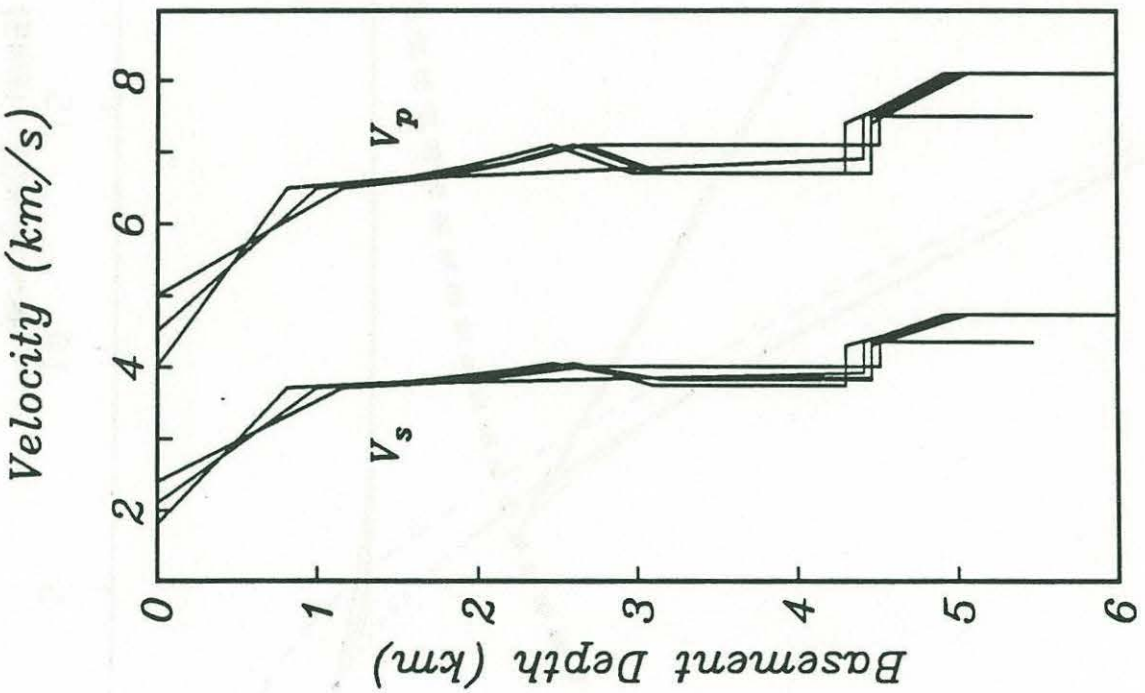

Figure 8c

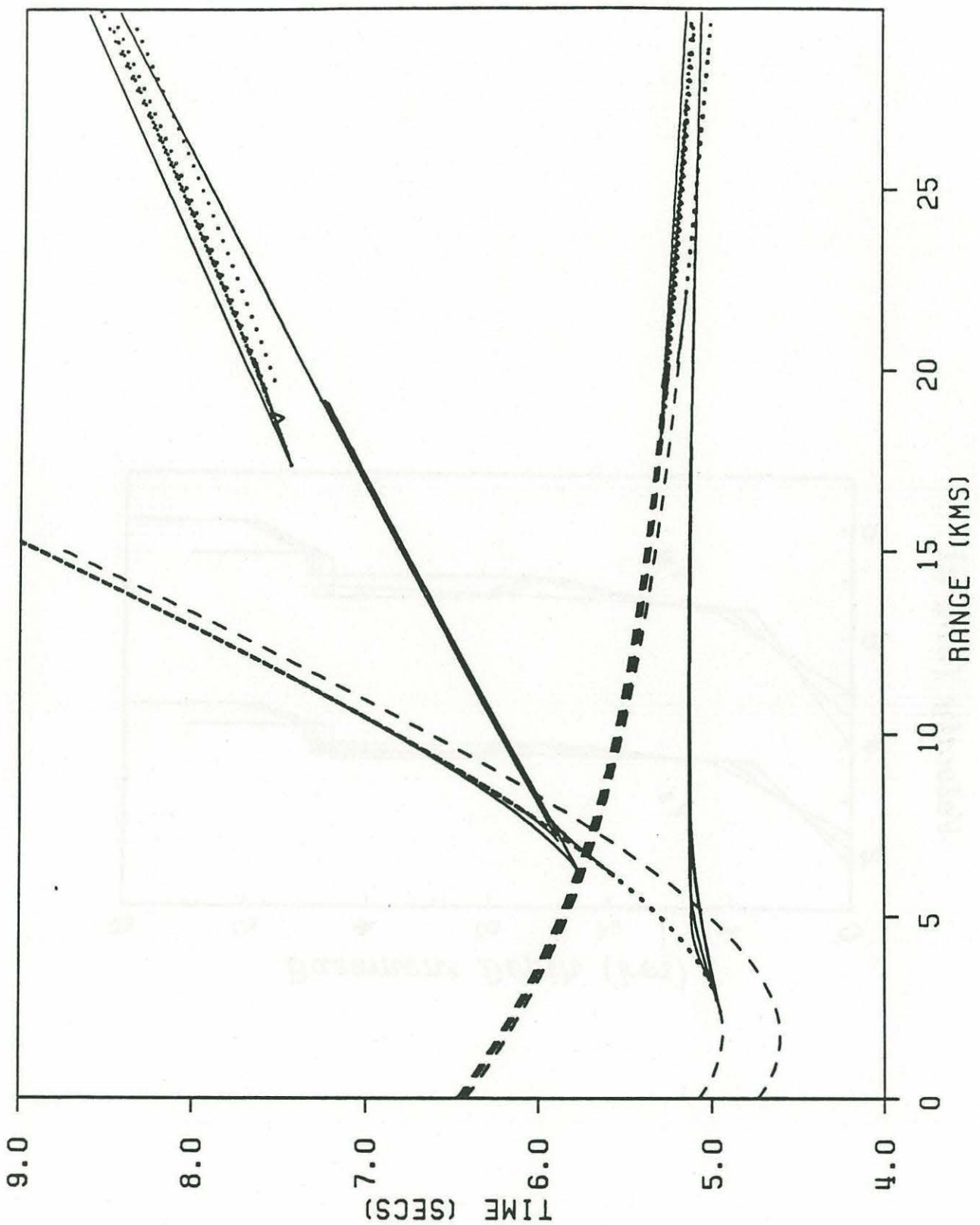

Figure 9

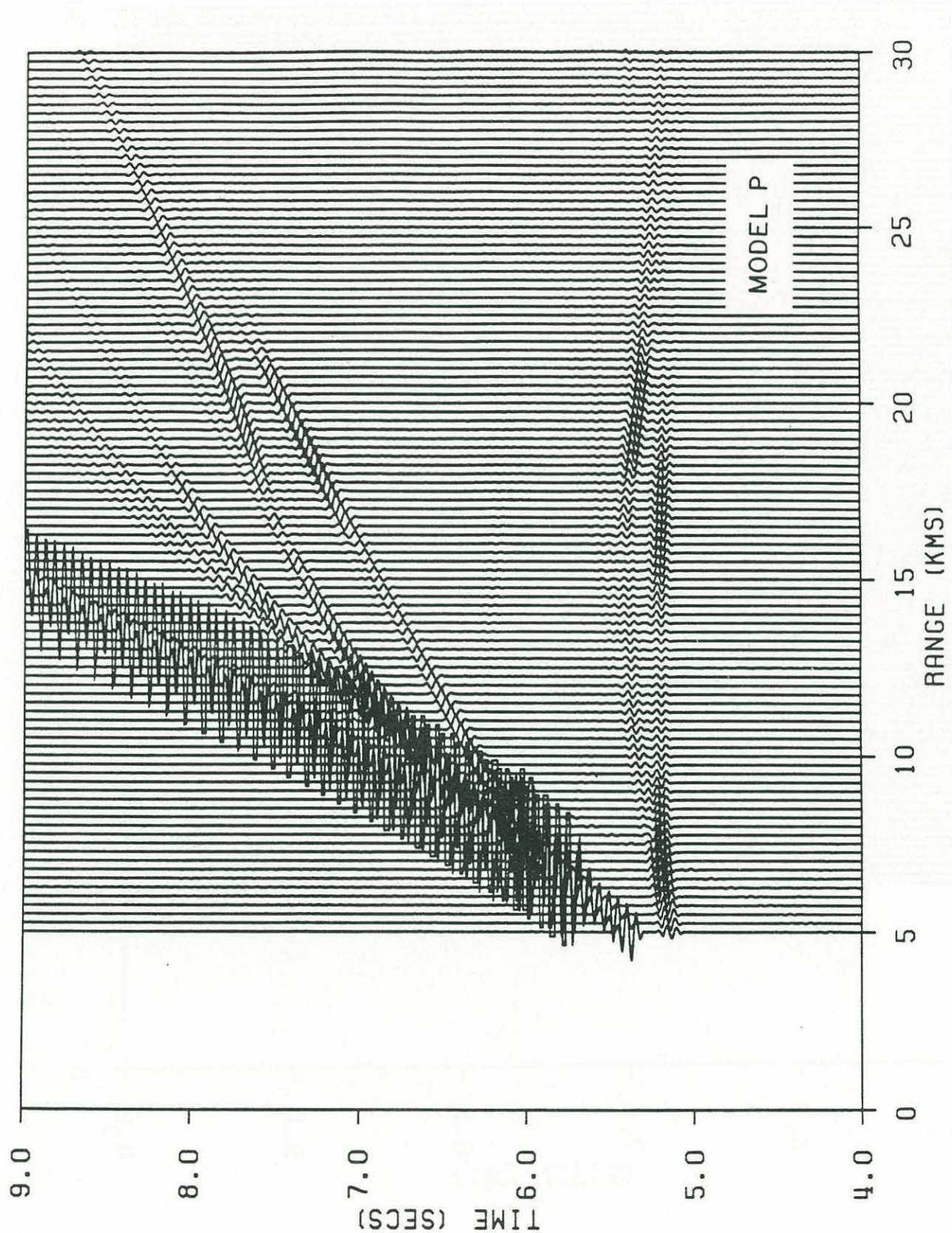

Figure 10a

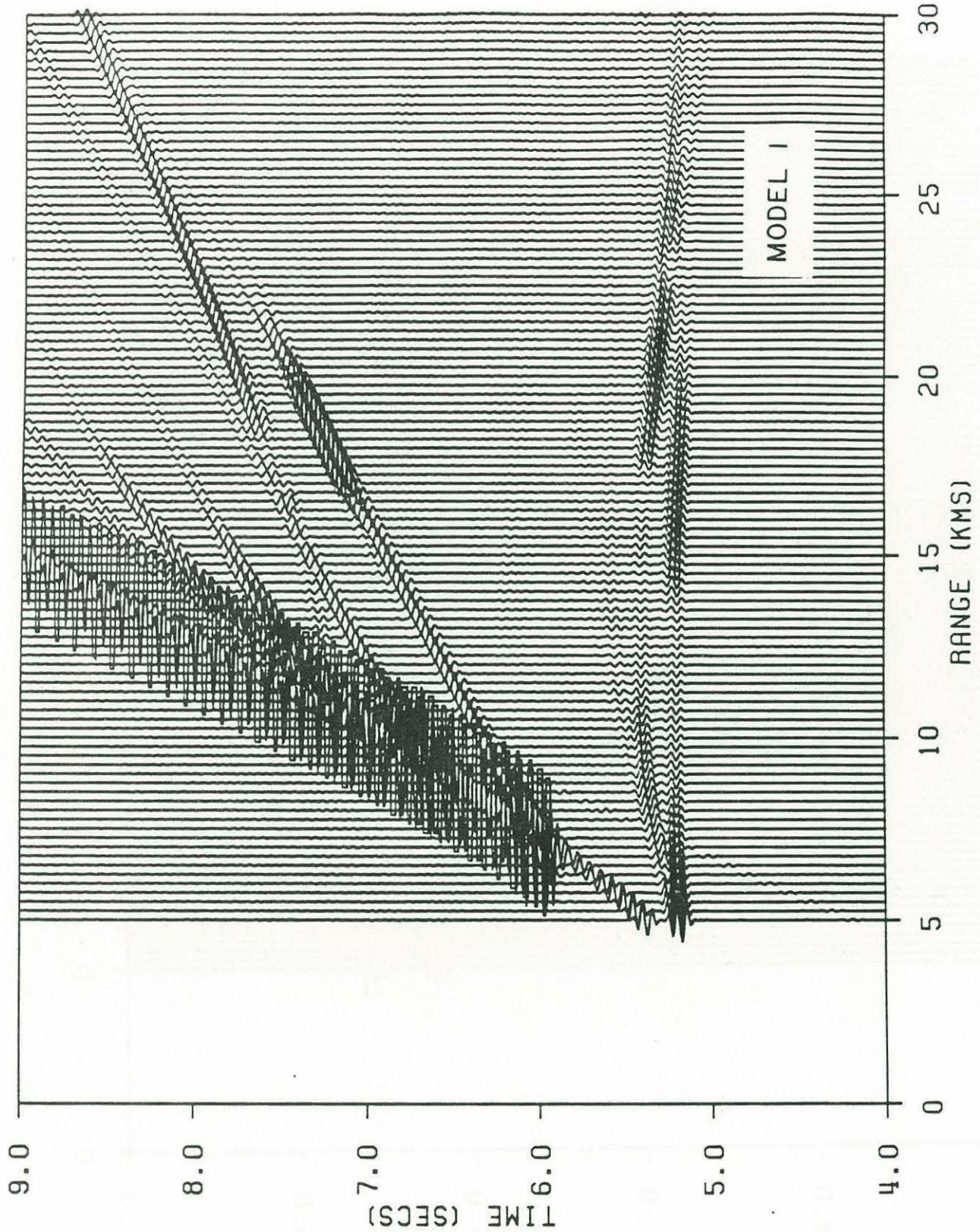

Figure 10b

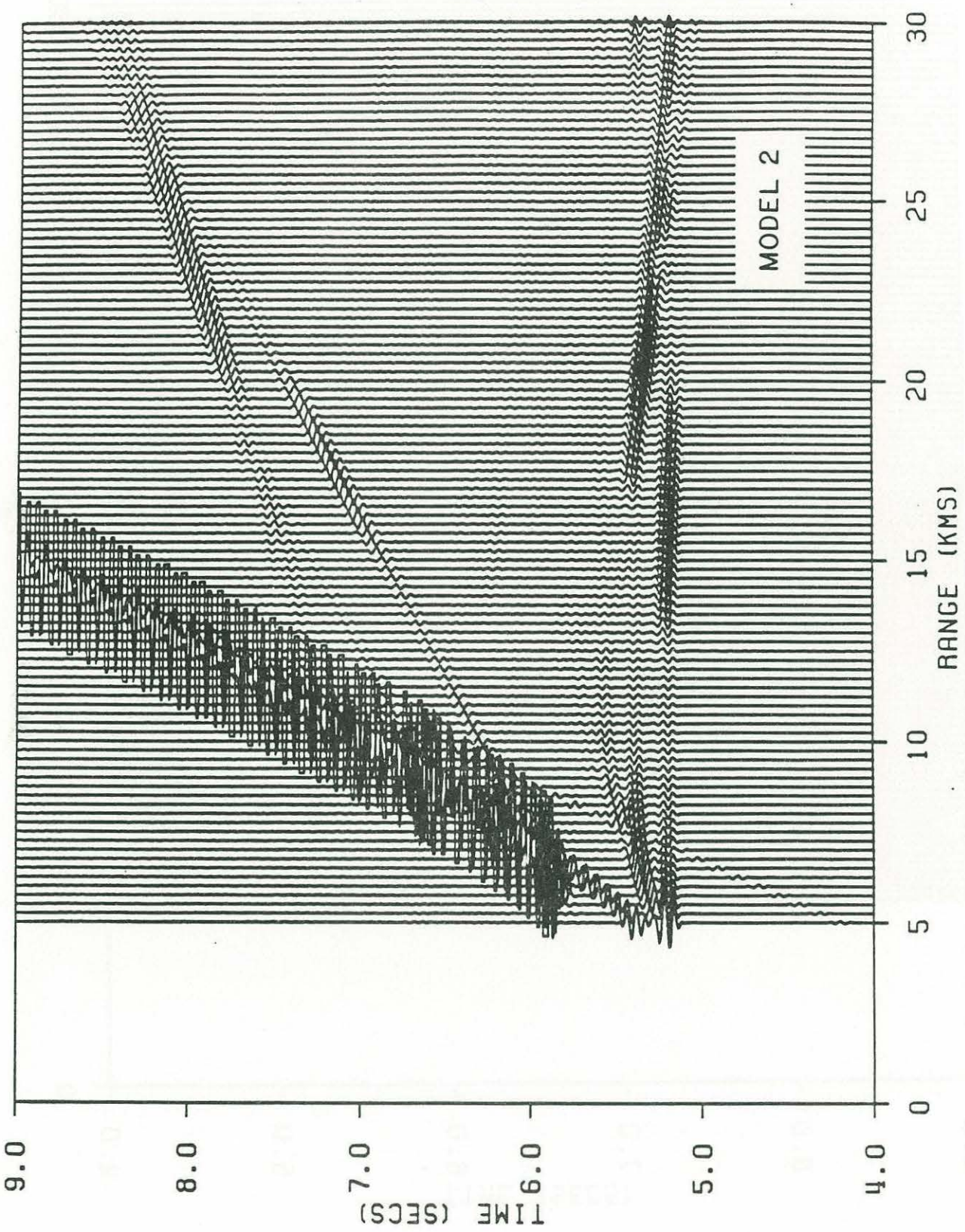

Figure 10c

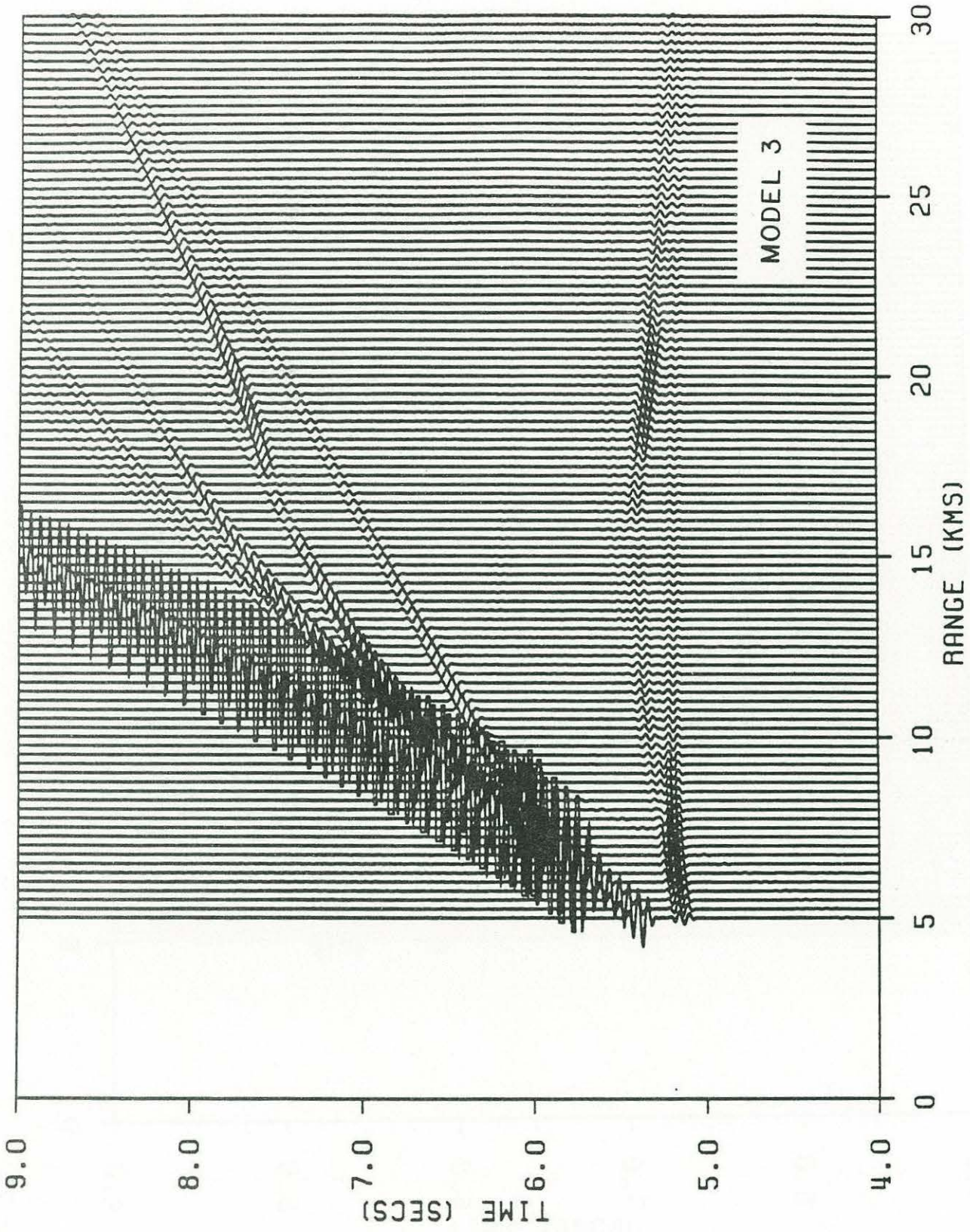

Figure 10d

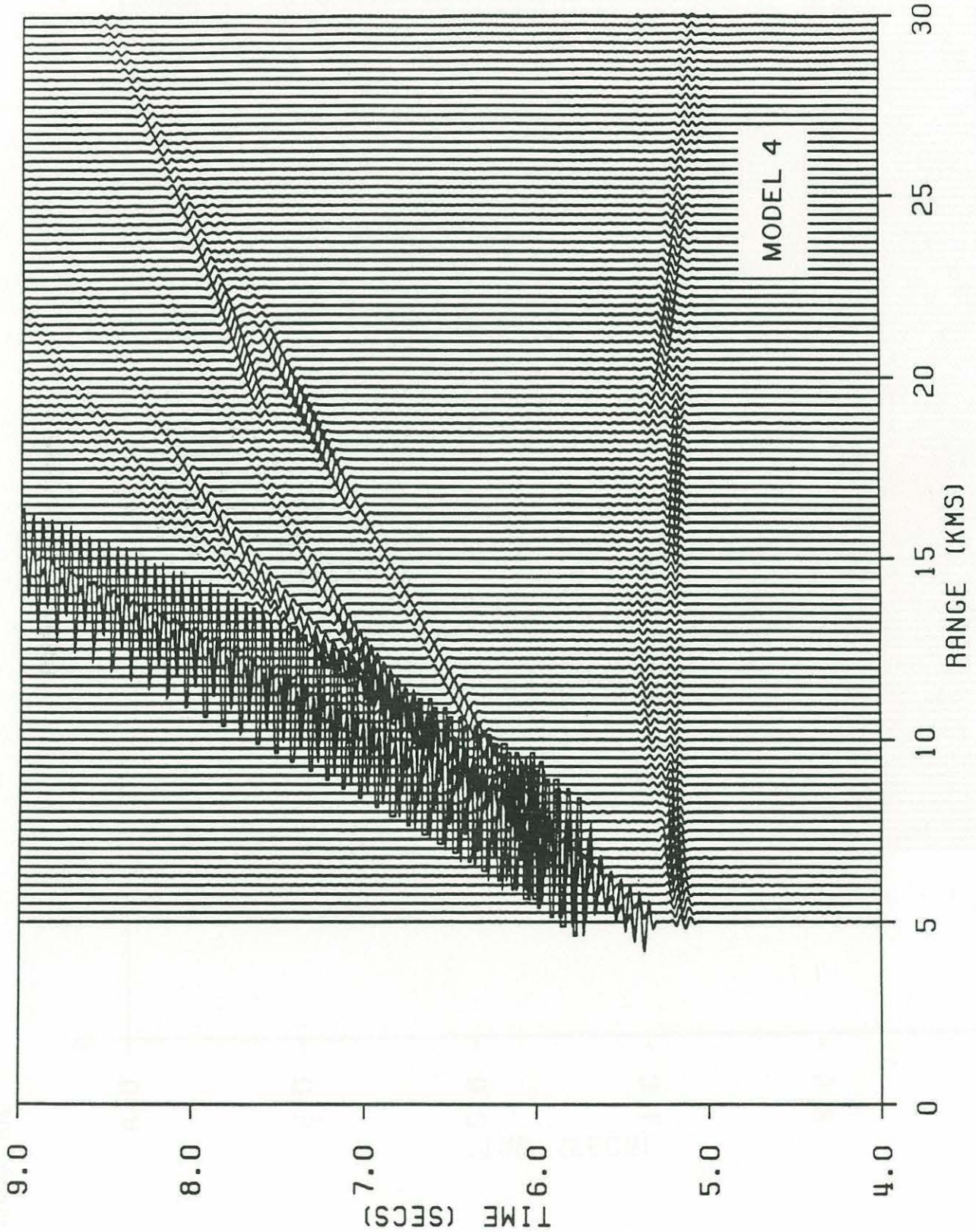

Figure 10e

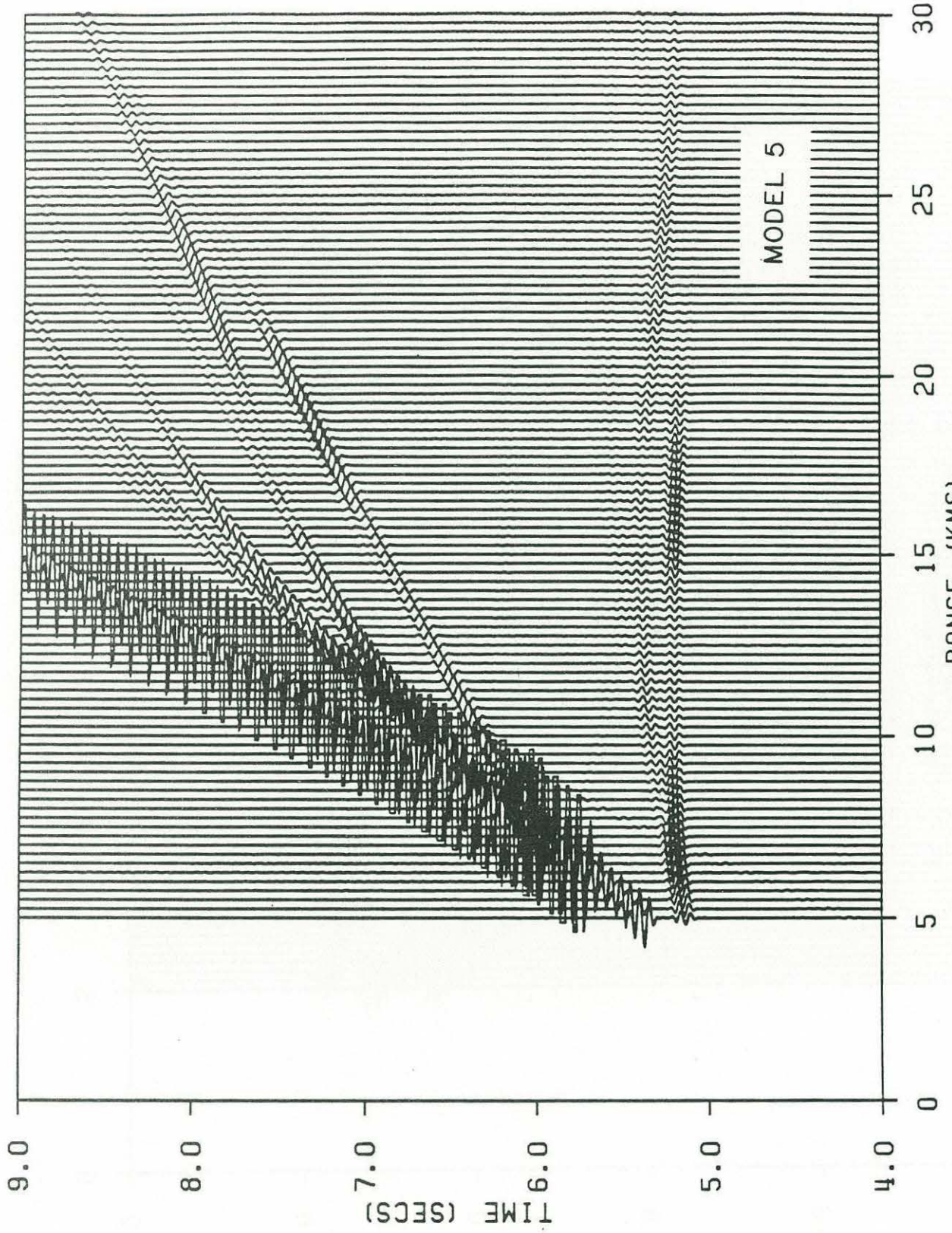

Figure 10f

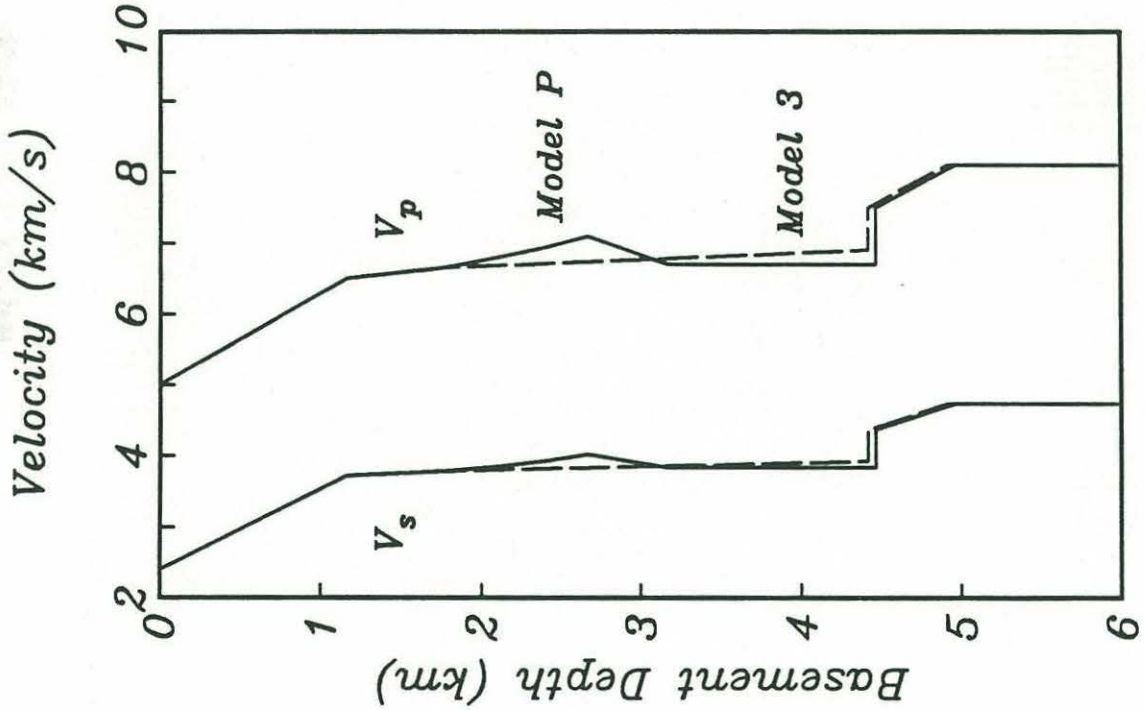
Velocity (km/s)
2
4
6
8
10
V_p
V_s
Model P
Model 3
0
1
2
3
4
5
6
Basement Depth (km)

Figure 11

CHAPTER 3

SEISMIC REFLECTION STRUCTURE OF THE UPPER OCEANIC CRUST: IMPLICATIONS FROM DSDP SITE 504B, PANAMA BASIN

ABSTRACT

We investigate the seismic reflectivity structure of the upper oceanic crust by comparing multichannel seismic (MCS) reflection data collected at Deep Sea Drilling Project (DSDP) Site 504B to the results of downhole logging. Extensive processing of the MCS data, required to remove high-amplitude side-scattered arrivals, revealed no conclusive evidence for laterally coherent reflection events generated within the upper 1-2 km of the crust. A reflection event with a travel time 0.25-0.3 s greater than the travel time of the basement reflection is probably a source-reverberation phase or a sediment-column multiple. The difficulty in identifying a shallow-crustal reflection event is surprising because drilling shows a well-defined change in physical properties at sub-basement depths of ~0.5-0.6 km, corresponding to the downward transition from volcanics to dikes. The crustal travel time to this boundary (~0.25 s) is similar to the travel times of shallow reflection events observed in other areas. In an attempt to understand this negative result, we calculated synthetic reflection seismograms for a series of velocity-depth profiles constructed from the logged downhole variations in physical properties. These seismograms were calculated with the source signature of the 1785 $inch^3$ airgun array used to acquire the MCS data. The synthetic seismograms demonstrate that low-amplitude reflections from the shallow crust are obscured by source reverberation and by sediment-column multiples. The low amplitudes of the predicted intracrustal reflection events suggest that the upper crustal structure at Site 504B differs from the crustal structure in those areas where high-amplitude, shallow reflection events have been previously identified.

Introduction

The application of near-normal-incidence, multichannel seismic (MCS) reflection profiling techniques to the study of oceanic crustal structure has resulted in the detection and mapping of reflecting horizons both within the crust and at the crust/mantle boundary. Shallow and deep intracrustal events (e.g. Musgrove and Austin, 1983; Mutter and NAT Study Group, 1985; McCarthy et al., 1988; Rohr et al., 1988), proposed magma chamber reflection events (Herron et al., 1978; Hale et al., 1982; Detrick et al., 1987; Rohr et al., 1988), and Moho reflections (e.g. Stoffa et al., 1980; Grow and Markl, 1977; Mutter and NAT Study Group, 1985) have been identified. The high spatial resolution and profiling rates attainable with the MCS technique, together with the easily interpretable seismic images that comprise the processed data, results in this technique being a powerful tool for mapping variations in seismic structure over a wide range of length scales. One of the first studies of oceanic crustal structure using MCS techniques consisted of the acquisition, in 1974, of a 3400 km long profile extending from the U.S. continental margin to the Mid-Atlantic Ridge (Grow and Markl, 1977). Since then, thousands to tens of thousands of kilometers of MCS data has been acquired on oceanic crust. In contrast to commonly observed reflections from the crust/mantle boundary, upper- and mid-crustal reflection events (Table 1) have been less frequently reported.

A limitation of the MCS technique is the difficulty in quantitatively characterizing seismic structure. Reflection amplitudes are a function of seismic impedance, but it is difficult to determine the impedance structure of oceanic crust because of the typically low signal-to-noise

TABLE 1. Characteristics of Upper- and Middle-Crust Reflections

Location	Sub-Basement Traveltime (s)	Crustal Thickness (s)	CMP Fold; Aperture	Source Size (in^3)
Angola Basin[1]	0.25–0.4	1.6–1.9	12; 2.7 km	4500
W. Atlantic[2]	0.6–1.0	2.5–3.0	60; 6 km	3300; 2932
Juan de Fuca Ridge[3]	0.3–0.55	2.2	60; 3 km	6000

[1] Musgrove and Austin (1983)
[2] Mutter et al. (1985); McCarthy et al. (1988)
[3] Rohr et al. (1988)

ratios of near-normal-incidence, intracrustal and Moho reflection events. Consequently, the primary information retrievable from MCS data is the travel time to a given reflector. In contrast to MCS techniques, the wide-angle reflection/refraction method allows the straightforward determination of seismic velocities, unambiguous numbers which are readily compared to the results of other experiments. Optimally, wide-angle reflection/refraction and near-normal-incidence MCS data are collected simultaneously. Such experiments allow the location of a reflective horizon within the layered velocity structure characteristic of oceanic crust. Although the shallow reflection events summarized in Table 1 can be identified with confidence, the lack of co-incident wide-angle reflection/refraction data prevents correlating these reflections to the layered velocity structure characteristic of the oceanic crust.

While combined MCS and wide-angle reflection/refraction techniques provide a clear picture of oceanic seismic structure, the large number of parameters that control rock velocity (e.g. Purdy and Ewing, 1986) makes

it difficult to correlate seismic and geological structure. Marine seismologists typically relate the layered velocity-depth structure that they derive from refraction experiments to geological structure in terms of the vertical distribution of lithologies that are found in ophiolite sequences. In this approach, seismic Layer 2 is correlated with extrusive volcanic and sheeted-dike sequences, seismic Layer 3 is correlated with a gabbroic sequence, and mantle velocities of 8.0 km s^{-1} or greater are associated with residual ultramafic rocks. Similarly, observed MCS reflection events are often associated with these geological boundaries. However, the validity of the ophiolite model of oceanic crustal stratigraphy is uncertain. An alternative viewpoint is that observed velocity layering can be correlated with approximately constant maximum depths of chemical alteration and cracking in either a compositionally homogeneous or layered crust (e.g. Lewis, 1983).

It is tempting to relate the reflection events of Table 1 to one or more of the geological boundaries recognized in ophiolites, namely the volcanics/sheeted-dike, greenschist facies/amphibolite facies, and sheeted-dike/gabbro transitions. Ophiolite studies show that the depths and thicknesses of these geological boundaries vary by hundreds of meters over length scales of kilometers (Casey et al., 1981), in agreement with the variable travel times and discontinuous occurence of these shallow reflection events. However, correlating these events to geological boundaries is ambiguous without direct sampling of the reflecting boundaries by crustal drilling.

In this paper, we investigate the seismic reflectivity structure of the upper 1-2 km of oceanic crust by comparing multichannel seismic (MCS)

reflection data collected at Deep Sea Drilling Project (DSDP) Site 504B to synthetic reflection seismograms computed for velocity-depth profiles constructed from downhole logging of physical properties. Hole 504B has been drilled to a total basement depth of 1.288 km, and is the deepest drillhole into oceanic crust at the time of writing. Hole 504B is the only site where the volcanic/dike boundary, predicted by the ophiolite model to be a fundamental feature of oceanic crust, has been drilled. The downward change in rock type coincides with changes in a variety of logged physical properties. The normal-incidence travel time to this boundary is similar to the travel times of shallow reflection events observed in other areas. Accordingly, Site 504B is an ideal location to test the hypothesis that shallow reflection events (Table 1) correlate with the downward transition from volcanics to dikes.

Study Area

DSDP Site 504B is located on the Nazca plate, about 225 km south of the Costa Rica Rift, the easternmost segment of the Cocos-Nazca plate boundary (Figure 1). Water depth and sediment thickness at the drillsite are 3460 m and 275 m respectively, and crustal age is estimated to be 5.9 Myr (Hobart et al., 1985). Within a radius of 50 km about the drillsite, basement topography has amplitudes typically less than 100 m (Langseth et al., 1983); basement topographic highs strike east-west, parallel to the Costa Rica Rift (Searle, 1983).

The sedimentary sequence at Site 504B consists of three lithological units (Figure 2). Unit 1, extending from the seafloor to a depth of 145 m, consists of nannofossil oozes that are characterized by a mean

compressional velocity and density of ~1.51 km s^{-1} and ~1.32 g cm^{-3}, respectively (Wilkens and Langseth, 1983). Unit 2, extending to a sub-seafloor depth of 227m, consists of chalks that are characterized by a mean compressional velocity and density of ~1.53 km s^{-1} and 1.48 g cm^{-3}, respectively. Lying immediately above basement, Unit 3 consists of up to 30 m of interbedded limestones and cherts (CCRUST, 1982). The P-wave velocity of a chert sample from Unit 3 was measured to be 4.25 km s^{-1} (Wilkens and Langseth, 1983).

From the top of oceanic crust downward (Figure 2), the drilled igneous sequence consists of 0.575 km of extrusive basalt flows and pillows, 0.209 km of extrusive/intrusive transitional lithologies, and finally 0.504 km of dikes (Anderson et al., 1982; Shipboard Scientific Party, 1988). The latter are distinguished from extrusive rocks on the basis of texture and the absence of volcanic glass (Anderson et al., 1982). The vertical sequence of extrusives and dikes drilled at 504B is consistent with the ophiolite model of oceanic crust (e.g. Coleman, 1977). Consequently, the dike succession at DSDP Site 504B is referred to as a sheeted-dike sequence. Velocity-depth profiles determined from wide-angle reflection/refraction experiments (Little and Stephen, 1985; Chapter 2) suggests that the current bottom of the drillhole is near the Layer 2/Layer 3 transition (Figure 2b).

Hole 504B is unique in the great variety of geophysical experiments that have been carried out downhole. Multichannel P- and S-wave sonic velocity logs, active-source neutron amd gamma-ray logs, conventional and large-aperture (10-80m) electrical resistivity logs, and borehole televiewer logs are discussed by Anderson et al. (1982), Anderson et al.

(1985a), Becker (1985), Newmark et al. (1985), and Moos et al. (1986). Variations in crustal permeability and in borehole heat flow are described by Anderson et al. (1985b), and Becker et al. (1985).

Inspection of the logged physical properties at Hole 504B demonstrates that electrical resistivity, as determined by the large-aperture array (Becker, 1985), shows the greatest variation as a function of depth. Resistivity values increase by about two orders of magnitude downhole, indicating a decrease in bulk porosity of ~10-15% in the same direction (Becker, 1985). In contrast to conventionally acquired resistivity data, the large-aperture data are less affected by borehole drilling fluids and drilling-induced fracture porosity, and are representative of the resistivity structure at distances of tens of meters rather than centimeters from the borehole. The large-aperture data represent averages over length scales that are more appropriate to controlled-source seismic experiments. Salisbury et al. (1985) show that bulk porosity, rather than rock type and composition, is the primary control on the P-wave velocity of the upper crust at Site 504B. Estimates of fracture porosity at Site 504B, derived by subtracting laboratory-measured porosities from the bulk porosity data, show that fracture porosity decreases to near zero toward the bottom of the drillhole (Salisbury et al., 1985).

The recognition of seismic layers 2A, 2B, and 2C in the upper 1-2 km of oceanic crust (e.g. Houtz and Ewing, 1976) has prompted a search for three zones of distinctive physical properties at Hole 504B. Such a sub-division is readily recognized in the estimates of bulk porosity derived from the large-aperture resistivity data (Figure 2a). These data

are characterized by two zones of rapidily decreasing porosity as a function of depth that are separated by a zone where the porosity is approximately constant. Correlating the location of the changes in porosity gradient with the Layers 2A/2B and 2B/2C boundaries indicates that these layers are ~200m, 350m and greater than 500m thick respectively. Porosity decreases by ~5% over a distance of ~50m across the volcanics/sheeted-dike transition. Anderson et al. (1985a) describe similar changes in gradient in other logged physical properties. Layers 2A and 2B are less readily distinguished in the sonic velocity data, and Layer 2A cannot be identified in borehole seismic data (Little and Stephen, 1985; Stephen, 1985), presumably because of its local occurrence and/or its limited thickness (Figure 2).

MCS Data

In May 1985, R.V. ROBERT D. CONRAD was used to collect approximately 1700 km of MCS data in the vicinity of DSDP Site 504B (Figure 1). The primary objective of this experiment was to conduct a regional reconnaissance of the crustal reflectivity structure around the drillsite. Shotpoint spacing was ~50 m, and the 2.4 km long receiver array consisted of 48 channels with a group separation of 50m. The MCS data were collected into 24-fold common-mid-point (CMP) gathers, with a CMP spacing of 25 m.

For the study described here, attention was focused on the shallow crust only. In order to correlate the drilled lithological sequence with possible intracrustal reflections in the MCS data, processing efforts were concentrated on short segments (15-25 km in length) of all five lines that

pass near the drillsite. In the following discussion, we present results for two of the five profiles, lines 485 and 490. These profiles trend east to west and north-west to south-east, respectively (Figure 1b). Both profiles were acquired with a four-element airgun array with chamber sizes of 235, 350, 500, and 700 in^3, fired at a pressures of 2000 pounds per square inch.

Processing of the MCS data consisted of the following sequences: (1) transformation of the shot records into CMP gathers followed by velocity analysis and CMP stack; (2) frequency-wavenumber (f-k) filtering of the shot gathers, followed by CMP gather and CMP stack; (3) transformation of the filtered shot gathers into receiver gathers, followed by f-k filtering, CMP gather and CMP stack. We attempted to optimize the stacking velocities using two approaches. We plotted CMP gathers every 1-2 km, and applied normal-moveout (NMO) corrections of 1.4-2.1 km s^{-1}, at intervals of 0.1 km s^{-1}, to each gather. In addition, the CMP gathers were stacked at constant velocities of 1.4-2.1 km s^{-1}, at intervals of 0.1 km s^{-1}, to generate constant-velocity stacks.

The frequency-wavenumber filtering of the shot and receiver gathers was prompted by the presence of arrivals in the shot records that were reflected from the sediment/basement interface both in front of and behind the receiver, and also from outside the vertical plane defined by the source and receiver (Figure 3). When transformed into CMP gathers (Figure 4), such scattered phases have moveouts similar to intracrustal reflection events (e.g. Larner et al., 1983). For the MCS data acquired at Site 504B, some of the scattered noise can be attenuated by applying an f-k filter to the shot gathers. However, those parts of the scattered

phases with small moveout (e.g. hyperbola apexes) cannot be attenuated without also attenuating intracrustal events (e.g. Figure 3). Simple calculations show that the moveout of these components of the scattered arrivals may increase when the data are transformed into receiver gathers. Accordingly, we regathered the previously filtered shot records into receiver gathers and again applied an f-k filter. A drawback of f-k filtering is the introduction of numerical phases with wavenumbers equal to the cut-off values of the filter, despite the use of a tapered bandpass window (Figure 3). For the MCS data collected at Site 504B, any positive effects of applying the second f-k filter appeared to have been outweighed by the introduction of additional spatially-aliased arrivals.

Constant-velocity stacks of a portion of Line 490 are shown in Figures 5 and 6. The reflection events in the profile showing the data stacked with a velocity of 1.5 km s^{-1} (Figure 5) probably represent source reverberation and sediment-column multiples. The 'tails' of some of the diffraction hyperbolae evident in Figure 5a are attenuated in the f-k filtered data shown in Figure 5b. Many of the reflection events evident in Figure 5 are not seen in the data stacked with a velocity of 1.8 km s^{-1} (Figure 6). The sonic-velocity log collected at Hole 504B predicts that this value is the appropriate stacking velocity for a reflection event from the volcanics/dike contact. The crustal travel time of this predicted event is 0.25 s. Accordingly, the reflection event with a travel time of 5.25-5.3 s (Figure 6) may be a reflection from this lithogical boundary.

Portions of Lines 490 and 485, stacked with depth-varying velocities, are shown in Figures 7 and 8. Stacking velocities were calculated from

the velocity-depth model derived from analysis of wide-angle reflection/refraction data collected at the drillsite (Chapter 2). This velocity-depth model predicts that a stacking velocity of ~1.9 km s^{-1} is appropriate for a reflection event with a crustal travel time of 0.25 s. Both profiles show a reflection event with a crustal travel time of 0.25-0.3 s. This event is the same as the event identified in the constant-velocity stacked section (Figure 6). The travel time and stacking velocity of this phase are consistent with it being a reflection from the volcanic/dike transition (Figures 7 and 8). However, the constant crustal travel time of this event is indicative of source reverberation or a 'peg-leg' multiple generated within the sedimentary section. This latter interpretation is supported by the lack of evidence for a reflection event in the CMP gathers with a stacking velocity greater than or equal to 1.8 km s^{-1} (Figure 4). A relatively high-amplitude reverberation or multiple might not be completely attenuated by the CMP stack. The 5.25-5.3 s reflection event can also be seen in the data stacked with a velocity of 1.5 km s^{-1} (Figure 5).

Synthetic Seismogram Models for Site 504B

The difficulty in identifying shallow-crustal reflection events may simply be due to the presence of high-amplitude, side-scattered arrivals. However, synthetic reflection seismograms calculated for a series of velocity-depth models constructed from the logged variations in physical properties at Hole 504B suggests that reflections from the shallow crust might be difficult to confidently identify even in the absence of noise.

Impedance Models

At Hole 504B, the seismic impedance of the upper crust is readily determined from downhole measurements of sonic velocity and density (e.g. Salisbury et al., 1985). However, the usefulness of these impedance values is uncertain because they represent averages over length scales of less than ~3 m (e.g. Salisbury et al., 1985), and consequently may not be representative of impedance variations at seismic length scales of tens of meters. A simple average of these impedance values is inappropriate because the logged data are not indicative of velocity variations away from the drillhole. The velocity and density of the upper crust at seismic length scales can be estimated from the bulk porosity data which are in turn estimated from the results of the large-scale resistivity experiment (Becker, 1985). Although these relationships are not unique, the range of velocity-depth profiles presented below probably bound the true values. The following argument assumes that velocity is a function of porosity only.

Bulk porosity (ϕ) and resistivity can be related via the empirical equation $r_m/r_f = a.\phi^{-n}$, where r_m and r_f are the resistivity of the rock medium and borehole fluid, respectively, and a is a constant. The value of the exponent n is a function of void geometry (Becker, 1985). The appropriate value of n in oceanic crust ranges from 1.5 to 2.5, where the lower values are characteristic of cracks and the higher values are characteristic of grain boundary porosity (e.g. Becker, 1985). For Hole 504B, the nature of the porosity changes with depth, and consequently no one value of the exponent n is appropriate (Salisbury et al., 1985).

The correlation of velocity with porosity is non-unique because the velocity of a porous medium is dependent on void geometry (e.g. Watt et al., 1979). However, irrespective of void size and shape, the velocity bounds on an isotropic n-phase aggregate can be calculated using the method described by Hashin and Shtrikman (1963). The Hashin-Shtrikman velocity bounds on a water-rock aggregate are shown in Figure 9; the P- and S-wave velocity of the rock phase (V_p=6.4 km s^{-1}, V_s=3.5 km s^{-1}) are the values predicted by the best-fit relationship between laboratory-measured values of velocity and porosity for samples recovered from Hole 504B (Salisbury et al., 1985). The density of the rock phase (2.94 g cm^{-3}) is that predicted by low-porosity (0.1%) samples recovered from the bottom of Hole 504B (Christensen et al., 1985).

Velocity and porosity can also be related via the self-consistent scheme (SCS) which allows the calculation of velocity assuming interacting voids of specific shape (Hill, 1965). The SCS prediction for fluid-filled spheres is shown in Figure 9; the prediction for disc-shaped voids coincides with the Hashin-Shtrikman lower bound. Also shown in Figure 9 is the porosity-velocity relationship derived from laboratory measurments (Salisbury et al., 1985).

The four paths through the velocity-porosity space appropriate to the rocks recovered from Hole 504B, together with the porosity-depth data, allow the calculation of velocity-depth profiles from the bulk porosity data. For each path, three velocity-depth profiles are presented, corresponding to different values of the exponent in Archie's Law (Figure 10). The bulk porosity of the upper 0.0528 km was assumed equal to the value at a sub-basement depth of 3.7873 km, where the first resistivity

measurement was made (Becker, 1985). The downhole variation in the density of the igneous crust is readily calculated from the density of the rock matrix and the bulk porosity. With the exception of the chert layer, the velocity and density of the sedimentary sequence are the laboratory-measured values of Wilkens and Langseth (1983). The density of the chert sequence was assumed to be 2.2 g cm^{-3}, typical of reported values (Hamilton, 1978).

Normal-Incidence Synthetic Seismograms

The normal-incidence synthetic seismograms shown in Figures 12-14 were calculated with a frequency-domain reflectivity code (Berryman et al., 1958) and include all multiply-reflected phases. The layers of the input models were assumed to be non-attenuative. The signatures and spectra of the source functions used to calculate the seismograms presented here are shown in Figure 11. Source LDGO is the source signature (manufacturer's specification) of the 1785 in^3 airgun array used to acquire the MCS data. The tuned source is a 4170 $inch^3$ airgun array described by Brandsaeter et al. (1979).

Comparison of the seismograms presented in either Figures 12 or 13 demonstrates that both sediment-column and internal multiples contribute significantly to the computed seismogram. No primary phases are predicted at times greater than ~5.4 s. Given realistic attenuation values, the amplitude of these multiple events would be attenuated. Seismic attenuation values for the rock types (oozes and chalks) that constitute the sedimentary section at Site 504B have not been reported in the literature. However, assigning attenuation values of 0.01-0.005 dB m^{-1}

to the sedimentary sequence does not significantly affect the amplitude of the multiply-reflected events. These attenuation values, corresponding to seismic Q values of 72 and 144, are typical of fine-grained sedimentary rock (Hamilton, 1972; 1976). The importance of multiply-reflected arrivals is evident on inspection of the observed data shown in Figure 5.

The most readily recognized reflection event is seen at 5.35 s (Figures 12, 13) and is generated in the vicinity of the Layer 2/Layer 3 transition (Figure 2b). However, the sonic-velocity logs may be unreliable at these depths because these data were acquired close to the bottom of the drillhole. At shallower depths, the reflection event at 5.2 s (Figures 12, 13) correlates with the volcanics/dike boundary. This event has a greater amplitude in the seismogram calculated for the observed velocity-depth profile than in the seismogram calculated for the velocity-depth model without the sedimentary section. This is probably due to the reduced impedance contrast at the sediment/basement interface in the former model. The 5.2 s reflection event has a travel time that is only 0.25 s greater than the basement reflection event, and consequently is obscured by the latter signal in the seismograms calculated with source LDGO (Figure 12). Without accurate source deconvolution, the 5.2 s event might be difficult to distinguish from source reverberation in observed data. This event is more readily recognized in the seismograms calculated with the signature of the tuned array. Reflections generated from within the volcanic sequence are also identifiable in the latter seismograms. The synthetic seismograms calculated for the velocity-depth profiles derived from the velocity-

porosity relationships shown in Figure 9 are clearly dominated by source reverberation and sediment-column multiples (Figure 14). Only velocity-depth profile HS^- generates a readily recognized reflection event.

CMP Synthetic Seismograms

The normal-incidence synthetic seismograms of Figures 12-14 are not strictly analogous to the seismograms of MCS data which are generated by stacking tens of seismograms having a common mid-point. Layer boundaries with low seismic impedance may be more readily detected by recording arrivals at horizontal ranges close to the P-wave critical point where the amplitudes of reflected phase are significantly greater than at normal-incidence. Accordingly, we calculated wide-aperture synthetic seismograms for Models OBS and EMP20 (Figures 15, 16) using the reflectivity method (Fuchs and Muller, 1971; Kennett 1975). Seismograms within the range window 0.3-2.7 km were summed using stacking velocities calculated from the input velocity models. These seismograms were computed for frequencies of 10-30 Hz because comparison of filtered and unfiltered samples of the observed MCS data demonstrates that the observed data has negligible energy at frequencies greater than 30 Hz. The 5.2 s reflection event in the stacked seismogram calculated for model OBS (Figure 15b) correlates with the volcanics/dike boundary. However, this event is difficult to distinguish from source reverberation. The stacked seismogram computed for model EMP20 does not show a readily identifiable event from this geological boundary. Inspection of Figures 15 and 16 suggests that a receiver array with an aperture greater than 2.4 km would not necessarily increase the amplitude of the 5.2 s event.

At ranges greater than 2.7 km, both CMP gathers are dominated by refracted arrivals.

In the reflectivity method, the Fourier transform of the pressure response at the receiver is represented by a Hankel transform over incidence-angle of the product of the reflectivity function and Bessel functions of the first kind. Stephen (1977, 1983) shows that for accurate seismogram calculation the limits of integration of the Hankel transform must be chosen wide enough to avoid the introduction of false arrivals with phase velocities corresponding to one or other of the integration limits. In addition, the angle increment must be sufficently small so that the computed seismograms do not show reverberative noise (Stephen, 1977; 1983; Mallick and Frazier, 1987).

For the velocity structures of interest in this paper, the minimization of the noise sources described above requires excessive computation. The synthetic seismograms shown in Figures 15 and 16 were computed using an angle increment of 0.023° and integration limits of 0.07° and 40°. These limits correspond to phase velocities of 1100 km s^{-1} and 2.175 km s^{-1}, respectively. This choice of parameters introduces a high-amplitude numerical arrival with a phase velocity of 2.175 km s^{-1} but results in negligible reverberative noise. The false arrival has negligible effect on the seismograms included in the CMP stack.

In the implementation of the reflectivity method used to compute the near-normal-incidence synthetic seismograms shown in Figures 15 and 16, the Bessel functions in the integrand of the Hankel transform are approximated by Hankel functions. This approximation is satisfactory

when the argument of the Bessel function is greater than 15 for those values of frequency and incidence-angle that contribute most to the integrand (Stephen, 1977). When the approximation is inappropriate, values of the reflectivity function at large angles of incidence are weighted more heavily than they should be. For the near-normal-incidence synthetic seismograms shown here, the minimum value of the Bessel function argument is ~0.15. To check the accuracy of these calculations, we computed synthetic seismograms for which the Bessel functions were alternately approximated by Hankel functions and by Chebyshev polynomials. The latter are a better approximation than the former when the argument of the Bessel function is small. For horizontal ranges of 0.3-3.0 km, and using the incidence angles and frequencies listed above, the seismograms for both of these approximations were not observably different.

Wide-Aperture Synthetic Seismograms

Synthetic reflection modeling shows that the smooth velocity transition that characterizes the velocity profiles derived from estimates of the bulk porosity data are dominated by source reverberation and sediment-column multiples (Figure 14). However, wide-aperture synthetic seismograms for model EMP20 (Figure 10) show that this velocity gradient, which defines the extrusives/sheeted-dike transition, generates high-amplitude refracted arrivals at horizontal ranges of 6-7 km (Figure 17). These seismograms were calculated using an angle increment of 0.051° and integration limits of 0.17° and 89°, corresponding to phase velocities of 500 km s^{-1} and 1.5001 km s^{-1}. In contrast to the seismograms presented in Figure 15 and 16, this choice of parameters does not

introduce false arrivals but does cause low-amplitude reverberative noise. However, this noise has negligible effect on the observed amplitude focusing at 6-7 km range.

The observation of high-amplitude refracted arrivals (Figure 17) suggests that the depth to the extrusives/sheeted-dike transition at Site 504B might be be more readily mapped with the wide-angle reflection/refraction technique than with conventional MCS techniques. Wide-angle reflection/refraction data acquired at Site 504B show amplitude focusing at ranges of 5-7 km (Chapter 2), as predicted by the synthetic seismogram modeling.

Discussion

The difficulty in identifying a reflection event generated within the upper crust at Site 504B is probably due to a combination of experimental technique and geological structure. The high-amplitude, side-scattered arrivals characteristic of the MCS data (e.g. Figure 3) cannot be completely removed by f-k filtering, and these events probably obscure intracrustal reflections. Given this noise problem, the ability to confidently identify an intracrustal reflection event at Site 504B would probably be improved if MCS data were acquired with a receiver array characterized by a shorter group separation. The shorter group separation would allow more accurate f-k filtering, minimizing the effects of spatial aliasing. Side-scattered arrivals in MCS data acquired on the Juan de Fuca ridge were successfully removed by f-k filtering (Rohr et al., 1988). These data, which show an intracrustal reflection event with a crustal travel time of 0.3-0.55 s (Table 1), were acquired with a

receiver array having a group separation of only 25 m (Rohr et al., 1988).

The synthetic seismograms shown in Figure 12 demonstrate that it would be difficult to assert that the 5.2 s event represents an intracrustal reflection rather than source reverberation without knowledge of the velocity-depth model and the source signature. This problem does not arise for the seismograms calculated with the shorter-duration source signature (Figure 13). Clearly, accurate deconvolution of the MCS data using the measured source signature would aid in identifying a reflection event from the volcanics/dike boundary. We did not attempt to deconvolve the MCS data collected at Site 504B because of lack of knowledge of the source signature. The signature shown in Figure 11 is only an approximation to the true signature. We did not use the seafloor reflection as an estimate of the source signature because inspection of the synthetic seismograms calculated with source LDGO (Figure 12) shows that the seafloor reflection phase overlaps the reflection event generated at the sedimentary unit 1/unit 2 boundary. This event is also evident in the observed data (Figures 7, 8). The low amplitude of the 5.2 s event ensures that mis-identification of the source pulse would prevent the accurate deconvolution required to image this event.

The side-scattered noise evident in the MCS data and the relative shallowness of the extrusives/sheeted-dike boundary at Site 504B clearly hinder the detectability of a reflection event from this horizon. However, it is also possible that the geological structure of the shallow crust at Site 504B differs from the crustal structure in those areas where high-amplitude shallow reflection events have been identified (Table 1). The geological structures of the sites listed in Table 1 are

unknown. In the MCS data collected on the Juan de Fuca Ridge (Rohr et al., 1988), the reflection event from the shallow crust is of sufficent amplitude to be readily identifiable on the individual traces of CMP gathers (K. M. M. Rohr, pers. comm.). While additional processing of the MCS data collected at Site 504B might result in the imaging of a shallow reflection event, the amplitude of such an event is unlikely to be comparable to the high-amplitude event mapped on the Juan de Fuca Ridge. The effective impedance contrast across the geological structure generating this high-amplitude event must be much greater than the impedance contrast across the volcanics/dike boundary at Site 504B. This does not rule out the possibility that the event described by Rohr et al. (1988) was generated at a similar lithological transition. Ophiolite studies show that the depth and thickness of the volcanics/dike boundary varies varies by hundreds of meters over length scales as short as kilometers (Casey et al., 1981). If the thickness of the volcanics/dike boundary at Site 504B was less than that observed, the effective impedance would be significantly enhanced (Conclusion). Clearly it would be rewarding to drill to the geological boundary generating such shallow reflection events. Mapping the depth to this structure might help constrain models of lithosphere accretion and evolution.

REFERENCES

Anderson, R. N., J. Honnorez, K. Becker, A. C. Adamson, J. C. Alt, R. Emmermann P. D. Kempton, H. Kinoshita, C. Laverne, M. Mottl, and R. L. Newmark, DSDP Site 504B, the first reference section over 1 km through layer 2 of the oceanic crust, Nature, 300, 589-594, 1982.

Anderson, R. N., H. O'Malley, and R. L. Newmark, Use of geophysical logs for quantitative determination of fracturing, alteration, and lithostratigraphy in the upper oceanic crust, Deep Sea Drilling Project, Hole 504B and 556, Init. Rep. Deep Sea Drill. Proj., 83, 443-478, 1985a.

Anderson, R. N., M. D. Zoback, S. H. Hickman, and R. L. Newmark, Permeability versus depth in the upper oceanic crust: in situ measurements in Deep Sea Drilling Project Hole 504B, eastern equatorial Pacific, Init. Rep. Deep Sea Drill. Proj., 83, 429-442, 1985b.

Becker, K., Large-scale electrical resistivity and bulk porosity of the oceanic crust, Deep Sea Drilling Project Hole 504B, Costa Rica Rift, Init. Rep. Deep Sea Drill. Proj., 83, 419-427, 1985

Becker, K., M. G. Langseth, R. P. Von Herzen, R. N. Anderson, and M. A. Hobart, Deep crustal geothermal measurements, Hole 504B, Deep Sea Drilling Project Legs, 69, 70, 83, and 92, Initial Rep. Deep Sea Drill. Proj., 83, 405-418, 1985.

Berryman, L. H., P. L. Goupillaud, and K. H. Waters, Reflections from multiple transition layers, part 1, theoretical results, Geophysics, 23, 223-243, 1958.

Bratt, S. R., and G. M. Purdy, Structure and variability of oceanic crust on the flanks of the east Pacific Rise between 11° and 13°N, J. Geophys. Res., 89, 6111-6125, 1984.

Brandsaeter, H., A. Farestveit, and B. Ursin, A new high-resolution or deep penetration airgun array, Geophysics, 44, 865-879, 1979.

Casey, J. F., J. F. Dewey, P. J. Fox, J. A. Karson, and E. Rosencrantz, Heterogeneous nature of oceanic crust and upper mantle: a perspective from the Bay of Islands ophiolite complex, in The Sea, vol. 7, edited by C. Emiliani, pp. 305-338, John Wiley, New York, 1981.

Christensen, N. I., and M. H. Salisbury, Seismic velocities, densities, and porosities of Layer 2B and Layer 2C basalts from Hole 504B, Initial Rep. Deep Sea Drill. Proj., 83, 367-370, 1985.

Coleman, R. G., Ophiolites, ancient oceanic crust?, Springer-Verlag, Berlin, 229 pp., 1977.

CRRUST, Geothermal regimes of the Costa Rica Rift, east Pacific, investigated by drilling, DSDP-IPOD Legs 68,69, and 70, Geol. Soc. Am. Bull., 93, 862-875, 1982.

Detrick, R. S., P. Buhl, E. Vera, J. Mutter, J. Orcutt, J. Madsen, and T. Brocher, Multi-channel seismic imaging of a crustal magma chamber along the East Pacific Rise, Nature, 326, 35-41, 1987.

Fuchs, K. M., and G. Muller, Computation of synthetic seismograms with the reflectivity method and comparison with observations, Geophys. J. R. Astron. Soc., 23, 417-433, 1971.

Grow, J. A., and R. G. Markl, IPOD-USGS multichannel seismic reflection profile from Cape Hatteras to the Mid-Atlantic Ridge, Geology, 5, 625-630, 1977.

Hale, L. D., C. J. Morton, and N. H. Sleep, Reinterpretation of seismic reflection data over the East Pacific Rise, Jour. Geophys. Res., 87, 7707-7717, 1982.

Hamilton, E. L., Compressional-wave attenuation in marine sediments, Geophysics, 37, 620-646, 1972.

Hamilton, E. L., Sound attenuation as a function of depth in the seafloor, J. Acoust. Soc. Am., 59, 528-535, 1976.

Hamilton, E. L., Sound velocity-density relations in sea-floor sediments and rocks, J. Acoust. Soc. Am., 63, 366-377, 1978.

Hashin, Z. and S. Shtrickman, A variational approach to the theory of the elastic behaviour of multiphase materials, J. Mech. Phys. Solids, 11, 127-140, 1965.

Herron, T. J., W. J. Ludwig, P. L. Stoffa, T. K. Kan, and P. Buhl, Structure of the East Pacific Rise crest from multichannel seismic reflection data, J. Geopys. Res., 83, 798-804, 1978.

Hey, R. N., G. L. Johnson, and A. Lowrie, Recent plate motions in the Galapagos area, Geol. Soc. Am. Bull. 88, 1385-1403, 1977.

Hill, R., A self-consistent mechanic of composite materials, J. Mech. Phys. Solids, 13, 213-222, 1965.

Hobart, M. A., M. G. Langseth, and R. N. Anderson, A geothermal and geophysical survey on the south flank of the Costa Rica Rift: Sites 504 and 505, Initial Rep. Deep Sea Drill. Proj., 83, 517-528, 1985.

Houtz, R., and J. Ewing, Upper crustal structure as a function of plate age, J. Geophys. Res, 81, 2490-2498, 1976.

Kennett, B. L. N., The effect of attenuation on seismograms, Bull. Seis. Soc. Am., 65, 1643-1651, 1975.

Klitgord, K. D., S. P. Huestis, J. D. Mudie, and R. L. Parker, An analysis of near-bottom magnetic anomalies: seafloor spreading and the magnetized layer, Geophys. J. Roy. Astr. Soc., 43, 387-424, 1975.

Langseth, M. G., J. R. Cann, J. H. Natland, and M. Hobart, Geothermal phenomena at the Costa Rica Rift: Background and objectives for drilling at Deep Sea Drilling Project Sites 501, 504 and 505, Initial Rep. Deep Sea Drill. Proj., 69, 5-29, 1983.

Langseth, M. G., M. J. Mottl, M. A. Hobart, and A. Fischer, The distribution of geothermal and geochemical gradients near Site 501/504: implications for hydrothermal circulation in the oceanic crust, Proc. ODP, Init. Repts. (Pt. A), 111, 23-32, 1988.

Larner, K., R. Chambers, M. Yang, W. Lynn, and W. Wai, Coherent noise in marine seismic data, Geophysics, 48, 854-886, 1983.

Little, S. A., and R. A. Stephen, Costa Rica Rift borehole seismic experiment, Deep Sea Drilling Project Hole 504B, Leg 92, Initial Rep. Deep Sea Drill. Proj., 83, 517-528, 1985.

Lewis, B. T. R., The processes of formation of ocean crust, Science, 220, 151-157, 1983.

Mallick, S., and L. N. Frazer, Practical aspects of reflectivity modeling, Geophysics, 52, 1355-1364, 1987.

McCarthy, J, J. C. Mutter, J. L. Morton, N. H. Sleep, and G. T. Thompson, Relic magma chamber structures preserved within the Mesozoic North Atlantic crust?, Geol. Soc. Am. Bull., 100, 1423-1436, 1988.

Moos, D., Goldberg, D., Hobart, M. A., and R. N. Anderson, Elastic wave velocities in Layer 2A from full waveform sonic logs at Hole 504B, Initial Rep. Deep Sea Drill. Proj., 92, 563-570, 1986.

Musgrove, L. A., and J. A. Austin, Intrabasement structure in the southern Angola Basin, Geology, 11, 169-173, 1983.

Mutter, J. C., and North Atlantic Transect (NAT) Group, Multichannel seismic images of the oceanic crust's internal structure: Evidence for a magma chamber beneath the Mesozoic Mid-Atlantic Ridge, Geology, 13, 629-632,

Newmark, R. L., R. N. Anderson, D. Moos, and M. D. Zoback, Sonic and ultrasonic logging of Hole 504B and its implications for the structure, porosity and stress regime of the upper 1 km of the oceanic crust, Init. Rep. Deep Sea Drill. Proj., 83, 479-510, 1985.

Purdy, G. M., and J. I. Ewing, Seismic structure of oceanic crust, in The Geology of North America: The Western Atlantic Region, edited by B. E. Tulcholke, and P. R. Vogt, DNAG Ser., vol. 1, Geological Society of America, Boulder, Colo., 313-331, 1986.

Rohr, K. M. M., Milkereit, B, C. J. Yorath, Asymmetric structure across the Juan de Fuca Ridge, Geology, 16, 533-537, 1988.

Searle, R. C., Gloria survey over Costa Rica Rift: Sites 501, 504 and 505, Initial Rep. Deep Sea Drill. Proj., 69, 217-222, 1983.

Salisbury, M. H, N. I. Christensen, K. Becker, and D. Moos, The velocity structure of layer 2 at Deep Sea Drilling Project site 504 from logging and laboratory experiments, Initial Rep. Deep Sea Drill. Proj., 83, 529-539, 1985.

Shipboard Scientific Party, Site 504: Costa Rica Rift, Proc. Ocean Drill. Proj., Init. Repts. (Pt. A), 111, 35-251, 1988.

Stephen, R. A., Synthetic seismograms for the case of the receiver within the reflectivity zone, Geophys. J. Roy. Astr. Soc., 51, 169-181, 1977.

Stephen, R. A., A comparison of finite difference and reflectivity seismograms for marine models, Geophys. J. Roy. Astr. Soc., 72, 39-58, 1983.

Stephen, R. A., Seismic anisotropy in the upper oceanic crust, J. Geophys. Res., 90, 11383-11396, 1985.

Stoffa, P. L., P. Buhl, T. J. Herron, T. K. Kan, and W. J. Ludwig, Mantle reflections beneath the crestal zones of the East Pacific Rise from multichannel reflection data, Mar. Geol., 35, 83-97, 1980.

Watt, J. Peter, G. F. Davies, and R. J. O'Connell, The elastic properties of composite materials, Rev. Geophys. 14, 541-563, 1976.

Wilkens, R. H., and M. G. Langseth, Physical properties of sediments of the Costa Rica Rift, Deep Sea Drilling Project Sites 504 and 505, Initial Rep. Deep Sea Drill. Proj., 69, 659-674, 1983.

FIGURE CAPTIONS

Figure 1 Location of DSDP Site 504B. MCS track lines for R.V. CONRAD cruise RC2606 are shown. (b) Bathymetry in the immediate vicinity of the drillsite (from Langseth et al., 1988). The infilled circles indicate the locations of DSDP and ODP drill sites. Contour interval is 10 m.

Figure 2. (a) Schematic representation of the drilled sedimentary and igneous sequence at Hole 504B. From top to bottom, o represents nannofossil ooze, ck indicates chalks, c signifies cherts, v represents extrusive volcanics, t indicates the volcanics/sheeted-dike transition, and d represents the sheeted-dike sequence. The sonic velocity profile was acquired on DSDP Leg 83 (Salisbury et al., 1985). The velocity profile on the right was derived from the bulk porosity log (Becker, 1985) as described in the text. A possible subdivision into seismic Layers 2A, 2B, and 2C is indicated. (b) The observed sonic velocity profile (OBS) for Hole 504B plotted alongside the preferred velocity profiles of Little and Stephen (1985) (dashed) and Chapter 2.

Figure 3. (a) Shot gather 2489 from MCS Line 485, acquired ~5 km from the drillsite. Ranges increase from right to left, from 0.3 km to 2.65 km. Seismograms are unfiltered. Amplitudes are multiplied by an exponential, time-varying function. The time window over which the gain function was applied ranges from 4.5 to 6.0 s; the gain at 6.0 s is 40 dB. Note the hyerbolic-shaped noise phases. These side-scattered phases are repeated at ~0.1 s intervals, implying that the side-scattered energy is multiply reflected/refracted in the sedimentary section. This type of

coherent noise is typical of all the MCS data. (b) As for (a) but an f-k filter has been applied to the shot gather. The filter was designed to attenuate arrivals with moveouts of 6 milliseconds/trace and greater. Note that portions of the side-scattered phases have been attenuated. However, the f-k filter cannot remove the energy falling along the apexes of the hyperbolas. Note also the aliased energy, arriving before the seafloor reflection, introduced by the f-k filtering.

Figure 4. (a) CMP gather 5000 from MCS Line 490, acquired ~4 km from the drillsite. Ranges increase from right to left, from 0.3 km to 2.65 km. The seismograms are unfiltered. Amplitudes are scaled using an automatic-gain-control (AGC) window of 0.25 s. A Normal Moveout (NMO) correction corresponding to a stacking velocity of 1.8 km s^{-1} has been applied to the data. Consequently, all of the phases that dip from right to left have stacking velocities less than this value. Note the horizontally-directed phase at 5.6 s. This phase has a stacking velocity of 1.8 km s^{-1}, anomalously low for a reflection event with a crustal travel time of 0.7 s. (b) As for (a) but an f-k filter has been applied to the shot gather prior to CMP gather. Note that the 5.6 s event has been attenuated, implying that this is a side-scattered phase.

Figure 5. (a) A portion of MCS Line 490, stacked at velocity of 1.5 km s^{-1}. From left to right, CMP numbers range from 4550-5100. The data are unfiltered. Amplitudes are scaled using an AGC window of 0.25 s. (b) As for (a) but an f-k filter has been applied to the shot gathers prior to CMP sorting and stacking.

Figure 6. (a) A portion of MCS Line 490, stacked at a velocity of 1.8 km s^{-1}. CMP numbers are as given in Figure 5. The data are unfiltered, and the amplitudes are scaled using an AGC window of 0.25 s. (b) As for (a) but an f-k filter has been applied to the shot gathers prior to CMP sorting and stacking.

Figure 7. CMP-stacked seismograms for MCS Line 490. CMP numbers are as given in Figure 5. Stacking velocities were determined from velocity analysis of wide-angle reflection/refraction data collected in the immediate vicinity of the drillsite. The unfiltered seismograms are scaled with an AGC window of 0.25 s duration. The seismograms to the left of the stacked profile are synthetic normal-incidence seismograms computed for the logged sonic-velocity data. Seismogram 0 was computed for the sonic-velociy data measured in both the sedimentary and igneous sections. Seismogram S was computed for the sonic-velocity data measured in the sedimentary section only. The single arrow shows the reflection event generated at the volcanics/dike boundary, while the double arrow indicates the primary sediment-column multiple. For seismogram S, the phases between the basement reflection phase and the primary multiple represent source reverberation and the peg-leg multiple generated within the sedimentary section. The source pulse used to compute the seismogram is that for the airgun array used to acquire the CMP data. The synthetic seismograms are scaled in an identical manner to the observed data, and have been filtered 5-60 Hz.

Figure 8. CMP-stacked seismograms for MCS Line 485. From right to left, CMP numbers range from 7400-8000. Data and synthetics are stacked and scaled as described in Figure 7.

Figure 9. Possible porosity-velocity relationships for Site 504B calibrated to the physical properties of samples recovered at Hole 504B. Curves HS^+ and HS^- represent the the Hashin and Shtrikman upper and lower bounds on velocity-porosity space, curve SCS is the relationship predicted by the self-consistent scheme, and curve EMP is the empirical relationship between laboratory measured values of velocity and porosity. These curves were calculated using the formulae presented in Watt et al. (1976).

Figure 10. (a) Velocity-depth profiles for Hole 504B. Model OBS is the observed sonic-velocity data, averaged in 10 m bins. The remaining models correspond to the velocity-porosity relationships illustrated in Figure 9. With the exception of Model OBS, all of the models are shown for three different values of Archies Law exponent. (b) Velocity-two-way-time profiles corresponding to (a).

Figure 11. Source signatures and spectra of the two source pulses used to calculate synthetic seismograms. While the spectra are similar, the primary-to-bubble pulse ratio of the tuned array is superior to the LDGO source.

Figure 12. Normal-incidence reflectivity synthetic seismograms, computed with source LDGO, for the sonic-velociy data measured in both the sedimentary and igneous sections (OBS), the sedimentary section only, and the igneous section only. Amplitudes have been multiplied by an exponential, time-varying function. The time window over which the gain function was applied ranges from 5 to 5.5 s; the gain at 5.5 s is 20 dB.

Figure 13. As for Figure 6, but the normal-incidence synthetic seismograms were computed with the tuned source function. This source has significantly greater resolution than source LDGO.

Figure 14. Normal-incidence synthetic seismograms for the velocity-depth models shown in Figure 10. The seismograms calculated for the porosity-derived velocity profiles are similar, indicating that they are dominated by the source reverberation and by multiply reflected energy trapped within the sedimentary layer.

Figure 15. (a) Reflectivity synthetic seismograms calculated for velocity-depth model OBS. Amplitudes are multiplied by a constant scaling factor, and are plotted with a reduction velocity of 4.5 km s^{-1}. The linear phase preceding the seafloor reflection represents numerical noise. (b) Seismograms resulting from stacking seismograms in the ranges window 0.3-2.7 km compared to the normal-incidence seismograms. Amplitudes have been multiplied by an exponential, time-varying function. The time window over which the gain function was applied ranges from 5 to 5.5 s; the gain at 5.5 s is 30 dB. The amplitudes of

the two normal-incidence seismograms are comparable, as are those of the CMP stacked seismograms. The stacking velocities used to calculate the seismogram labeled "CMP Stack" were calculated from the input velocity-depth model. A constant stacking velocity of 1.5 km s^{-1} was used to calculate the seismogram on the far right in order to accentuate sediment-column multiples.

Figure 16. (a) Reflectivity synthetic seismograms calculated for velocity-depth model EMP20, and plotted as described in the caption to Figure 9. (b) Stacked seismograms, resulting from summing seismograms in the ranges window 0.3-2.7 km, compared to the normal-incidence seismograms. Amplitudes have been scaled as described in Figure 9.

Figure 17. (a) Reflectivity synthetic seismograms calculated for velocity-depth model EMP20. Amplitudes are multiplied by a linear function of range, and are plotted with a reduction velocity of 6.0 km s^{-1}. The velocity gradient corresponding to the volcanics/dike transition generates high-amplitude refracted arrivals at horizontal ranges of 6-7 km. (b) Power versus range for the seismograms shown in (a). The time window over which power was computed extended from 4.8 to 5.1 s reduced time. The power peak corresponds to the amplitude focusing observed at 6-7 km range.

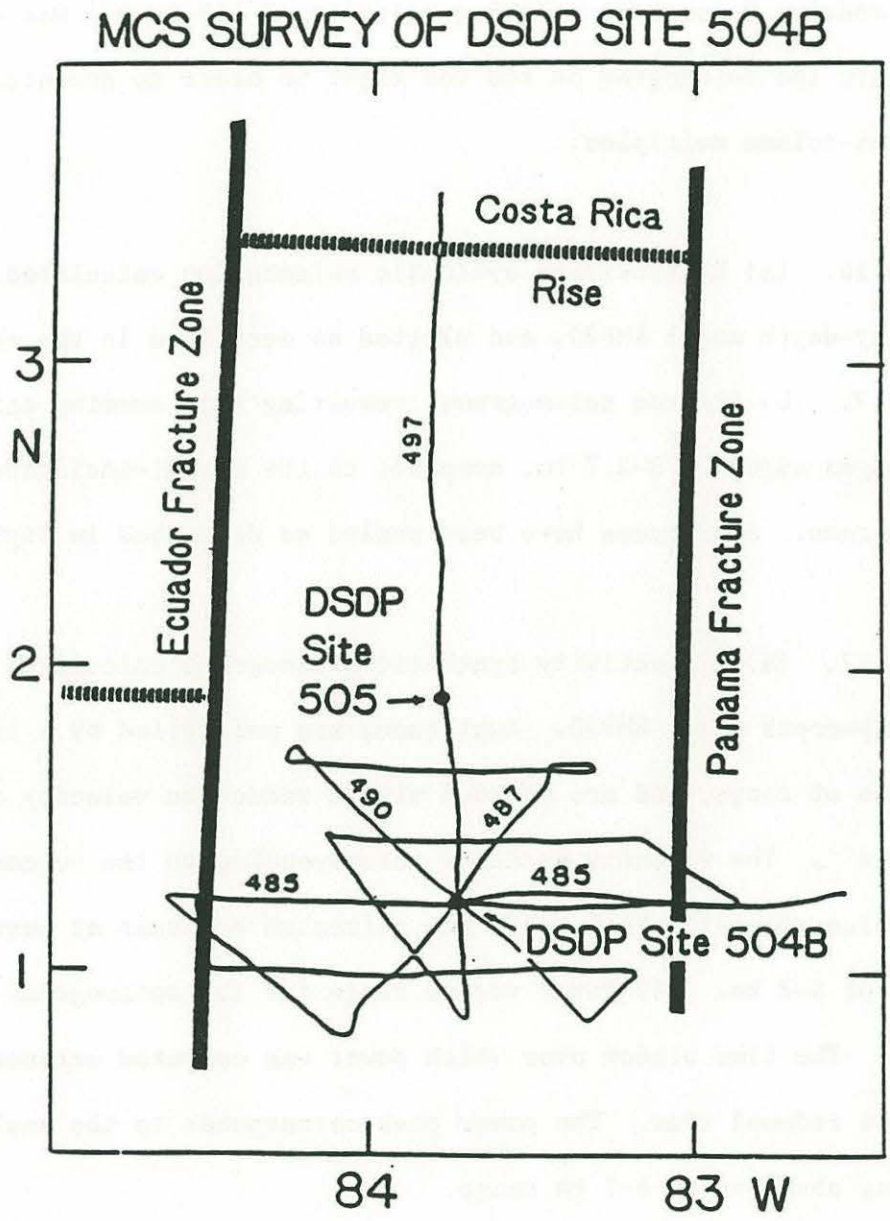
MCS SURVEY OF DSDP SITE 504B
Costa Rica
Rise
Ecuador Fracture Zone
Panama Fracture Zone
497
DSDP
Site
505
490
487
485
485
DSDP Site 504B
3
2
1
N
84
83 W

Figure 1a

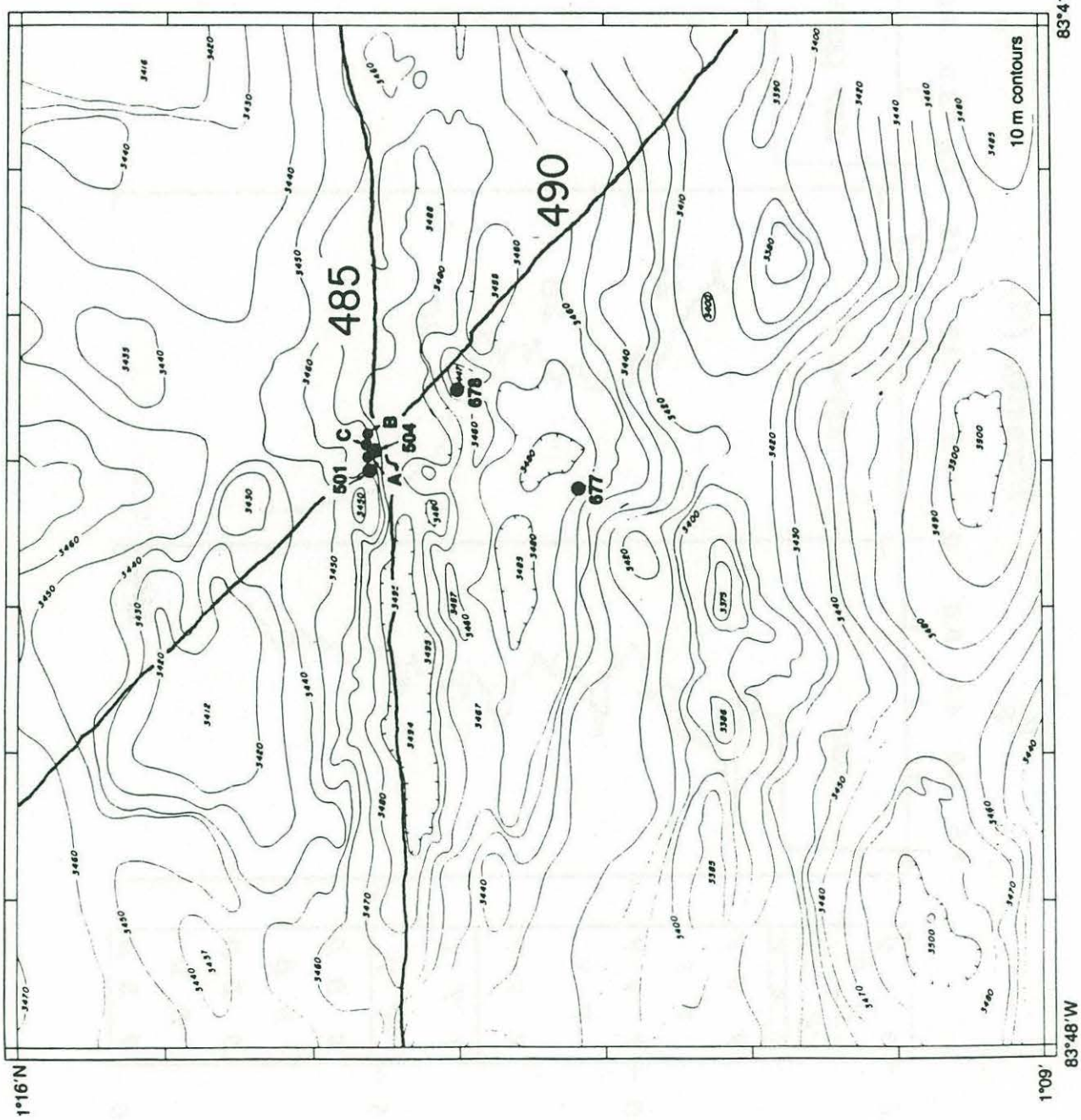

Figure 1b

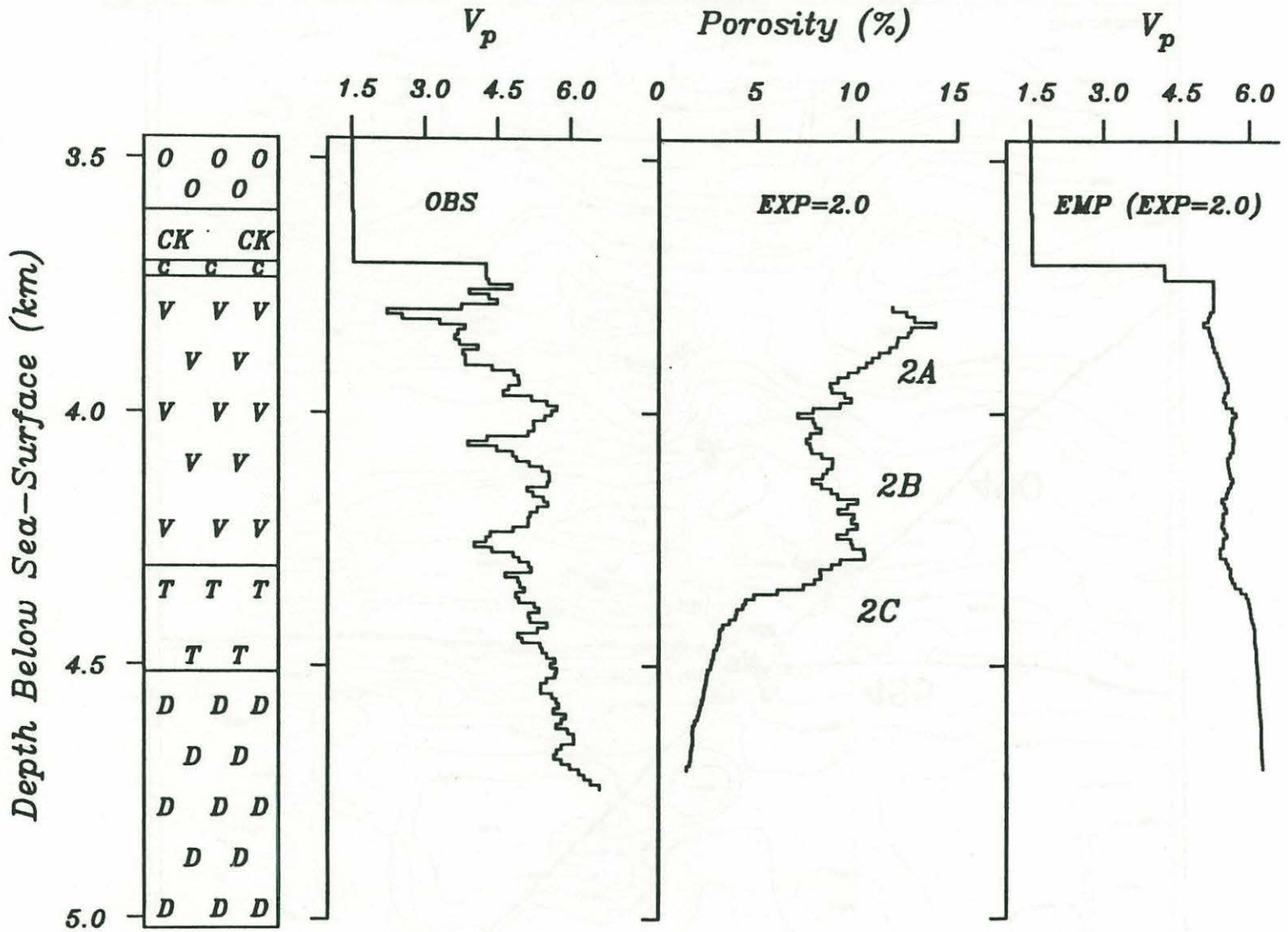
V_p
Porosity (%)
V_p
1.5 3.0 4.5 6.0
0 5 10 15
1.5 3.0 4.5 6.0
OBS
EXP=2.0
EMP (EXP=2.0)
2A
2B
2C
Depth Below Sea-Surface (km)
3.5
4.0
4.5
5.0
O
CK
C
V
T
D

Figure 2a

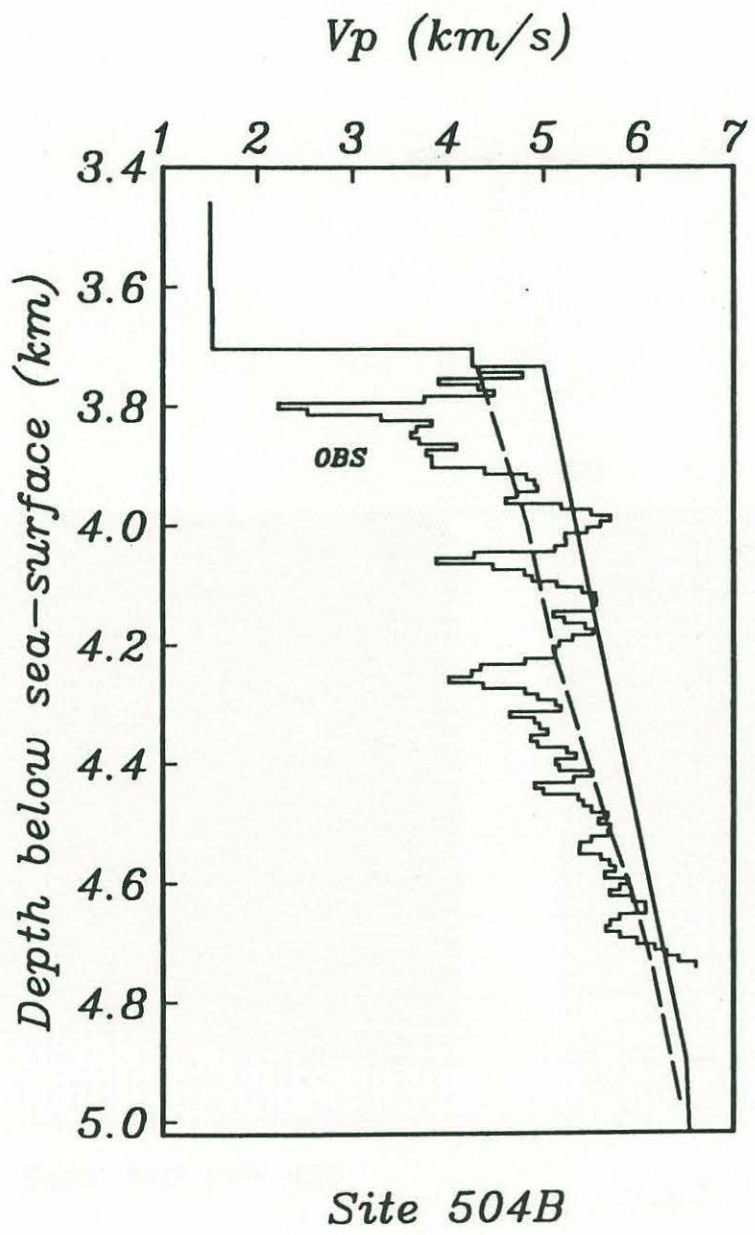
Vp (km/s)
1
2
3
4
5
6
7
3.4
3.6
3.8
4.0
4.2
4.4
4.6
4.8
5.0
Depth below sea-surface (km)
OBS
Site 504B

Figure 2b

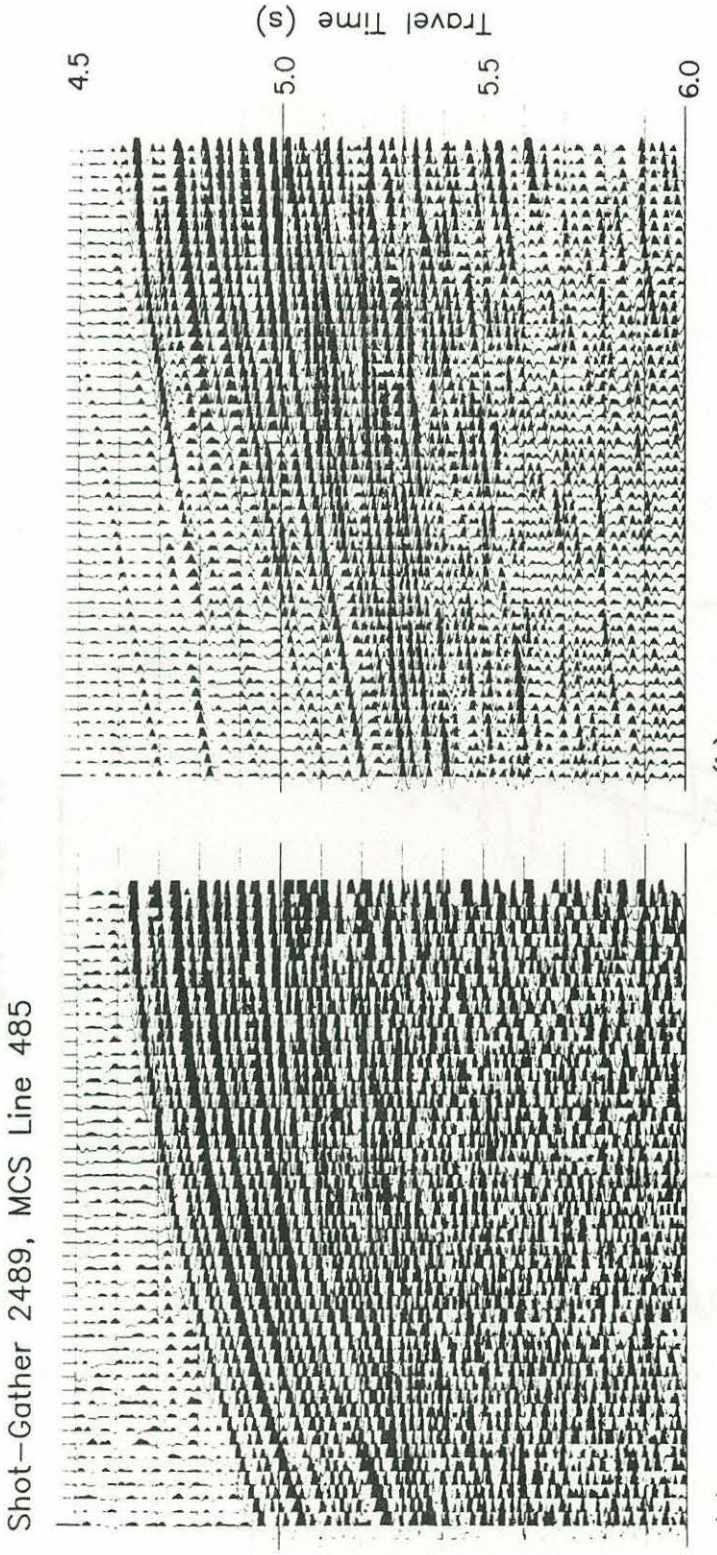

Figure 3

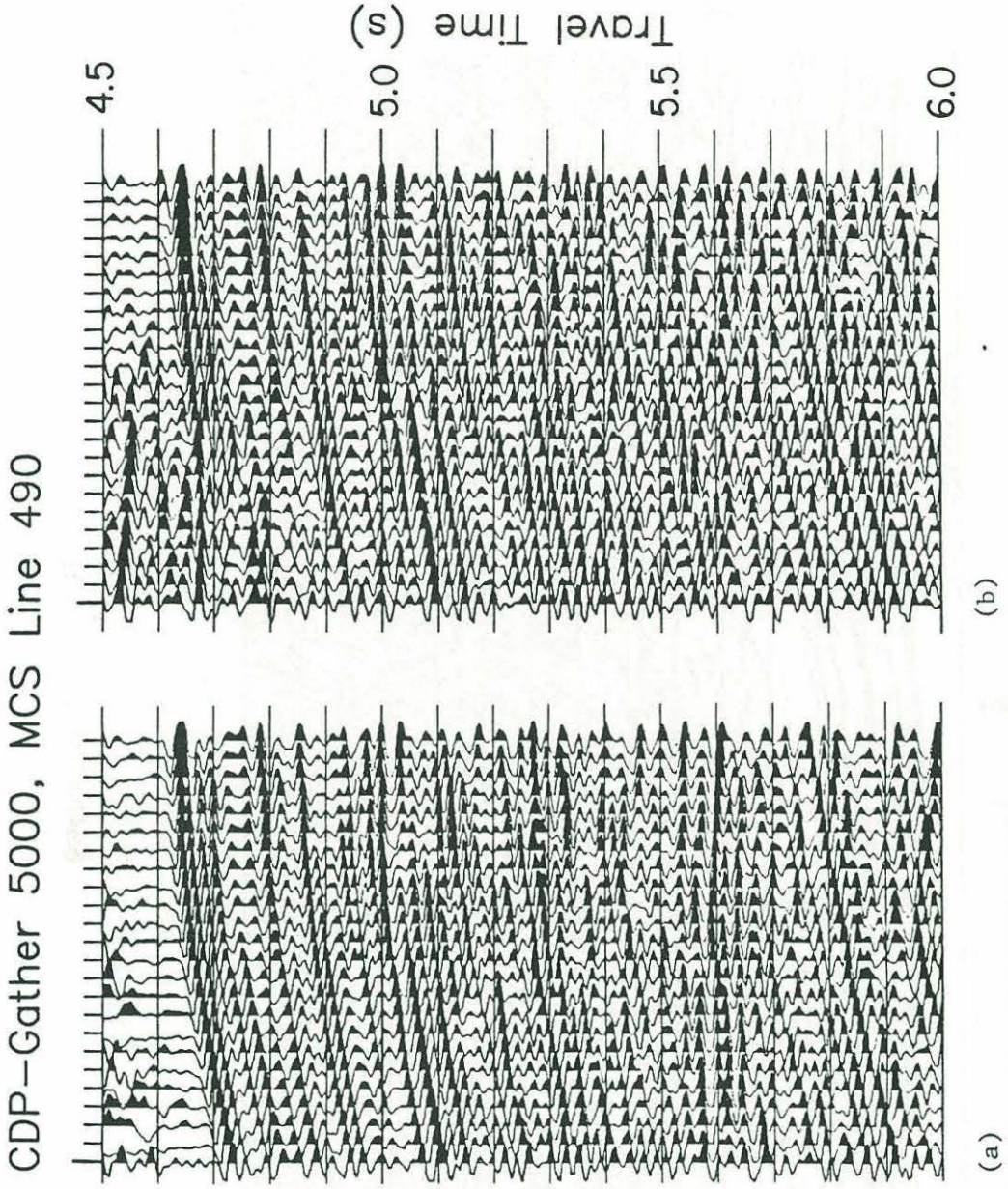

Figure 4

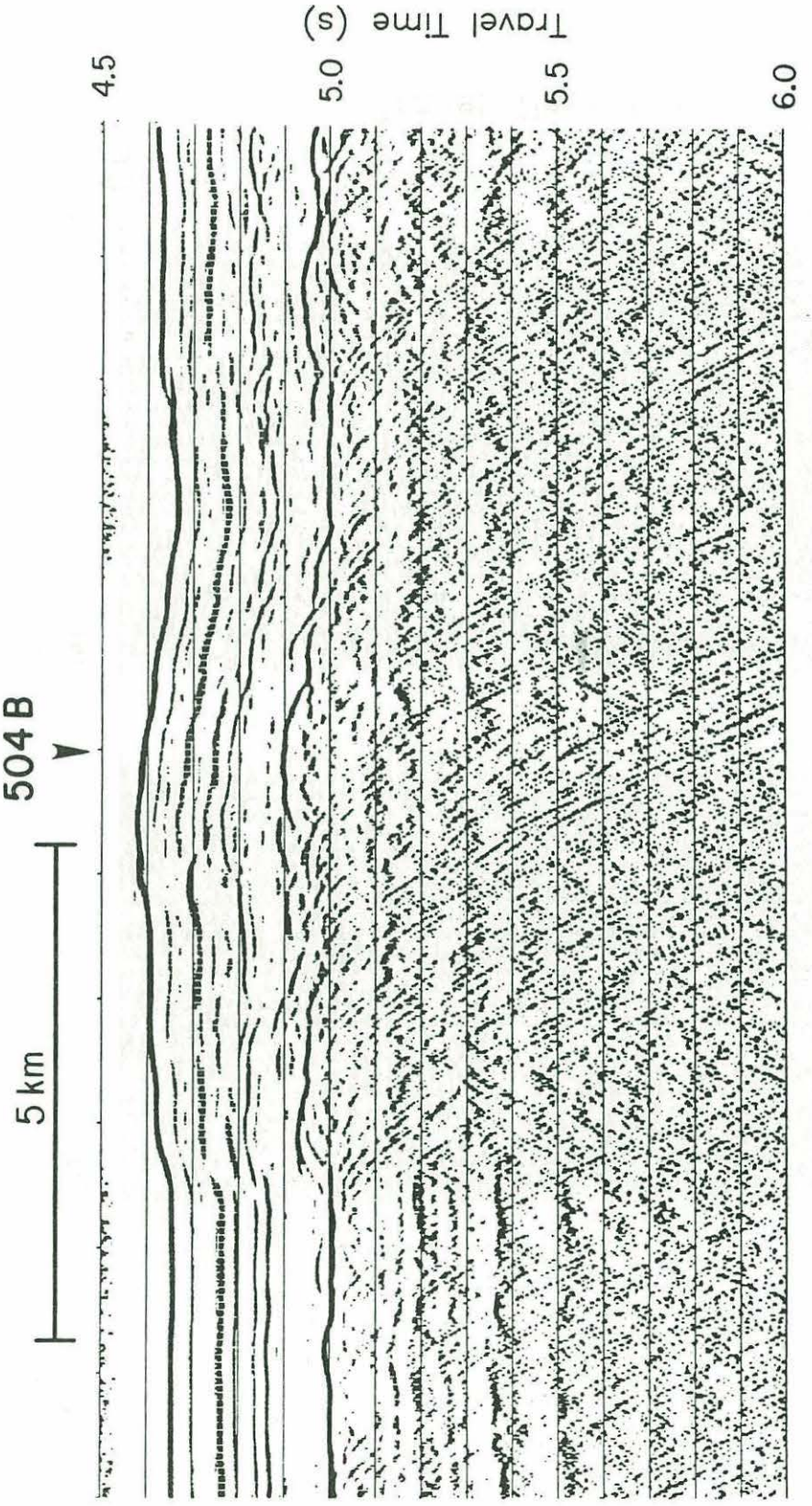

Figure 5a

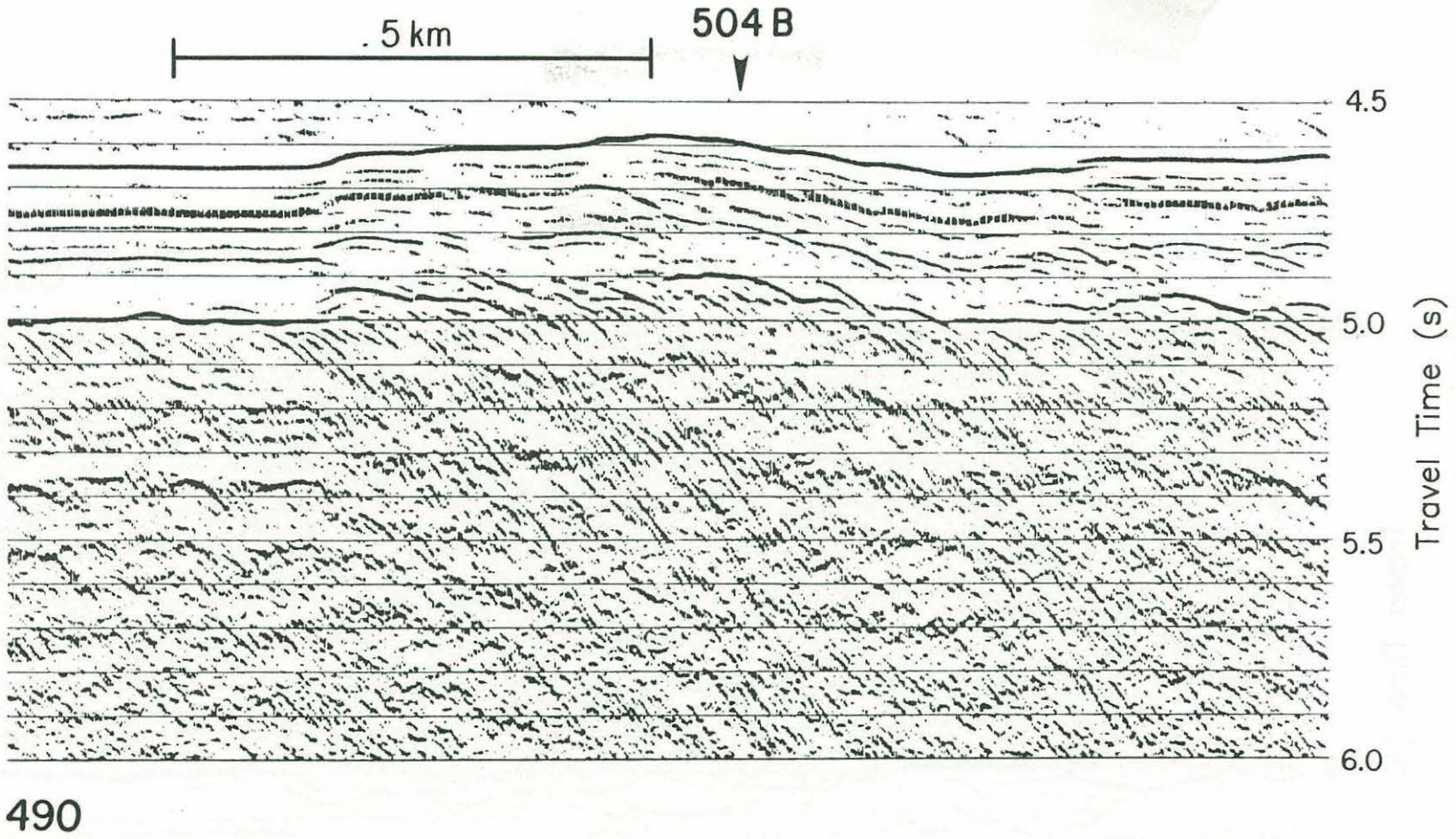

Figure 5b

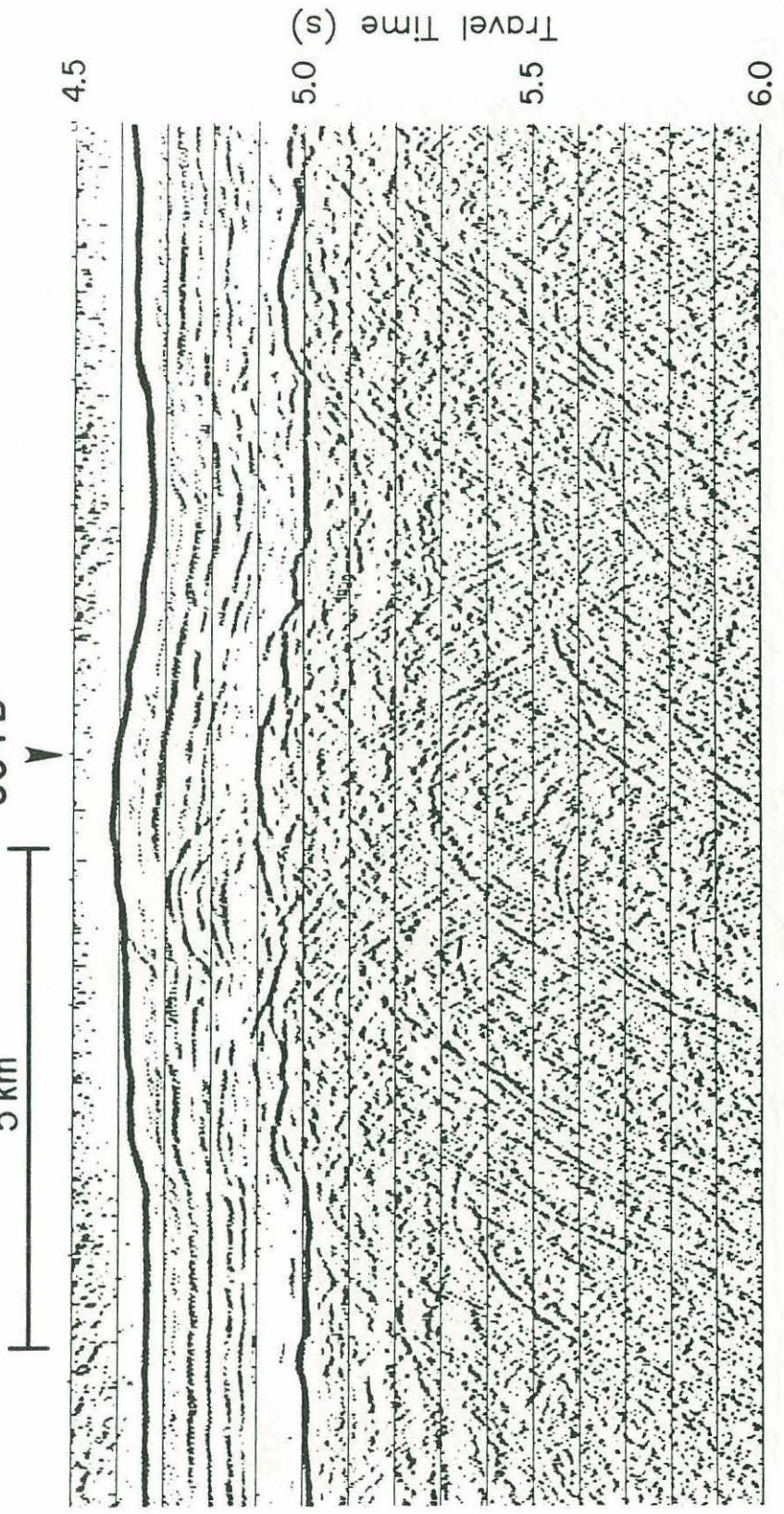

Figure 6a

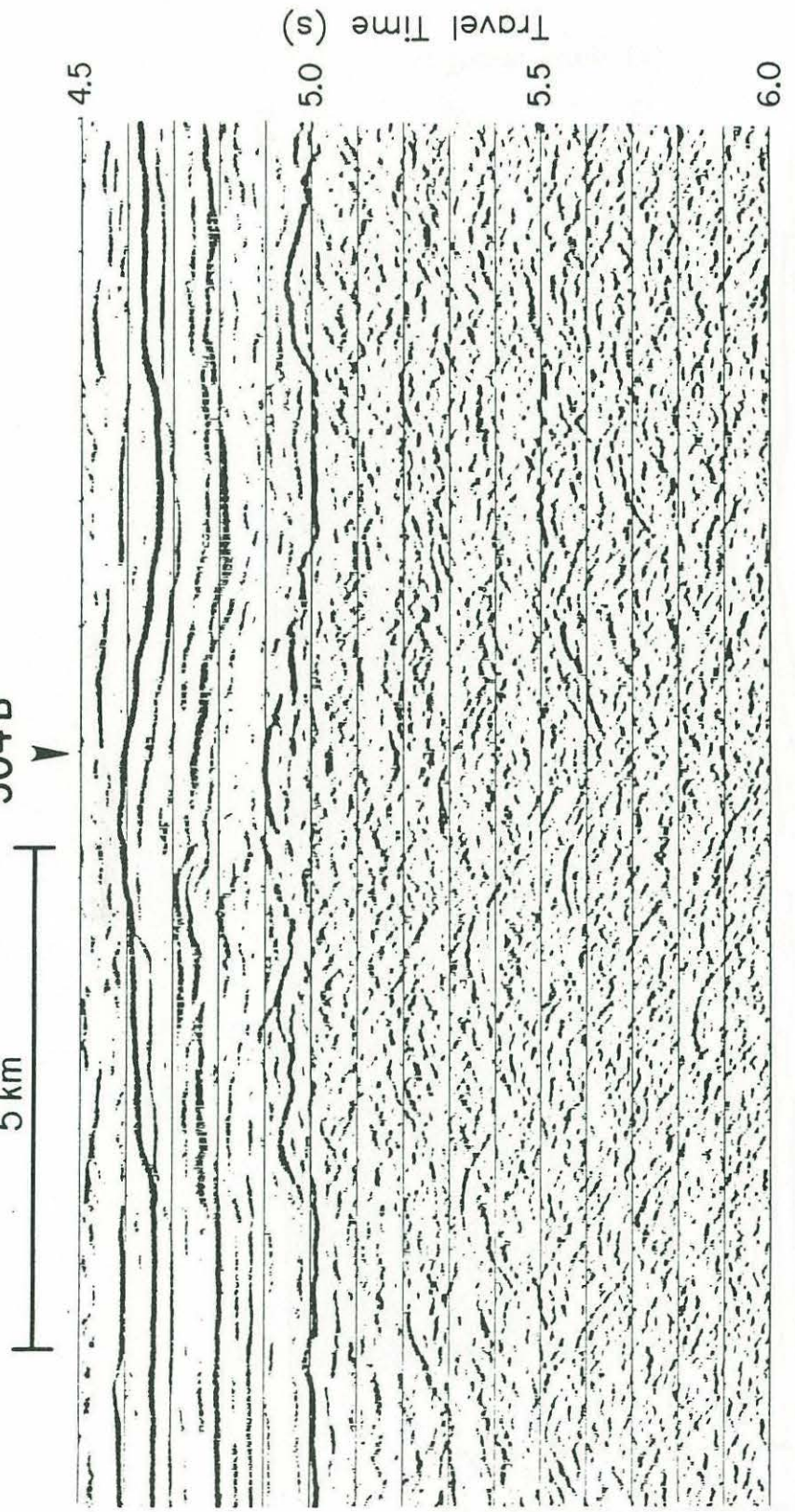

Figure 6b

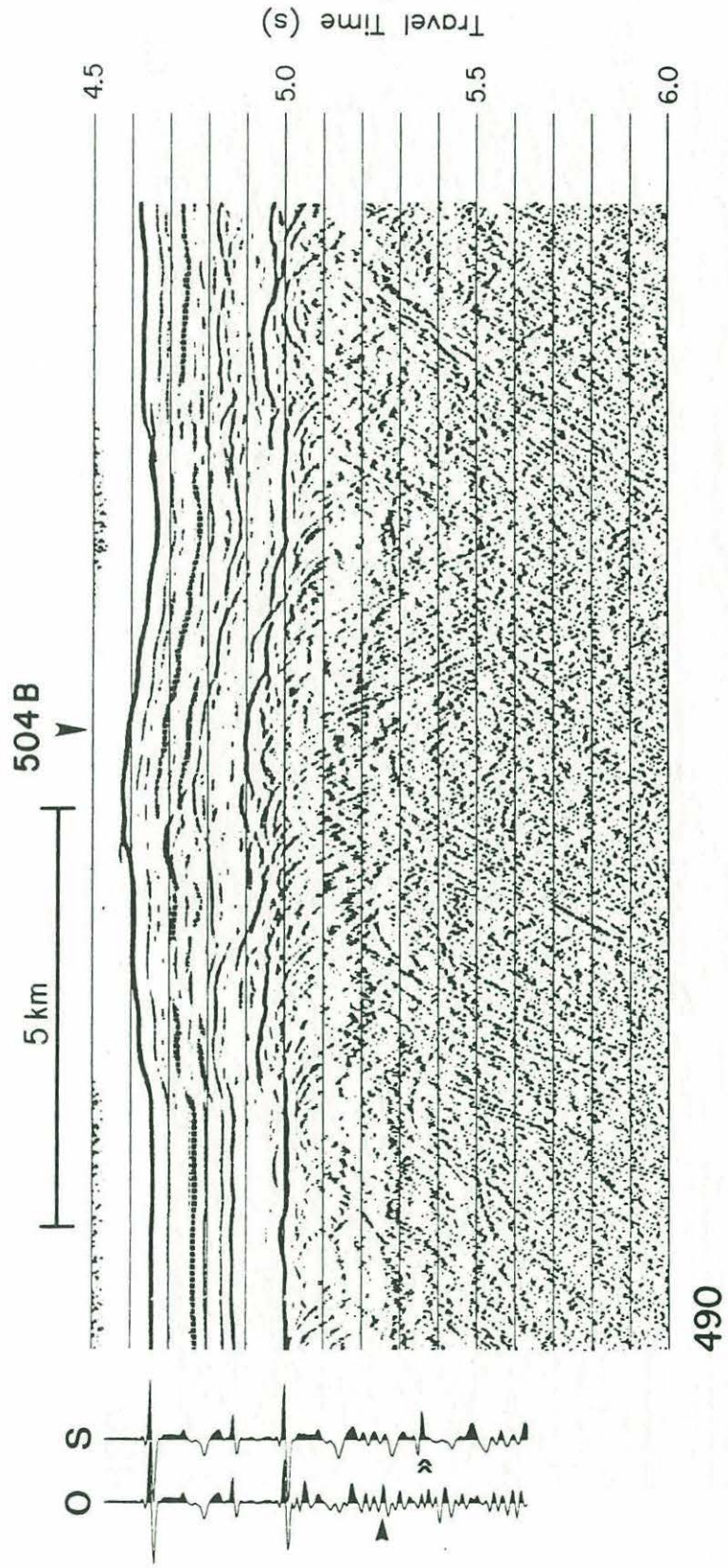

Figure 7

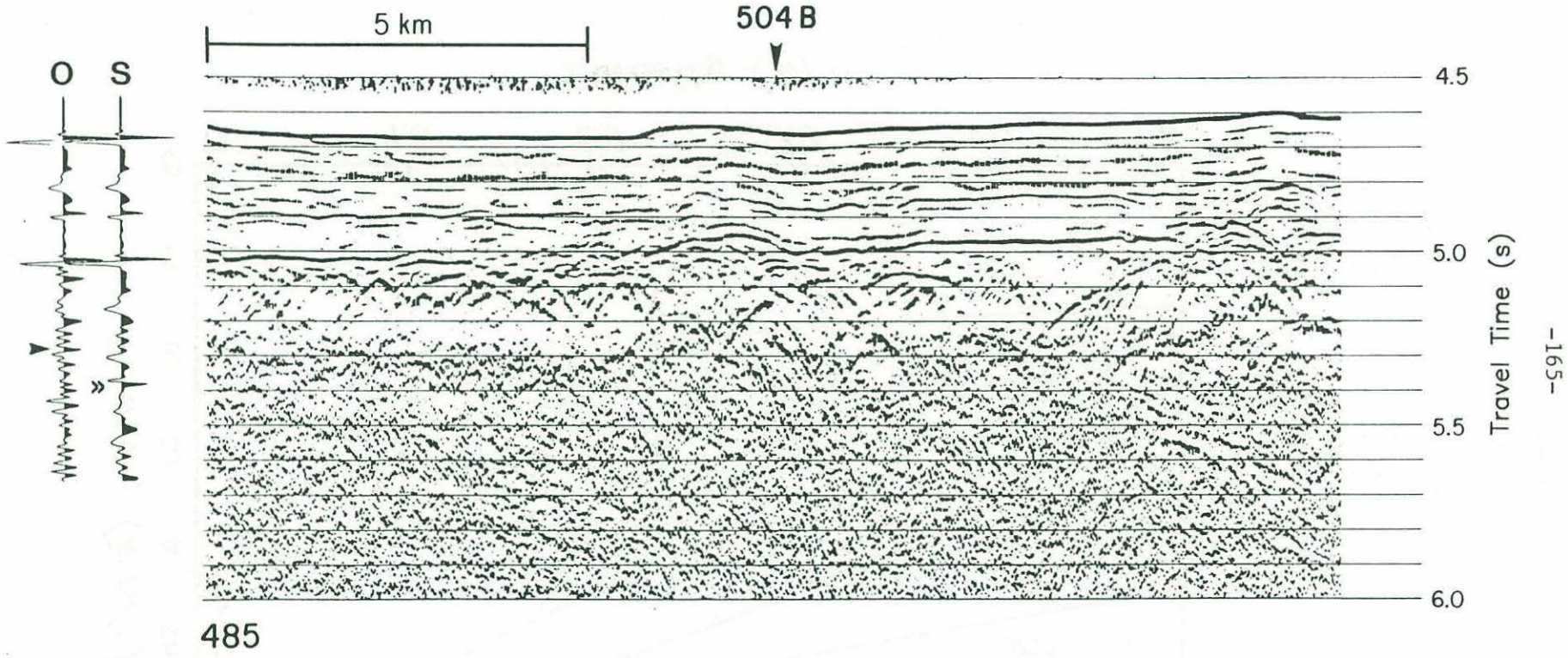

Figure 8

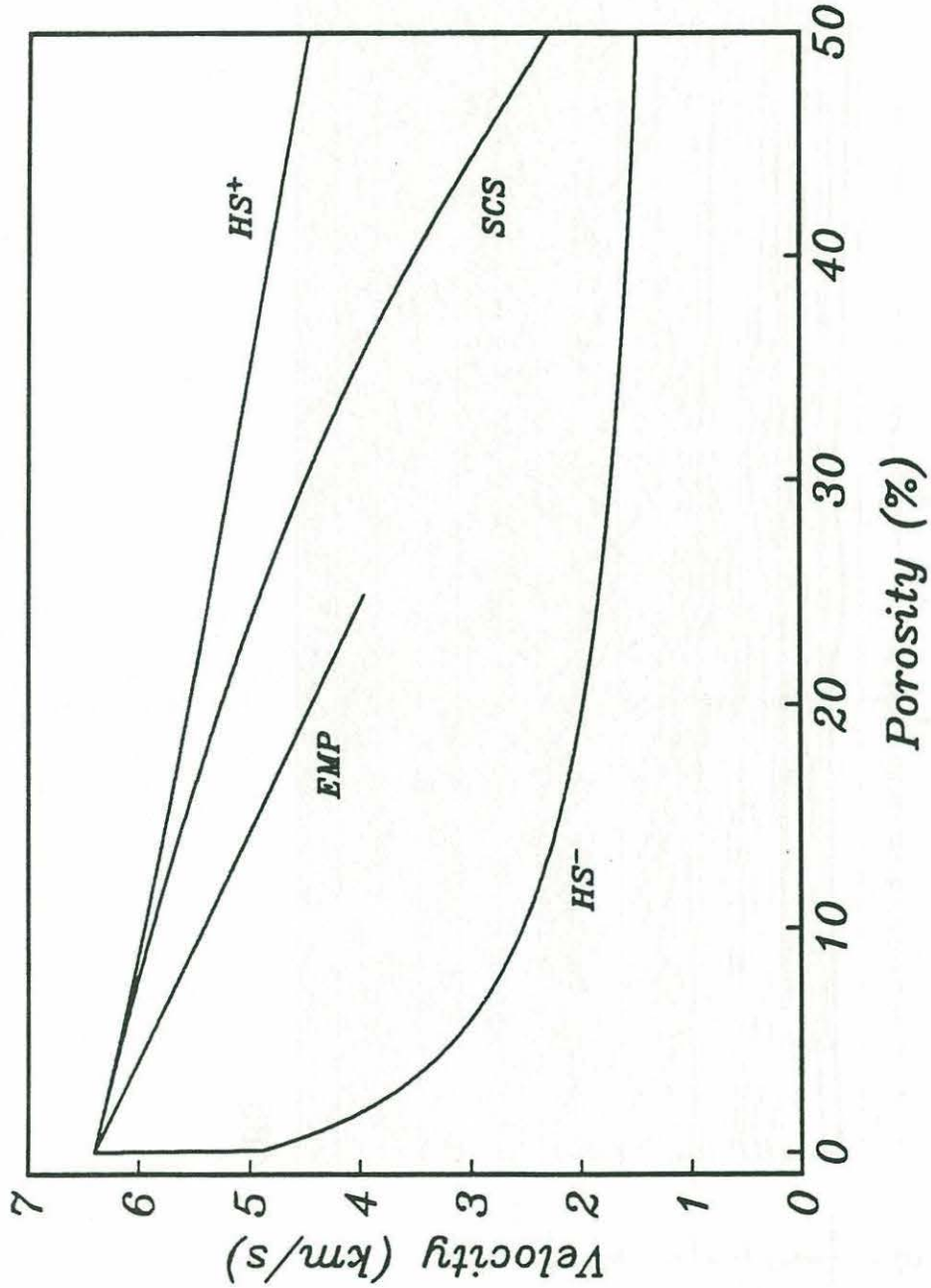

Figure 9

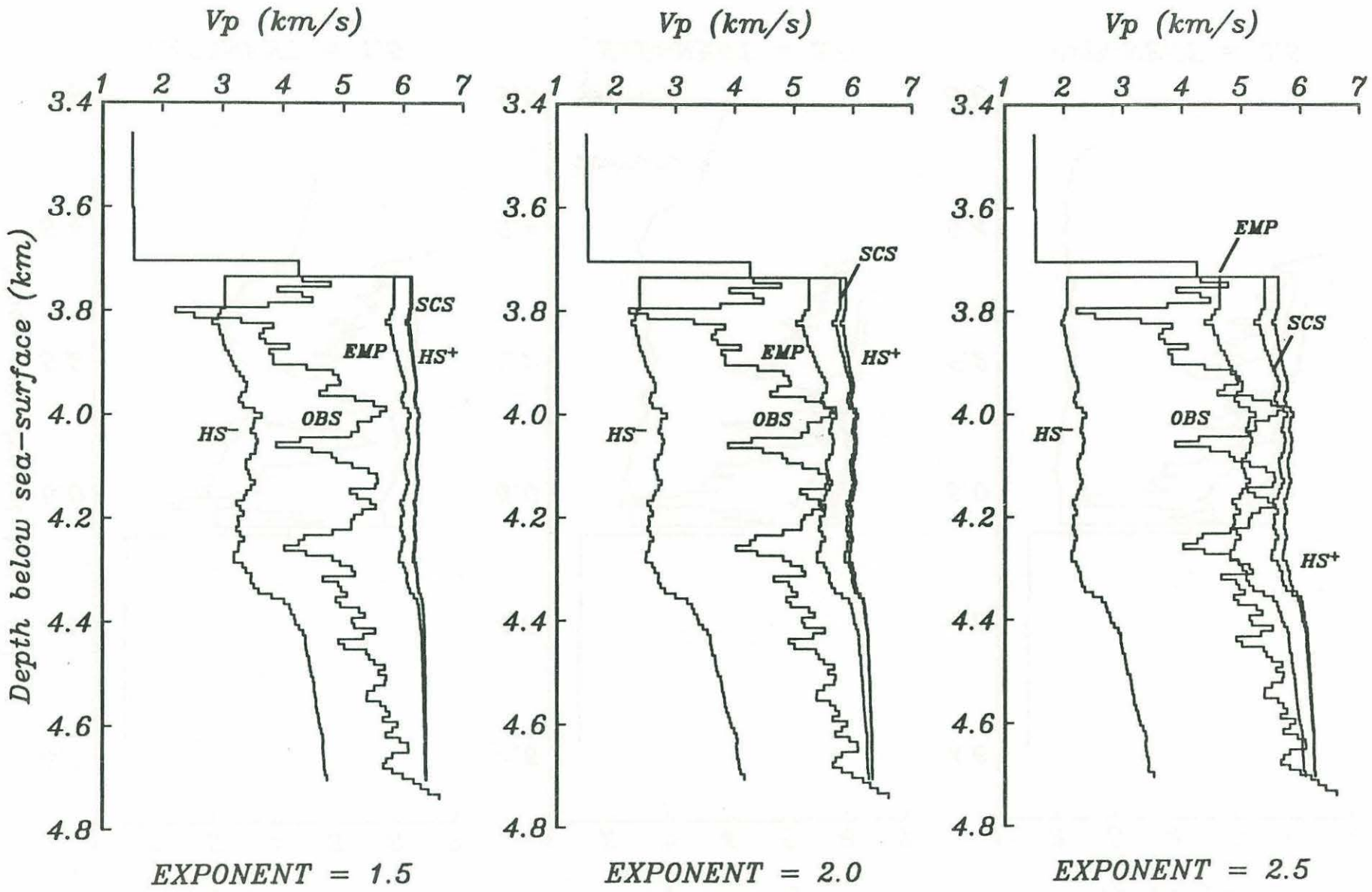
Vp (km/s)
1 2 3 4 5 6 7
3.4
3.6
3.8
4.0
4.2
4.4
4.6
4.8
Depth below sea-surface (km)
SCS
EMP
HS+
OBS
HS−
EXPONENT = 1.5
EXPONENT = 2.0
EXPONENT = 2.5

Figure 10a

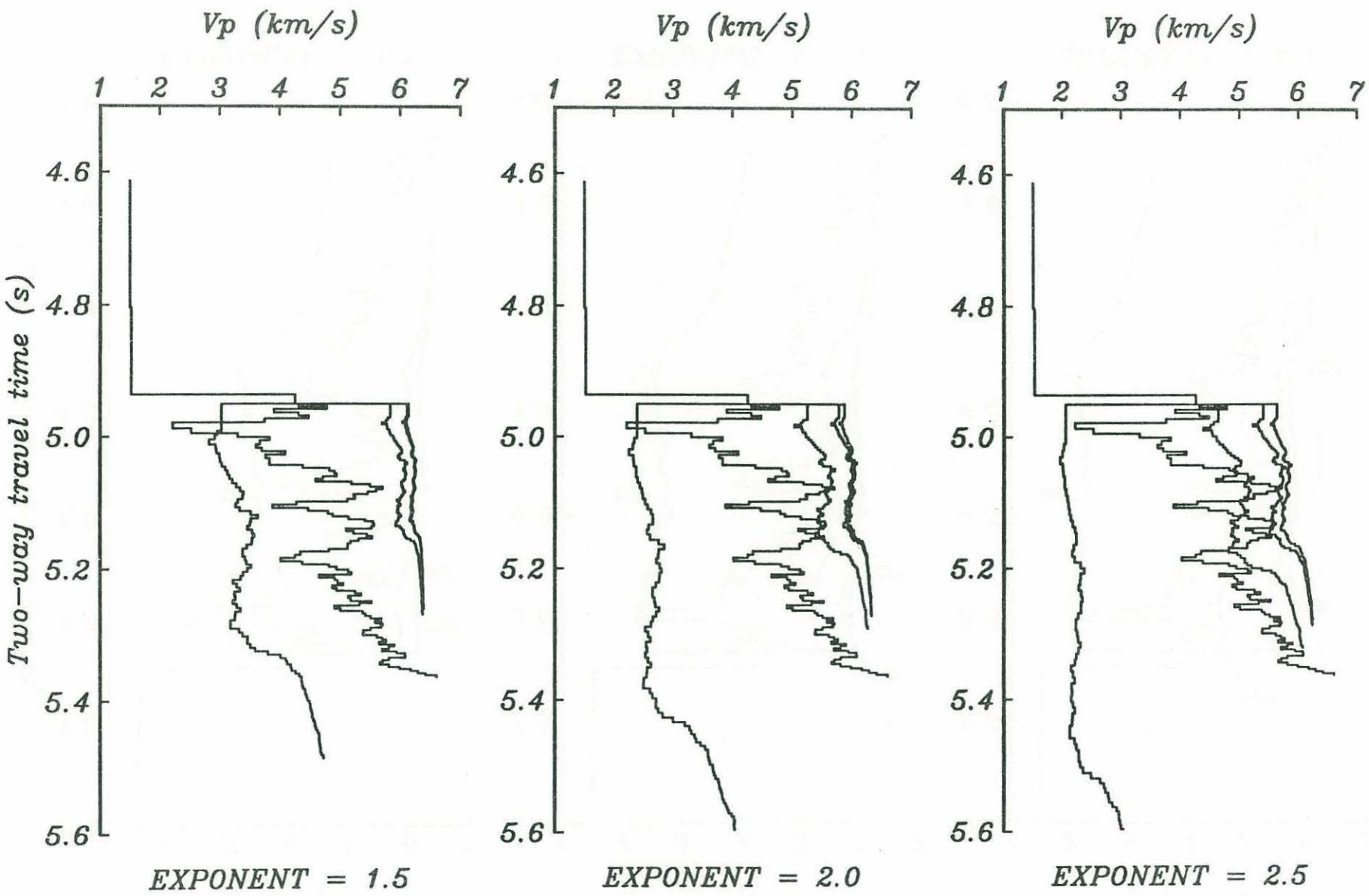
Vp (km/s)
1 2 3 4 5 6 7
Two-way travel time (s)
4.6
4.8
5.0
5.2
5.4
5.6
EXPONENT = 1.5
EXPONENT = 2.0
EXPONENT = 2.5

Figure 10b

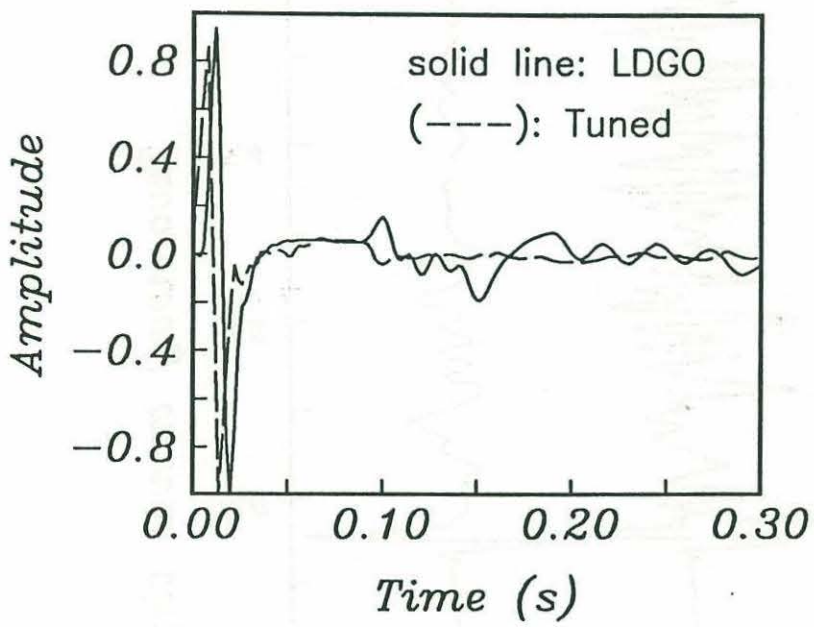
solid line: LDGO
(---): Tuned
Amplitude
0.8
0.4
0.0
−0.4
−0.8
0.00
0.10
0.20
0.30
Time (s)

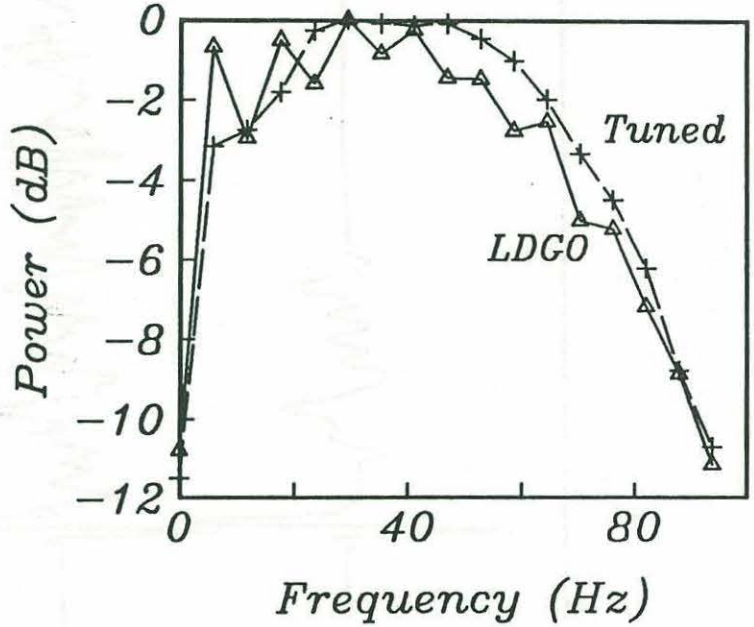
Power (dB)
0
−2
−4
−6
−8
−10
−12
Tuned
LDGO
0
40
80
Frequency (Hz)

Figure 11

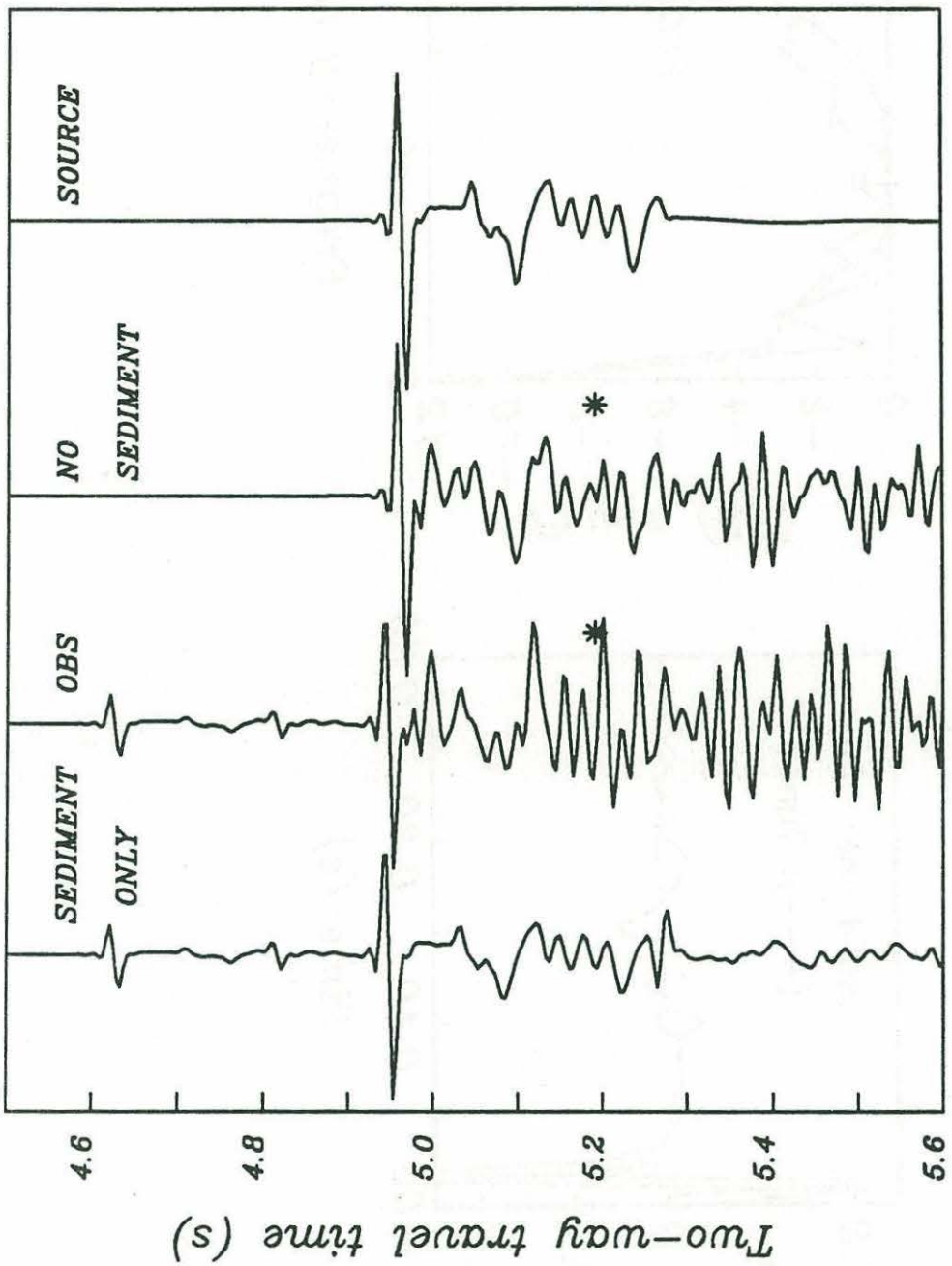
SOURCE
NO SEDIMENT
OBS
SEDIMENT ONLY
LDGO Array; 5-60 Hz; TVG
4.6
4.8
5.0
5.2
5.4
5.6
Two-way travel time (s)

Figure 12

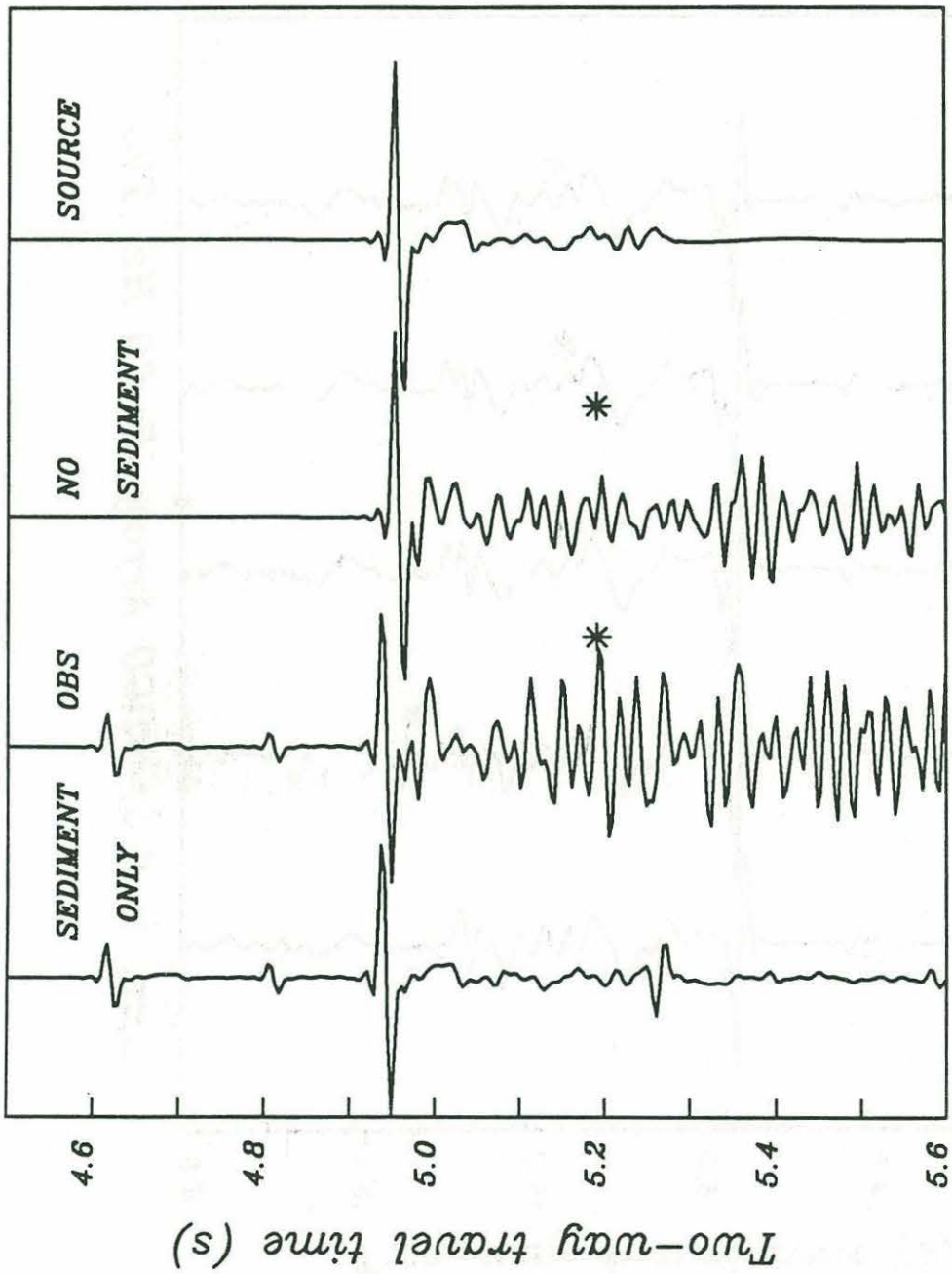
SEDIMENT ONLY
OBS
NO SEDIMENT
SOURCE
Tuned Array; 5-60 Hz; TVG
Two-way travel time (s)
4.6
4.8
5.0
5.2
5.4
5.6

Figure 13

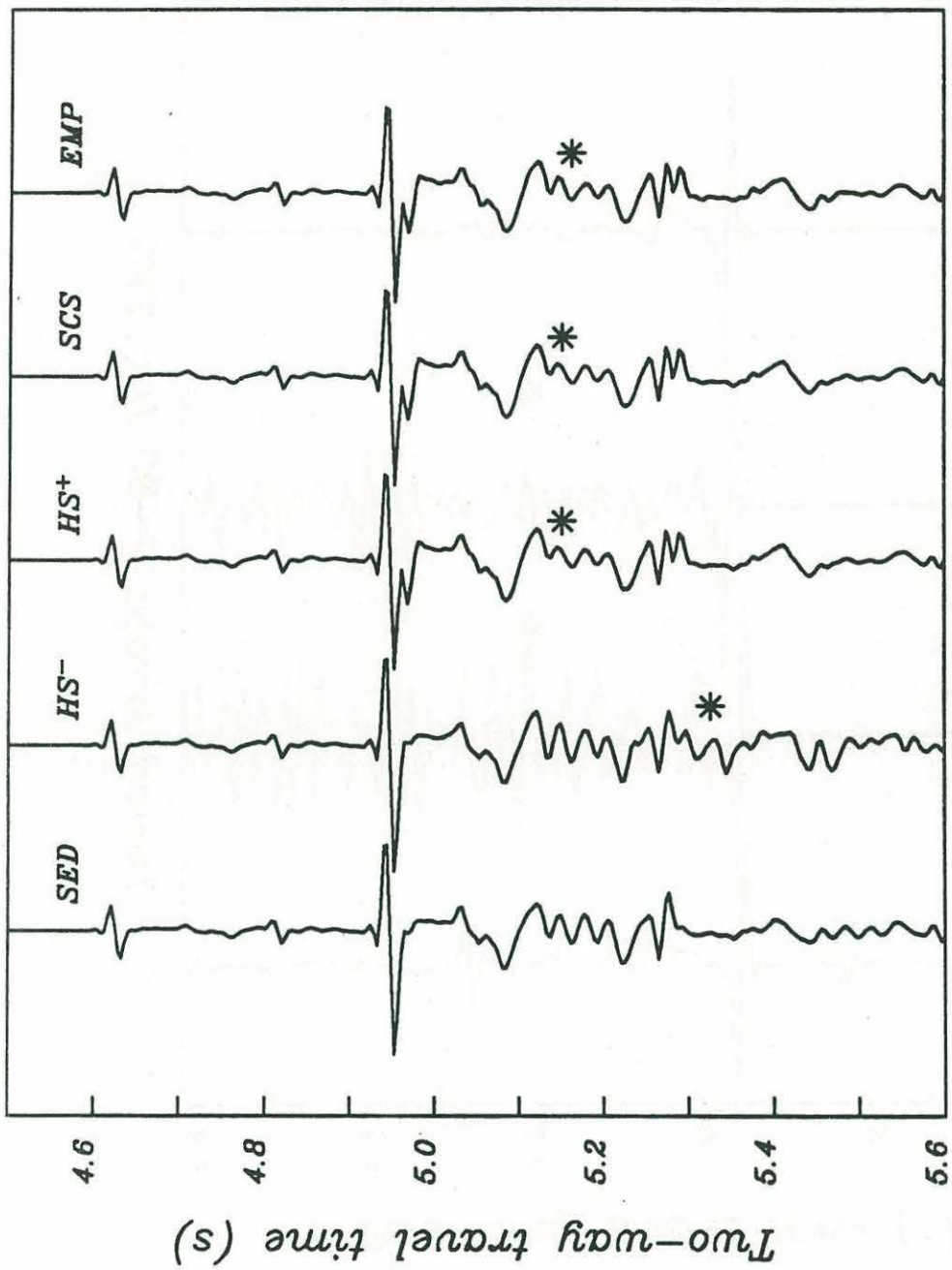
EMP
SCS
HS+
HS−
SED
Exp. = 1.5; LDGO Array; 5−60 Hz; TVG
4.6
4.8
5.0
5.2
5.4
5.6
Two−way travel time (s)

Figure 14a

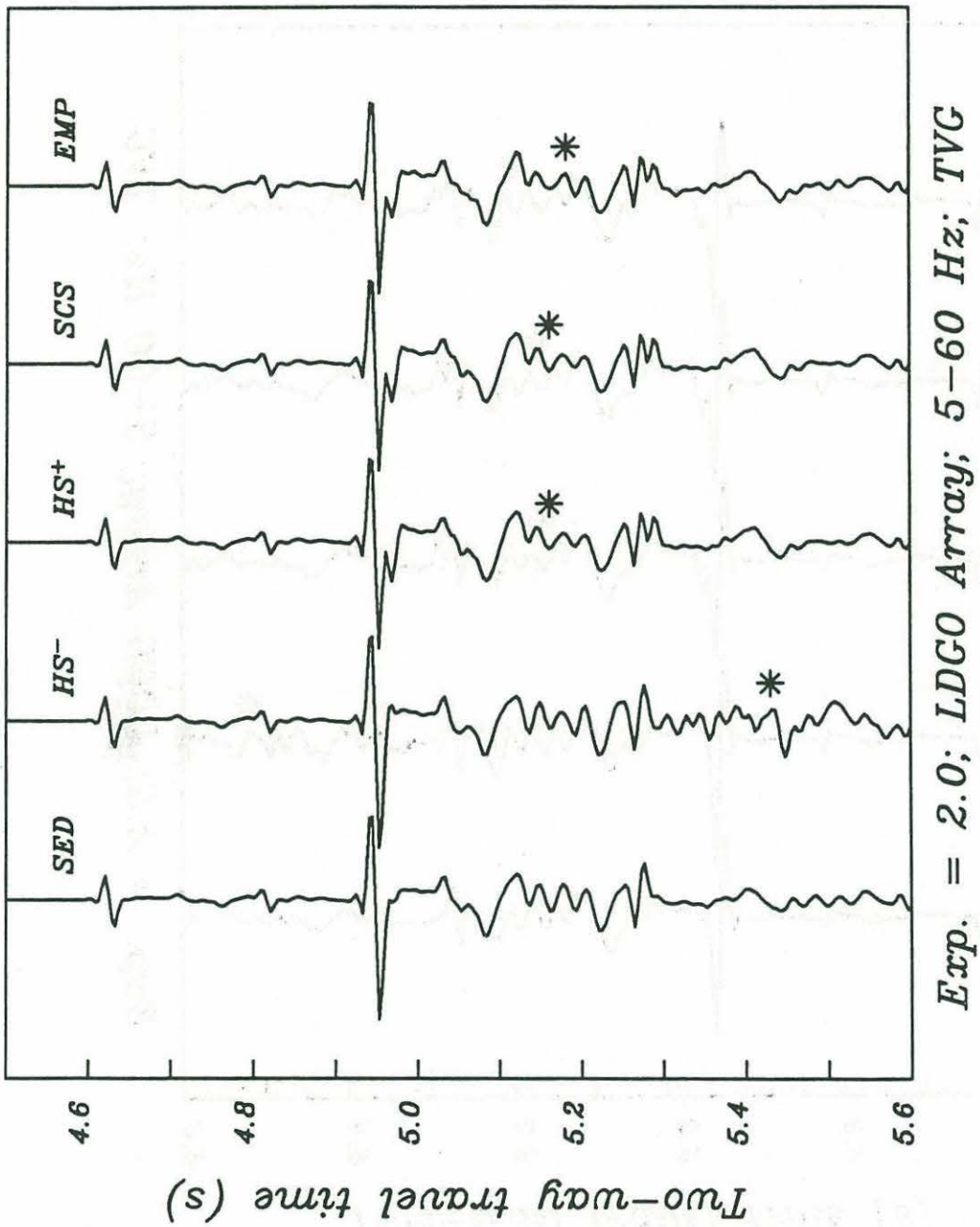
SED
HS−
HS+
SCS
EMP
4.6
4.8
5.0
5.2
5.4
5.6
Two−way travel time (s)
Exp. = 2.0; LDGO Array; 5−60 Hz; TVG

Figure 14b

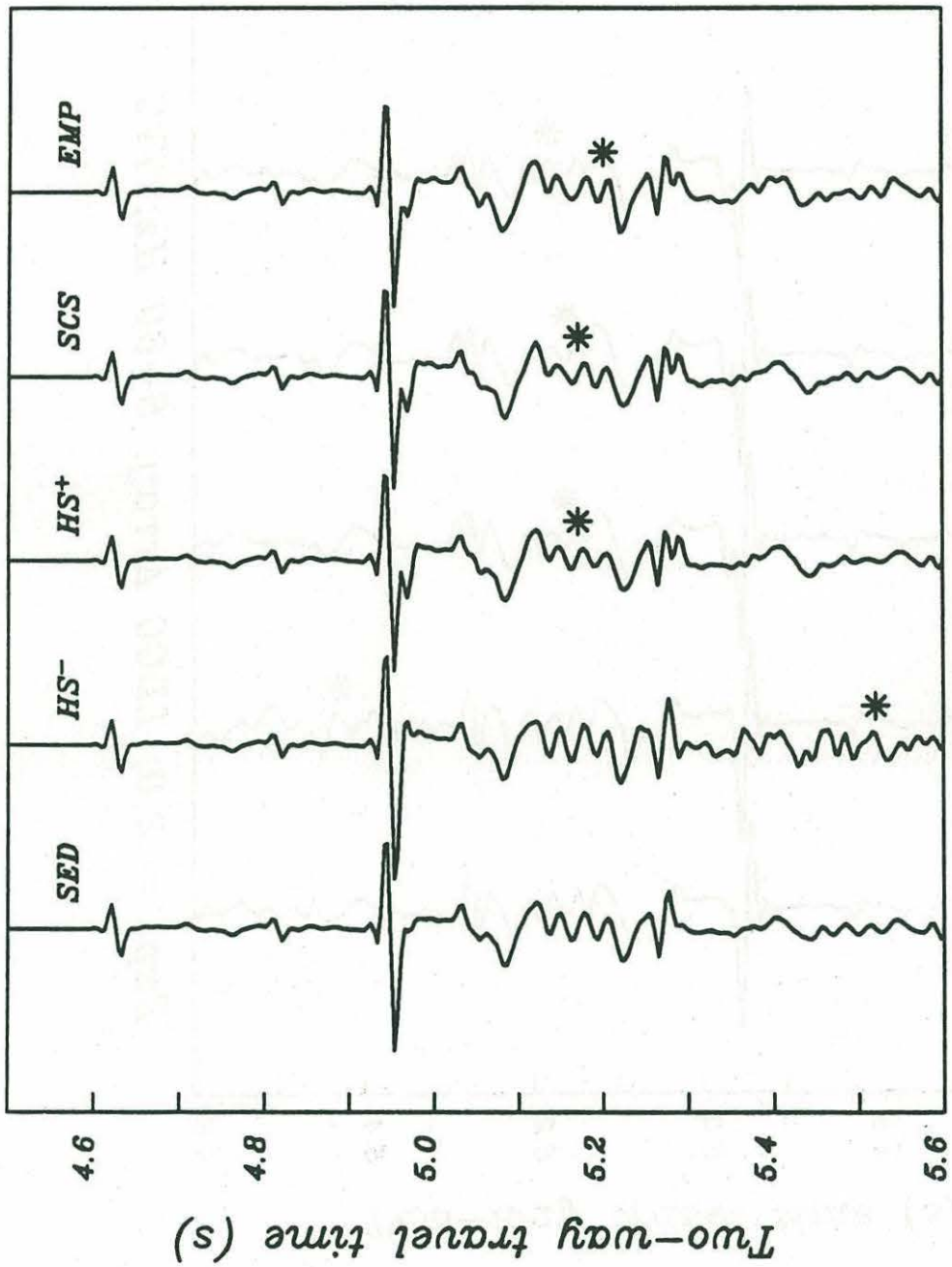
EMP
SCS
HS+
HS−
SED
Exp. = 2.5; LDGO Array; 5–60 Hz; TVG
Two–way travel time (s)
4.6
4.8
5.0
5.2
5.4
5.6

Figure 14c

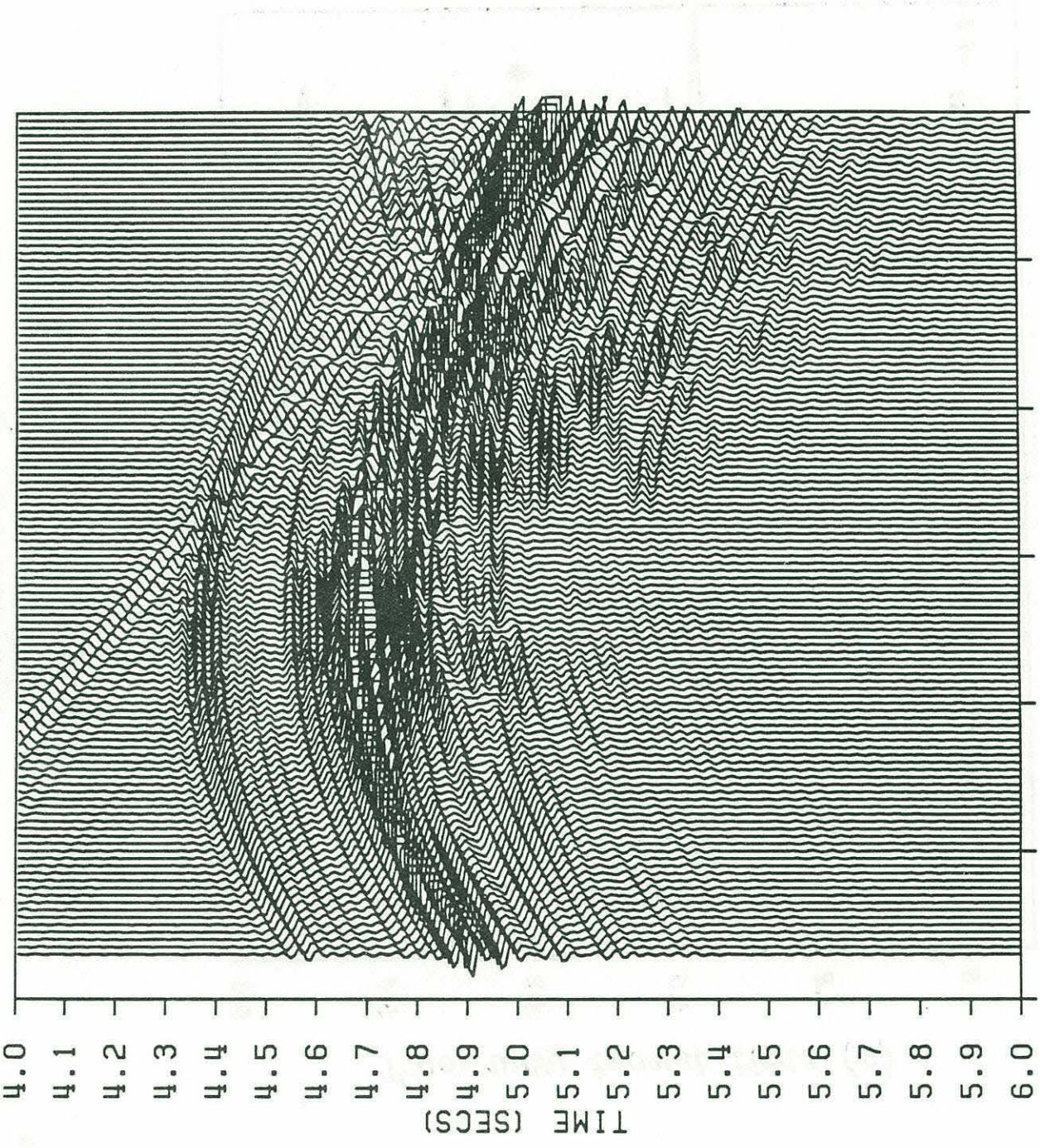
TIME (SECS)
4.0
4.1
4.2
4.3
4.4
4.5
4.6
4.7
4.8
4.9
5.0
5.1
5.2
5.3
5.4
5.5
5.6
5.7
5.8
5.9
6.0
0
1
2
3
4
5
6
RANGE (KMS)

Figure 15a

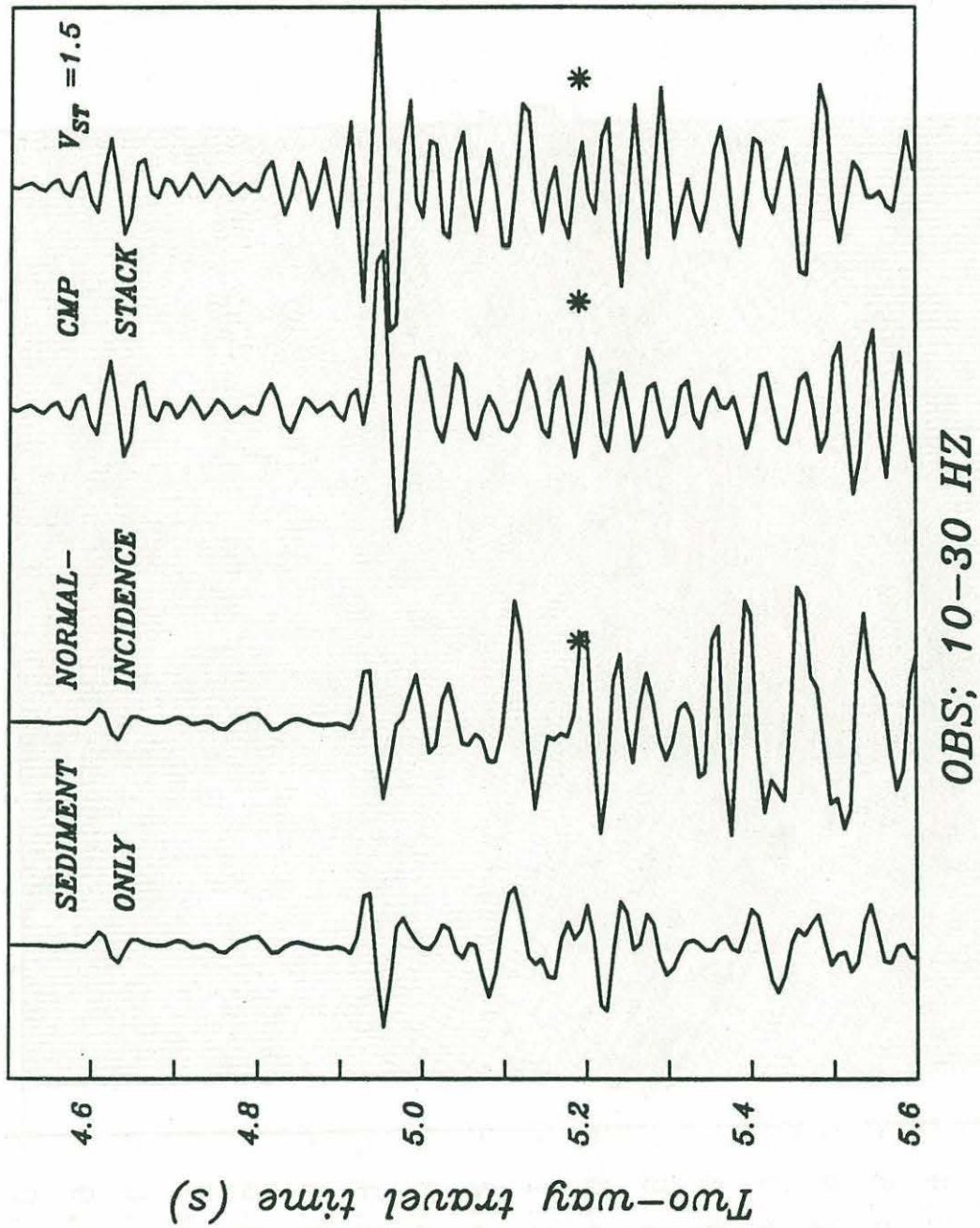
SEDIMENT ONLY
NORMAL-INCIDENCE
CMP STACK
V_{ST} =1.5
OBS; 10-30 HZ
Two-way travel time (s)
4.6
4.8
5.0
5.2
5.4
5.6

Figure 15b

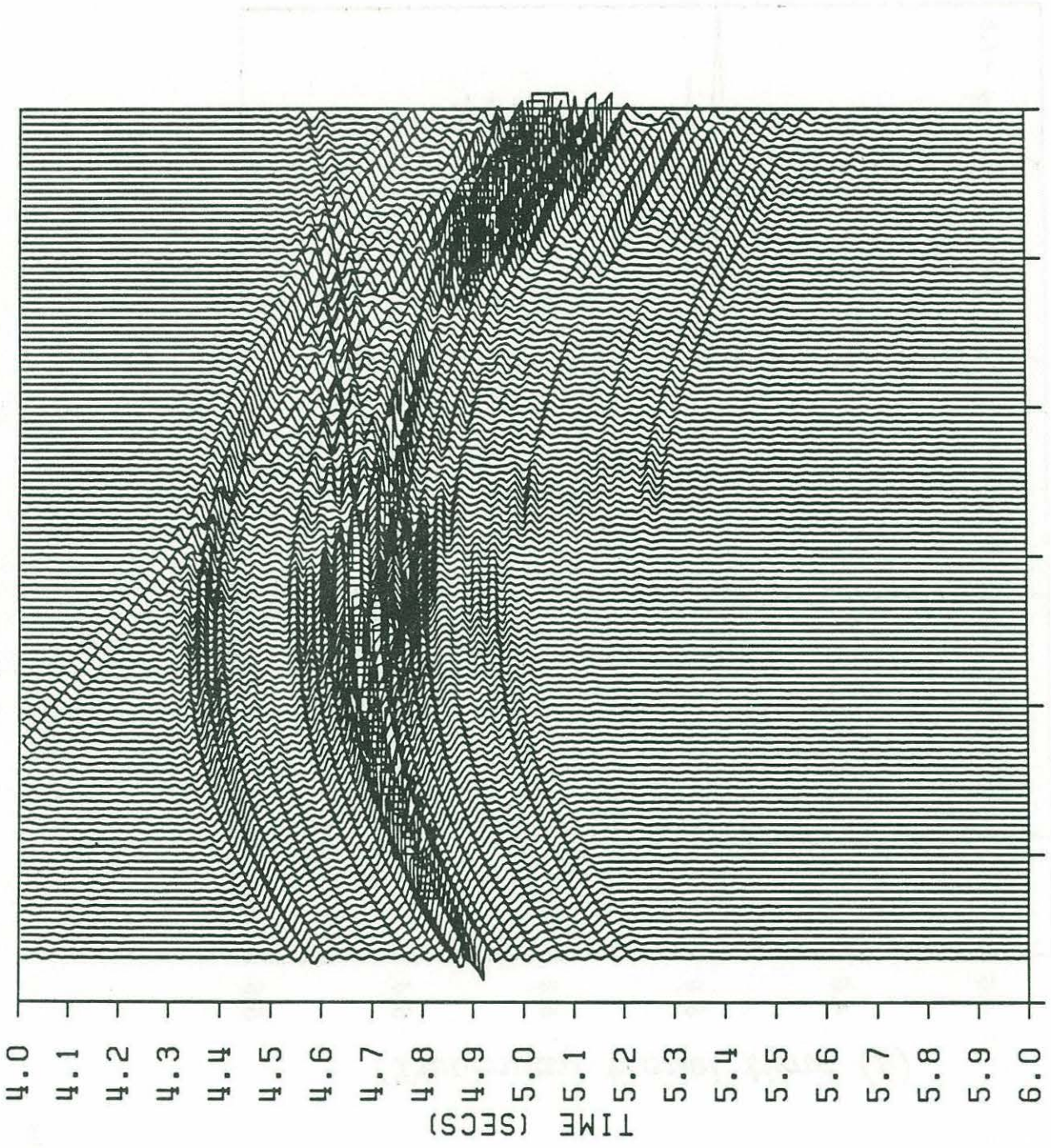
TIME (SECS)
4.0
4.1
4.2
4.3
4.4
4.5
4.6
4.7
4.8
4.9
5.0
5.1
5.2
5.3
5.4
5.5
5.6
5.7
5.8
5.9
6.0
0
1
2
3
4
5
6
RANGE (KMS)

Figure 16a

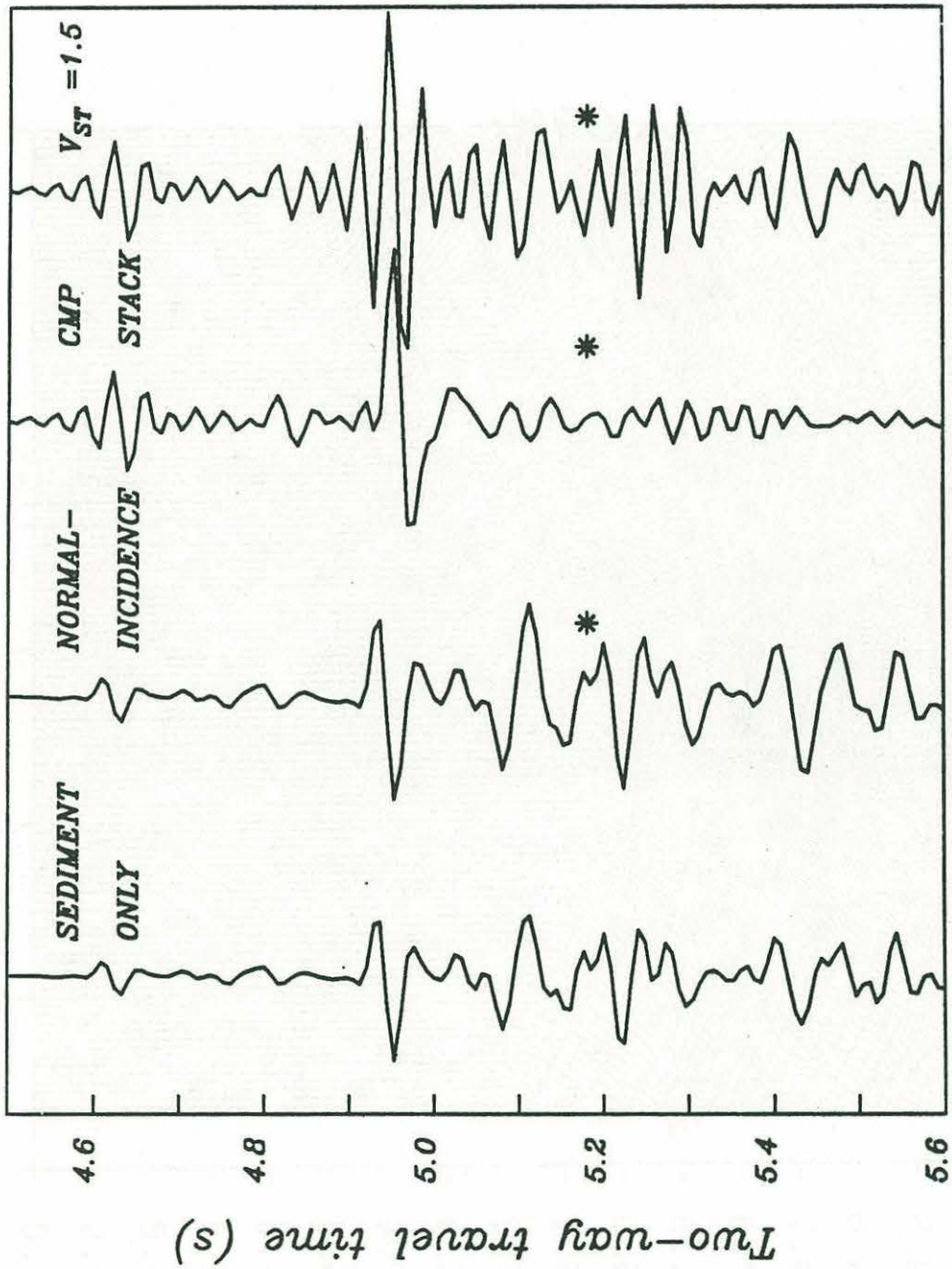
SEDIMENT ONLY
NORMAL-INCIDENCE
CMP STACK
V_{ST} =1.5
EMP20; 10-30 HZ
Two-way travel time (s)
4.6
4.8
5.0
5.2
5.4
5.6

Figure 16b

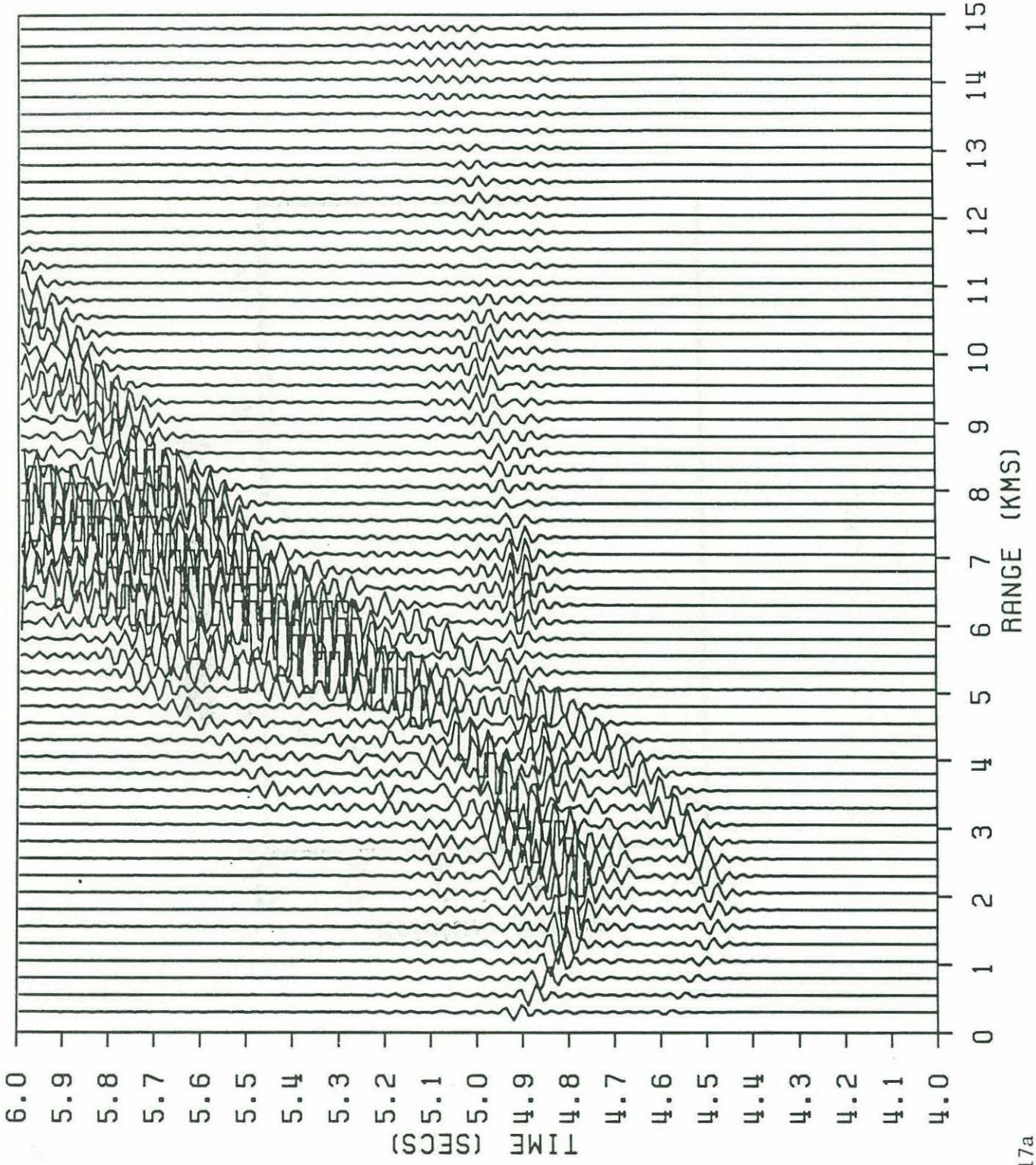
TIME (SECS)
6.0
5.9
5.8
5.7
5.6
5.5
5.4
5.3
5.2
5.1
5.0
4.9
4.8
4.7
4.6
4.5
4.4
4.3
4.2
4.1
4.0
0 1 2 3 4 5 6 7 8 9 10 11 12 13 14 15
RANGE (KMS)

Figure 17a

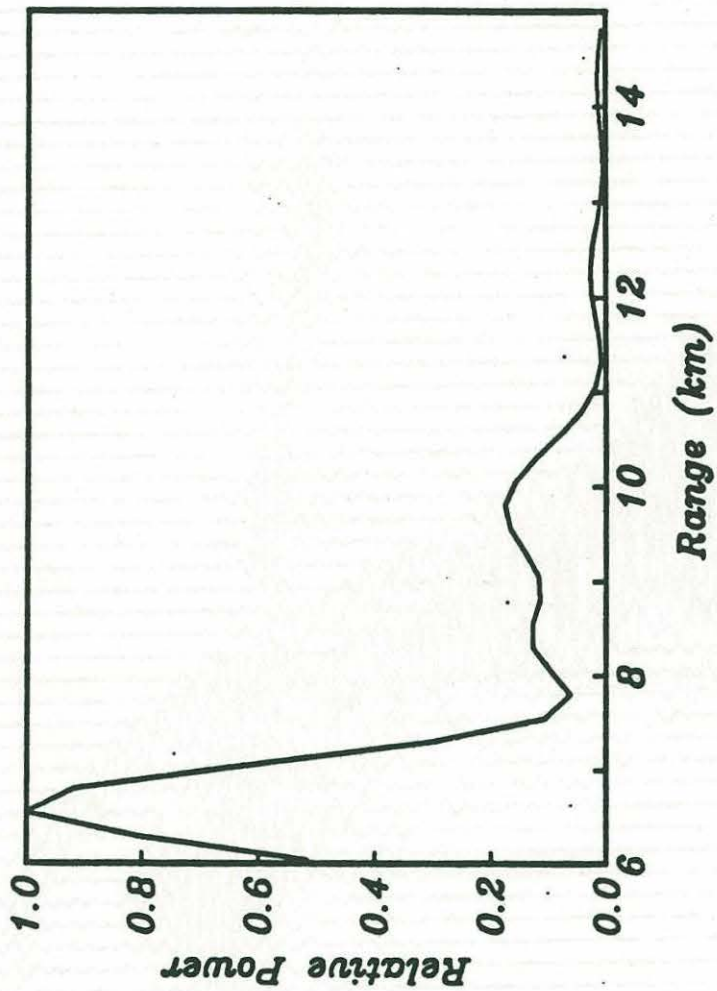

Figure 17b

CONCLUSION

A common theme to the three chapters that comprise this dissertation is the relationship between the geologic and seismic structures of the oceanic crust. This relationship is explored by comparing observed seismic data to synthetic seismograms calculated (i) for the fossil Moho structure mapped in ophiolites (Chapter 1), and (ii) for the downhole geological structure at DSDP Site 504B (Chapter 3). Correlation of the velocity and geological structure of the middle and lower crust at Site 504B (Chapter 2) awaits additional drilling. A related theme shared by these chapters is the importance of careful seismic modeling as a guide to the geological interpretation of seismic structure. Modeling of plausible geological models demonstrates the capability of seismic methods to detect geological boundaries, and highlights potential pitfalls in the interpretation of seismic data.

The primary results of this dissertation are summarized here. In Chapter 1, the geological structures that generate Moho reflections are investigated by calculating reflection profiles for laterally-varying velocity models appropriate to the fossil crust/mantle boundary exposed in the Bay of Islands Ophiolite. The geometry and duration of the single- and multi-phase Moho reflection events are similar to those observed on MCS data. The similarities between the synthetic and observed data suggest that the complicated interlayered sequences of mafic and ultramafic rocks that comprise the fossil crust/mantle transition in ophiolites might also be characteristic of the oceanic crust.

In Chapter 2, combined interpretation of MCS data and wide-angle reflection/refraction data collected at DSDP Site 504B demonstrates that the crustal thickness is only 5 km, about 1-2 km less than values typically reported for oceanic crust located away from fracture zones. The location of this deep drillhole on relatively thin crust is fortuitous, and makes Site 504B an attractive location for renewed crustal drilling. The velocity-depth profile of the middle and lower crust at Site 504B is also unusual in comparison to typically reported profiles in having high velocity gradients (up to 0.6 km s^{-1} km^{-1}) in the middle crust and a 1.8 km thick low-velocity zone (V_p=7.1-6.7 km s^{-1}) immediately above Moho. A simple explanation for this unusual profile is that the velocity of the middle crust has been increased by the addition of a high-velocity mineral component such as olivine. The olivine concentration of the middle crust need be no greater than 34-37%. Both the relatively thin crust and high-velocity layer in the middle crust are consistent with the geochemistry of basalts recovered from Hole 504B. These rocks are slightly depleted in incompatible elements relative to typical mid-ocean ridge basalts, and may be indicative of a mantle source depleted by an earlier melting event.

In Chapter 3, extensive processing of the MCS data collected at Site 504B shows no conclusive evidence for laterally coherent reflection events generated within the upper 1-2 km of the crust. This is a surprising observation because drilling shows a well-defined change in physical properties at sub-basement depths of ~0.5-0.6 km, corresponding to the volcanics/sheeted-dike transition. In addition, the normal-incidence travel time to this boundary is similar to the travel times of

shallow reflection events observed in other areas. The difficulty in identifying a reflection event generated within the upper crust at Site 504B is understandable on inspection of synthetic reflection seismograms calculated for velocity-depth profiles constructed from the logged downhole variations in physical properties. Low-amplitude reflections from the extrusives/sheeted-dike transition are obscured by sediment-column multiples and by the 0.3-0.4 s duration of the source pulse.

Synthetic modeling of the upper oceanic crust at Site 504B shows that correlaton of geologic and seismic structure is non trivial. This is particularly true where low-impedance boundaries lie close to the high-impedance boundary at the top of the igneous crust. In this case, the duration of the source pulse must be less than the crustal travel time to the boundary of interest. Additional complications are introduced by sediment-column multiples. The acquisition of both near-normal-incidence reflection data and wide-angle reflection/refraction data improves the chances of correlating geologic and seismic structure. Geological boundaries that are transparent to reflection methods may generate high-amplitude refracted arrivals.

The complementary nature of the near-normal-incidence and wide-angle reflection/refraction methods is unambiguously demonstrated by comparing the reflection and refraction signatures of simple velocity transitions (Figure 1). These layer boundaries are characterized by a constant velocity contrast but variable gradient thicknesses. Synthetic seismogram modeling demonstrates that the amplitude of the reflected signal from these gradients decreases rapidly as the gradient thickness

increases (Figure 2). Computation of the total power in the reflected signal as a function of gradient thickness shows an exponential relationship between these two variables (Figure 3). For MCS data characterized by random or coherent noise, the reflected signal from similar boundaries might be undetectable when the gradient thickness exceeds a couple of hundred meters.

In contrast to the reflected signature, the refracted signal of these boundaries increases as the gradient thickness increases. The profiles displayed in Figure 4 show high-amplitude arrivals caused by diving waves refracted within the gradient layers. The horizontal range at which the maximum amplitudes are observed coincides with the triplication point in the travel time curve for each of these models. This critical range increases as the gradient thickness increases (Figure 4). Computation of the power in the refracted signal shows that the relative change in signal magnitude as a function of gradient thickness (Figure 5) is significantly less than that observed for the near-normal-incidence reflection case (Figure 5). As the gradient thickness increases from 0.25 km to 0.75 km, the magnitude of the refraction power peak increase by less than 4 dB. In contrast, the near-normal-incidence reflection power decreases by more than 15 dB.

FIGURE CAPTIONS

Figure 1. Examples of simple layer boundaries characterized by a constant increase in velocity of 1.5 km s^{-1} but variable thicknesses ranging from 0.0 km to 0.75 km. These profiles approximate the Layer 2/Layer 3 transition of the oceanic crust.

Figure 2. Near-normal-incidence reflection seismograms calculated for the velocity-depth profiles shown in Figure 1. These seismograms, generated by stacking 48-fold CMP gathers with seismograms ranges of 0.3-2.7 km, were computed using the reflectivity method (see references, chapter 3). The integration limits were 0.16° and 40°, corresponding to phase velocities of 500 km s^{-1} and 2.175 km s^{-1}, respectively. The angle increment was 0.023°. This choice of parameters introduces a high-amplitude numerical arrival with a phase velocity of 2.175 km s^{-1} but results in negligible "ringing". However, the false arrival has negligible effect on the seismograms included in the CMP stack. The star symbol indicates the travel times to the top and bottom of the velocity gradient. Amplitudes are comparable for (a) and for (b).

Figure 3. Relative power of the reflected arrivals in the seismograms shown in Figure 2 as a function of gradient thickness. Power was computed in a time window extending from 5.5 to 6.1 s.

Figure 4. Reflectivity synthetic seismograms for gradient thicknesses of (a) 0.0 km, (b) 0.25 km, (c) 0.50 km, and (d) 0.75 km. Amplitudes are multiplied by a linear function of range, and plotted with a reduction

velocity of 4.5 km s^{-1}. The seismograms were calculated using integration limits of 0.07° and 69°, corresponding to phase velocities of 1100 km s^{-1} and 1.5 km s^{-1}, respectively. The angle increment was 0.04°. This choice of parameters does not introduce false arrivals but does cause low-amplitude reverberative noise. However, this noise has negligible effect on the observed amplitude focusing.

Figure 5. Power of the refracted arrivals shown in Figure 4 as a function of horizontal range and gradient thickness. The time window over which power was computed extended from 4.2-5.0 s reduced time. The magnitudes of the power values are comparable to those shown in Figure 3.

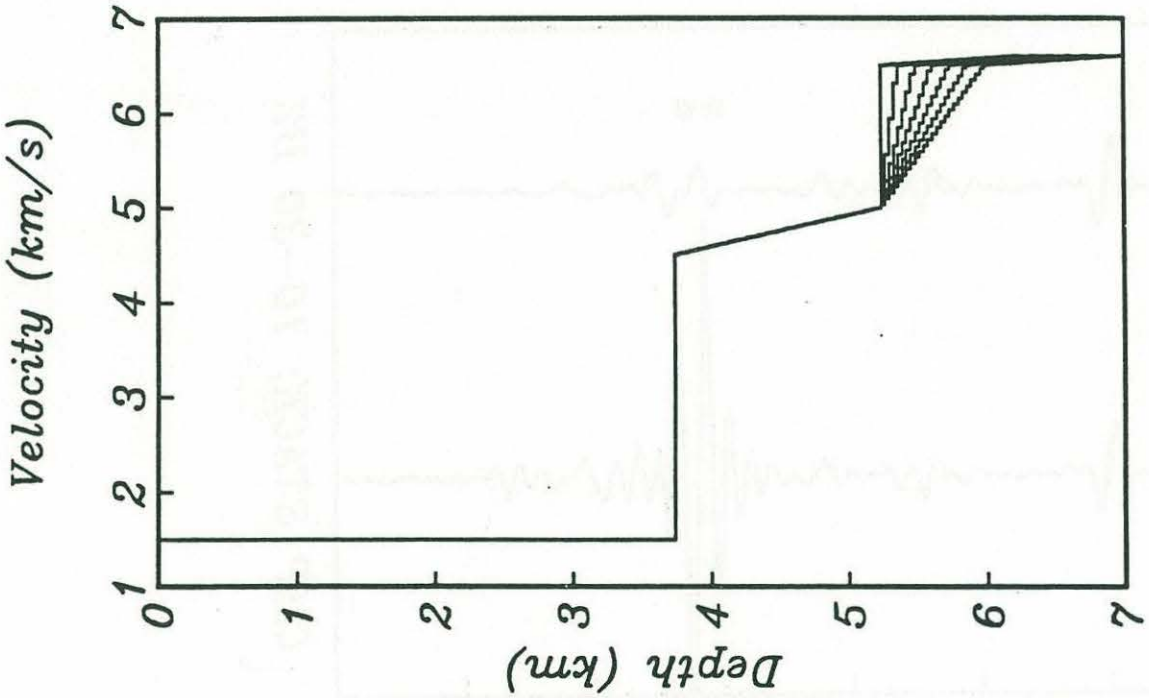

Figure 1

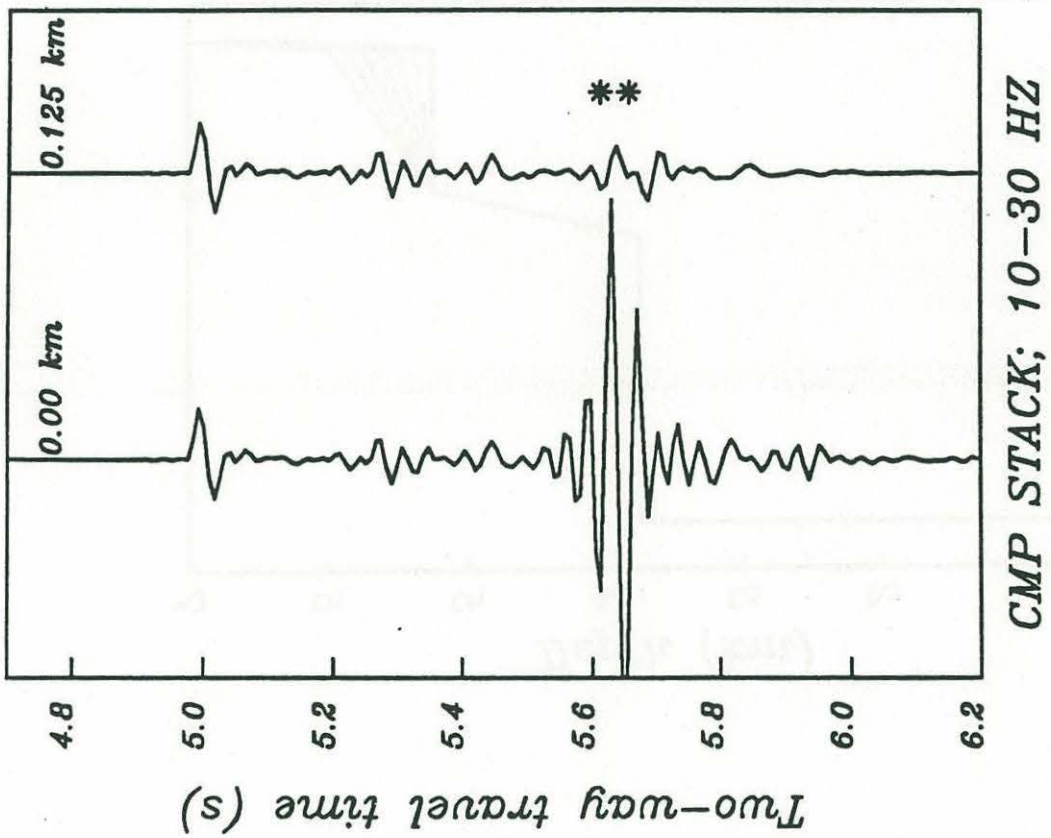
0.125 km
0.00 km
**
CMP STACK; 10-30 HZ
4.8
5.0
5.2
5.4
5.6
5.8
6.0
6.2
Two-way travel time (s)

Figure 2a

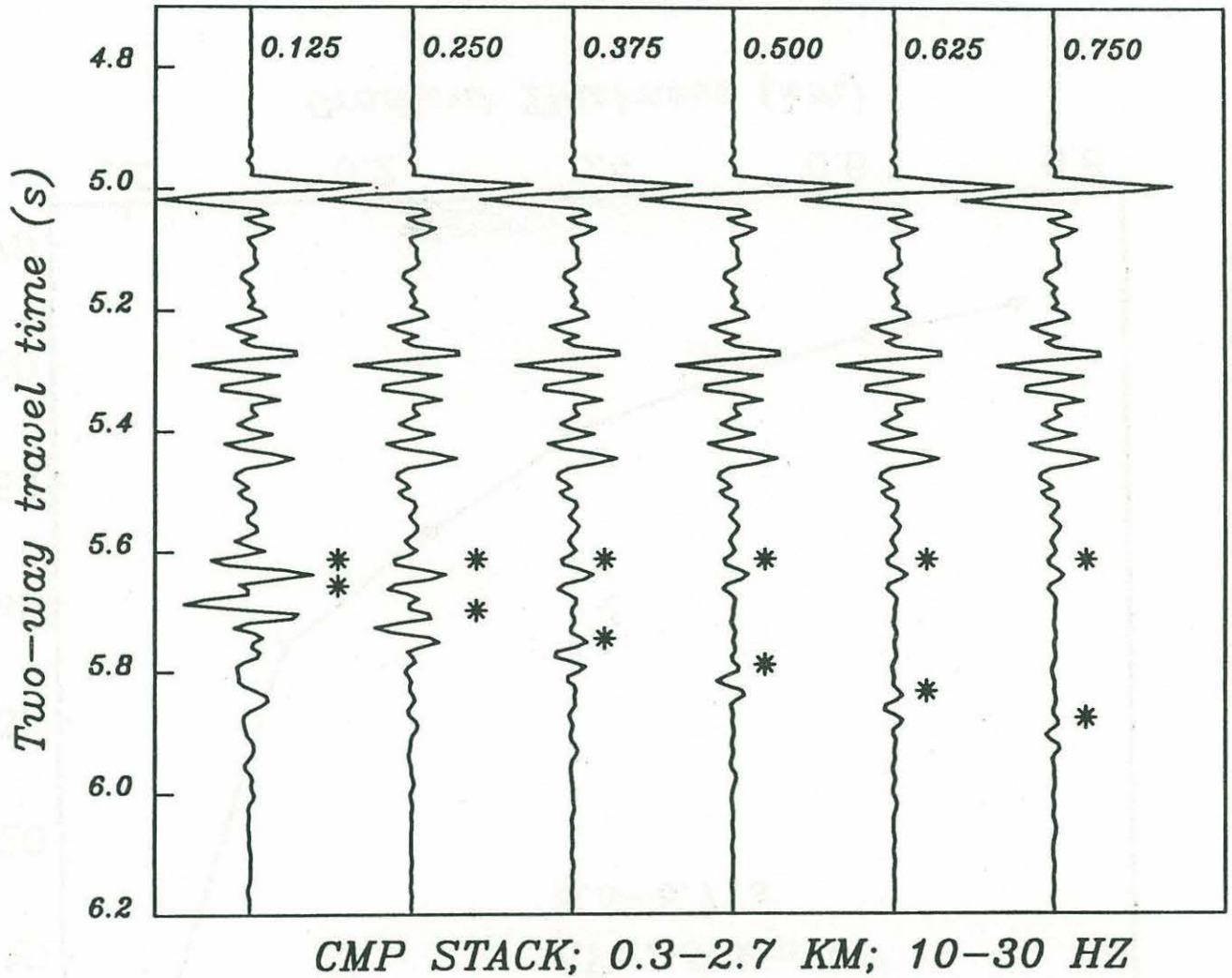
0.125
0.250
0.375
0.500
0.625
0.750
4.8
5.0
5.2
5.4
5.6
5.8
6.0
6.2
Two-way travel time (s)
CMP STACK; 0.3-2.7 KM; 10-30 HZ

Figure 2b

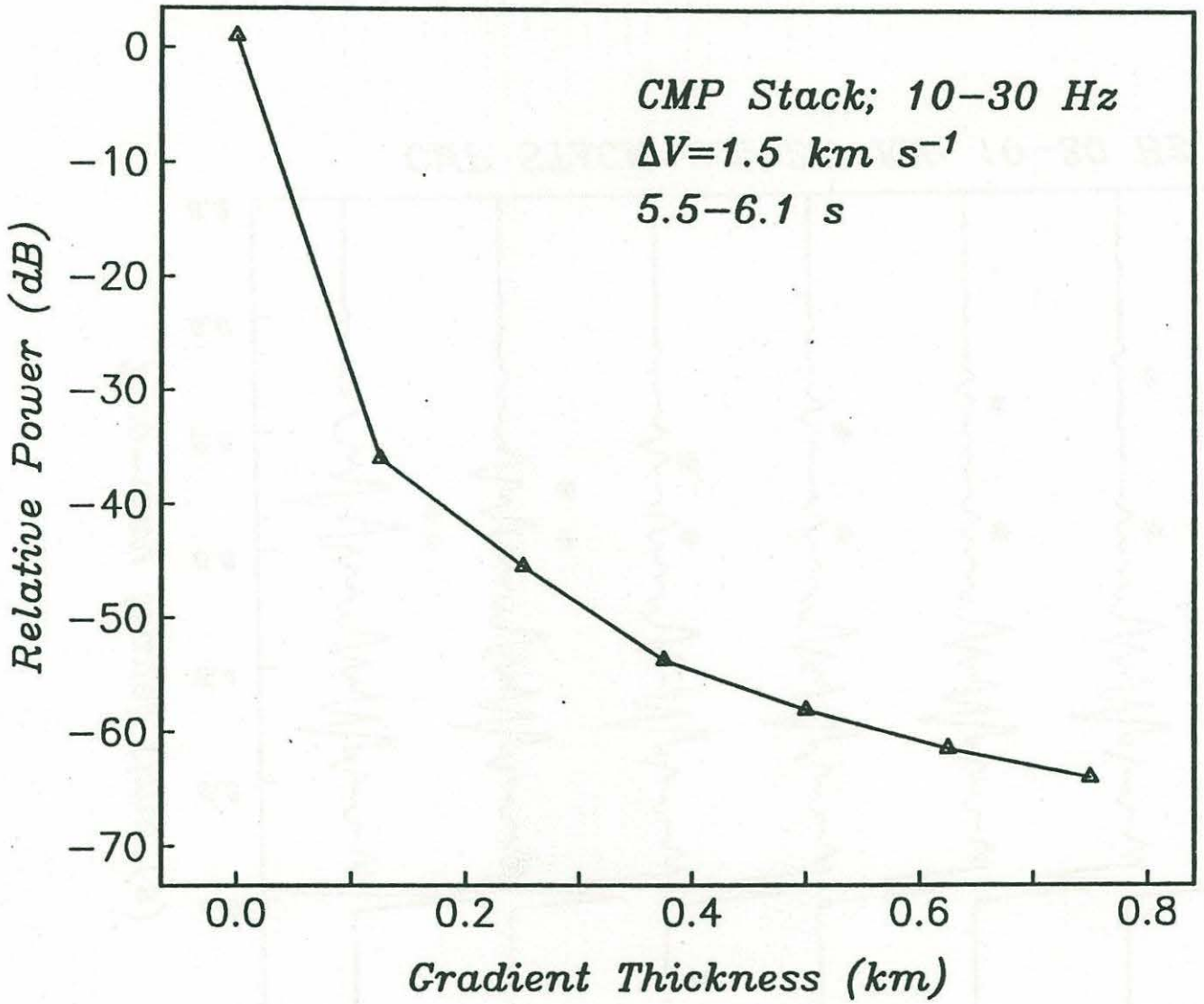
CMP Stack; 10–30 Hz
ΔV=1.5 km s⁻¹
5.5–6.1 s
Relative Power (dB)
0
−10
−20
−30
−40
−50
−60
−70
0.0
0.2
0.4
0.6
0.8
Gradient Thickness (km)

Figure 3

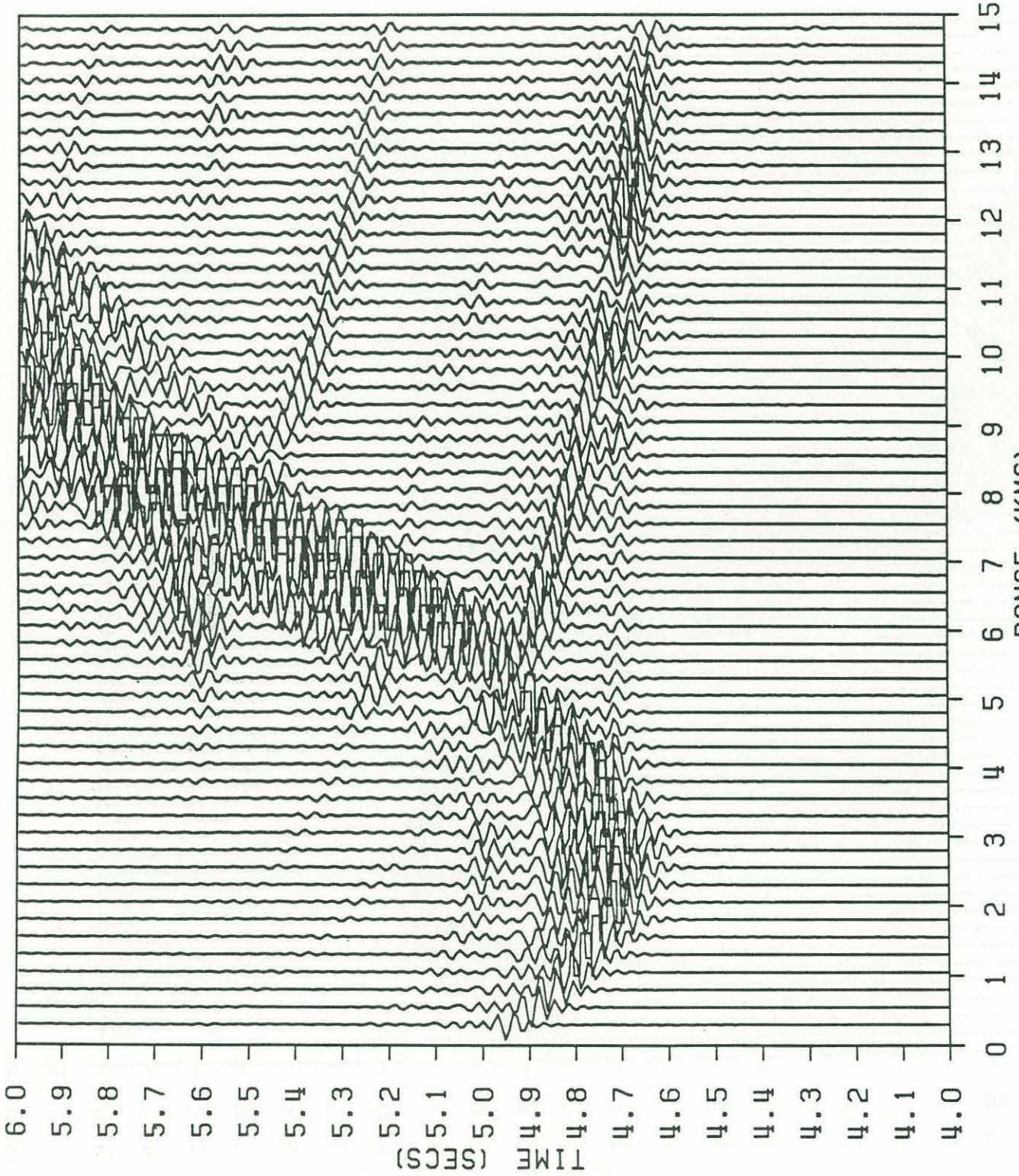
TIME (SECS)
6.0
5.9
5.8
5.7
5.6
5.5
5.4
5.3
5.2
5.1
5.0
4.9
4.8
4.7
4.6
4.5
4.4
4.3
4.2
4.1
4.0
0 1 2 3 4 5 6 7 8 9 10 11 12 13 14 15
RANGE (KMS)

Figure 4a

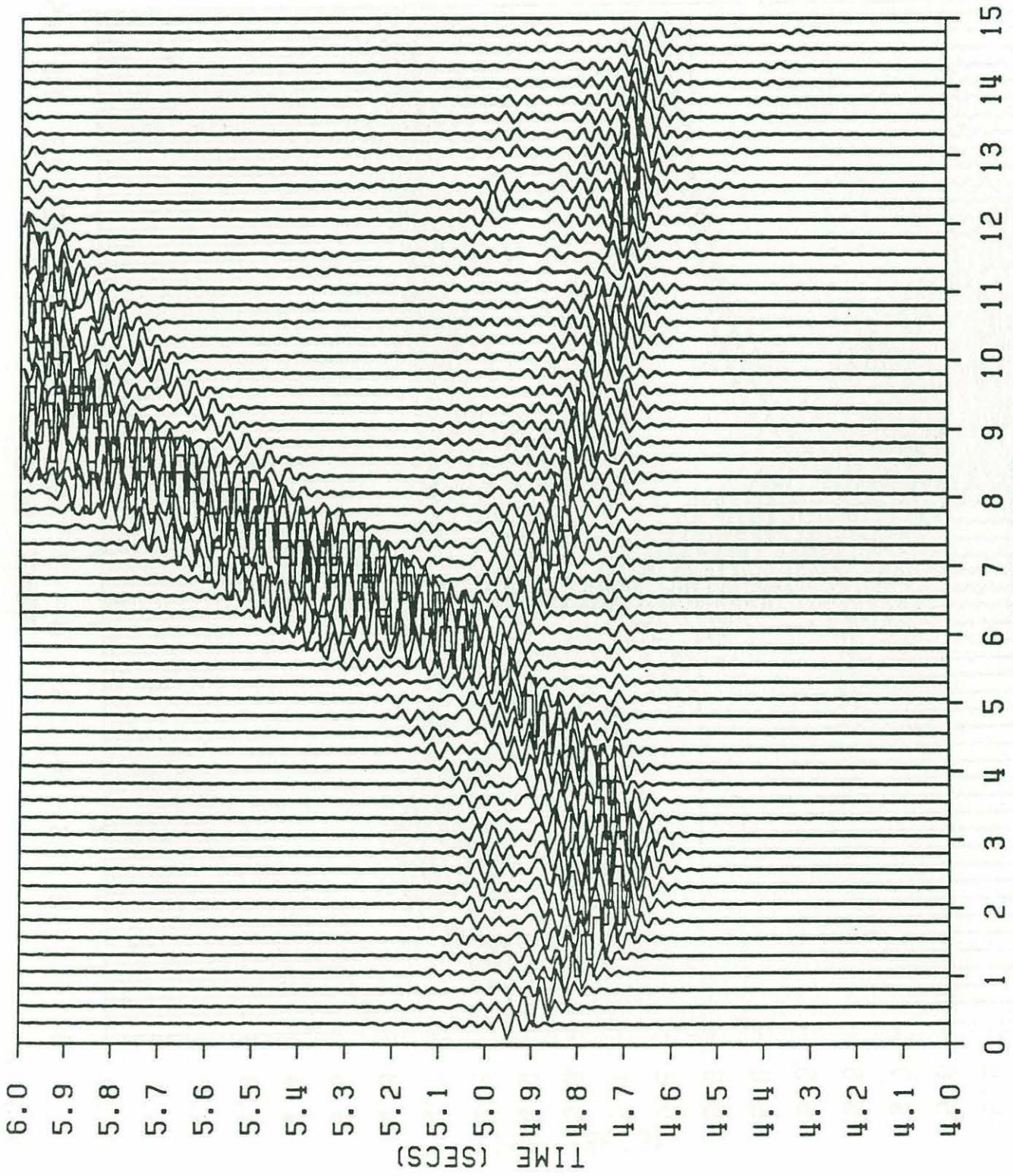
TIME (SECS)
6.0
5.9
5.8
5.7
5.6
5.5
5.4
5.3
5.2
5.1
5.0
4.9
4.8
4.7
4.6
4.5
4.4
4.3
4.2
4.1
4.0
0
1
2
3
4
5
6
7
8
9
10
11
12
13
14
15
RANGE (KMS)

Figure 4b

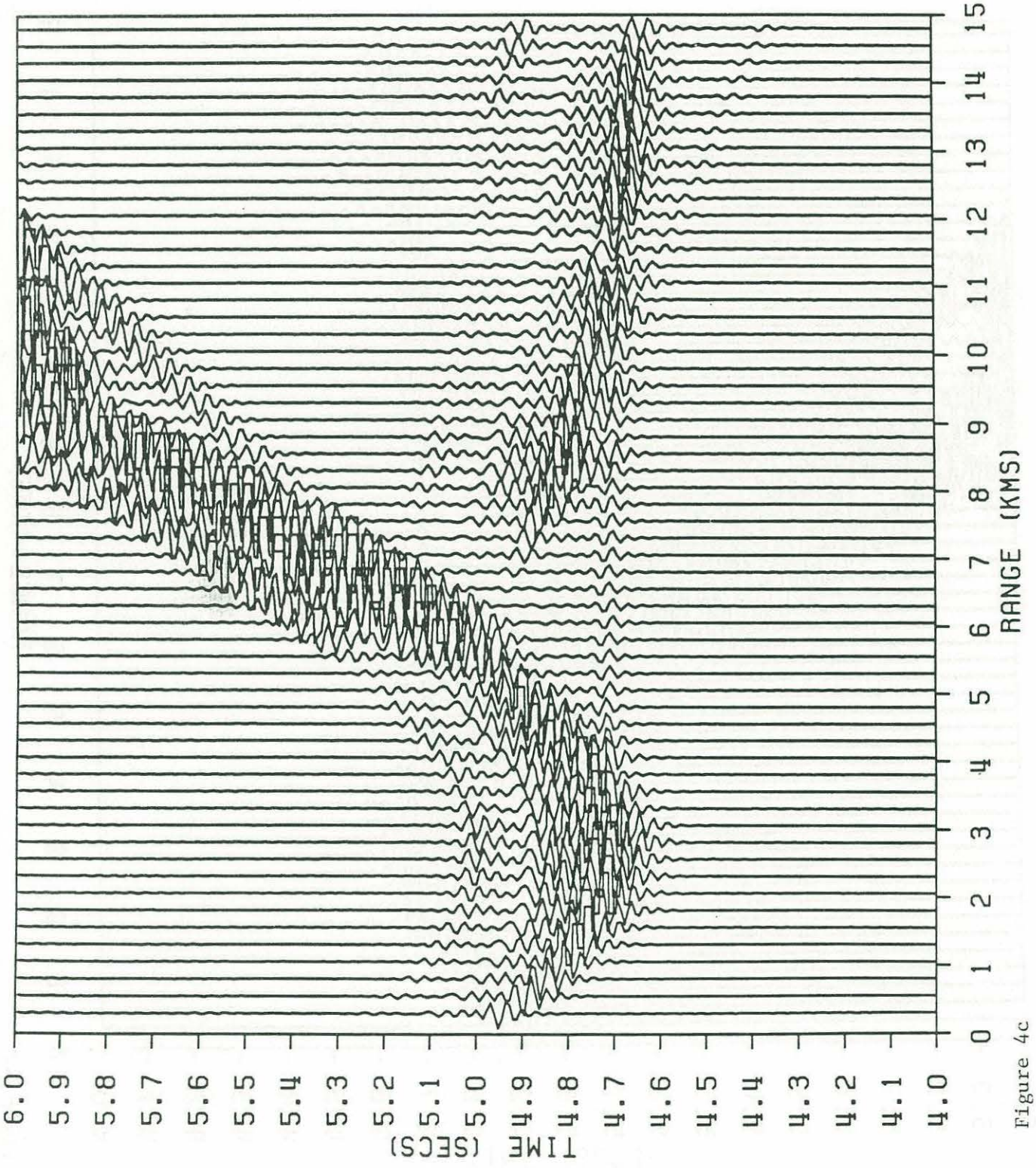
TIME (SECS)
6.0
5.9
5.8
5.7
5.6
5.5
5.4
5.3
5.2
5.1
5.0
4.9
4.8
4.7
4.6
4.5
4.4
4.3
4.2
4.1
4.0
0 1 2 3 4 5 6 7 8 9 10 11 12 13 14 15
RANGE (KMS)

Figure 4c

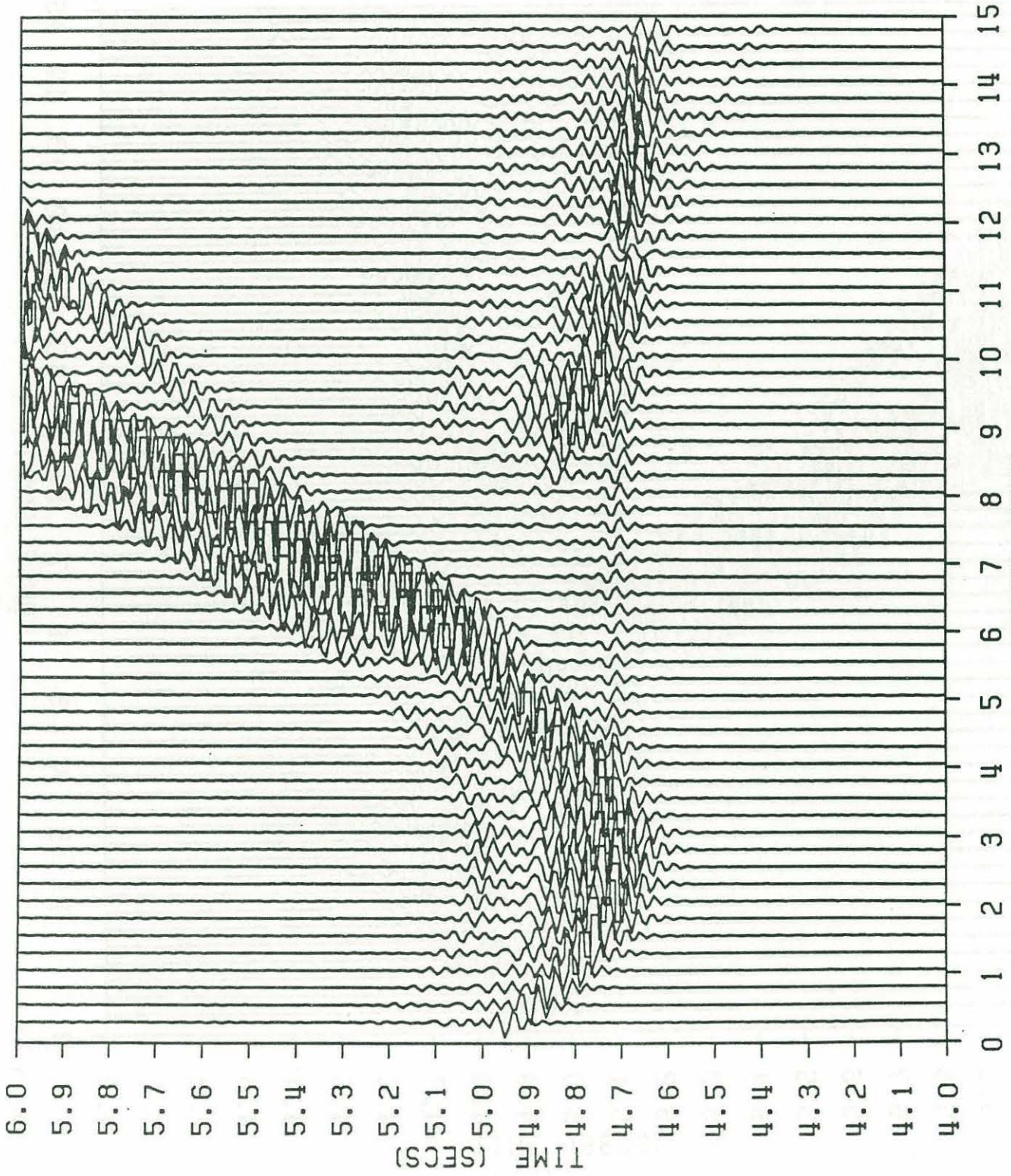
TIME (SECS)
6.0
5.9
5.8
5.7
5.6
5.5
5.4
5.3
5.2
5.1
5.0
4.9
4.8
4.7
4.6
4.5
4.4
4.3
4.2
4.1
4.0
0 1 2 3 4 5 6 7 8 9 10 11 12 13 14 15
RANGE (KMS)

Figure 4d

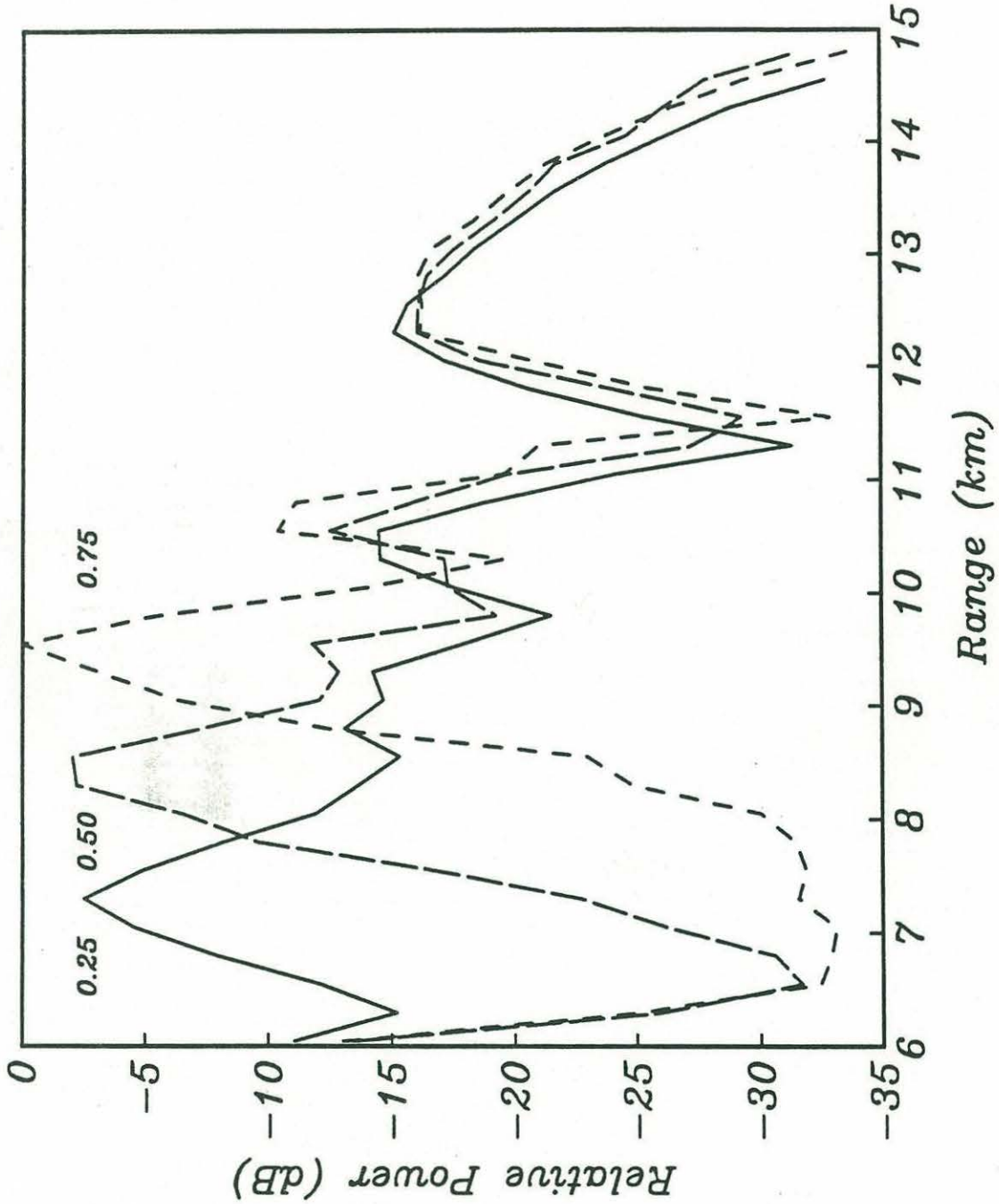
0
−5
−10
−15
−20
−25
−30
−35
Relative Power (dB)
6
7
8
9
10
11
12
13
14
15
Range (km)
0.25
0.50
0.75

Figure 5